Volume: 3 Issue: 2 e-ISSN: 2791-7630

JIENS

Journal of Innovative Engineering and Natural Science

Yenilikçi Mühendislik ve Doğa Bilimleri Dergisi

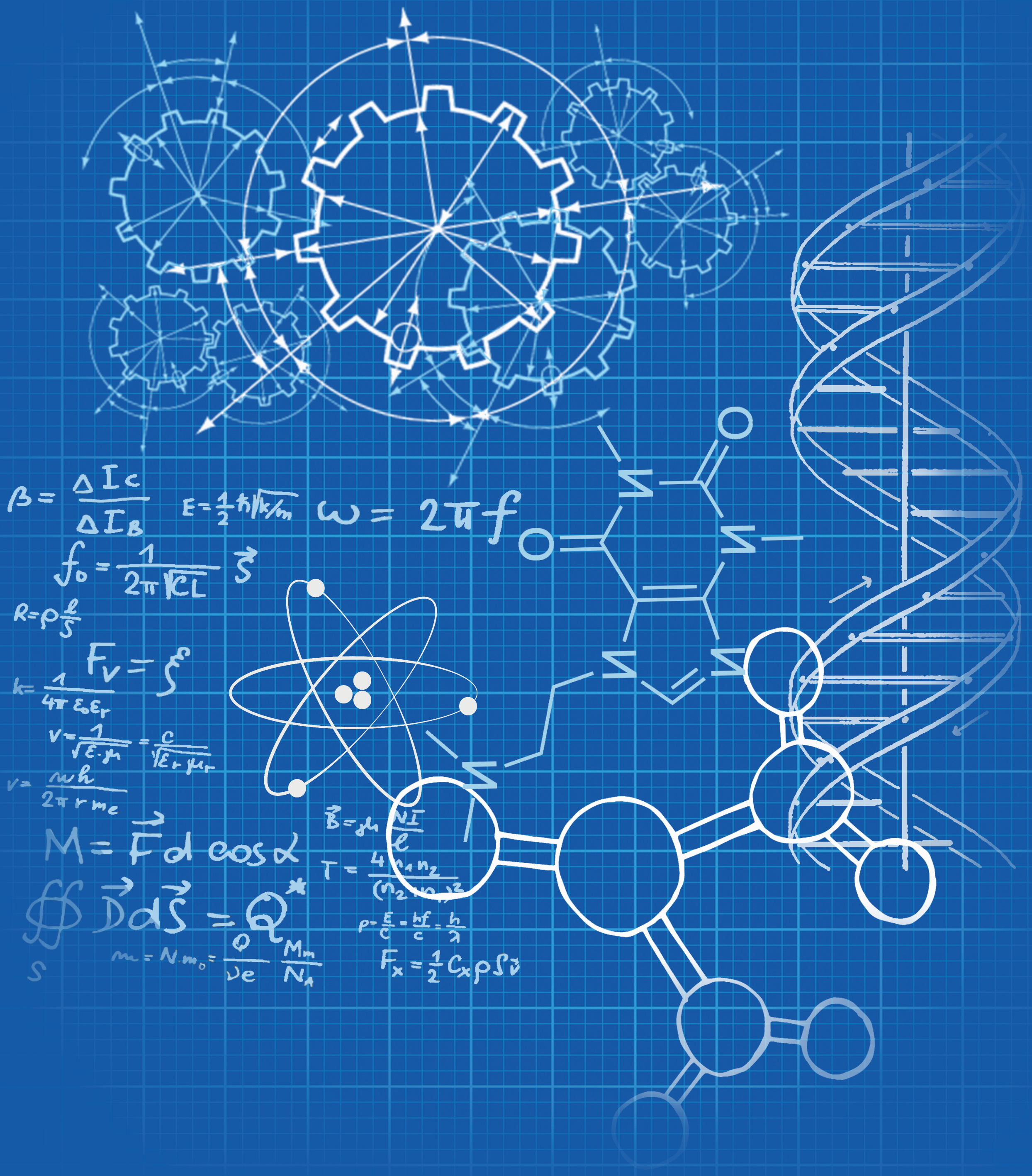

www.jiens.org

JOURNAL OF INNOVATIVE ENGINEERING AND NATURAL SCIENCE

YENİLİKÇİ MÜHENDİSLİK VE DOĞA BİLİMLERİ DERGİSİ

e-ISSN: 2791-7630

Yalova – Turkey

Year / *Yıl*	Volume / *Cilt*	Issue / *Sayı*
2023	**3**	**2**

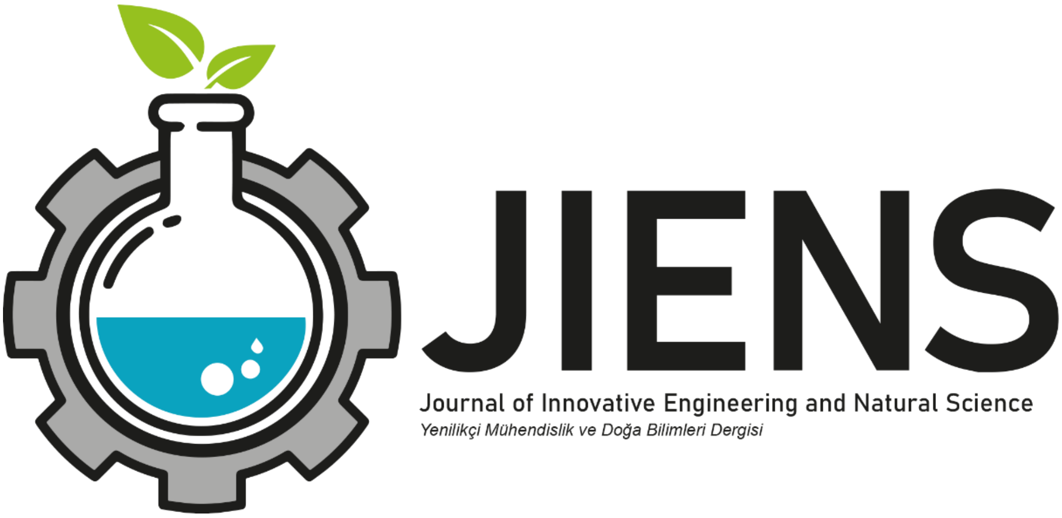

Journal Cover Design / Dergi Kapak Tasarımı: İdris Karagöz

Journal Cover Artwork / Dergi Kapak Resmi: Fatma Aleyna Ceylan

Journal of Innovative Engineering
and Natural Science
(Yenilikçi Mühendislik ve Doğa Bilimleri Dergisi)
journal homepage: https://jiens.org

Product Information / Ürün *Bilgisi*

Publisher *Yayıncı*	İdris Karagöz
Owner *Sahibi*	İdris Karagöz
Editor-in-Chief *Baş Editör*	İdris Karagöz
Publishing Manager *Sorumlu Yazı İşleri Müdürü*	İdris Karagöz
e-ISSN Number *e-ISSN Numarası*	2791-7630
Web Page *Web Sayfası*	https://jiens.org
Date of Online Publication *Online Basım Tarihi*	31.07.2023
Language *Dili*	English / Turkish *İngilizce / Türkçe*
Frequency *Yayın Aralığı*	Published two times in a year Yılda iki kere yayınlanır
Type of Publication *Yayın Türü*	Periodical Süreli yayın
Abstracted and indexed in *Tarandığı ve Özetlendiği Dizinler*	
Telephone *Telefon*	+90 (226) 815 61 81
Fax *Faks*	+90 (226) 815 54 00
E-mail *E-posta*	jiens@jiens.org
Correspondence Adress *Yazışma Adresi*	Yalova University Faculty of Engineering, Yalova University Central Campus, On the Çınarcık Road 77200 Yalova, Turkey *Yalova Üniversitesi Mühendislik Fakültesi, Yalova Üniversitesi Merkez Yerleşkesi, Çınarcık Yolu Üzeri 77200 Yalova, Turkiye*

Journal of Innovative Engineering and Natural Science
(Yenilikçi Mühendislik ve Doğa Bilimleri Dergisi)
journal homepage: https://jiens.org

Editor-in-Chief
Baş Editör
İdris Karaagöz

Associate Editors
Yardımcı Editörler
Zakaria Boumerzoug, University of Biskra, Algeria
Gürel Çam, İskenderun Technical University, Turkey
Emel Taban, Kocaeli University, Turkey
Yahya Bozkurt, Marmara University, Turkey
Ayşe Bedeloğlu, Bursa Technical University, Turkey
Ilda Kazani, Polytechnic University of Tirana, Albania
Yasemin Tamer, Yalova University, Turkey

Editorial Board
Alan Editörleri ve
Yayın Kurulu
Ramzi Khiari, Université Grenoble Alpes, France
Edin Dolićanin, State University of Novi Pazar, Serbia
Kulathuiyer Seshan, University of Twente, Netherlands
Sinan Şen, Yalova University, Turkey
Uğur Özsaraç, Sakarya University of Applied Sciences, Turkey
Mehmet Özgür Seydibeyoğlu, İzmir Katip Çelebi University, Turkey
İsmail Gökhan Temel, Yalova University, Turkey
Salih Yazıcıoğlu, Gazi University, Turkey
Melda Altıkatoğlu Yapaöz, Yıldız Technical University, Turkey
Figen Beyhan, Gazi University, Turkey
Naci Genç, Yalova University, Turkey
Eyüp Debik, Yıldız Technical University, Turkey
Barbaros Nalbantoğlu, Yıldız Technical University, Turkey
Mustafa Yavuz, Süleyman Demirel University, Turkey
Ilda Kazani, Polytechnic University of Tirana, Albania
Oğuzhan Gündüz, Marmara University, Turkey
Stanislav Roshchupkin, Sevastopol State University, Sevastopol
Mustafa Çakır, Marmara University, Turkey
Halil İbrahim Kurt, Gaziantep University, Turkey
İsrafil Küçük, Gebze Technical University, Turkey
Mehmet Büyükyıldız, Bursa Technical University, Turkey
Yeşim Müge Şahin, Arel University, Turkey
İlyas Kartal, Marmara University, Turkey
Mahmut Yıldız, Gebze Technical University, Turkey
Turgut Ak, National Defence University, Turkey

Journal of Innovative Engineering and Natural Science
(Yenilikçi Mühendislik ve Doğa Bilimleri Dergisi)
journal homepage: https://jiens.org

From the Editors

Dear Readers,

As the Journal of Innovative Engineering and Natural Sciences, we are excited to share with you a recent development that fills us with joy and pride. In the rapidly advancing world of technology and scientific research, we have taken an important step towards increasing the recognition of our journal in Turkey and playing an active role on the international stage.

We proudly announce that the Journal of Innovative Engineering and Natural Sciences is now indexed in TR Index, one of the prominent directories in Turkey. This achievement is considered a strong reference to the quality and scientific impact of our journal. We extend our heartfelt thanks to all our editorial board members, reviewers, and contributing authors for their invaluable contributions.

Adhering to our publishing principles of "academic discipline" and "ethical values," the Journal of Innovative Engineering and Natural Sciences continues to fulfill its mission of providing an important academic platform for researchers. Our primary goal is to offer scientific approaches and solutions to the current issues in the fields of engineering and natural sciences and share these works swiftly with academia and industry.

We take great pride in joining the ranks of distinguished national and international journals by taking this significant step. The success of our journal continues to grow thanks to the contributions of our esteemed readers and researchers. We look forward to sharing your valuable works in engineering and natural sciences in our future issues.

With this update, we aim to enhance the quality and national recognition of our journal. We assure you that we will continue to enlighten you by keeping up with the latest developments in the world of science.

Thank you for your participation, support, and interest.

Best regards,

Editors

Editörden

Değerli Okuyucularımız,

Yenilikçi Mühendislik ve Doğa Bilimleri Dergisi olarak, sizlere büyük bir heyecan ve mutlulukla duyurmak istediğimiz güncel bir gelişmeyi paylaşmak istiyoruz. Gelişen teknoloji ve bilimsel araştırmaların hızla ilerlediği günümüzde, dergimizin Türkiye'de tanınırlığını artırmak ve uluslararası arenada etkin bir rol oynamak adına önemli bir adım atmış bulunmaktayız.

Gururla duyuruyoruz ki, Yenilikçi Mühendislik ve Doğa Bilimleri Dergisi artık Türkiye'deki önemli dizinlerden biri olan TR dizinde yerini almıştır. Bu gelişme, dergimizin kalitesi ve bilimsel etkisi konusundaki güçlü bir referans olarak kabul edilmektedir. Bu başarıyı elde etmemizde emeği geçen tüm yayın kurulu üyelerimize, hakemlerimize ve katkıda bulunan yazarlarımıza en içten teşekkürlerimizi sunarız.

Yayın ilkelerimiz olan "akademik disiplin" ve "etik değerler" çerçevesinde, Yenilikçi Mühendislik ve Doğa Bilimleri Dergisi olarak, araştırmacılar için önemli bir akademik platform sağlama misyonumuzu sürdürüyoruz. Dergimizin temel amacı, mühendislik ve doğa bilimleri alanında yapılan araştırmalara bilimsel yaklaşımlarla çözümler sunmak ve bu çalışmaları akademi ve sektörle hızlı bir şekilde paylaşmaktır.

Bu önemli adımı atarak ulusal ve uluslararası seçkin dergiler arasında yer almaktan büyük gurur duyuyoruz. Siz değerli okuyucularımızın ve araştırmacıların katkıları sayesinde dergimizin başarısı artarak devam etmektedir. Gelecek sayılarımızda da mühendislik ve doğa bilimleri alanında yürüttüğünüz değerli çalışmaları paylaşmanızı arzu ediyoruz.

Sizlere sunduğumuz bu güncellemeyle, dergimizin kalitesini ve ulusal çapta tanınırlığını artırmayı hedefliyoruz. Bilim dünyasındaki yeni gelişmeleri takip ederek sizleri aydınlatmaya devam edeceğimizi taahhüt ediyoruz.

Katılımınız, desteğiniz ve ilginiz için teşekkür ederiz.

Saygılarımızla,

Editörler

Journal of Innovative Engineering and Natural Science
(Yenilikçi Mühendislik ve Doğa Bilimleri Dergisi)
journal homepage: https://jiens.org

CONTENTS / *İÇİNDEKİLER*

Journal of Innovative Engineering and Natural Science
(Yenilikçi Mühendislik ve Doğa Bilimleri Dergisi)
journal homepage: https://jiens.org

CONTENTS / *İÇİNDEKİLER*

J. Innovative Eng. Nat. Sci., vol. 3, no. 2, pp. 67-74, 2023.
http://dx.doi.org/10.29228/JIENS.69363

Original Paper

Journal of Innovative Engineering
and Natural Science
(Yenilikçi Mühendislik ve Doğa Bilimleri Dergisi)
journal homepage: https://jiens.org

Investigation of effect of chestnut sawdust on mechanical properties of epoxy matrix composites

İlyas Kartal[a,*], Zerrin Özcan[b]

[a]Marmara Üniversitesi, Teknoloji Fakültesi, Metalurji ve Malzeme Mühendisliği, İstanbul 34854, Türkiye.
[b]MEB, Başakşehir Şehit Muhammed Eymen Demirci İlkokulu, İstanbul 34480, Türkiye.

ARTICLE INFO

Article history:
Received 10 Apr 2023
Received in revised form 13 May 2023
Accepted 23 May 2023

Available online

Keywords:
Epoxy resin,
Chestnut sawdust,
Mechanical properties,
Natural filler

ABSTRACT

Composites have many important properties such as high specific hardness and strength, dimensional stability, adequate electrical properties and excellent corrosion resistance. The composite industry is mostly dominated by thermosetting resins such as epoxy, vinyl ester, unsaturated polyester, phenolic, polyimides. These resins have many advantages such as their relative ease of processing, lower equipment cost for processing and lower material costs. In this study, the effect of chestnut sawdust on the mechanical properties of epoxy matrix composites was investigated. As the resin, thermosetting epoxy resin was preferred as the matrix. As a filler, chestnut wood sawdust, which is produced as a natural waste by local furniture manufacturers, was used. The sawdust was prepared up to 400 micron size and was added to the resin at rates of 5-10-15-20% by weight. Sample preparation was terminated as the resin reached saturation with the addition of 20% sawdust. PTFE material was preferred as the mould because of the very weak adhesion property of epoxy. The prepared mixture was kept in the oven at 180oC for 3 hours to completely harden. Mechanical properties of the samples such as tensile, hardness and impact were investigated. Examination of the broken surfaces was made with SEM images. At the end of the study, it was determined that the addition of 10% by weight chestnut sawdust increased the mechanical properties of epoxy composites. It was also understood from the SEM images that there was a homogeneous mixture in the sample structure.

I. INTRODUCTION

Composites are defined as a combination of two or more materials with a distinguishable interface. Composite materials are widely used in many areas such as automotive, maritime, aviation, textile, defence industry. Composite-based materials contain additives and fillers together with a polymer matrix. The most important advantage of filling materials is that they reduce the cost significantly. However, it is known that it provides many advantages with its contributions to mechanical properties [1-2].

Ceramic-based fillers are mostly used in composites. However, in recent years, the use of natural fillers and fibres has been intensely preferred [3-8]. Natural fibres have attracted the attention of many researchers because they are low cost, highly available, biodegradable and environmentally friendly materials [9]. However, the main disadvantages of wood particles are their relatively low degradation temperatures, which weaken their adhesion with hydrophobic polymers. However, wood fibres show very good mechanical properties [10]. At the same time, the use of natural fibres and polymers from renewable resources has attracted increasing attention recently, mainly due to environmental concerns and depletion of petroleum resources [11-12]. Natural fillers have relatively high strength and hardness, as well as low cost, low density and low CO_2 emissions, and are biodegradable and renewable. One of the natural fillers is wood sawdust. Wood sawdust are suitable for use in polymeric composites due to its lightness, micro grain size, easy availability from local sources and natural waste [13-14].

*Corresponding author. Tel.: +90-216-777-3992; e-mail: ilyaskartal@marmara.edu.tr

In this study, epoxy resin was preferred due to its widespread use as a matrix material. Epoxies have a wide range of applications, from dental fillings to rocket shells [15-16]. The properties that allow such a wide variety of applications are explained by the chemistry of the epoxy functional group as well as the curing reaction [17]. Functionally, this resin exhibits excellent properties due to its high crosslinking properties, adequate strength, low curing shrinkage, increased fatigue and impact resistance, excellent thermal properties, chemical resistance and dimensional stability. Epoxy/hardener ratios and ideal curing conditions are important to obtain the desired properties of composite materials [18].

These new generation environmentally friendly materials with natural fillings are used in many areas as an alternative to synthetic plastics. Products made of these materials, also called green composites, are used extensively in the automotive, furniture, construction and packaging industries. As fibres and filling materials, materials such as cellulose, nutshell, bamboo fibres, wheat stalk, chestnut are preferred intensely [4-5, 7]. In this study, together with epoxy, waste chestnut sawdust will be used as filler. With the use of waste sawdust in composite applications, it will be ensured that the environmental effects are reduced, the cost of composite production is reduced, the amount of waste storage and gas emissions are reduced, and natural resources are protected.

II. EXPERIMENTAL METHOD

2.1 Materials

In this study, waste chestnut wood chips obtained from local furniture manufacturers were used as natural filling material. The chips were prepared in up to 400 micron sizes by passing through 400 micron sieves. Epoxy resin, Epikot 828 (Shell Chemical, density 1.16 kg/liter), which is heavily preferred in composite applications, was chosen as the matrix material. Epikot 828 is a medium viscosity liquid epoxy resin produced from bisphenol A resin and epichlorohydrin. It is free of diluents, providing good pigment wetting and good resistance to filler precipitation and high mechanical and chemical resistance properties in the cured condition. Epicure (Shell Chemical) was used as epoxy resin hardener and benzyl dimethyl amine (BMDA-Aldrich) was used as accelerator.

2.2 Preparation of Samples

Chestnut wood sawdust in the size up to 400 micron was added to the epoxy resin at the rates of 5-10-15-20% by weight. Since saturation was reached in 20% filled samples, no other samples were prepared.

The ratio of hardener used for epoxy resin is 1:1, that is, the same amount of hardener is used by weight of the epoxy resin. In order to remove the air bubbles formed in the mixture of Epikot 828 and Epicure, it was kept in an oven at 50 ºC for about 20 minutes. In addition, 1% by weight of benzyl dimethyl amine (BDMA) was added as accelerator. The mixture poured into the PTFE mould was cured at 180 ºC for 3 hours to completely harden.

PTFE mould was used as open mold in this study. PTFE mould was preferred in order to easily separate the epoxy from the mould due to its weak adhesion property.

2.3 Mechanical Tests

The tensile test was applied in the Zwick brand Z010 universal type tensile test device according to the ISO 527 standard at a tensile speed of 5 mm per minute. The impact strength of the unnotched test specimens was used with a 5.4 J Izod hammer on the Zwick brand B5113.30 impact tester. The hardness test was carried out on the Zwick brand Shore D tester. For SEM analysis, the samples were coated with a 10 Å thick gold/palladium alloy. The SEM test was performed with the Polaron SC branded device located in the Marmara University, Faculty of Technology Laboratory.

III. RESULTS AND DISCUSSIONS

Tensile test, Izod impact test and hardness measurements were performed on composite samples. Tensile strength values and % strain values are given in Table 1. The tensile strength value of the composite, which has a particle reinforced polymer matrix structure, varies depending on the active load transfer between the matrix structure and the particle reinforcements. Factors such as the particle additive ratio, the bond strength between the particles of the fiber layer and the resin affect the strength at the same rate.

Table 1. Tensile strength and % strain values of samples

Filler Rate, by weight	**Tensile Strength** *(MPa)*	**Strain %**
Pure Epoxy	36,9	2,1
5%	37,7	2,2
10%	40,1	2,2
15%	34	1,9
20%	28	1,8

The variation trends for the tensile strength of the samples were close to each other. It is also possible to see from the graph in figure 1 that a partial increase in the tensile strength of the mixture is achieved with the increase of % sawdust ratio in epoxy-chestnut wood chips mixture samples. The pure epoxy sample exhibited a low tensile strength. However, due to the reinforcing effect of sawdust, the tensile strength values of the composites increased partially. With the addition of 10% sawdust, the tensile strength of the pure epoxy was increased by 8%. With the addition of sawdust after 10%, a decrease in tensile strength was observed in the samples.

This may be because the percentage of epoxy resin that firmly binds the composite is reduced. Another possible reason may be that the weak interfacial bond between the polymer matrix and the filler content reduces the tensile strength of the composite. It has been stated in the studies that the tendency to agglomerate with the increase in the amount of sawdust or the insufficient hydrogen bond between the chip particles and the epoxy resin matrix cause a decrease in the tensile strength [10, 18-20].

Shore D hardness value of the samples is given in figure 2. As in the tensile strength, the hardness values also increased as the chip ratio increased, and decreased after 10% sawdust amount. In Figure 3, the variation of Izod impact strength with increasing sawdust ratio is given. A slight decrease in the impact resistance of the composite was observed with the increase in the sawdust ratio by weight. The impact strength of the epoxy decreased by 20% with the addition of sawdust. The reason for this is thought to be due to the fact that the sawdust filler is available in very different sizes (up to 400 micron size) and structures.

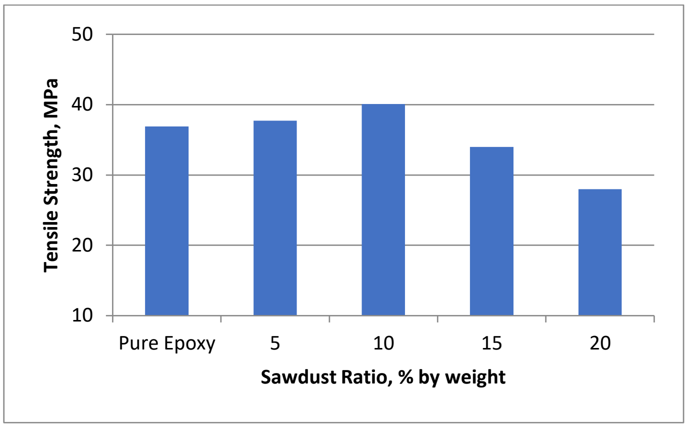

Figure 1. Variation of the tensile strength of the samples depending on sawdust ratio

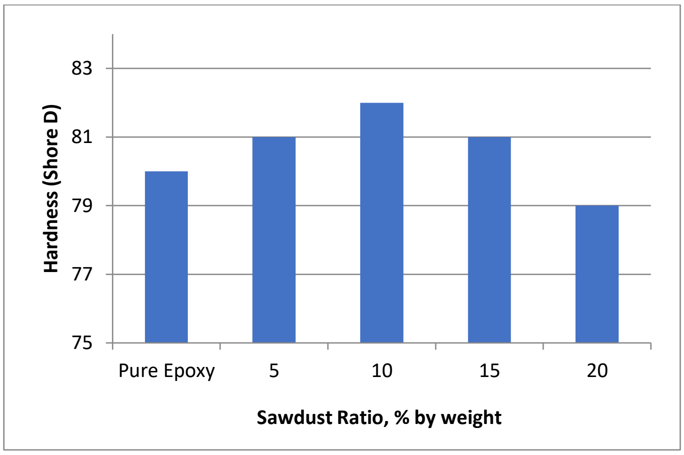

Figure 2. Variation of Shore D hardness value in samples depending on sawdust ratio

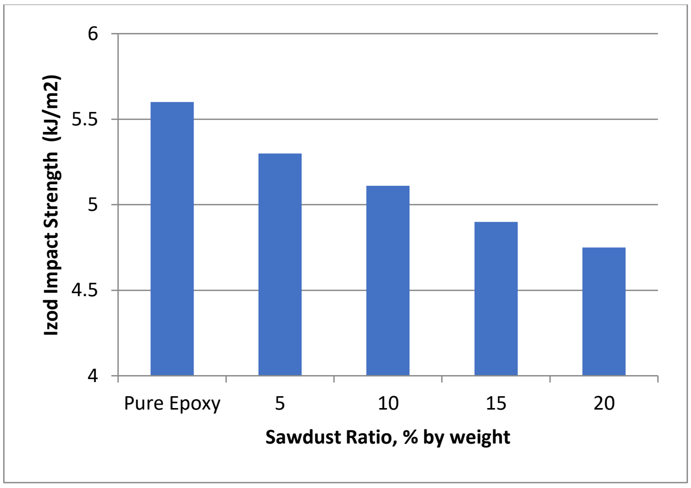

Figure 3. Variation of Izod impact strength of samples depending on sawdust ratio

SEM images of the samples are given in Figure 4. In Figure 4a, it is seen that there is a brittle fracture on the fracture surface of the pure epoxy. The other SEM image figure 4b contains 10% chestnut sawdust. It is clear that the sawdust adheres well to the epoxy resin. There are chestnut sawdust in many different sizes and shapes in the sample. As it can be seen from the images, it is seen that there are sawdust in the size of 10 microns, as well as in the size of 400 microns. However, as the weight ratio of sawdust particles in the resin increased, agglomeration was observed. This is thought to cause the formation of bubbles and pores that may interfere with the mechanical properties of the composites.

It can be thought that 10% by weight of sawdust filled epoxy has good adhesion, and with the increase in the amount of sawdust by weight, there may not have been enough epoxy resin to completely cover all cellulosic surfaces. Thus, from these images, it can be understood why composites containing 10% by weight sawdust show better mechanical properties than composites containing 20% by weight of sawdust. Similar observations in this study were also observed in other studies [19, 21].

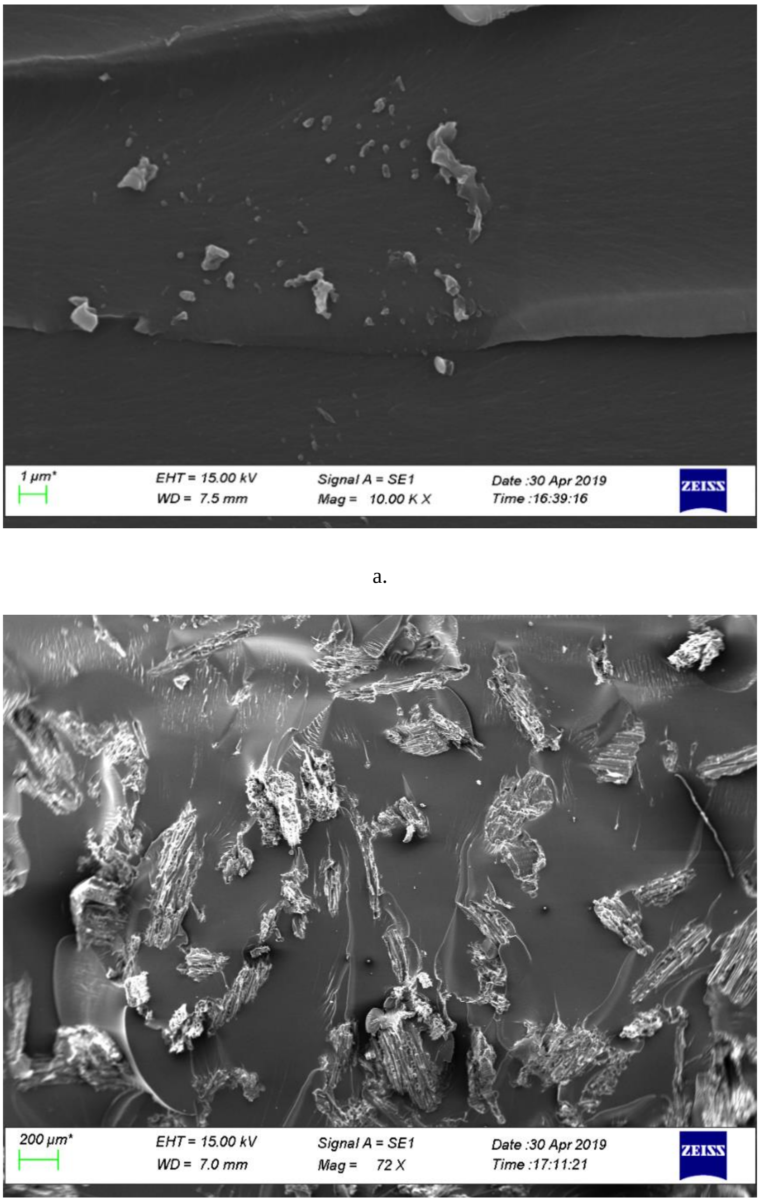

a.

b.

Figure 4. SEM images of the fracture surfaces of pure epoxy (a) and 10% chestnut sawdust filled (b) samples

IV. CONCLUSIONS

In this study, the use of chestnut sawdust as a filler in thermosetting epoxy-based composite material was investigated. A slight improvement in tensile, hardness properties was observed as the chestnut sawdust filler silently increased in the epoxy. According to the tensile test data, it was observed that 10% sawdust filler showed a better strength than all other samples. There was also a partial increase in the hardness value. Impact test values showed a partial decrease due to the different sizes of sawdust filling in the structure. When the data of all samples were examined, it was understood from the SEM images that the sawdust ratio was ideal in the samples with 10% sawdust filling and that the sawdust was homogeneously mixed in the structure.

At the end of the study, it has been determined that the addition of chestnut sawdust filler will reduce the amount of heat-cured epoxy usage, which will reduce the cost to some extent and contribute positively to the mechanical properties. However, it is clear that the use of natural fillings instead of synthetic fillings will contribute to the solution of environmental problems. Therefore, it has been concluded that the use of chestnut sawdust as a filler in thermosetting epoxy matrix composite material applications may be an appropriate decision.

REFERENCES

[1] Jose JP, Joseph K (2012) Introduction to Polymer Composites. In: Sabu T, Kuruvilla J, Kumar M, Goda K, Sreekala MS (ed) Polymer Composites, First edn. Wiley, New York, pp 1-16

[2] Cakir Yigit N (2022) Alev geciktirici polimerlerin sentezine yönelik güncel yaklaşımlar. Journal of innovative engineering and natural science 2(2): 95-113. https://doi.org/10.29228/JIENS.63353

[3] Kartal İ (2020) Effect of hornbeam sawdust size on the mechanical properties of polyethylene composites. Emerging Materials Research 9(3):979-984.

[4] Kartal İ, Naycı G, Demirer H (2019) Investigation of the Mechanical Properties of Chestnut/Hornbeam Sawdust Filled Vinyl Ester Composites. European Journal of Science and Technology 16:723-728.

[5] Kartal İ, Naycı G, Demirer H (2020) The effect of chestnut wood flour size on the mechanical properties of vinyl ester composites. Emerging Materials Research 9(3):960-965

[6] Şengör İ, Cesur S, Kartal İ, Oktar FN, Ekren N, İnan AT, Gündüz O (2018) Fabrication and Characterization of Hazelnut ShellPowder with Reinforced Polymer Composite Nanofibers. ICNMA: 2018 20th International Conference on Nanostructured Materials and Applications

[7] Kartal İ, Naycı G, Demirer H (2019) Investigation of Mechanical Properties of Glass and Bamboo Fiber Reinforced Vinylester Composites. Multidisciplinary Studies and Innovative 3(1):34-37.

[8] Demirer H, Kartal İ, Yıldırım A, Büyükkaya K (2018) The Utilisability of Ground Hazelnut Shell as Filler in Polypropylene Composites. Acta Phys. Pol. A 134:254-256.

[9] Ashori, A (2008) Wood-plastic composites as promising green-composites for automotive industries. Bioresource Technology 99(11):4661-4667.

[10] Marcovich NE, Reboredo MM, Aranguren MI (1996) Composites from sawdust and unsaturated polyester. J. Appl. Polym. Sci. 61(1):119-124.

[11] Ridzuan MJM, Majid MSA, Afendi M, Azduwin K, Amin NAM, Zahri JM, Gibson AG (2016) Moisture absorption and mechanical degradation of hybrid Pennisetum purpureum/glass-epoxy composites. Composite Structures 141:110-116. https://doi.org/10.1016/j.compstruct.2016.01.030

[12] Vijayan D, Thiagarajan R. (2020) Influence of stacking sequence on mechanical and metallurgical properties of ramie/areca laminates using B4C nano filled epoxy. Resin Journal of Natural Fibres 1-17. https://doi.org/10.1080/15440478.2020.1848713

[13] Kamdem DP, Jiang H, Cui W, Freed J, Matuana LM (2004) Properties of wood plastic composites made of recycled HDPE and wood flour from CCA-treated wood removed from service. Composite Part A: Applied Science and Manufacturing 35(3):347-355. https://doi.org/10.1016/j.compositesa.2003.09.013

[14] Deka BK, Baishya P, Maj TK (2014) Synergistic effect of SiO2, ZnO and nanoclay on mechanical and thermal properties of wood polymer nanocomposite. Journal of Thermoplastic Composite Materials 27(4):464-480. https://doi.org/10.1177/0892705712452739

[15] Kartal İ (2019) Investigation of Wear Properties of Toughened Epoxy Resin using Silane Terminated Urethane. Acta Physica Polonica A 135(5):1100-1101.

[16] Kartal İ, Boztoprak Y, Bilici MK, Çakır M (2006) Investigation of Wear Properties of Epoxy-Polyester Mixtures. 13th International Metallurgy and Materials Congress

[17] Bilyeu B, Brostow W, Menard KP (1999) Epoxy thermosets and their applications. I: Chemical structures and applications. Journal of Materials Education 21(5&6):281-286.

[18] Khan M, Abas M, Noor S, Salah B, Saleen W, Khan R (2021) Experimental and statistical analysis of sawmill wood waste composite properties for practical applications. Polymers 13(4038):1-19.

[19] Lette MJ, Elhadji Babacar LY, Ndiaye D, Takasaki A, Okabe T (2018) Evaluation of sawdust and rice husks as fillers for phenolic resin based wood polymer composites. Journal of Composite Materials 8(3):124-137 https://doi.org/10.4236/ojcm.2018.83010

[20] Huda MS, Drzal LT, Misra M, Mohanty AK (2006) Wood-fiber-reinforced poly(lactic acid) composites: Evaluation of the physicomechanical and morphological properties. J. Appl. Polym. Sci. 102:4856-4869.

[21] Kumara R, Kumarb K, Sahooc P, Bhowmika S (2014) Study of mechanical properties of wood dust reinforced epoxy composite. Procedia Materials Science 6:551-556.

J. Innovative Eng. Nat. Sci., vol. 3, no. 2, pp. 75-88, 2023.
http://dx.doi.org/10.29228/JIENS.70259

JIENS
Journal of Innovative Engineering and Natural Science
Yenilikçi Mühendislik ve Doğa Bilimleri Dergisi

Original Paper

Journal of Innovative Engineering and Natural Science
(Yenilikçi Mühendislik ve Doğa Bilimleri Dergisi)
journal homepage: https://jiens.org

Converting polyolefin fibres into CO_2 adsorbent by radiation induced grafting

Noor Ashikin Mohamad[a,b], Nur Afifah Zubair[a,b], Mohamed Mahmoud Nasef[a,b,*], Teo Ming Ting[c]

[a]Malaysia-Japan International Institute of Technology, Universiti Teknologi Malaysia, Jalan Sultan Yahya Petra, 54100 Kuala Lumpur, Malaysia.
[b]Center of Hydrogen Energy, Institute of Future Energy, Universiti Teknologi Malaysia, Jalan Sultan Yahya Petra, 54100 Kuala Lumpur, Malaysia.
[c]Radiation Processing Technology Division, Malaysian Nuclear Agency, 43000, Kajang, Selangor, Malaysia.

ARTICLE INFO

Article history:
Received 24 May 2023
Received in revised form 09 June 2023
Accepted 16 June 2023

Available online

Keywords:
PE/PP fibrous sheet
Grafting reactions
Amination treatment
CO_2 selective adsorption
Air pollution

ABSTRCT

Polyethylene (PE)/polypropylene (PP) bicomponent fibres were converted into three types of CO_2 adsorbents by radiation induced graft copolymerization (RIGC) of glycidyl methacrylate (GMA) and N-vinylformamide (NVF) followed by treatment of poly(GMA) grafted fibres with polyethyleneimine (PEI) or ethylenediamine (EDA) and poly(NVF) grafted counterpart with hydrolysis to yield grafted poly(vinylamine) poly(VAm). The incorporation of poly(GMA) having same degree of grafting (DG%) and their subsequently aminated samples were verified by Fourier transform infrared (FTIR) and scanning electron microscopy (SEM). The performance of the three adsorbents was evaluated with pure CO_2 and N_2 gases and their mixtures of different ratios. The adsorbent with PEI showed CO_2 adsorption capacity of 1.03 mmol/g, which was increased to 1.43 mmol/g when it was substituted with EDA, whereas this value was raised to 1.69 mmol/g in the adsorbent containing poly(VAm) at 30 bar and room temperature. Such CO_2 adsorption capacity values were decreased when CO_2/N_2 mixtures were adsorbed, and the decrease was more profound at lower CO_2 content in all adsorbents, but the performance of poly(VAm)-containing adsorbent remained superior. It can be concluded that RIGC provides a versatile method to convert PE/PP fibres into highly selective CO_2 adsorbents with NVF grafting route is simpler and yield more efficient adsorbent for CO_2 capture.

I. INTRODUCTION

Polyolefins are a class of polymers that include materials like polyethylene (PE) and polypropylene (PP) with high versatility making them one of the most popular plastics. Polyolefins are widely used in various industrial applications including packaging materials, pipes and fittings, automotive parts, electrical insulation, textiles, automotive parts, and consumer goods. This is due to their excellent chemical resistance, mechanical integrity including toughness and resistance abrasion in addition to hydrophobicity and low cost [1]. One of the appealing applications that has indeed been explored is the use of PE and PP fibres/nonwoven fabrics as substrates for developing functionalized adsorbents for various environmental applications. This area has gained an ever increasing attention as a means to mitigate rising levels of water and air pollution [2].

To develop SFA, specific ionic groups can be introduced to the surface of polymer substrates such as PE or PP fibres/nonwoven fabrics using graft copolymerization that can be initiated using thermal initiation, plasma treatment, redox initiation, photo-initiation in presence of UV and ionizing radiation [3, 4]. Of all methods, initiation of graft copolymerization using ionizing radiation (known as radiation induced graft copolymerization or RIGC such as γ-rays and electron beam (EB), offers several advantages, including clean and environmentally friendly approach because eliminating the detrimental residues and providing precise and uniform control over the level of grafting and its homogeneity [5].

---

*Corresponding author. Tel.: +603-2203-1229; e-mail: mahmoudeithar@cheme.utm.my

RIGC method works on the principle of exposing polymer substrates to ionizing "radiation generates free radicals by H abstraction from polymer backbone that initiate copolymerization when the irradiated substrates are brought in contact with polar monomer molecules which can be performed with simultaneous grafting or pre-irradiation grafting. The former method involves irradiation of the polymer substrate and the monomer together under controlled conditions whereas in the latter one, the substrate is irradiated separately before being brought into contact with the monomer under controlled conditions. The grafting yield can be easily optimized by controlling the grafting conditions. Both grafting methods lead to formation of covalently bonded side chain grafts on the substrate leaving capable of hosting ionic groups either by grafting of an ionic monomer or indirectly in a post grafting reaction when a non-ionic monomer is used. These ionic groups have strong affinity that can enhance the adsorption capacity of the material for targeted pollutants. For example, functional groups such as sulfonate ($-SO_3H$), carboxyl (-COOH), hydroxyl (-OH) or amino ($-NH_2$) groups can be incorporated onto the surface imparting ionic moieties [6].

The functionalized adsorbents based on PE and PP fibres/nonwoven fabric have several advantages. Firstly, the large surface area and porous structure of these materials provide ample contact sites to adsorb pollutants. Secondly, the presence of specific ionic groups increases the affinity between the adsorbent and target pollutants, enhancing the adsorption efficiency. The use of PE and PP fibres/nonwoven fabric as substrates also allows for easy handling, scalability, and potential reusability of the adsorbents. Particularly, these fibrous adsorbents offer crucial advantages over traditional adsorbent beads in packed-bed columns, particularly in applications involving high-pressure gas treatment, such as the removal of CO_2 from natural gas where the treated gas loses a great deal of pressure. Additionally, these adsorbents eliminate the feed channelling taking place upon using adsorbent beads in packed-bed columns [7]. The feed channelling refers to the phenomenon in which the fluid flow within the adsorption column using beads becomes concentrated in specific areas while bypassing certain regions of the bed causing an uneven feed distribution and contact time reduction leading to an inefficient adsorption process [8].

Many studies reported the development of various radiation grafted fibrous adsorbents with different functional groups. Most of such adsorbents were dedicated for wastewater treatment applications involving removal of various pollutants such as heavy metals, dyes, boron, arsenic, and oil spills [9-11]. However, less efforts were exerted to develop selective radiation grafted adsorbents to mitigate air pollution by CO_2 capture [2, 12]. Indeed, there have been some studies on using aminated electrospun nanofibrous substrates made of PP [13-15], polyacrylonitrile (PAN) [2], PAN/polystyrene (PS) [16] for application in CO_2 capture by RIGC and subsequent amine loading. Degrees of grafting (DG) above 100% were maintained in the adsorbent precursors to ensure having sufficient sites to load the desired amine groups and eventually acquire higher adsorption capacities coupled with faster kinetics than commercial resins. However, such nanofibrous adsorbents are facing challenges related to not only poor mechanical stability and textural as well as geometric properties of the nanofibrous substrates but also difficult scalability.

This work represents another part of our continuous efforts to prepare cost-effective CO_2 adsorbents in which three fibrous adsorbents containing amine were prepared using different routes involving RIGC of glycidyl methacrylate (GMA) and N-vinyl formamide (NVF) onto PE/PP bicomponent fibres in a form of nonwoven sheet followed by amine immobilization and subsequent evaluation of the material for CO_2 capture. The PE/PP bicomponent fibres were selected because they are cheap, nonpolar, hydrophobic and have radiation resistance. The properties of the obtained adsorbents were evaluated using various analytical techniques and the performance of the samples having same degree of grafting (DG%) was tested for pure CO_2 and N_2 gases together with their mixtures at different ratios.

II. EXPERIMENTAL METHOD

The preparation of the adsorbents involves irradiation with electron beam (EB) followed by grafting of GMA or NVF monomers and subsequent incorporation desired amine. All preparation were conducted under controlled parameters. Details of chemicals used and preparation procedures, characterization and CO_2 testing are presented below:

2.1 Chemicals and reagents

PE/PP fibrous sheets were obtained from Kurashiki Co., Japan. The GMA and NVF monomers were obtained from Sigma Aldrich (Saint Louis, MO, USA). Ethylenediamine (EDA) (purity ≥99) was purchased from Merck Millipore and was used without any further dilution. Polyethyleneimine (PEI) (purity 50 wt% aqueous solution, branched) was purchased from Acros Organics and was further diluted with dimethylformamide (DMF) and isopropanol both were of analytical grade and purchased from Merck Millipore. Deionized water (DI) was produced by Barnstead Nanopure Diamond Lab Water Purification System (ThermoFisher) and was used for washing all samples and preparation of 2 M NaOH solution required for hydrolysis reaction. Lastly, pure CO2 gas (99.8%), pure N2 (99.999%) and pure He gas (99.995%) were supplied by Alpha Gas Solution (Sdn. Bhd., Malaysia).

2.2 Grafting of monomers onto PE/PP fibres

PE/PP fibrous sheet was irradiated under vacuum in a sealed plastic bag by an EPS3000 electron beam accelerator operating at an acceleration voltage of 1 MeV, beam current of 10 mA and dose per pass of 10 kGy to total doses of 10 and 300 kGy. Grafting of GMA was carried out by placing the irradiated samples in an evacuated ampoule containing deoxygenated monomer of desired concentration diluted with DI and 0.5 wt% Tween-20 and reaction was allowed at 40 °C for 0.5 h. On the other hand, grafting of NVF on PE/PP was carried out in a similar manner but in toluene solvent under conditions of 300 kGy absorbed dose and 70 °C temperature for 1 h. The grafted samples were extracted and washed with methanol few times and rinsed under sonication overnight before drying in a vacuum oven followed by weighing. The degree of grafting (DG%) in samples was calculated from the sample weight gain as follows:

$$DG\ (\%) = \frac{W_g - W_o}{W_o} \times 100\% \tag{1}$$

where, W_g and W_o are weights of samples after and before grafting, respectively.

2.3 Amination of grafted PE/PP fibres

PE/PP-*g*-poly(GMA) substrate was treated with pure EDA amine in round bottom flask. The reaction was carried out at 83 ºC under reflux for 24 h. Another sample of PE/PP-*g*-Poly(GMA) was treated with PEI solution diluted with a mixture of DMF and isopropanol comprising 16% and 20% of the total volume. The reaction was performed for 24 h at 90 ºC under reflux. Finally, the amine functionalized substrates were removed and washed repeatedly with DI water and ethanol before drying in a vacuum oven at 60 ºC for overnight. The following equation was used to calculate the amine percentage:

$$\text{Amine content (\%)} = \frac{(W_a - W_g)\ /MW_{amine}}{(W_a - W_o)/MW_{GMA}} \times 100\% \qquad (2)$$

where, MW_{GMA} is the molecular weight of GMA (142.15) and MW_{amine} is the molecular weight of EDA (g/mol). W_a and W_g are the weights (g) of the PE/PP-*g*-poly(GMA) substrate before and after amination, respectively. The Wo is the weight of pristine PE/PP polymer before grafting. The amine content in PE/PP-*g*-poly(GMA)/PEI and PE/PP-*g*-poly(GMA)/EDA was found to be 24.3 and 23.2%, respectively.

PE/PP fibres grafted with poly(NVF) samples were fully converted into poly(VAm) group by hydrolysis with a 2 M NaOH solution. The reaction was performed on samples of known weights at 80 °C for 4 h under reflux according to the procedure reported elsewhere [5]. The treated samples were removed and the excess NaOH was washed with DI water 4 times and kept in ethanol for 24 h. The samples were removed and dried in a vacuum oven (80 °C for 16 h) before their weights were determined. The amine percentage in the hydrolysed samples was calculated taking the molar masses of NVF (71.08 g/mol) and VAm (43.07 g/mol) into consideration as reported in our previous study [17]. The conversion of the formamide to amine was found close to 100%.

2.4 Characterization of samples

The three adsorbents that were denoted as PE/PP-g-poly(GMA)/PEI, PE/PP-g-poly(GMA)/EDA and PE/PP-g-poly(VAm) were characterized using the Fourier transform infrared (FTIR, Nicolet iS50, ThermoFisher Scientific Inc.) spectroscopy and measurements were in the range of 500-4500 cm^{-1} using 32 scans with 4 cm^{-1} resolution. Scanning electron microscopy (SEM) images were recorded using the GEMINISEM 500 microscope (ZEISS Microscopy) with the magnification of 500x to study the surface morphological changes of the samples.

2.5 CO_2 adsorption tests

The CO_2 adsorption capacity measurements were carried out using the magnetic suspension balance (MSB) named as isoSORP® gravimetric analyser from RUBOTHERM (Germany). A blank measurement without any sample was carried out to determine the volume of the container using He gas at room temperature after evacuation. Later, the adsorbent sample was inserted in the sample container before it was pre-treated at 80 °C for 3 h under vacuum and the actual weight and volume of the sample were determined using buoyancy mode prior to adsorption tests. Finally, the adsorption measurements were carried out using pure gases of CO_2 and N_2 and their gaseous mixtures having 5, 10, 20, and 40 % CO_2 ratios at a total flow rate of 500 ml/min, a temperature of 30 °C and an ascending pressure range up to 30 bar. The equilibrium sorption was achieved in about 50 min for every pressure reading. The desorption steps for each adsorbent were carried to evaluate the remaining adsorption capacity and were carried after each adsorption measurements were completed at 30 bars. The desorption process was performed by depressurizing the vessel containing the adsorbent until reaching vacuum before heating to 80 ˚C for 4.5 h until no weight loss was detected in the adsorbents. All adsorption/desorption cycles experiments were repeated 3 times and the average values were reported.

III. RESULTS AND DISCUSSIONS

3.1 Grafted PE/PP fibrous samples

PE/PP fibres were grafted with GMA and NVF to provide precursors for hosting amine groups. Figure 1 shows the variation of DG with the concentrations of GMA and NVF monomers while the rest of grafting conditions were kept unvaried. As can be seen, the DG in both grafting systems was found to increase with the rise in the monomer concentrations. For instance, the DG increased from 51 to 150% when the GMA concentration increased from 2 to 8% in the emulsion medium as depicted in Figure 1a. On the other hand, DG increased from 44 to 130% with the increase in NVF concentration in the range of 10-40% (Figure 1b). Such increasing trends in DG in both grafting systems is going along with the literature and can be attributed to the increase in the monomer diffusion and its availability in the grafting sites leading to more counts of initiation and propagations reactions [17-19]. For comparison purpose, grafted PE/PP samples from GMA and NVF with 130% DG were chosen for further functionalization with amine.

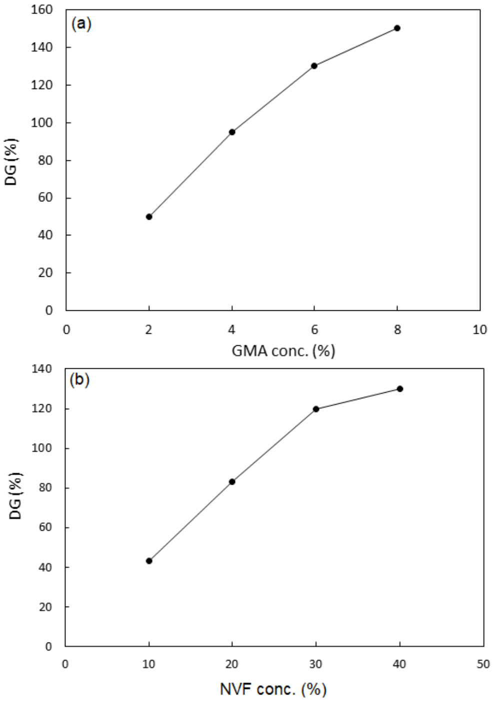

Figure 1. Variation of degree of grafting with monomer concentration **(a)** grafting of GMA on PE/PP fibres under emulsion conditions of 10 kGy absorbed dose, 40 ºC temperature and 0.5 h reaction time and **(b)** grafting of NVF on PE/PP fibres in toluene solvent under conditions of 300 kGy absorbed dose, 70 ºC temperature and 1 h reaction time.

3.2 Chemical and morphological changes in adsorbents

Figure 2 shows FTIR spectra of pristine PE/PP, PE/PP-*g*-poly(GMA), PE/PP-*g*-poly(GMA)/PEI, PE/PP-*g*-poly(GMA)/EDA and PE/PP-*g*-poly(NVF), and PE/PP-*g*-poly(VAm) fibres. Compared to pristine PP/PE characteristic peaks, the new peaks appeared at 751 (for C-O-C), 1161 (for C-O) and 1740 cm^{-1} (for O-C=O) in the spectrum *b* represent epoxy and ester features of poly(GMA) chains grafted to PE/PP fibres. The emergence of –NH bands at 1658 and 1527 cm^{-1} coupled with reduction in the intensity of ester related bands (spectra c and d) confirms the presence of EDA or PEI amines after the amination reaction [14]. The appearance of the new peak at 1650 cm^{-1} provides evidence for the incorporation of poly(NVF) grafts into PE/PP that resembles the stretching vibration of carbonyl group (>C=O) originated from amide group (spectrum *e*). This was coupled with N-H stretching and bending vibration at 3280 and 1542 cm^{-1} together with -CN stretching vibration at 1270 cm^{-1} from amide. The conversion of the amide to primary amine after hydrolysis illustrated in the spectrum f was confirmed from the complete disappearance of >C=O at 1650 cm^{-1} that was coupled with the presence of primary amine features in the range of 1542-1650 cm^{-1} and the peak at 3360 cm^{-1} representing NH_2 group [5]. These results confirm the incorporation of poly (GMA) or poly(NVF) grafts into PE/PP fibres and subsequent immobilization of EDA or PEI and formation of poly(VAm).

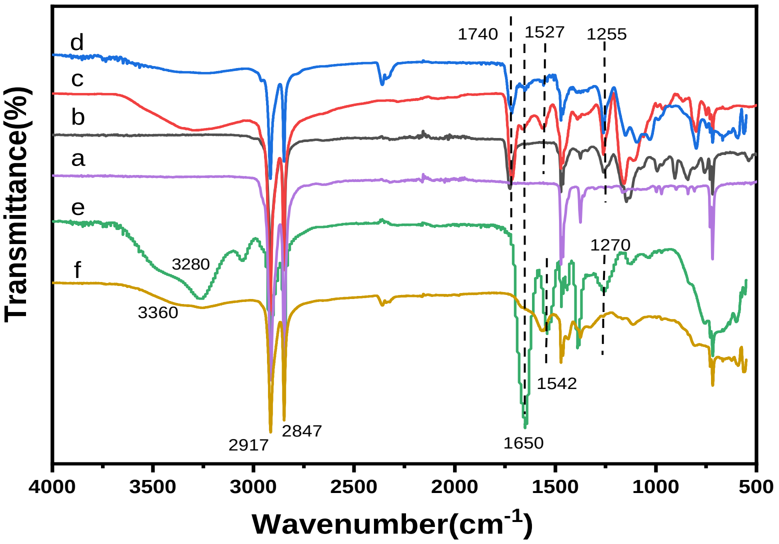

Figure 2. FTIR spectra of **(a)** pristine PE/PP substrate and grafted PE/PP with **(b)** poly(GMA), **(c)** PEI, **(d)** EDA, **(e)** poly(NVF), and **(f)** poly(VAm).

Based on the changes in chemical composition of PE/PP after grafting and subsequent functionalization with amine, the following three plausible mechanisms presented in Figure 3 can be suggested for the preparation of the three adsorbents in the present study via grafting and amination.

(a) PPE/PP adsorbent with PEI

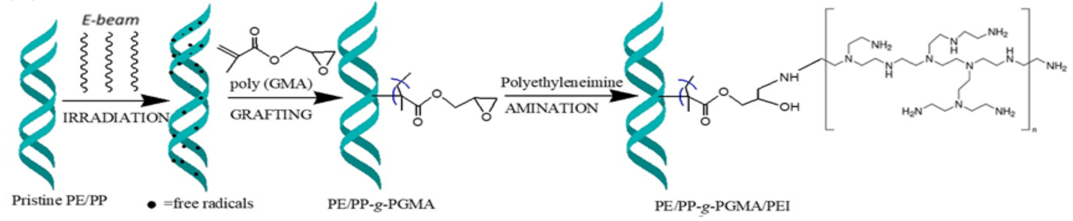

(b) PE/PP fibrous adsorbent with EDA

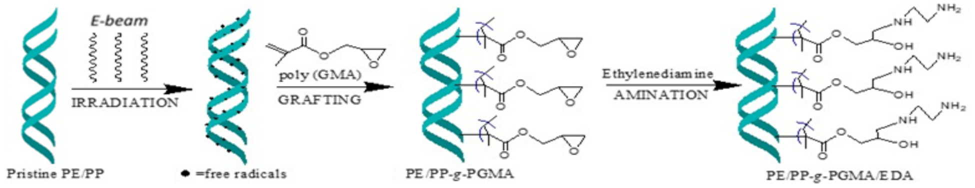

(c) PE/PP fibrous adsorbent with poly(NVF)

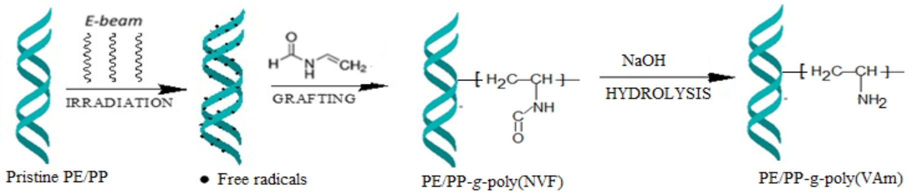

Figure 3. Schematic representation of reaction mechanisms for preparation of adsorbents containing- **(a)** PEI, **(b)** EDA and **(c)** poly(VAm).

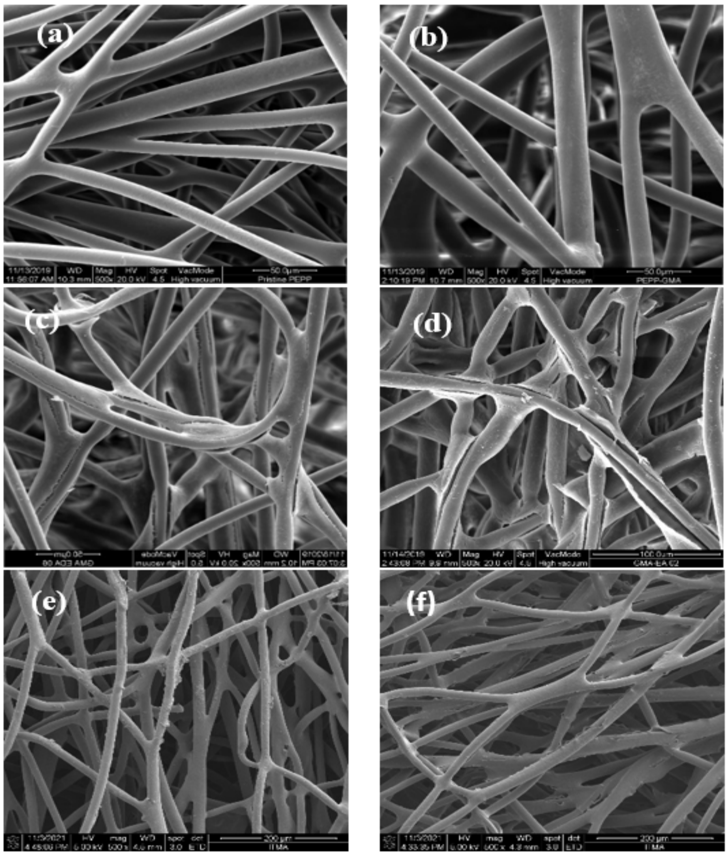

Figure 4. SEM images of **(a)** pristine PE/PP, **(b)** poly(GMA) grafted PE/PP, **(c)** PE/PP-*g*-poly(GMA)/EDA, **(d)** PE/PP-*g*-poly(GMA)/PEI, **(e)** poly(NVF) grafted PE/PP and **(f)** poly(VAm).

The morphology of the adsorbents with respect to average fibre diameter (AFD) was investigated to verify the changes accompanied grafting and amination. SEM images shown in Figure 4 portray the changes in the fibre diameters after grafting, amination, and hydrolysis. The AFD of pristine PE/PP was 14.0 ± 0.3 µm (Figure 3a), which was increased after grafting with poly(GMA) to 19.3 ± 0.2 µm (Figure 3b). After amination with EDA and PEI, the AFD was increased by ~52% and 13% reaching values of 29.3 ± 1.2 and 21.9 ± 0.8 µm, respectively (Figure 3c and d). The AFD of PE/PP was also increased to 15.2 ± 0.3 µm after grafting with poly(NVF) and further increased after conversion of amide to amine by hydrolysis reaching 22.0 ± 0.9 µm (Figure 3e and f). These morphological changes confirm monomers grafting and subsequent amination of the pristine PE/PP fibres [15].

3.3 Adsorption of pure CO_2 and N_2

Figure 5 (a-c) shows the adsorption isotherms of pure CO_2 and pure N_2 over the three adsorbents. The CO_2 adsorption capacity increased with pressure rise on all adsorbents. On the other hand, N_2 adsorption seems to be very tiny (negligible) at all pressures suggesting that the present adsorbents have low affinity towards N_2. The CO_2 adsorption isotherms seem to follow the type II that suggest the CO_2 uptake took place not only by a monolayer adsorption but also by multilayers adsorption with the pressure rise. For instance, the adsorbent with PEI showed CO_2 adsorption capacity of 1.03 mmol/g, which was raised to 1.43 mmol/g when EDA was immobilized on poly(GMA) grafted fibres at same pressure of 30 bar and room temperature. This value was further increased in PE/PP adsorbent containing poly(VAm) to 1.69 mmol/g at the same conditions. The increasing capacity trend with pressure is generally due to the increase in the diffusion of CO_2 gas prompting a wider access to amine groups in all adsorbents [20]. The results suggest that poly(VAm)-bearing adsorbent outperformed the other two counterparts originated from PE/PP-*g*-poly(GMA) fibres. This can be understood based on the amine content where the adsorbent with poly(VAm) has approximately100% degree of amination following the conversion of the amide into primary amine by hydrolysis with NaOH solution [17]. Moreover, the 63% lower performance of PEI-adsorbent, which carries a substantial quantity of tertiary amines is significantly affected by presence of the bulky structure of PEI immobilized in the adsorbent impeding CO_2 access to the amine sites and thus, the adsorbent attains lower working capacity [21]. Furthermore, the 18% lower capacity of EDA-containing adsorbent than that of poly(VAm)-containing adsorbent despite having two primary amines in its structure is most likely caused by the lower degree of amination (23.2%) and low amine utilization efficiency. It can be concluded that RIGC of NVF on PE/PP fibres provide a simpler rout that is more effective for conversion of PE/PP fibres into highly selective adsorbent for CO_2 capture. It is noteworthy mentioning that the microfibrous adsorbents in this study are perfroming better than the porous polyurethane (PU)/PS electrospun nanofibrous composite membrane that was physically impregnated with PEI or trimethylamine (TMA) in adsorption of CO_2. The former showed an adsorption capacity of 0.71 mmol/g when loaded with 100% PEI whereas the latter attained 0.48 mmol/g adsorption capacity upon loading with 100% TMA. Additionally, both types of nanofibrous composite adsorbents demonstrated an adsorption isotherm of type I suggesting the presence of monolayer adsorption [22].

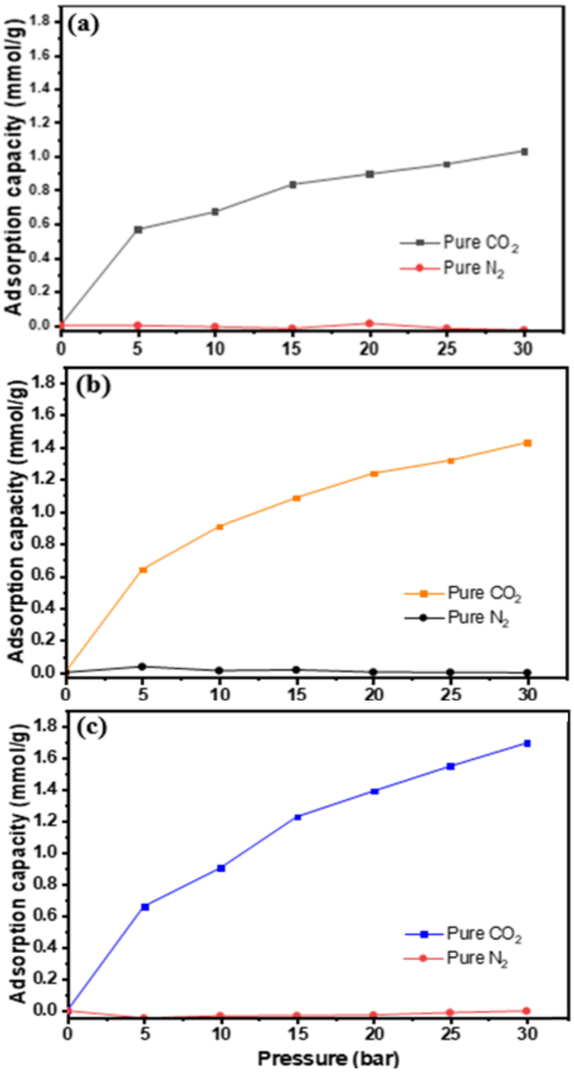

Figure 5. Adsorption isotherms of pure CO_2 and pure N_2 over prepared adsorbents **(a)** PE/PP-*g*-poly(GMA)/EDA, **(b)** PE/PP-*g*-poly(GMA)/PEI, and **(c)** PE/PP-*g*-poly(VAm).

3.4 Adsorption of CO_2 and N_2 mixtures

Figure 6 shows the adsorption isotherms of CO_2/N_2 gas mixtures having composition ratios up to 40% on the adsorbents. The EDA- and poly(VAm)-containing adsorbents were chosen based on their higher performance as illustrated in Figure 6a. The CO_2 adsorption capacity at all CO_2 ratios was found to increase with the applied pressure but attained values lesser than those of pure CO_2 adsorption. Similar trends with respect to pressure dependancy and lower CO_2 adsorption capacities were observed for the three adsorbents when a mixture of CO_2/N_2 with a ratio of 40% CO_2 was used. This behaviour can be attribuated to the competitive diffusion between CO_2 and N_2 gases leading to a partial hinderance in the accessibility of amine groups for CO_2 molecules.

In Figure 6b, the PEI-containing adsorbent showed the lowest adsorption capacity values with CO_2/N_2 mixtures compared to the other two counterparts in a way resembling the adsorption trend of pure CO_2. Unlikely, the poly(VAm)-containing adsorbent showed the highest adsorption capacity compared to its counterparts containing PEI and EDA for all CO_2 ratios and pressure values. This further confirms the superiority of poly(VAm) adsorbent compared to PEI- and EDA-containing adsorbents suggesting that the poly(VAm) adsorbent has a high amine utilization efficiency and high competitive adsorption capacity compared to other adsorbents in this study. However, the CO_2 adsorption capacity of PEI- and EDA-containing adorbents was found to be lower than radiation grafted dsorbents containing poly(GMA)/ethanolamine (EA) based on electrospun nanofibres of PP [13-15], PAN/PS [16] and PAN [23]. This can be understood taking into account not only the greater surface area of nanofibrous structure but also the higher DG and amine utilization efficiency in these adsorbents.

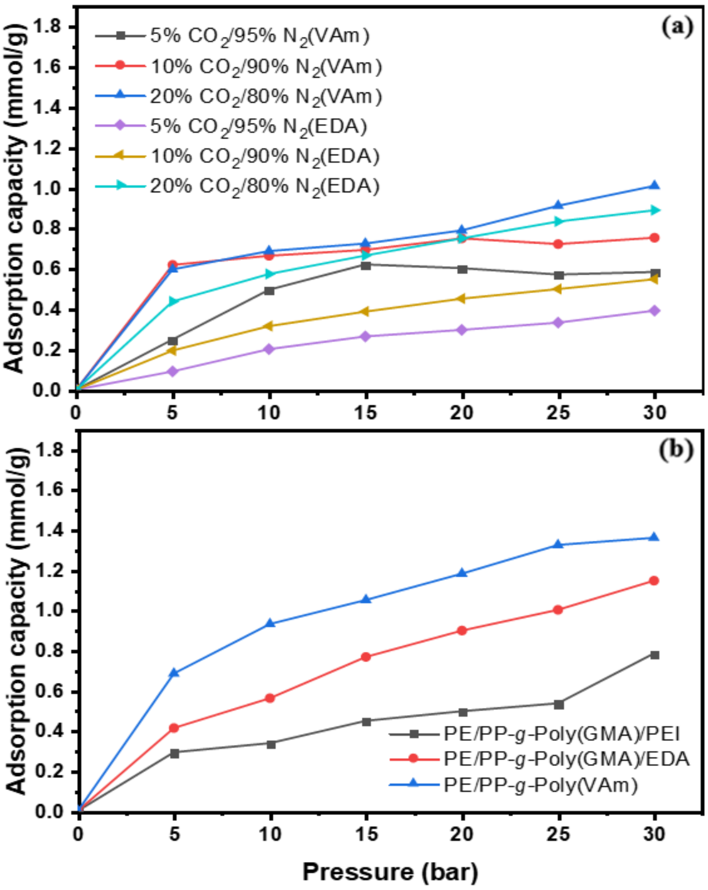

Figure 6. Isotherms for adsorption of CO_2/N_2 gas mixtures having composition ratio **(a)** the range of 5-20% CO_2 and **(b)** ratio of 40% CO_2 on various adsorbents.

The stability of the three adsorbents were evaluated using several adsorption/desorption cycles as illustrated in Figure 7. The three adsorbents showed negligible losses in their CO_2 adsorption capacity after 8 cycles suggesting the presence of an excellent stability. This further confirms that the grafting step with RIGC was efficient in covalently bonding the poly(GMA) or poly(NVF) side chain grafts to PE/PP fibrous backbone before functionalization with amine. The trend of stability and regeneration of adsorbents in this study is similar to that of tetraethylenepentamine-containing adsorbent prepared by RIGC of GMA onto PE/PP microfibres followed by amination reported earlier [11]. Tetraethylenepentamine-containing adsorbent with optimized amination efficiency based on grafted polyolefin microfibrous substrate for CO2 adsorption [12]. On the other hand, aminated adsorbents with electrospun nanofibrous networks such as ethanolamine (EA)-containing PP scaffolds [15], aminated (PEI and TMA) PU/PS nanofibers [22] and EA-containing PU/PAN nanofibers grafted with GMA [16] along with its counterpart-based pristine PAN nanofibers [23] showed higher rate of loss in adsorption capacity compared to the marginal loss in the three adsorbents in the present study. This certainly, indicate that aminated adsorbents based on microfibrous PE/PP have more practical advantages than nanofibrous counterparts.

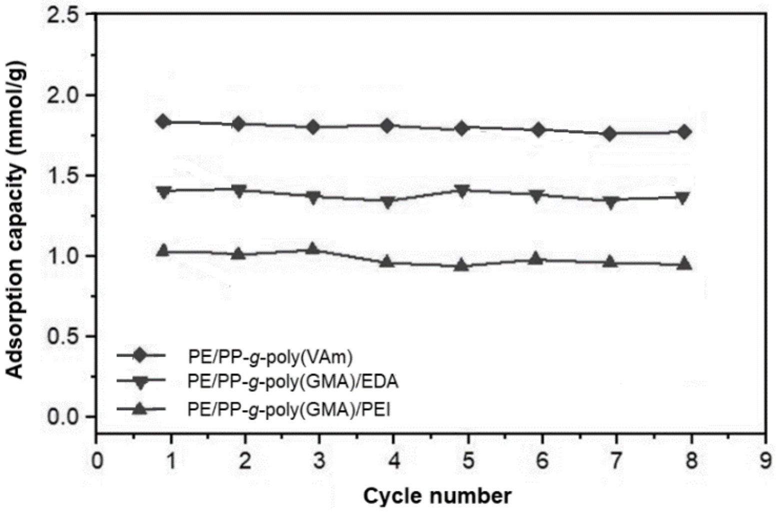

Figure 7. Variation of CO_2 adsorption capacity with number of adsorption/desorption cycles of three adsorbents.

IV. CONCLUSIONS

Three different adsorbents containing PEI, EDA, and poly(VAm) for CO_2 capture were successfully prepared by modification of PE/PP fibres with poly(GMA) and poly(NVF) grafts using RIGC followed by amination reactions. The adsorption of pure CO_2 and its mixtures with N_2 at different ratios showed increasing trends with pressure rise. The adsorption capacity of pure CO_2 gas at room temperature and 30 bar was 1.03, 1.43 and 1.69 mmol/g for PEI-, DEA- and poly(VAm)-containing adsorbents, respectively. Such values were reduced when various CO_2/N_2 mixtures of different CO_2 ratios were absorbed on the same adsorbents and the decrease is more profound at low CO_2 content in the gas mixture suggesting that N_2 partially blocked the access to some amine sites despite its low affinity towards amine. All the adsorbents were proven to be highly selective to CO_2 and have excellent adsorption/desorption stability. Finally, it can be concluded that RIGC provide distinctive tool for converting PE/PP fibres into efficient adsorbents and poly(VAm)-containing fibrous adsorbent has the best CO_2 capture performance. Hence, this adsorbent has a high potential for CO_2 capture from CO_2/N_2 mixtures resembling post combustion flue gas.

ACKNOWLEDGMENT

The authors wish to acknowledge the financial support for this work from Malaysia Thailand Joint Authority (MTJA) under the grant no. R.J130000.7609.4C172 and from the coordinated research projects (CRP # F22072) from International Atomic Energy Agency (IAEA) under the grant no. R.K130000.7343.4B623.

REFERENCES

[1] Jang KS (2018) Exploring polyethylene/polypropylene nonwoven fabrics derived from two-dimensionally co-extruded composites: Effects of delamination, consolidation, drawing and nanoparticle incorporation on mechanics, pore size and permeability, Composites Sci Technol 165: 380-387. https://doi.org/10.1016/j.compscitech.2018.07.022

[2] Tourzani AA, Hormozi F, Asadollahzadeh M, Torkaman R (2023) Effective-CO_2 capture by using poly(acrylonitrile) nanofibers based on the radiation grafting procedure in fixed-bed adsorption column. Sci Rep 13: 6173. https://doi.org/10.1038/s41598-023-33036-y

[3] Ishihara R, Asai S, Saito K (2020) Recent progress in charged polymer chains grafted by radiation-induced graft polymerization: adsorption of proteins and immobilization of inorganic precipitates. Quantum Beam Sci 4: 20. https://doi.org/10.3390/qubs4020020

[4] Bhattacharya A, Misra BN (2004) Grafting: a versatile means to modify polymers, Techniques, factors and applications, Prog Polym Sci 29: 767-814. https://doi.org/10.1016/j.progpolymsci.2004.05.002

[5] Zubair NA, Nasef MM, Mohamad NA, Abouzari-Lotf E, Ting TM, Abdullah EC (2020) Kinetic studies of radiation induced grafting of N-vinylformamide onto polyethylene/polypropylene fibrous sheets and testing its hydrolysed copolymer for CO_2 adsorption. Radiat Phys Chem 171: 108727. https://doi.org/10.1016/j.radphyschem.2020.108727

[6] Zubair, NA, Moawia, RM, Nasef MM, Hubbe M, Zakeri M (2022) A critical review on natural fibers modifications by graft copolymerization for wastewater treatment, J Polym Environ 30: 1199-1227. https://doi.org/10.1007/s10924-021-02269-1

[7] Nasef MM, Ting TM, Abbasi A, Layeghi-moghaddam A, Sara Alinezhad S, Hashim K (2016) Radiation grafted adsorbents for newly emerging environmental application. Rad Phys Chem 118: 55-60. https://doi.org/10.1016/j.radphyschem.2015.02.025

[8] Rezaei F, Mosca A, Webley P, Hedlund J, Xiao P (2010) Comparison of traditional and structured adsorbents for CO_2 separation by vacuum swing adsorption, Ind Eng Chem Res 49: 4832 - 4841. http://doi.org/10.1021/ie9016545.

[9] Dong D, Wang Y, Wen D, Peng J, Zhao L, Zhai M (2022) Recent progress in environmental applications of functional adsorbent prepared by radiation techniques: A review. J Hazard Mater 424: 126887. https://doi.org/10.1016/j.jhazmat.2021.126887

[10] Nasef MM, Guven O (2012) Radiation-grafted copolymers for separation and purification purposes: status, challenges and future directions, Prog Polym Sci 37: 1597-1656. http://doi.org/10.1016/j.progpolymsci.2012.07.004

[11] Torkaman R, Maleki F, Gholami M, Torab-Mostaedi M, Asadollahzadeh M (2021) Assessing the radiation-induced graft polymeric adsorbents with emphasis on heavy metals removing: A systematic literature review, J Water Process Eng 44: 102371. https://doi.org/10.1016/j.jwpe.2021.102371

[12] Mohamad NA, Nasef MM, Nia PM, et al (2021) Tetraethylenepentamine-containing adsorbent with optimized amination efficiency based on grafted polyolefin microfibrous substrate for CO_2 adsorption. Arab J Chem 14:103067. https://doi.org/10.1016/j.arabjc.2021.103067

[13] Abbasi A, Nasef MM, Faridi-Majidi R, et al (2018) Highly flexible method for fabrication of poly (Glycidyl Methacrylate) grafted polyolefin nanofiber. Rad Phys Chem 151: 283-291. https://doi.org/10.1016/j.radphyschem.2018.07.002

[14] Abbasi A, Nasef MM, Babadi FE, Faridi-Majidi R, Takeshi M, Abouzari-Lotf E, Choong T, Somwangthanaroj A, Kheawhom (2019) Carbon Dioxide Adsorption on Grafted Nanofibrous Adsorbents Functionalized Using Different Amines. Front Energy Res 7: 1-14. https://doi.org/10.3389/fenrg.2019.00145

[15] Abbasi A, Nasef MM, Kheawhom S, Faridi-Majidi R, Takeshi M, Abouzari-Lotf E, Choong T (2019) Amine functionalized radiation induced grafted polyolefin nanofibers for CO_2 adsorption. Rad Phys Chem 156: 58-66. https://doi.org/10.1016/j.radphyschem.2018.10.015

[16] Imanian Z, Hormozi F, Torab-Mostaedi M, Asadollahzadeh M (2022) Highly selective adsorbent by gamma radiation-induced grafing of glycidyl methacrylate on polyacrylonitrile/polyurethane nanofiber: Evaluation of CO_2 capture. Sep Purif Technol: 289, 120749. https://doi.org/10.1016/j.seppur.2022.120749

[17] Rojek T, Gubler L, Nasef MM, Abouzari-lotf E (2017) Polyvinylamine containing adsorbent by radiation induced grafting of N-vinylformamide onto UHMWPE films and hydrolysis for CO2 capture. Ind Eng Chem Res 56: 5925-5934. https://doi.org/10.1021/acs.iecr.7b00862

[18] Hidzir, NM, Hill DJT, Martin D, Grondahl L (2012) Radiation-induced grafting of acrylic acid onto expanded poly(tetrafluoroethylene) membranes. Polym 53: 6063–71. https://doi.org/10.1016/j.polymer.2012.10.042

[19] Afolabi HK, Nasef MM, Nordin NAH, Ting TM, Harun NY, Abbasi A (2021) Facile preparation of fibrous glycidol-containing adsorbent for boron removal from solutions by radiation-induced grafting of poly(vinylamine) and functionalisation. Rad Phys Chem 188: 109596. https://doi.org/10.1016/j.radphyschem.2021.109596

[20] Ahmed S, Ramli R, Yusup S (2017) Development of polyethylenimine-functionalized mesoporous Si-MCM-41 for CO2 adsorption. Fuel Process Technol 167: 622-630. https://doi.org/10.1016/j.fuproc.2017.07.036

[21] Mafra L, Čendak T, Schneider S, Wiper PV, Pires J, Gomes JRB, Pinto ML (2017) Amine functionalized porous silica for CO2/CH4 separation by adsorption: Which amine and why. Chem Eng J 336: 612–621. https://doi.org/10.1016/j.cej.2017.12.061

[22] Zain G, Babar AA, Iqbala N, Wang X, Yu JY, Ding B (2018) Amine-impregnated porous nanofiber membranes for CO_2 capture, Comp Commun 10: 45-51. https://doi.org/10.1016/j.coco.2018.06.005

[23] Tourzani AA, Hormozi F, Asadollahzadeh M, Torkaman R (2023) Effective CO_2 capture by using poly (acrylonitrile) nanofibers based on the radiation grafting procedure in fixed-bed adsorption column, Sci Reports 13: 6173. https://doi.org/10.1038/s41598-023-33036-y

J. Innovative Eng. Nat. Sci., c. 3, s. 2, ss. 89-102, 2023.
http://dx.doi.org/10.29228/JIENS.70375

JIENS
Journal of Innovative Engineering and Natural Science
Yenilikçi Mühendislik ve Doğa Bilimleri Dergisi

Araştırma Makalesi

Journal of Innovative Engineering and Natural Science
(Yenilikçi Mühendislik ve Doğa Bilimleri Dergisi)
journal homepage: https://jiens.org

Haloysit içeren stiren-bütadien kauçuk nanokompozitlerinin hazırlanması ve mekanik özelliklerinin incelenmesi

Seda Bekin Açar[a,*], Mehmet Atilla Taşdelen[a,*] ve Bağdagül Karaağaç[b]

[a]*Yalova Üniversitesi, Mühendislik Fakültesi, Polimer Malzeme Mühendisliği Bölümü, Yalova, 77200, Türkiye.*
[b]*Kocaeli Üniversitesi, Mühendislik Fakültesi, Kimya Mühendisliği Bölümü, Kocaeli, 41380, Türkiye.*

MAKELE BİLGİSİ

Makale Geçmişi:
Geliş 31 Mayıs 2023
Düzeltme 14 Haziran 2023
Kabul 20 Haziran 2023

Çevrimiçi mevcut

Anahtar Kelimeler:
Haloysit
Kauçuk
Nanokompozit
Stiren-bütadien kopolimeri

ÖZET

Bu çalışmada, saf haloysit (HNT) ile tiyol ve vinil gruplarıyla fonksiyonlandırılmış HNT nanodolguları, stiren-bütadien kauçuk (SBR) karışımlarına 3 phr olacak şekilde eklenerek farklı SBR nanokompozitleri hazırlanmış ve bu nanokompozitler reolojik, mekanik ve morfolojik olarak karakterize edilmiştir. Hazırlanan nanokompozitlerin termal yaşlanma prosesleri ve çapraz bağ yoğunlukları da HNT nanotüpleri varlığında incelenmiştir. SBR nanokompozitleri kükürt ile vulkanize edilmiş ve pişme özellikleri döner kalıp reometresi ile belirlenmiştir. Tiyol ile modifiye edilmiş HNT nanodolgusu ile hazırlanan SBR nanokompozitinin, saf HNT ve vinil modifiyeli HNT içeren nanokompozitlere göre daha fazla çapraz bağ yoğunluğu içerdiği bulunmuştur. Ayrıca, saf ve fonksiyonlandırılmış HNT içeren tüm SBR nanokompozitlerinin, nanodolgu içermeyen kauçuk karışımına kıyasla daha iyi mekanik özellikler gösterdiği belirlenmiştir. Bu sonuç, SBR matrisinde bulunan HNT'nin takviye etkisini göstermiştir. Ayrıca, uygulanan termal yaşlanma sonrası SBR/HNT nanokompozitlerinin çapraz bağ yoğunlukları ile mekanik kuvvetleri artmıştır. Bu durum ise ısı etkisiyle ilave çapraz bağ oluşumunu ifade eden post-cure etkisini doğrulamıştır.

Preparation and mechanical characterization of halloysite containing styrene-butadiene rubber nanocomposites

ARTICLE INFO

Article history:
Received 31 May 2023
Received in revised form 14 Jun 2023
Accepted 20 Jun 2023

Available online

Keywords:
Halloysite
Nanocomposite
Rubber
Styrene-butadiene copolymer

ABSTRACT

In this study, different SBR nanocomposites were prepared by adding pure halloysite (HNT) and thiol- and vinyl- modified HNT nanofillers to styrene-butadiene rubber (SBR) compounds at 3 phr. These nanocomposites were characterized in terms of rheological, mechanical, and morphological properties. The aging process and crosslinking density of the prepared nanocomposites were also investigated in the presence of HNT nanotubes. The sulfur curing characteristics of SBR vulcanizates were determined by moving die rheometer. It was found that the SBR nanocomposite including thiol- modified HNT had higher crosslinking density than the other nanocomposites prepared with pure HNT and vinyl- modified HNT. Also, all SBR nanocomposites containing pure and functionalized HNT showed better mechanical properties compared to the reference sample without nanofillers. This result showed the reinforcement effect of HNT in the SBR matrix. In addition, the crosslink density and mechanical strength of SBR/HNT nanocomposites increased with thermal aging process. This confirmed the post-cure effect.

---

*Sorumlu yazar. Tel.: +90-226-815-5424; e-mail: seda.acar@yalova.edu.tr

I. GİRİŞ

Kauçuk malzemeler gerekli mekanik, termal, optik, elektriksel ve kimyasal özellikleri sağlamak için farklı roller oynayan çeşitli katkı maddeleriyle birlikte iki veya daha fazla elastomer içerebilen birçok bileşen bulunduran karmaşık sistemlerdir. Vulkanize olmuş elastomerler genellikle yüksek mukavemet gerektiren yerlerde kullanılırlar. Bu nedenle, mekanik dayanımlarını arttırmak ve artan yeniliklerle istenen özellikleri sağlamak için kauçuk bileşimine farklı takviye maddelerinin eklenmesi gerekmektedir [1, 2]. Takviye-kauçuk etkileşimi, hazırlanan kauçuk kompozitlerin fiziksel özelliklerinin iyileştirilmesi için önemli bir parametredir. Kullanılan takviyelerin çoğu mikron boyutunda mineraller veya karbonize organik bileşiklerdir. Takviye boyutunu mikrometreden nanometreye indirerek elde edilen, nano boyutlu parçacıklarla güçlendirilmiş nanokompozitler üstün özellikler sergilerler [3]. Son zamanlarda, kauçuk esaslı nanokompozitlerin geliştirilmesi büyük ilgi görmektedir. Katmanlı silikatlar, karbon nanotüpler, metal oksitler ve haloysitler gibi nano boyutlu dolgu maddeleri kullanılarak hazırlanan kauçuk nanokompozitler, esnekliğin önemli bir gereklilik olduğu lastiklerde ve teknik parçalarda yaygın olarak kullanılmaktadır [4, 5].

HNT, $Al_2Si_2O_5(OH)_4 \cdot nH_2O$ genel formülüne sahip, doğal, nano yapılı ve boru şeklinde bir silika-alümina kildir. Silikon benzeri bir dış yüzeye ve tüpün içinde alüminyum benzeri bir yapıya sahip kaolinit katmanlarından oluşan HNT nanotüpleri, karbon nanotüplere kıyasla kolayca elde edilebilir ve çok daha ekonomiktir [6]. Ayrıca, montmorillonit gibi diğer silikat bazlı kil minerallere benzer kimyasal yapıları nedeniyle, HNT'ler polimer matris ile kimyasal veya fiziksel olarak kolayca birleştirilebilen potansiyel nanodolgu maddeleri haline gelmiştir [7]. Buna ek olarak, haloysitin büyük uzunluk-çap oranı, takviye edici nanodolgu maddesi olarak kullanıldığı polimer ve kauçuk nanokompozitlere ek faydalar sağlar. Polimer/kauçuk matrislere HNT ilavesi, geliştirilmiş mekanik, termal, alev geciktirici ve bariyer özelliklerine sahip nanokompozitlerle sonuçlanır [8, 9]. Bu sayede HNT, farklı termoplastik polimer ve SBR gibi kauçuk matrislerde takviye dolgu maddesi olarak kullanılmaktadır.

Stiren-bütadien kauçuğu (SBR), stiren ve bütadienin kopolimeri olan ve polar olmayan sentetik kauçuk türlerinden biridir [10, 11]. Ayrıca SBR iyi hava ve nem direnci ve yüksek dolgu yükleme kapasitesi gibi değerli özelliklerinden dolayı ağırlıklı olarak lastik endüstrisinde ham madde olarak kullanılmaktadır [11-13]. SBR'nin özelliklerini geliştirmek için küresel karbon siyahı ve silika, yüksek yükleme oranlarıyla geleneksel takviye dolgu maddeleri olarak uzun süredir kullanılmaktadır. Ancak dolgu maddelerinin aşırı yüklenmesi, kauçuk matrislerde topaklaşmaya neden olur ve bu durum kauçuk kompozitlerin yorulma performansı gibi mekanik özelliklerini olumsuz etkiler [14]. Bu nedenle, son yıllarda nano boyutlu dolgular akademik ve endüstriyel alanlarda daha fazla ilgi görmektedir. Nanodolgular yüksek en-boy oranı ve gelişmiş arayüz uyumluluğu sayesinde düşük dolgu konsantrasyonlarında bile kauçuk nanokompozitlerin mekanik özelliklerinde önemli gelişmeler sağlarlar [11].

Bu çalışmada, saf HNT ve modifiye edilmiş HNT nanodolgularının SBR reçetelerinde takviye edici olarak kullanılmasıyla SBR nanokompozitleri ve ayrıca nanodolgu içermeyen referans SBR kompoziti hazırlanmıştır. Homojen bir kauçuk/HNT karışımı elde etmek, HNT ile kauçuk makromoleküllerinin düşük karışabilirliği nedeniyle oldukça zordur ve bu durum HNT nanodolgusunun sağladığı pozitif etkiyi azaltır [15]. Dolayısıyla, hidrofobikliğin ve SBR ile arasındaki etkileşimin artması amacıyla HNT modifiye edilebilir [16]. Bu amaçla öncelikle farklı fonksiyonel gruplar içeren silan bağlama ajanlarıyla HNT modifikasyonu gerçekleştirilmiştir.

HNT-Tiyol (3-merkaptopropil) trimetoksisilan ile modifikasyon sonucu, HNT-Vinil ise viniltrietoksisilan ile modifikasyon sonucu elde edilmiştir. Fonksiyonlandırma işleminin gerçekleştiği FTIR analizi ile doğrulandıktan sonra bu nanodolgular ile saf HNT'nin 3 phr olacak şekilde SBR reçetelerine eklenmesiyle SBR nanokompozitleri elde edilmiştir. Çapraz bağlama maddesi olan kükürt, tüm kompozit reçetelerde 1,5 phr olacak şekilde kullanılmıştır. Hazırlanan nanokompozitler ile referans numunesinin yapısal, reolojik, mekanik ve morfolojik özellikleri ile çapraz bağ yoğunlukları incelenmiştir. Ayrıca, SBR nanokompozitlerinin termal yaşlanma sürecinden sonra özelliklerinde meydana gelen değişim de belirlenmiştir.

II. DENEYSEL METOT

2.1 Malzemeler

Stiren-bütadien kauçuğu (%27 stiren içeriğine sahip, SBR 1502) Arlanxeo, Almanya firmasından temin edilmiştir. Saf HNT nanodolgusu Sigma Aldrich, tiyol ve vinil modifikasyonu için kullanılan silan bağlama ajanları olan (3-merkaptopropil) trimetoksisilan ve viniltrietoksisilan ise Alfa Aesar firmalarından satın alınmıştır. Çinko oksit (ZnO), stearik asit (SA), 2,2,4-trimetil-1,2-dihidrokinolin (TMQ), n-izopropil-n'-fenil 1,4-fenilendiamin (IPPD), ozon wax, tetrametiltiyuram disülfür (TMTD), N-sikloheksil-2-benzotiyazol sülfenamid (CBS) ve kükürt (S) Rubber Chem, Türkiye firmasından alınmış ve satın alındığı şekliyle, ayrıca bir saflaştırma yapılmadan kullanılmıştır.

2.2 HNT Modifikasyonu

Saf HNT, SBR matrisi ile arasındaki etkileşimin artması amacıyla tiyol ve vinil grupları ile modifiye edilmiştir. Tiyol modifikasyonu için (3-merkaptopropil) trimetoksisilan kullanılmış ve elde edilen nanodolgu HNT-Tiyol olarak adlandırılmıştır. Vinil fonksiyonlu haloysit sentezi için ise viniltrietoksisilan kullanılmış ve elde edilen nanodolgu HNT-Vinil şeklinde isimlendirilmiştir.

2.2.1. HNT-Tiyol ve HNT-Vinil sentezleri

Modifikasyon için kullanılmadan önce 100 ^{o}C'de 1 gün kurutulan 2 g HNT, ultrasonik banyo ile 50 ml toluende dağıtılmış ve ardından bu çözeltiden 15 dk boyunda azot gazı geçirilerek inert ortam sağlanmıştır. HNT-Tiyol sentezi için 0,021 mol (3-merkaptopropil) trimetoksisilan, HNT-Vinil sentezi için ise 0,021 mol viniltrietoksisilan eklenen bu çözelti tekrar azot gazından geçirilmiştir. Daha sonra manyetik karıştırıcıda 110 ^{o}C'de reflux edilerek 18 saat boyunca karıştırılmıştır. Reaksiyon sonunda önce oda sıcaklığına soğutma, daha sonra filtrasyon ve toluenle yıkama işlemleri yapılmış ve alınan katı faz 60 ^{o}C'deki vakum etüvünde 2 gün kurutularak fonksiyonlandırılmış HNT nanodolguları elde edilmiştir. Modifikasyonun başarılı olup olmadığı FTIR analizi ile doğrulanmıştır.

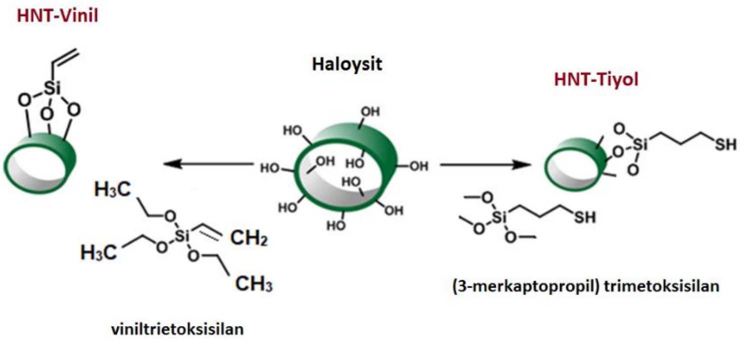

Şekil 1. HNT'nin vinil ve tiyol grupları ile fonksiyonlandırılması

2.3 SBR/HNT Nanokompozitlerinin Hazırlanması

Saf HNT, HNT-Tiyol ve HNT-Vinil nanodolguları kullanılarak hazırlanan SBR nanokompozitlerine ait reçete Tablo 1'de verilmiştir. Kauçuk hamur karışımları 50 rpm motor hızına sahip laboratuvar tipi banbury kullanılarak hazırlanmıştır. Hamurları hazırlamak için öncelikle SBR banbury içinde 2 dk boyunca karıştırılmıştır. Bu şekilde mastikasyonu yapılan SBR'nin bulunduğu banbury'ye nanodolgu (saf HNT, HNT-Tiyol veya HNT-Vinil) ilave edilerek 1 dk karıştırılmıştır. Ardından ZnO ve stearik asit eklenerek 0,5 dk daha karıştırıldıktan sonra TMQ, IPPD ve ozon wax ilave edilmiş ve 0,5 dk daha karıştırılmıştır. Son olarak TMTD ve CBS hızlandırıcıları ile pişirici olan kükürt eklenmiş ve 1 dk daha karıştırılmıştır. Banbury içindeki 5 dakikalık karıştırma prosesinden sonra yaklaşık 80 °C sıcaklıktaki kauçuk hamuru elde edilmiştir. Verilen reçetede nanodolgu kullanılmadan hazırlanan örnek ise referans numunesidir. Hazırlanan nanokompozitler ile referans hamurunun vulkanizasyon işlemi, reometre eğrilerinden belirlenen optimum pişme süreleri boyunca 160 °C sıcaklıkta ve 150 bar basınçta çalışan bir hidrolik sıcak pres ile 2 mm ve 6 mm kalınlığındaki levha kalıplarda yapılmıştır. Vulkanize edilen kauçuk karışımlarının termal yaşlanma prosesleri bir hava sirkülasyonlu etüvde 70 °C sıcaklıkta 70 saat boyunca bekletilerek yapılmış ve yaşlanma sonrası numunelerin yapısal ve mekanik özellikleri ile çapraz bağ yoğunlukları incelenmiştir.

Tablo 1. Saf HNT, HNT-Tiyol ve HNT-Vinil nanodolguları ile hazırlanan SBR nanokompozit reçeteleri

Malzeme	İçerik (phr)	Malzeme	İçerik (phr)
SBR	100	IPPD	1
Saf HNT HNT-Vinil HNT-Tiyol	3	Ozon wax	1
ZnO	5	TMTD	1
SA	2	CBS	1
TMQ	1	S	1,5

2.4 SBR/HNT Nanokompozitlerinin Karakterizasyonu

Önemli pişme özellikleri ve reolojik parametreler bir döner kalıp reometresi (MDR, Alpha Teknolojileri) ile ASTM D5289 standardına göre belirlenmiştir. Fonksiyonlandırılan HNT nanodolguları ile hazırlanan kauçuk kompozitlerin yapısal özellikleri Perkin Elmer Spectrum 100 model Fourier Dönüşümlü Kızılötesi Spektrometresi (FTIR) ile incelenmiş ve ATR ünitesindeki germanyum kristal üzerine yerleştirilmiş numunelerin 650-4000 cm^{-1} aralığında IR spektrumları alınmıştır. SBR/HNT nanokompozitleri ile referans numunesinin mekanik özellikleri, Instron marka 3345 model universal test cihazı kullanılarak ASTM D412 standardına göre ve 500 mm/dk çekme hızı ile belirlenerek kopma dayanımı, kopmadaki uzama ve modül değerleri ölçülmüştür. Kauçuk vulkanizatların sertlik ölçümleri Zwick Roell durometre ile ASTM D2240 standardına uygun olacak şekilde her numune için 5 farklı örnek üzerinden yapılmıştır. Kalıcı deformasyon testi ise ASTM D395 standardına uygun şekilde gerçekleştirilmiştir. Referans ve SBR/HNT vulkanizatlarının ve tüm yaşlandırılmış numunelerin çapraz bağ yoğunlukları, toluende şişen örneklerin, denge çözücü-şişme prensibine göre Flory-Rehner eşitliğinin uygulanmasıyla belirlenmiştir [5, 11]. Çapraz bağ yoğunlukları hesaplanırken kauçuk matris ve toluenin yoğunlukları [17], polimerin ve çözücünün hacim fraksiyonları [18] ve polimer-çözücü etkileşim parametresi [18-20] dikkate alınmıştır. HNT içeren SBR nanokompozitlerinin taramalı elektron mikroskobu (SEM) analizi, FEI QUANTA FEG 250 SEM-EDX cihazı ile 80000 kat büyütme ve 5 kV hızlanma voltajında gerçekleştirilmiştir. SEM analizinden önce, çekme testinde kopan numune yüzeyleri altın püskürtme ile kaplanmıştır.

III. BULGULAR VE TARTIŞMA

3.1 Reolojik Karakterizasyon

Saf HNT, HNT-Tiyol ve HNT-Vinil bulunduran SBR nanokompozitleri ile referans numunesinin 160 ºC'de belirlenen reometre eğrileri Şekil 2'de verilmiştir. Her bir örnek için 3 kez reometre testi yapılmış ve önemli reolojik parametreleri içeren ortalama sonuçlar Tablo 2'de sunulmuştur. Tüm nanokompozitlerin viskozite ile orantılı olan minimum tork (ML) değerleri oldukça benzerdir. Bunun yanında, SBR/HNT-Tiyol örneğinin maksimum tork (MH) ve pişme genliği (CE) değerleri en yüksek iken, SBR/HNT-Vinil örneğinin bu değerleri en düşüktür. Maksimum ve minimum torklar arasındaki farktan hesaplanan CE değeri, karışımın çapraz bağ yoğunluğu ile yakından ilgilidir. Dolayısıyla, HNT-Tiyol ile hazırlanan SBR nanokompozitin en yüksek, HNT-Vinil ile hazırlananın ise en düşük çapraz bağ yoğunluğuna sahip olduğu öngörülmektedir. Ön pişme süresi (t_{s2}) HNT modifikasyonundan etkilenmemiş ve hazırlanan tüm SBR nanodolguları için benzer sonuçlar alınmıştır. Optimum pişme süresi (t_{90}) ise MH ve CE'deki trendin aksine, SBR/HNT-Tiyol için en düşük, SBR/HNT-Vinil için ise en yüksektir. Çapraz bağ yoğunluğu ile t_{90} değerlerinde gözlenen bu değişiklik, HNT-Tiyol'deki tiyol gruplarında mevcut olan kükürdün vulkanizasyon reaksiyonuna katılarak çapraz bağlanma sağlayacak kükürt miktarını arttırması ve reaksiyon mekanizmasını bu yönde değiştirmesine atfedilebilir. Kauçuk hamurlarının pişmesini karakterize eden ve önemli reolojik parametrelerden bir diğeri olan pişme hız indisi (CRI) ise Denklem 1'e göre hesaplanmaktadır.

$$CRI = \frac{100}{t_{90} - t_{s2}} \tag{1}$$

Tablo 2’de verilen CRI değerleri, HNT-Vinil içeren SBR karışımının daha hızlı çapraz bağlandığını ifade etmektedir. Bu karışımda, reçetede bulunan kükürdün vulkanizasyon reaksiyonunun erken aşamasında tükenmesi çapraz bağ yoğunluğunu azaltan bir etkiye neden olmuştur. Bu durum, SBR/HNT-Vinil için öngörülen düşük çapraz bağ yoğunluğunu doğrulamaktadır.

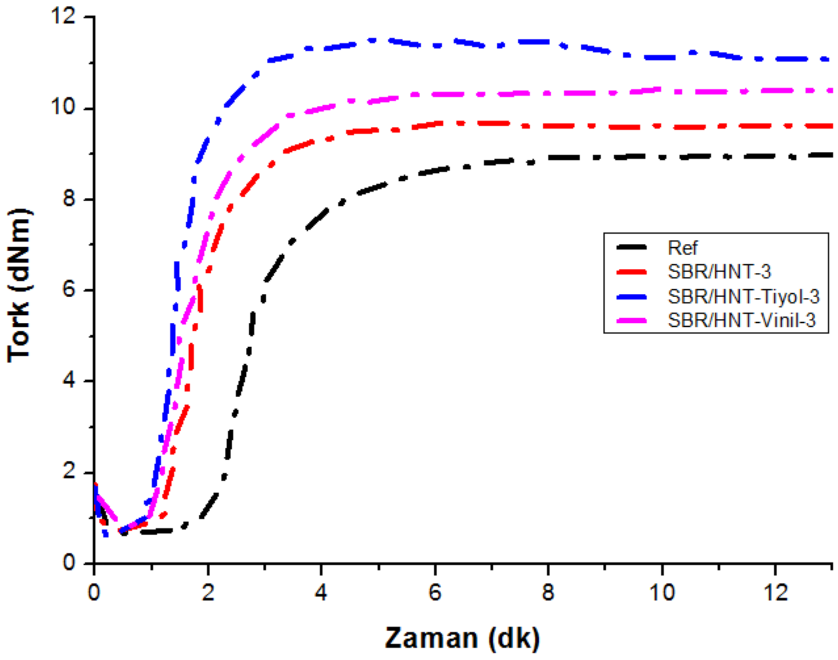

Şekil 2. SBR/HNT nanokompozitlerinin reometre eğrileri

Tablo 2. SBR/HNT nanokompozitlerinin reometre verileri

Örnekler	ML (dNm)	MH (dNm)	CE (dNm)	t_{s2} (dk)	t_{90} (dk)	CRI (dk^{-1})
SBR/HNT	0,70	10,29	9,59	1,63	3,32	59,43
SBR/HNT-Tiyol	0,63	11,86	11,24	1,35	2,64	77,80
SBR/HNT-Vinil	0,67	8,64	7,97	1,71	4,35	43,90

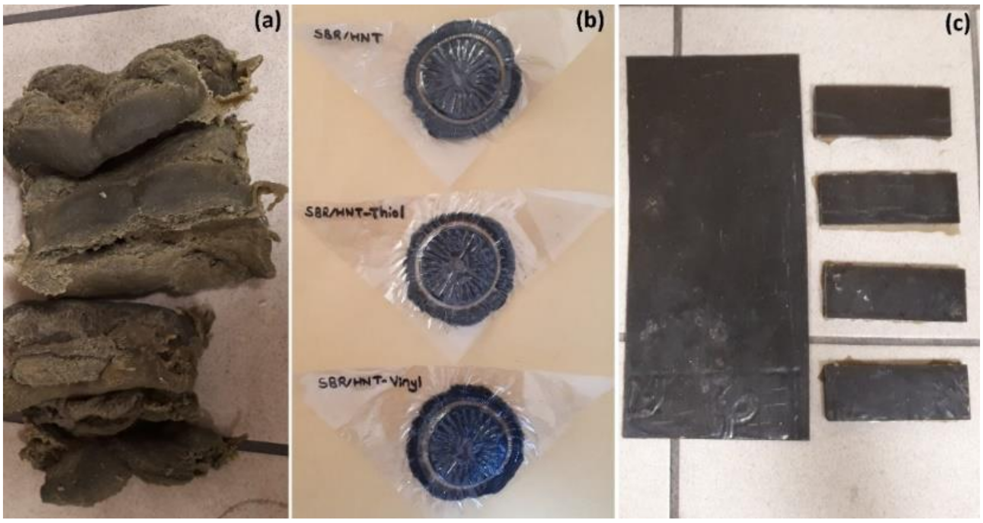

Şekil 3. (a) Banbury’den çıkan SBR/HNT kauçuk hamuru, (b) Reometreden çıkan SBR/HNT, SBR/HNT-Tiyol ve SBR/HNT-Vinil örnekleri, (c) 2 mm ve 6 mm’lik levhalar şeklinde preste basılarak vulkanize edilen SBR/HNT nanokompozitleri

3.2 FTIR Karakterizasyonu

Öncelikle saf HNT, HNT-Tiyol ve HNT-Vinil nanodolgularının FTIR karakterizasyonu yapılmış, modifiye edilmiş HNT'lerin FTIR spektrumları saf HNT'ninki ile karşılaştırılarak modifikasyonun başarıyla gerçekleştiği doğrulanmıştır. HNT-Tiyol nanodolgusunun FTIR spektrumunda S-H piki 2550 cm^{-1} ve C-H piki 2920 cm^{-1} dalga boyunda tespit edilmiştir [21]. HNT-Vinil nanodolgusunda ise 1620 ve 1425 cm^{-1}'de C=C pikleri, 2970 ve 3050 cm^{-1}'de ise C-H pikleri gözlenmiştir [21, 22].

SBR/HNT nanokompozitlerinin FTIR spektrumları Şekil 4'te, referans örneğinin spektrumlarına ait piklerin dalga boyları ise Tablo 3'te verilmiştir [13, 17, 23]. HNT'de bulunan Si-O gruplarına ait bağın gerilme titreşimi HNT-Tiyol içeren kauçuk nanokompozitinde 1094 cm^{-1}'de, saf HNT ve HNT-Vinil içeren nanokompozitlerde ise 1101 cm^{-1}'de görülmüştür. Vulkanizasyondan sonra yapılan FTIR analizinde 1643 cm^{-1}'de pik gözlenmemesi vulkanizasyon prosesinin başarısını doğrulamaktadır. Bunun yanında, yaşlandırılmış SBR/HNT, SBR/HNT-Tiyol ve SBR/HNT-Vinil nanokompozitlerinin FTIR spektrumlarında sırasıyla 1725, 1731 ve 1732 cm^{-1} dalga boylarında görülen C=O karbonil pikleri oksidatif yaşlanma prosesini doğrulamıştır. SBR'nin ana zincirinde ve yan gruplarında gerçekleşen termal oksidasyon sonrası alkol, ester ve eter gibi oksijen bulunduran moleküller kolay bir şekilde oluşabilmektedir [24].

Tablo 3. Referans numunesinin FTIR spektrumuna ait dalga boyları

Referans örneğindeki bağ türü	Dalga boyu (cm^{-1})
O-H gerilmesi	3400-3450
C-H gerilmesi	2917 ve 2847
C=O gerilmesi	1719
C=C gerilmesi	1638
C-H bağının asimetrik eğilme titreşimleri	1451
C-H bağının simetrik eğilme titreşimleri	1396
C-O gerilmesi	1075
Bütadienin trans 1,4 –C=C faz dışı deformasyonu	964
SBR'ye ait polistirenin C=C grupları	758
Aromatik =C-H düzlem dışı titreşimleri	694

3.3 Mekanik Karakterizasyon

Hazırlanan kauçuk nanokompozitlerin vulkanizasyon ve yaşlandırma sonrası ayrı ayrı mekanik karakterizasyonları yapılmıştır. Mekanik özellikleri incelemek amacıyla SBR/HNT nanokompozitlerine çekme-kopma, sertlik ve kalıcı deformasyon testleri uygulanmıştır. Bu testlere ait veriler 5 test sonucunun ortalaması alınarak standart sapma değerleri ile Şekil 5, Şekil 6 ve Şekil 7'de verilmiş ve Tablo 4'te özetlenmiştir.

Çekme testi sonucunda en iyi mekanik özellikleri gösteren SBR/HNT-Tiyol nanokompozitinin kopma dayanımı (2,62 MPa), SBR/HNT nanokompozitinin kopma dayanımına (2,27 MPa) kıyasla %15 daha yüksektir. SBR/HNT nanokompozitleri, kopma dayanımı 1,41 MPa olan ve nanodolgu kullanmadan hazırlanan referans numunesiyle kıyaslandığında ise, kauçuk karışımına saf HNT eklenmesiyle mekanik dayanımda %61, HNT-Tiyol eklenmesiyle ise %86'lık bir artış sağlanmıştır. Bu sonuçlara göre HNT nanodolgusunun SBR matrisi ile iyi etkileşim ve kauçuk reçetesi için iyi bir takviye etkisi göstererek gelişmiş mekanik özellikler sağladığı söylenebilir [5, 11]. SBR/HNT-Vinil nanokompozitinde ise düşük çapraz bağ yoğunluğu nedeniyle mekanik özelliklerde beklenen artış görülememiştir. Buna rağmen saf HNT, HNT-Tiyol ve HNT-Vinil ile hazırlanan her

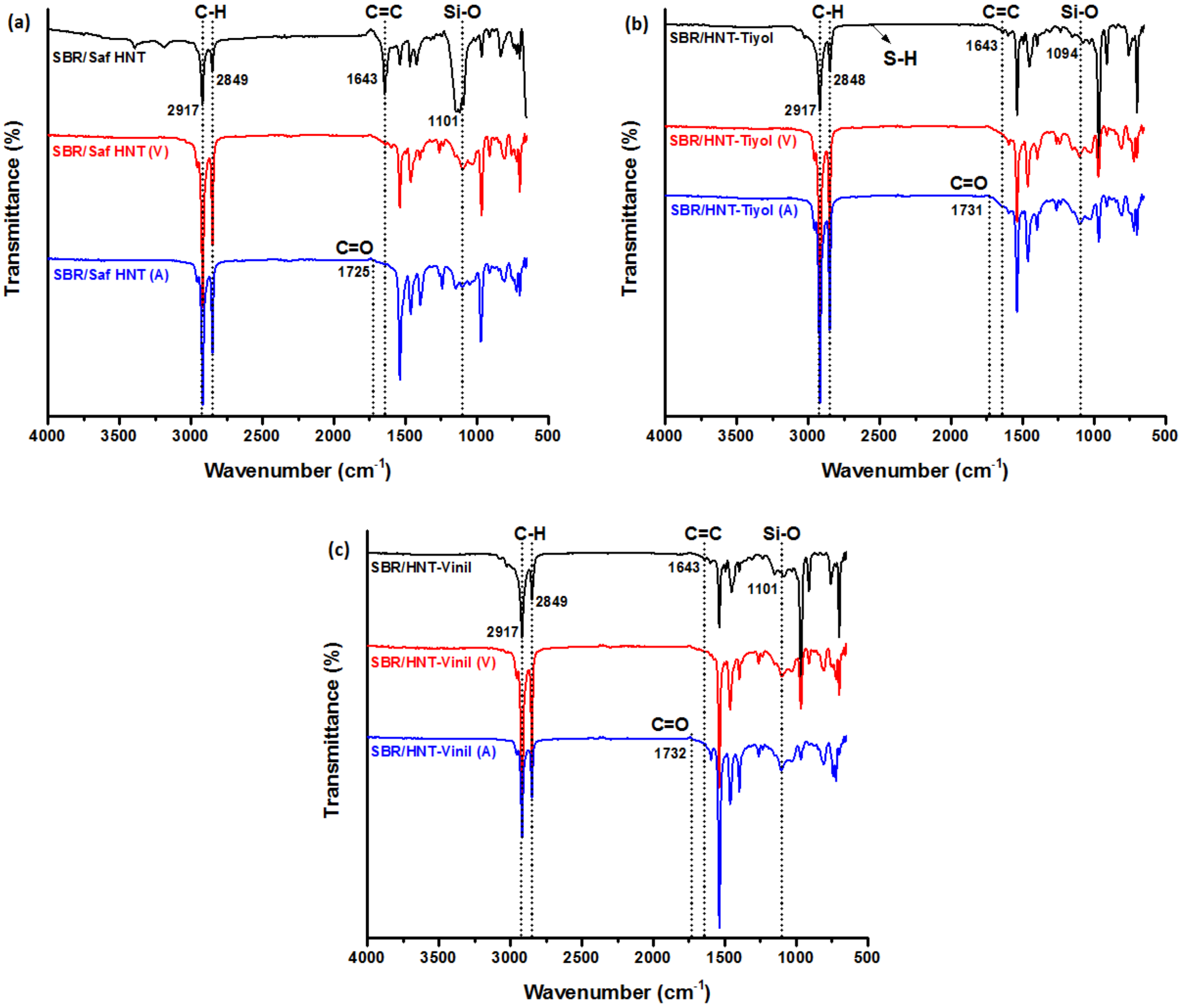

Şekil 4. SBR/HNT, SBR/HNT-Tiyol ve SBR/HNT-Vinil nanokompozitlerinin hamur, vulkanizat (V) ve yaşlandırılmış (A) durumlarındaki FTIR spektrumları

üç nanokompozitin de mekanik özellikleri HNT içermeyen referans numunesinden daha yüksektir. Kopmadaki uzama değerleri de kopma dayanımı ile benzer bir değişim trendi göstererek SBR/HNT-Tiyol için en yüksek iken SBR/HNT-Vinil için en düşüktür. SBR/HNT-Tiyol nanokompozitinin kopmadaki uzaması SBR/HNT'ye göre %48,7, referans numunesine göre ise %81,3 daha yüksektir. Termal yaşlandırma prosesinden sonra saf HNT ve HNT-Tiyol ile hazırlanan SBR nanokompozitlerinin kopma dayanımında artış olduğu görülmüştür. Bu durum ısı etkisi ile ekstra çapraz bağlar oluştuğunu gösteren post-cure etkisinin gerçekleştiğini düşündürmektedir. HNT-Vinil içeren kauçuk nanokompozitlerde ise post-cure etkisi gözlenmemiştir.

Kauçuk türüne, çapraz bağ yoğunluğuna ve dolgu miktarına bağlı olan sertlik değerleri ve çekme testi ile belirlenen modül değerleri, SBR/HNT-Tiyol için en yüksek iken, SBR/HNT-Vinil için en düşüktür. Kauçuk nanokompozit reçetelerine HNT-Vinil eklendiğinde Shore A sertliğinin oldukça fazla düştüğü görülmüştür. Bu sonuç, HNT-Vinil nanodolgusunun reaksiyon mekanizmasını tamamen değiştirdiğini göstermekte ve çapraz bağ yoğunluğunun azaldığını ifade eden reolojik verileri doğrulamaktadır. Ayrıca, polimerlerin modülleri artan rijitlik ile artmaktadır. Termal yaşlandırma işleminden sonra, rijitlik artışına bağlı olarak kauçuk nanokompozitlerinin sertlik ve modül değerleri de artmıştır [25-27].

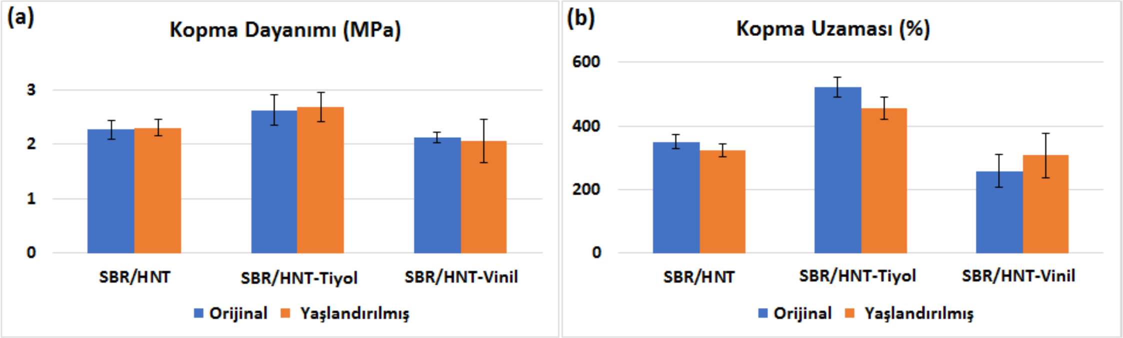

Şekil 5. SBR/HNT nanokompozitlerinin vulkanizat ve yaşlandırılmış durumlardaki (a) kopma dayanımları ve (b) kopmadaki uzamaları

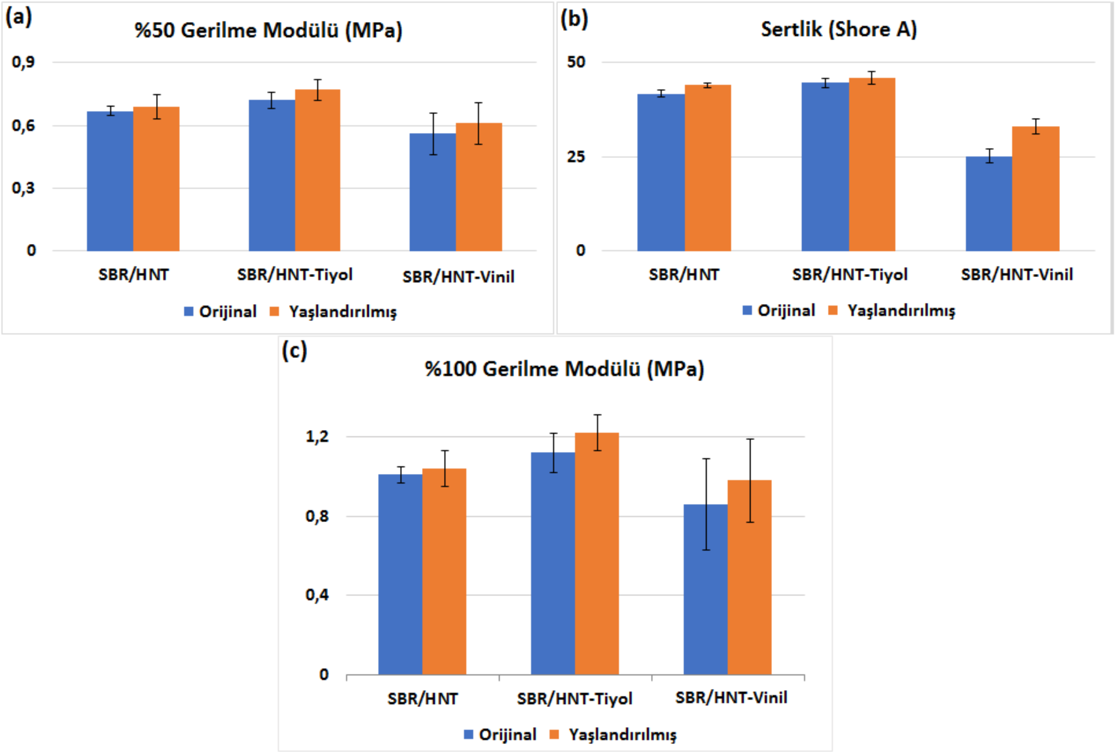

Şekil 6. SBR/HNT nanokompozitlerinin vulkanizat ve yaşlandırılmış durumlardaki (a) %50 gerilme modülleri, (b) Shore A sertlikleri ve (c) %100 gerilme modülleri

Saf HNT ile tiyol ve vinil fonksiyonel gruplarına sahip HNT nanodolguları ile hazırlanan SBR nanokompozitlerin kalıcı deformasyon testleri ASTM D395 metot B'ye göre gerçekleştirilmiştir. Bu test, nanodolgunun, kauçuk karışımlarının kalıcı deformasyonu üzerindeki etkisini ve uzun süreli sıkıştırma sonrasında elastik özelliklerdeki değişimi belirlemek için oda sıcaklığında 22 saat ve 70 ^{o}C'de 70 saat olacak şekilde yapılmıştır. Şekil 7'de görüldüğü gibi her iki koşulda gerçekleştirilen test sonrası SBR/HNT-Tiyol en düşük, SBR/HNT-Vinil ise en yüksek kalıcı deformasyon değerlerini sergilemiştir. Yüksek kalıcı deformasyon değerleri ve azalan elastik özellikler, reometre verilerinden de öngörüldüğü üzere SBR/HNT-Vinil nanokompozitinin düşük çapraz bağ yoğunluğunu doğrulamaktadır.

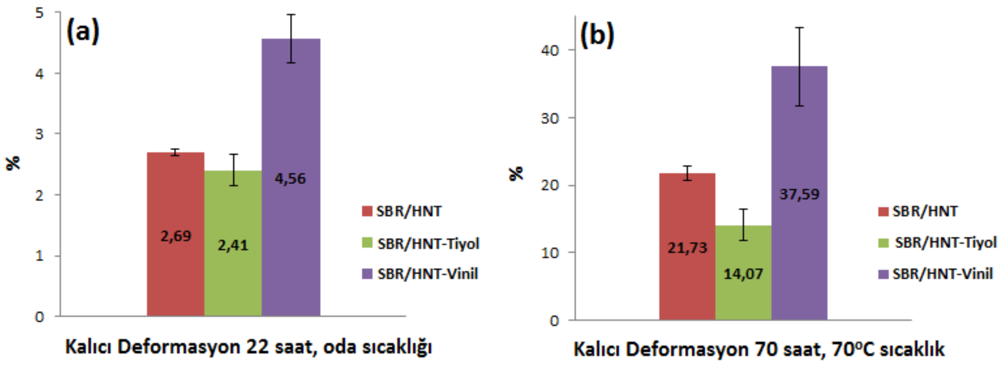

Şekil 7. SBR/HNT nanokompozitlerinin (a) oda sıcaklığında 22 saat, (b) 70°C sıcaklıkta 70 saat yapılan kalıcı deformasyon testi sonuçları

Tablo 4. Vulkanizasyon ve yaşlandırma sonrası SBR/HNT nanokompozitlerinin mekanik özellikleri

Örnek	Kopma Dayanımı[b] (MPa)	Kopmadaki Uzama[b] (%)	%50 Gerilme Modülü[b] (MPa)	%100 Gerilme Modülü[b] (MPa)	Sertlik[c] (Shore A)	Kalıcı Deformasyon[d] (%)
SBR/HNT	2,27 ± 0,17	351 ± 23	0,67 ± 0,02	1,01 ± 0,04	41,8 ± 0,8	2,69 ± 0,06
SBR/HNT (A)[a]	2,30 ± 0,15	324 ± 20	0,69 ± 0,06	1,04 ± 0,09	44,0 ± 0,7	21,73 ± 1,03
SBR/HNT-Tiyol	2,62 ± 0,28	522 ± 30	0,72 ± 0,04	1,12 ± 0,10	44,6 ± 1,1	2,41 ± 0,25
SBR/HNT-Tiyol (A)[a]	2,68 ± 0,26	463 ± 35	0,77 ± 0,05	1,22 ± 0,09	46,0 ± 1,6	14,07 ± 2,32
SBR/ HNT-Vinil	2,13 ± 0,10	259 ± 50	0,66 ± 0,05	0,97 ± 0,18	25,2 ± 1,8	4,56 ± 0,40
SBR/HNT-Vinil (A)[a]	2,06 ± 0,40	307 ± 70	0,59 ± 0,09	0,87 ± 0,20	33,0 ± 2,0	37,59 ± 5,80

[a] (A): Yaşlandırılmış örnekler; [b]ASTM D412'ye göre; [c]ASTM D2240'a göre; [d]ASTM D395'e göre.

3.4 Çapraz Bağ Yoğunluğu (CLD)

SBR/HNT nanokompozitlerinin vulkanizasyon ve yaşlandırma sonrası çapraz bağ yoğunlukları, Flory-Rehner yaklaşımı uygulanarak ve her numune için 3 kez tekrarlanarak hesaplanmış, ortalama sonuçlar standart sapma değerleriyle Şekil 8 ve Tablo 5'te verilmiştir. Buna göre, tiyol fonksiyonlu HNT ile hazırlanan SBR nanokompoziti en yüksek çapraz bağ yoğunluğuna sahip iken, vinil fonksiyonlu HNT ile hazırlanan nanokompozitin en düşük çapraz bağ yoğunluğuna sahip olduğu belirlenmiştir. Bu sonuç, reometre ve mekanik karakterizasyon verileriyle tutarlılık sergilemektedir. Ayrıca, yaşlandırma sonrasında SBR/HNT ve SBR/HNT-Tiyol örneklerinin çapraz bağ yoğunlukları artmış, SBR/HNT-Vinil örneğininki ise azalmıştır. Bu sonuç ise, SBR/HNT-Vinil vulkanizatlarında post-cure etkisi olmadığını ancak diğer iki nanokompozitte bu etkinin gerçekleştiğini kanıtlamıştır.

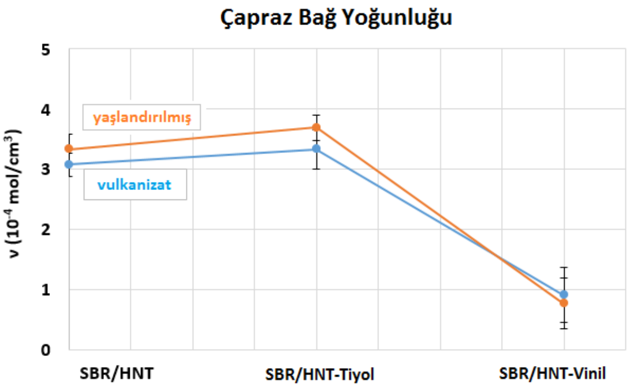

Şekil 8. Vulkanizasyon ve yaşlandırma sonrası SBR/HNT nanokompozitlerinin çapraz bağ yoğunlukları

Tablo 5. Vulkanizasyon ve yaşlandırma sonrasında SBR/HNT nanokompozitlerinin çapraz bağ yoğunlukları

Örnek Adı	CLD değeri (mol/cm^3)
SBR/HNT	3,076 ± 0,19
SBR/HNT (A)	3,330 ± 0,25
SBR/HNT-Tiyol	3,330 ± 0,33
SBR/HNT-Tiyol (A)	3,696 ± 0,21
SBR/HNT-Vinil	0,912 ± 0,46
SBR/HNT-Vinil (A)	0,770 ± 0,42

[a] (A): Yaşlandırılmış örnekler

3.5 Morfolojik Karakterizasyon

SBR/HNT nanokompozitlerinin morfolojik karakterizasyonu, örneklerin çekme testinden sonraki kopma yüzeylerinden alınan SEM görüntüleri ile yapılmıştır. Şekil 9'da verilen SEM analizi sonucunda nanodolgu dağılımı net şekilde gözlenemese de boyutları 154,5-337 nm arasında değişen HNT nanotüplerinin SBR matrisindeki varlığı kanıtlanmıştır. Ancak daha önceki karakterizasyon yöntemleri ile birlikte analiz edildiğinde, saf ve tiyol ile fonksiyonlandırılmış HNT nanodolgularının vinil fonksiyonlu HNT'ye göre nispeten daha homojen dağıldığı sonucuna varılabilir.

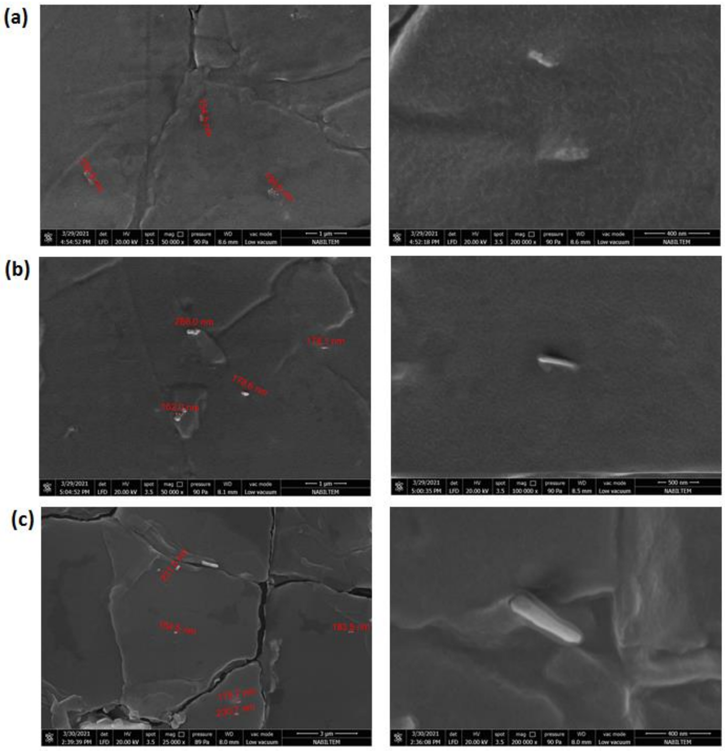

Şekil 9. (a) SBR/HNT, (b) SBR/HNT-Tiyol ve (c) SBR/HNT-Vinil nanokompozitlerinin düşük ve yüksek boyutlardaki SEM görüntüleri

IV. SONUÇLAR

Bu çalışmada, SBR matrisi için nano boyutlu bir takviye dolgusu olarak HNT kullanılmıştır. SBR ile nanodolgu etkileşimini arttırmak amacıyla HNT, tiyol ve vinil gruplarıyla modifiye edilmiş ve saf HNT, HNT-Tiyol ve HNT-Vinil nanodolgularının SBR karışımlarındaki etkisi incelenmiştir. Nanokompozitlerin kükürt vulkanizasyonu karakteristikleri reometre ve çözücü-şişme ölçümleri ile belirlenmiştir. Çapraz bağlanma derecesini ifade eden CE değeri, SBR/HNT-Tiyol nanokompozitinde en yüksek iken SBR/HNT-Vinil'de en düşüktür. Bu durum HNT-Tiyol nanodolgusundaki tiyol gruplarında bulunan kükürdün reaksiyon mekanizmasını değiştirerek çapraz bağ oluşumuna katkı sağlaması ve bunun neticesinde çapraz bağ yoğunluğunu arttırması olarak yorumlanabilir. Mekanik karakterizasyon sonucunda SBR/HNT-Tiyol nanokompozitinin kopma dayanımının SBR/HNT nanokompozitine kıyasla %15, referans örneğine kıyasla ise %86 daha yüksek olduğu hesaplanmıştır. Dolayısıyla, HNT-Tiyol nanodolgusu ile SBR matrisi arasında iyi bir etkileşim olduğu ve HNT'nin iyi bir takviye etkisi göstererek gelişmiş mekanik özellikler sağladığı belirlenmiştir. Benzer şekilde SBR reçetesine HNT-Tiyol eklenmesiyle kopmadaki uzama değeri SBR/HNT'ye kıyasla %48,7, referans numunesine kıyasla ise %81,3 oranında artmıştır. Reolojik ve mekanik karakterizasyon sonuçlarından öngörüldüğü üzere Flory-Rehner yaklaşımı ile hesaplanan CLD değerleri SBR/HNT-Tiyol için en yüksek SBR/HNT-Vinil için ise en düşüktür. Ayrıca, termal yaşlandırma prosesinden sonra SBR/HNT ve SBR/HNT-Tiyol nanokompozitlerinin kopma dayanımları ve CLD değerleri artmıştır. Bu durum, bu nanokompozitlerdeki post-cure etkisini doğrulamaktadır.

TEŞEKKÜR

Bu çalışma 2018/DR/0007 numaralı Yalova Üniversitesi BAPKO Lisansüstü Tez projesi kapsamında desteklenmiştir.

KAYNAKLAR

[1] De Matos CF, Zarbin AJ, Galembeck F (2019) Nanostructures and compatibility in rubber nanocomposites containing carbon nanofillers. In: Carbon-Based Nanofillers and Their Rubber Nanocomposites. Elsevier, pp 1-26.
[2] Leblanc JL (2002) Rubber–filler interactions and rheological properties in filled compounds. Progress in Polymer Science 27(4):627-687.
[3] Lu YL, Zhang LQ (2010) Physical properties of rubber-based nanocomposites. In: Physical Properties and Applications of Polymer Nanocomposites. Woodhead, pp 787-831.
[4] Di Gianni A, Colucci G, Priola A, Conzatti L, Alessi M, Stagnaro P (2009) Exfoliated/intercalated rubber/organo-montmorillonite nanocomposites: preparation and characterization. Macromolecular Materials and Engineering 294(10):705-710.
[5] Acar SB, Tasdelen MA, Karaagac B (2023) The effect of POSS nanoparticles on crosslinking of styrene-butadiene rubber nanocomposites. Turkish Journal of Chemistry 47(2):417-425.
[6] Murphy Z, Kent M, Freeman C, Landge S, Koricho E (2020) Halloysite nanotubes functionalized with epoxy and thiol organosilane groups to improve fracture toughness in nanocomposites. SN Applied Sciences 2(12):2130.
[7] Liu M, Jia Z, Jia D, Zhou C (2014) Recent advance in research on halloysite nanotubes-polymer nanocomposite. Progress in Polymer Science 39(8):1498-1525.
[8] Zhang Y, Tang A, Yang H, Ouyang J (2016) Applications and interfaces of halloysite nanocomposites. Applied Clay Science 119:8-17.
[9] Acar SB, Ciftci M, Bouharras FE, Raihane M, Tasdelen MA (2021) In-situ preparation of halloysite nanotube-epoxy thermoset nanocomposites via light-induced cationic polymerization. European Polymer Journal 158:110682.
[10] Bülbül Ş, Ergün ME (2022) Effect of mica powder-filled styrene-butadiene rubber compounds on crosslink density and mechanical properties. Thermal Science 26:3019-3028.
[11] Acar SB, Tasdelen MA, Karaagac B (2021) Methacrylate-functionalized POSS influence on cross-linking and mechanical properties of styrene-butadiene rubber. Iranian Polymer Journal 30(7):697-705.
[12] Yang JK, Park W, Ryu C, Kim SJ, Kim DI, Seo G,Chung CB (2020) Estimation of silica flocculation in SBR/BR compounds reinforced with different silica contents from their rheocurves. Journal of Applied Polymer Science 137(15):48559.

[13] Khalifeh S, Tavakoli M (2019) Styrene butadiene rubber/epoxidized natural rubber/carbon filler nanocomposites: microstructural development and cure characterization. Iranian Polymer Journal 28(12):1023-1033.

[14] Xu Z, Jerrams S, Guo H, Zhou Y, Jiang L, Gao Y, Wen S (2020) Influence of graphene oxide and carbon nanotubes on the fatigue properties of silica/styrene-butadiene rubber composites under uniaxial and multiaxial cyclic loading. International Journal of Fatigue 131:105388.

[15] Jia ZX, Luo YF, Yang SY, Guo BC, Du Ml, Jia DM (2009) Morphology, interfacial interaction and properties of styrene-butadiene rubber/modified halloysite nanotube nanocomposites. Chinese Journal of Polymer Science 27(06):857-864.

[16] Rybiński P, Janowska G, Plis A (2013) Thermal properties and flammability of ethylene-vinyl acetate rubbers (EVM) and their cross-linked blends with nitrile rubber (NBR). Thermochimica Acta 568:104-114.

[17] Barghamadi M, Ghoreishy MHR, Karrabi M, Mohammadian-Gezaz S (2021) Modeling of nonlinear hyper-viscoelastic and stress softening behaviors of acrylonitrile butadiene rubber/polyvinyl chloride nanocomposites reinforced by nanoclay and graphene. Polymer Composites 42(2):583-596.

[18] Abd-El-Messieh S, Abd-El-Nour K (2003) Effect of curing time and sulfur content on the dielectric relaxation of styrene butadiene rubber. Journal of Applied Polymer Science 88(7):1613-1621.

[19] Khan M, Mishra S, Ratna D, Sonawane S, Shimpi NG (2020) Investigation of thermal and mechanical properties of styrene–butadiene rubber nanocomposites filled with SiO2–polystyrene core–shell nanoparticles. Journal of Composite Materials 54(14):1785-1795.

[20] Harandi MH, Alimoradi F, Rowshan G, Faghihi M, Keivani M, Abadyan M (2017) Morphological and mechanical properties of styrene butadiene rubber/nano copper nanocomposites. Results in Physics 7:338-344.

[21] Albdiry M, Yousif B (2013) Morphological structures and tribological performance of unsaturated polyester based untreated/silane-treated halloysite nanotubes. Materials & Design 48:68-76.

[22] Peixoto AF, Fernandes AC, Pereira C, Pires J, Freire C (2016) Physicochemical characterization of organosilylated halloysite clay nanotubes. Microporous and Mesoporous Materials 219:145-154.

[23] Raef M, Razzaghi-Kashani M (2019) The role of interface in gas barrier properties of styrene butadiene rubber-reduced graphene oxide composites. Polymer 182:121816.

[24] He S, Bai F, Liu S, Ma H, Hu J, Chen L, Du X (2017) Aging properties of styrene-butadiene rubber nanocomposites filled with carbon black and rectorite. Polymer Testing 64:92-100.

[25] Barghamadi M, Karrabi M, Ghoreishy MHR, Mohammadian-Gezaz S (2019) Effects of two types of nanoparticles on the cure, rheological, and mechanical properties of rubber nanocomposites based on the NBR/PVC blends. Journal of Applied Polymer Science 136(25):47550.

[26] Choi SS (2000) Influence of rubber composition on change of crosslink density of rubber vulcanizates with EV cure system by thermal aging. Journal of Applied Polymer Science 75(11):1378-1384.

[27] Choi SS (2001) Influence of internal strain on change of crosslink density of natural rubber vulcanizates by thermal ageing. Polymer International 50(1):107-112.

J. Innovative Eng. Nat. Sci., vol. 3, no. 2, pp. 103-110, 2023.
http://dx.doi.org/10.29228/JIENS.70341

Original Paper

Journal of Innovative Engineering and Natural Science
(Yenilikçi Mühendislik ve Doğa Bilimleri Dergisi)
journal homepage: https://jiens.org

PVDF nanofibers composite containing core-shell (ZnO@ZIF-8) for use in smart textile applications

Miladi Atighi[a], Moein Jalali[a], Mahdi Hasanzadeh[a]* and Seyed Mansour Bidoki[a]

[a]*Department of Textile Engineering, Yazd University, Yazd 89195-74, Iran.*

ARTICLE INFO

Article history:
Received 29 May 2023
Received in revised form 03 July 2023
Accepted 04 July 2023

Available online

Keywords:
Electrospinning
Metal-organic framework
Nanofiber
PVDF
Zinc oxide

ABSTRACT

Currently, electronic textiles (E-textiles) have gained tremendous attention. In recent years, there has been significant interest in metal-organic frameworks (MOFs), which are emerging porous materials and have gained immense interest in recent years. In this study, we successfully synthesized a core-shell zinc oxide @ zeolite imidazolate framework-8 (ZnO@ZIF-8) composite and used it to fabricate electrospun polyvinylidene fluoride (PVDF) nanofibrous composites. Nanofibers were produced using an electrospinning machine. We analyzed the synthesized (ZnO@ZIF-8) powder and PVDF and PVDF/(ZnO@ZIF-8) nanofibrous composite using field emission scanning electron microscopy and X-ray diffraction techniques to investigate their morphological and crystallographic structures. The results demonstrated the successful fabrication of uniform and bead-free nanofibers. The incorporation of (ZnO@ZIF-8) composite particles into the PVDF polymer solution resulted in an increased β-phase content in the fabricated PVDF/(ZnO@ZIF-8) nanofibrous composite compared to the pristine PVDF nanofibrous composite. The nanofibrous mat has various applications, including E-Textiles, flexible sensors, energy scavenging, smart textiles, wearable devices, and energy harvesting.

I. INTRODUCTION

Recently, Electronic textiles (E-textiles) based on piezoelectric properties have gained tremendous attention based on the piezoelectric effect with the ability to convert mechanical energy into electricity and vice versa. poly vinylidene fluoride (PVDF) as a Polymeric Piezoelectric Materials (PPM) have many advantages over Ceramics Piezoelectric Materials (CPM) such as flexibility, low processing cost, biocompatibility, high chemical resistance and other properties. To improve the piezoelectric performance of PVDF for sensor application, the amount of electroactive crystalline phases, specially the β-phase with the largest spontaneous polarization, should be enhanced [1-5].

Various studies showed that the incorporation of piezoelectric nano materials was found to be efficient for improving the piezoelectric properties of PVDF-based nanofibrous mat. Examples include nano-clay [6], zinc oxide (ZnO) particle [7], Co-doped ZnO [8], Metal Organic Frameworks (MOFs) [9] and TiO_2 [10] which their piezoelectric enhancing effect has been shown, recently.

Recently, porous crystalline materials consisting of organic ligands and metal ions, called Metal-organic frameworks (MOFs), linked through coordination bonds have been attended. These nanostructures have attracted a lot of interest in a wide range of applications [11-14] Due to their superior unique structural features including high porosity, tunable pore size, specific surface area and versatile performance. [15, 16]. Zeolitic imidazolate

*Corresponding author. Tel.: +98-9120381392; e-mail: mahdi.hasanzadeh3077@gmail.com

frameworks (ZIFs) are a category of MOFs with the same structures to zeolites. They have are built upon 4-connected nets of tetrahedral units, wherein metal ions, such as Zn^{2+} or Co^{2+}, are linked through N atoms in diatopic imidazolate anions. Between the ZIFs, Zeolite Imidazolate Framework-8(ZIF-8), which is a type of albite zeolite with a nanoporous structure, is a regular representative of ZIFs [17].

Electrospinning is a simple, scalable, and widely used technique for fabricating nanofibers, it has been Multipurpose and used for several applications [18, 19]. Owing to the high voltage which will be applied to the electrospinning solution, caused the $-CF_2/-CH_2$ molecules to align. Molecular $-CF_2/-CH_2$ dipoles tend to be aligned [19]. According to this case, no additional polarization process is needed to increase the β phase value of PVDF nanofibers [1]. For example, Hasanzadeh et al. [1] produce PVDF nanofiber containing Graphene-ZnO. Their result show an increase in the β phase value of PVDF nanofiber containing the above composite from 51.08% for pristine PVDF nanofiber to 62.36%. In another research, Hadavi Moghadam et al. [2] fabricate a piezoelectric sensor based on PVDF nanofiber containing MOFs, exactly UIO-66, according to the XRD and FTIR results amount of the β crystalline phase is enhanced in the presence of MOF during electrospinning from 64% for raw PVDF to 67% for PVDF-5 wt % MOF. In this work, the synthesis and characteristics of (ZnO@ZIF-8) composite and PVDF, PVDF/(ZnO@ZIF-8) nanofibers were studied.

II. EXPERIMENTAL METHOD / TEORETICAL METHOD

2.1 Materials

Zinc oxide (ZnO, 99.0%), 2-methylimidazole (2-MIM) and, ($Zn(NO_3)_2.6H_2O$, 98%) were obtained from Merck Co. (Germany), Poly(vinylidene fluoride) (PVDF) (Mw =350,000 g/mol) was obtained from Kynar Co. (USA) and N,N-dimethylformamide (DMF, Mw=73.09 g/mol, 99.0%) was obtained from Neutron Pharmachemical Co. (Iran) and used without any further purification.

2.2 Synthesis of ZnO@ZIF-8

Core–shell ZnO@ZIF-8 composite was synthesized by a modified method that described by Zhan et al. [20]. In a typical experiment, 0.164 g 2-methylimidazole (2-MIM) was dissolved in 15 mL N, N-dimethylformamide (DMF), and the solution was pre-heated at 70 °C. After that, 0.140 g of ZnO powder was added into 5 ml deionized water and stirred for 15 minutes then ZnO suspension wasadded to the pre-heated solution. After that, three drops of anionic soap were added to the above mixture for the emulsifying role. Then the mixed suspension was heated at 70 °C with stirring for 5 h. The ZIF-8 powder was synthesized as in the previous works with a slight change [11-14].

2.3 Synthesis of ZnO@ZIF-8

A 25 wt % solution of PVDF in DMF was prepared and then stirred for 12 h at 50 °C. Different percent of composites (1,3,5,10 wt %) was added to the prepared solution, followed by another 12 h stirring and finally sonicated for 20 min to obtain a homogenous mixture. PVDF/(ZnO@ZIF-8) nanofibers fabrication done by an horizontal electrospinning machine (Nano-Azma, Iran). Table 1 shows the electrospinning solutions condition.

The mixture solutions were filled into 5mL syringes (22-gauge needle). The flow rate of the device was 0.2 mL/h. A DC high-voltage power supply (25 kV) was applied between grounded collector (12 cm spinning distance) and the needle tip. A rotating drum (2000 RPM) with traverse mode used to collect the nanofibrous mat. The electrospinning process was done at 28% relative humidity and 27 °C temperature for 4 h. The parameters of electrospinning were obtained based on a series of trial-and-error experiments.

Table 1. Electrospinning conditions of PVDF/(ZnO@ZIF-8) nanofibrous mat

Composite amount *(wt%)*	**Applied voltage** *(kV)*	**Spinning distance** *(cm)*	**Volume flow rate** *(mL/h)*	**Drum speed** *(rpm)*
0	25	12	0.2	2000
1	25	12	0.2	2000
3	25	12	0.2	2000
5	25	12	0.2	2000
10	25	12	0.2	2000

2.4 Characterizations

The morphology of fabricated composite and nanofibers were studied by field-emission scanning electron microscopy (FESEM) (MIRA III, TESCAN). measuring the diameter of nanofibers done by Digimizer software . in FESEM images to determine the diameter distribution. crystalline characteristics of the synthesized composite and nanofibers were evaluated by X-ray diffraction (XRD).

III. RESULTS AND DISCUSSIONS

3.1 Characteristics of (ZnO@ZIF-8) Composite

The formation of a layer of perfect ZIF-8 shell over the core is a vital step in the fabrication of a core–shell ZIF-8 based structure. Generally, the core had to be modified with some organic groups or ZIF-8 seeds to facilitate the formation of ZIF-8 over the core. As shown in Figure 1, the surface of the ZnO core was closely packed with hexahedron ZIF-8 nanocrystals, showing that a layer of ZIF-8 shells had grown well on the core.

The X-ray diffraction (XRD) patterns of ZIF-8, ZnO, and ZnO@ZIF-8 powders are depicted in Figure 2. XRD analysis plays a crucial role in characterizing the crystalline structure and crystallographic planes present in the synthesized powders. ZnO crystals exhibited characteristic peaks at 2θ values of 31.8°, 34.5°, 36.42°, 47.5°, 56.6°, 62.8°, and 69.1°, corresponding to the (100), (002), (101), (102), (110), (103), (200), (112), and (201) planes, respectively. On the other hand, the XRD pattern of ZIF-8 demonstrated a crystalline structure with distinct peaks at 2θ values of 7.3°, 10.3°, 12.8°, 16.5°, 18.1°, 19.7°, 22.2°, 24.6°, 25.7°, 26.8°, 28.9°, and 29.8°, corresponding to the (011), (002), (112), (013), (222), (123), (114), (233), (224), (134), (125), and (044) planes, respectively. These findings are consistent with previously reported works [11, 12, 14] which provide valuable insights into the crystalline characteristics of ZIF-8. Importantly, the XRD pattern of the ZnO@ZIF-8 composite revealed the presence of characteristic peaks corresponding to both ZIF-8 and ZnO. This observation confirms the successful formation of the desired core-shell structure, as reported in similar studies [21, 22]. The agreement between the experimental results and previous findings strengthens the validity and reliability of the synthesized materials. Overall, the XRD analysis provides valuable information on the crystalline properties and crystallographic planes of the synthesized powders, supporting the successful synthesis of ZIF-8 and the formation of the core-shell structure in the ZnO@ZIF-8 composite.

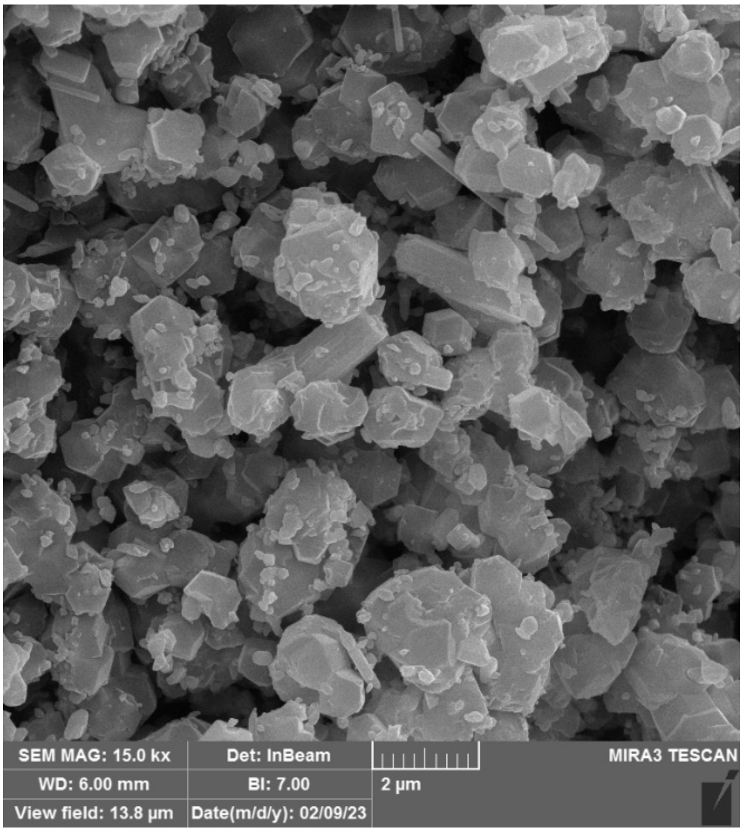

Figure 1. FESEM image of (ZnO@ZIF-8) composite

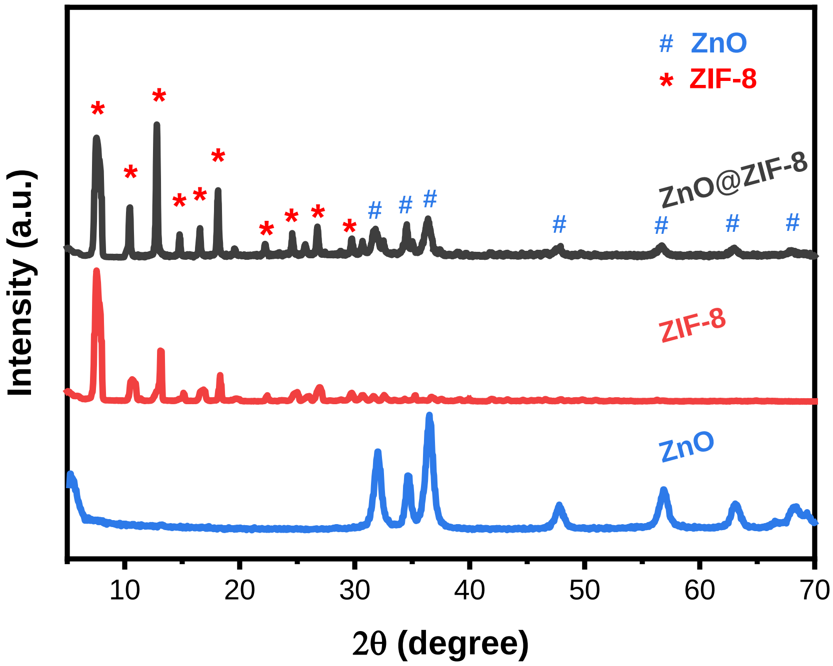

Figure 2. X-ray diffraction pattern of ZnO, ZIF-8 and (ZnO@ZIF-8) powders

3.2 Size and Morphology of Nanofibers

Figure 3 shows the PVDF and PVDF/(ZnO@ZIF-8)-10% electrospun nanofibrous mat surface morphology and diameter distribution. Both of the nanofibers show a uniform diameter distribution and an interconnected network of random fibers with smooth surfaces. Figure 3a the PVDF nanofibers exhibited a bead-free uniform morphology with an average diameter of 253 nm. According to Figure 3b by the addition of composite crystals to the PVDF nanofibers, the surface of the nanofibers, is wrapped with a layer of composite particles. Furthermore, the 10 wt% of composite in the PVDF solution reduced the average diameter of nanofibers to ~233 nm. Figure 3c and Figure 3d shows the normal distribution that in the raw PVDF sample, the dispersion of the data is more than that of the PVDF/(ZnO@ZIF-8)-10% sample.

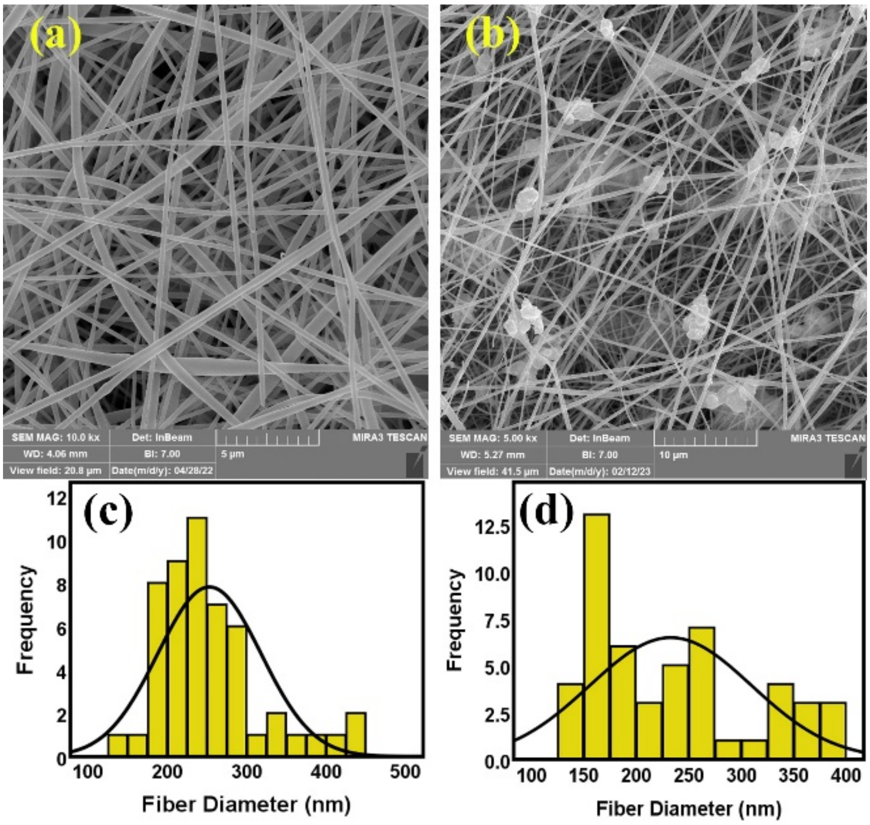

Figure 3. FESEM image and diameter distribution histogram of (a,c) PVDF and (b,d) PVDF/(ZnO@ZIF-8) nanofibers, Respectively

3.3 Phase Analysis

Both of the nanofibrous specimens exhibit the main diffraction peaks of PVDF at 18.8° and 20.5°, which correspond to the α and β-phases, respectively [23]. Figure 4 that refers to XRD analysis of PVDF/(ZnO@ZIF-8) nanofibrous specimen, shows main diffraction peaks signed as * and #, which are in good agreement with MOF and ZnO, respectively.

It can be seen that the β-phase peak intensity ($2\theta = 20.5°$) in the patterns for the PVDF/(ZnO@ZIF-8) nanofiber increased as the composite content was prolonged up to 10 wt.%. The incorporation of (ZnO@ZIF-8) composite into the PVDF nanofibers is deduced to be favorable for stretching the PVDF polymer chain and transforming the α-phase into the β-phase. Moreover, both components of the composite (ZnO and ZIF-8) can be effective as a nucleation agent in increasing the β-phase of PVDF/(ZnO@ZIF-8) nanofiber because of their metallic component that is Zn^{+2} [24-26]. In comparison with other research conducted in this study, our results, like others, confirm the increase in the amount of β-phase from the XRD and FTIR results for the sample containing the composite compared to the raw sample.

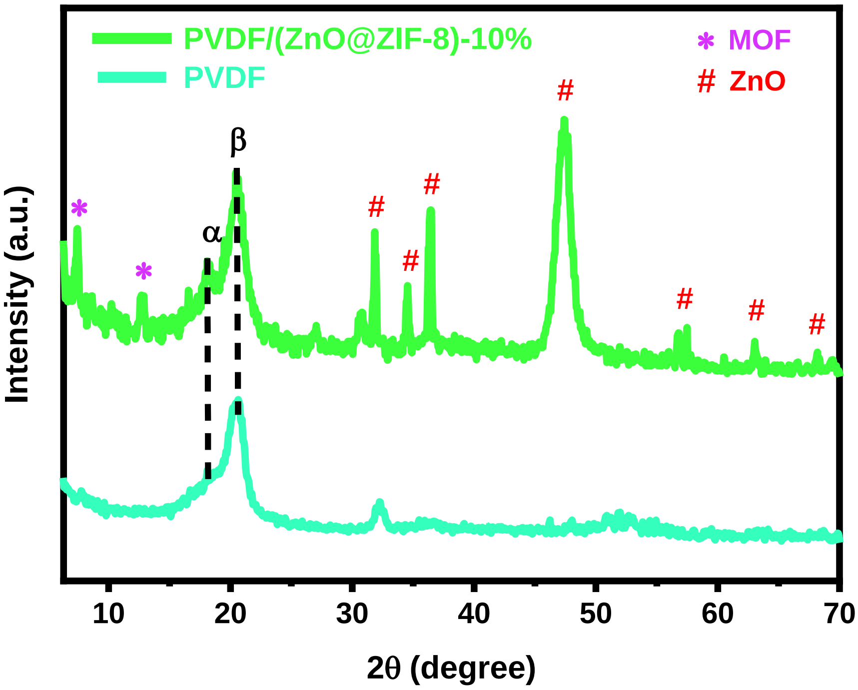

Figure 4. X-ray diffraction of PVDF and PVDF/(ZnO@ZIF-8)-10% nanofibers

IV. CONCLUSIONS

In this study, a successful synthesis of the core-shell (ZnO@ZIF-8) composite was achieved, and its characteristics were thoroughly investigated. Furthermore, electrospinning was employed to fabricate nanofibrous composites of polyvinylidene fluoride (PVDF) and PVDF/(ZnO@ZIF-8) with a composite loading of 10%. The analysis of the fabricated nanofibers revealed the production of uniform and bead-free structures. Moreover, the incorporation of the (ZnO@ZIF-8) composite into the PVDF polymer solution resulted in an increased amount of the β crystalline phase and a reduction in nanofiber diameter. These findings suggest that the composite addition enhances the crystalline properties of PVDF nanofibers and improves their structural characteristics. The fabricated nanofiber mat holds great potential for various applications, including E-Textiles, flexible sensors, and wearable devices. The uniformity and improved characteristics of the nanofibers make them suitable for these applications. Furthermore, based on the obtained results, it is anticipated that the incorporation of this composite can enhance the piezoelectric properties of PVDF nanofibers, opening up possibilities for their utilization in piezoelectric-based applications. Overall, this study successfully synthesized the core-shell (ZnO@ZIF-8) composite and demonstrated its positive impact on the fabrication and characteristics of PVDF nanofibers. The findings contribute to the development of functional nanofiber materials for various technological applications.

ACKNOWLEDGMENT

We acknowledge the Research Laboratory of Yazd University for their support.

REFERENCES

[1] Hasanzadeh M, Ghahhari MR, Bidoki SM (2021) Enhanced piezoelectric performance of PVDF-based electrospun nanofibers by utilizing in situ synthesized graphene-ZnO nanocomposites. Journal of Materials Science: Materials in Electronics. https://doi.org/10.1007/s10854-021-06132-w
[2] Moghadam BH, Hasanzadeh M, Simchi A (2020) Self-Powered Wearable Piezoelectric Sensors Based on Polymer Nanofiber–Metal–Organic Framework Nanoparticle Composites for Arterial Pulse Monitoring. ACS Appl Nano Mater 3(9):8742–8752. https://doi.org/10.1021/acsanm.0c01551
[3] You MH et al. (2018) A self-powered flexible hybrid piezoelectric-pyroelectric nanogenerator based on non-woven nanofiber membranes. J Mater Chem A Mater 6(8):3500–3509. https://doi.org/ 10.1039/c7ta10175a
[4] Bagherzadeh R, Abrishami S, Shirali A, and Rajabzadeh AR (2022) Wearable and flexible electrodes in nanogenerators for energy harvesting, tactile sensors, and electronic textiles: novel materials, recent advances, and future perspectives. Materials Today Sustainability 20:100233. https://doi.org/10.1016/j.mtsust.2022.100233
[5] Bagherzadeh R. Abrishami S, Shirali A, and Rajabzadeh AR (2022) Wearable and flexible electrodes in nanogenerators for energy harvesting, tactile sensors, and electronic textiles: novel materials, recent advances, and future perspectives. Materials Today Sustainability 20:100233. https://doi.org/10.1016/j.mtsust.2022.100233
[6] Tiwari S, Gaur A, Kumar C, Maiti P (2019) Enhanced piezoelectric response in nanoclay induced electrospun PVDF nanofibers for energy harvesting. Energy 171:485–492. https://doi.org/10.1016/j.energy.2019.01.043
[7] Sorayani Bafqi MS, Bagherzadeh R, Latifi M (2015) Fabrication of composite PVDF-ZnO nanofiber mats by electrospinning for energy scavenging application with enhanced efficiency. Journal of Polymer Research. https://doi.org/10.1007/s10965-015-0765-8
[8] Parangusan H, Ponnamma D, Al-Maadeed MAA (2018) Stretchable Electrospun PVDF-HFP/Co-ZnO Nanofibers as Piezoelectric Nanogenerators. Sci Rep. https://doi.org/10.1038/s41598-017-19082-3
[9] Shaukat RA et al. (2022) Ultra-robust tribo- and piezo-electric nanogenerator based on metal organic frameworks (MOF-5) with high environmental stability. Nano Energy 96:107128. https://doi.org/10.1016/j.nanoen.2022.107128
[10] Zhu J et al. (2019) Preparation of PVDF/TiO_2 nanofibers with enhanced piezoelectric properties for geophone applications. Smart Mater Struct 28(8):085006. https://doi.org/10.1088/1361-665X/ab29a9
[11] Atighi M and Hasanzadeh M (2022) Design and Characterization of Electrospun PVDF Nanofibers Containing Graphene Oxide/Metal-Organic Framework Composites for Potential Piezoelectric Applications. The 15th International Seminar on Polymer Science and Technology, ISPST2022, 8-10 November of 2022, IUT, Isfahan, Iran.
[12] Atighi M, Hasanzadeh M (2023) In-situ growth of zinc-based metal-organic framework (Zn-MOF) on Ti3C2Tx MXene nanosheets. The 9th International Congress on Nanoscience & Nanotechnology, ICNN2022, 1-2 March 2023, University of Tehran, Tehran, Iran.
[13] Falahati G, Atighi M, Hasanzadeh M (2023) Synthesis and characterization of novel MOF-GO nanocomposite for adsorptive removal of organic dyes from aqueous solution. The 9th International Congress on Nanoscience & Nanotechnology, ICNN2022, 1-2 March 2023, University of Tehran, Tehran, Iran.
[14] Atighi M, Hasanzadeh M, Sadatalhosseini AA, Azimzadeh HR (2022) Metal–Organic Framework@Graphene Oxide Composite-Incorporated Polyacrylonitrile Nanofibrous Filters for Highly Efficient Particulate Matter Removal and Breath Monitoring. Ind Eng Chem Res. https://doi.org/10.1021/acs.iecr.2c03825
[15] Far HS, Hasanzadeh M, Nashtaei MS, Rabbani M (2021) Fast and efficient adsorption of palladium from aqueous solution by magnetic metal–organic framework nanocomposite modified with poly(propylene imine) dendrimer. Environmental Science and Pollution Research 28(44):62474–62486. https://doi.org/10.1007/s11356-021-15144-2
[16] Khosravi F, Soltan M, Hajiani M, Haji A (2019) Application of Polymeric Nanofibers for Removal of Dyes Graphical abstract. Journal of Studies in Color World 9(1):39–62.
[17] Lee YR, Jang MS, Cho HY, Kwon HJ, Kim S, Ahn WS (2015) ZIF-8: A comparison of synthesis methods. Chemical Engineering Journal 271:276–280. https://doi.org/10.1016/j.cej.2015.02.094
[18] Abedi A, Hasanzadeh M, Tayebi L (2019) Conductive nanofibrous Chitosan/PEDOT:PSS tissue engineering scaffolds. Mater Chem Phys 237:121882. https://doi.org/10.1016/j.matchemphys.2019.121882
[19] Maddah B, Yavaripour A, Ramedani SH, Hosseni H, Hasanzadeh M (2020) Electrospun PU nanofiber composites based on carbon nanotubes decorated with nickel-zinc ferrite particles as an adsorbent for removal of

hydrogen sulfide from air. Environmental Science and Pollution Research 27(28):35515–35525. https://doi.org/10.1007/s11356-020-09324-9

[20] Zhan W, Kuang Q, Zhou J, Kong X, Xie Z, Zheng L (2013) Semiconductor@Metal–Organic Framework Core–Shell Heterostructures: A Case of ZnO@ZIF-8 Nanorods with Selective Photoelectrochemical Response. J Am Chem Soc 13585):1926–1933. https://doi.org/10.1021/ja311085e

[21] Ren G et al. (2019) ZnO@ZIF-8 core-shell microspheres for improved ethanol gas sensing. Sens Actuators B Chem 284:421–427. https://doi.org/10.1016/j.snb.2018.12.145

[22] Yu B, Wang F, Dong W, Hou J, Lu P, Gong J (2015) Self-template synthesis of core–shell ZnO@ZIF-8 nanospheres and the photocatalysis under UV irradiation, Mater Lett 156:50–53. https://doi.org/10.1016/j.matlet.2015.04.142

[23] Wu Y, Qu J, Daoud WA, Wang L, Qi T (2019) Flexible composite-nanofiber based piezo-triboelectric nanogenerators for wearable electronics. J Mater Chem A Mater 7(21):13347–13355. https://doi.org/10.1039/C9TA02345C

[24] Bafqi MSS, Sadeghi AH, Latifi M, Bagherzadeh R (2021) Design and fabrication of a piezoelectric out-put evaluation system for sensitivity measurements of fibrous sensors and actuators. Journal of Industrial Textiles 50(10):1643–1659. https://doi.org/10.1177/1528083719867443

[25] Cardoso VF, Minas G, Costa CM, Tavares CJ, Mendez SL (2011) Micro and nanofilms of poly(vinylidene fluoride) with controlled thickness, morphology and electroactive crystalline phase for sensor and actuator applications. Smart Mater Struct 2088):087002. https://doi.org/10.1088/0964-1726/20/8/087002

[26] Nunes JS, Wu A, Gomes J, Sencadas V, Vilarinho PM, Méndez SL (2009) Relationship between the microstructure and the microscopic piezoelectric response of the α- and β-phases of poly(vinylidene fluoride). Applied Physics A 95(3):875–880. https://doi.org/10.1007/s00339-009-5089-2

J. Innovative Eng. Nat. Sci., vol. 3, no. 2, pp. 111-126, 2023.
http://dx.doi.org/10.29228/JIENS.70357

Original Paper

Journal of Innovative Engineering and Natural Science
(Yenilikçi Mühendislik ve Doğa Bilimleri Dergisi)
journal homepage: https://jiens.org

Preparation and compatibilization effect of β-cyclodextrin end-functionalized polystyrene for immiscible PCL/PS blends

Neşe Çakır Yiğit[a,*]

[a]Department of Polymer Materials Engineering, Faculty of Engineering, Yalova University, Yalova, 77200, Turkey.

ARTICLE INFO

Article history:
Received 30 May 2023
Received in revised form 12 June 2023
Accepted 04 July 2023

Available online

Keywords:
Compatibilization
Solution casting
CuAAC
Inclusion complexation

ABSTRACT

The compatibilizing effect of β-cyclodextrin end-functionalized polystyrene (β-CD-PS) on immiscible PCL/PS blends has been studied using 2D NOESY NMR and DSC techniques. The β-CD-PS was obtained via copper(I)-catalyzed azide-alkyne click reaction (CuAAC) of mono azide functional β-CD (β-CD-N_3) and low molecular weight PS as a compatibilizer. The preparation of inclusion complexes based on β-CD and PCL (equimolar ratio) was investigated, aiming to reduce the interfaces of PCLand PS and compatibilizer the immiscible PCL/PS mixture. Compatibilization was visually observed when turbid PCL/PS solutions became clear upon heating and extended stirring. Several solutions were prepared with PCL/PS contents ranging from 100/0, 70/30, 50/50, and 30/70 (wt%) with β-CD-PS contents (equivalent to PCL moles) by solution casting technique. The 30/70 PCL/PS blend containing stoichiometric 1:1 inclusion complex of β-CD and PCL showed significant changes in DSC analysis. Moreover, 2-fold and 4-fold β-CD-PS (stoichiometric 2:1 and 4:1 β-CD:PCL) were tested to 50/50 PCL/PS blends to observe the amount of compatibilizer for obtaining good miscibility.

I. INTRODUCTION

Polymer blends have been used as a cost-effective, high-performance polymeric material and have become an essential science topic. Polymer blends are physical combinations of two or more polymers to form a new material with different physical properties. In these mixtures, most polymers do not mix homogeneously with each other and undergo phase separation [1, 2]. Compatibilizers can be used in the blending and stabilization of immiscible polymers. Compatibilizers create a homogeneous mixture by decreasing the interfacial tension in the mixture and increasing the adhesion between the two homopolymer phases. The compatibilizer is a block copolymer or graft copolymer of the monomers that make up the mixture. When such compatibilizers are used, one of the components is soluble in the co-solvent, and the other is insoluble and plays a surfactant-like role [3-5]. Polymer blends are generally prepared in two ways. The first way is the solvent-casting method, which is a method that is easily applied in the laboratory. According to this method, after the polymers are dissolved in a solvent in which both are soluble, they are mixed, the solvent evaporates, and the mixture is obtained as a film. The second method is the melt mixing method, usually done in extruders. In this method, all components are mixed by heating above their glass transition temperature (T_g) [6, 7].

Polystyrene (PS) is a standard thermoplastic polymer with atactic, amorphous, inexpensive, stiff, easily shaped, and good electrical and moisture resistance. Due to the benzene ring in its structure, its T_g is in the range of 90-100 °C. Due to this T_g value and its amorphous structure, it is considered a challenging and transparent material at

---

*Corresponding author. Tel.: +90-226-815-5958; e-mail: nese.cakir@yalova.edu.tr

room temperature. Above the softening temperature, it readily melts and is susceptible to processing by injection molding or extrusion [8, 9]. Polycaprolactone (PCL) is a hydrophobic and semi-crystalline biodegradable polyester. Its melting point is around 60 °C, and its glass transition temperature is around -60 °C. It is easily shaped and shows high mechanical strength [10, 11]. Kim et al. investigated the thermal and rheological properties of PCL/PS mixtures using differential scanning calorimetry and scanning electron microscopy. They explained that when low molecular weight PS is used in the mixture, the mixture is partially soluble in each other, and when high molecular weight PS is used, the mixture does not dissolve in each other [12]. Numerous combinations of immiscible PCL/PS mixtures have been made and investigated in the literature, focusing on their phase separation and separation morphology. These studies generally examined how the PS blocks are arranged within the crystal structure of PCL at low or high critical solution temperatures. By varying the composition of the mixture, the film's thickness (if applicable), the polydispersity of PS, and the molecular weight, researchers observed changes in the phase separation and surface morphology of the formed mixtures [13-16]. Ho et al. have proposed an exciting way to make PCL/PS blend as miscible blends. They said PCL mixed homogeneously when melted with PS-*b*-polyethylenepropylene (PEP) copolymer, not PS. Polarized light microscopy, transmission electron microscopy, and small-angle X-ray scattering were employed to study the morphology of the PCL/PS-PEP mixture [17].

Cyclodextrins (CDs) are a group of cyclic oligosaccharides comprising six to eight glucose units connected by glycosidic bonds. They are specified as α-, β-, and γ-CD, correspondingly. CDs exhibit a truncated cone shape, with primary hydroxyl groups on the narrower side and secondary hydroxyl groups on the wider side. It is known that these compounds form inclusion complexes with many molecules [18-20]. Harada et al. investigated for the first time the inclusion complex formation of polydimethylsiloxane (PDMS) with α-CD, β-CD, and γ-CD. As a result of the study, PDMS was observed to form complexes with β-CD and γ-CD, whereas no complexation occurred with α-CD. They explained that such complexes would create a new way to obtain new organic and inorganic materials and functional supramolecular structures [21]. The same working group investigated the formation of inclusion complexes with α-CD, β-CD, and γ-CD for polycaprolactone (PCL) and found that complex with β-CD in moderate yield [22]. Some papers proposed new types of compatibilizers based on CD-based polymers to form inclusion complexes [23-25]. For instance, Balik et al. used star polymers containing γ-CD core and PS arms as compatibilizers in the chloroform solution of PS/PDMS. Compatibilization was observed with the turbid solution becoming clear as CD-star was added. The coupling mechanism explained that the CD core complexed with PDMS, and the resulting complex increased its solubility with PS in the CD-star polymer. Thus, insoluble PDMS blocks were transformed into smaller, more stable micelles. 2D ROESY NMR demonstrated the complexation of the CD core with PDMS. To explore the impact of compatibilization, modifications were made to the PDMS molecular weight, concentration, and CD-star concentration, aiming to examine their effects [26].

Herein, we synthesized β-CD end-functionalized PS (β-CD-PS) to use it as a compatibilizer for immiscible PCL/PS blends. The 1:1 inclusion complexation was driven by β-CD and PCL by host-guest interaction and confirmed by 2D NOESY NMR. The miscibility behavior of resultant β-CD/PCL complexation occurring in PCL/PS blends reduced the interphase of polymers. This paper used morphological and thermal measurements and visual analysis to investigate the miscibility of PCL/PS blends.

II. EXPERIMENTAL METHOD

2.1 Materials

Polystyrene (PS) (average M_n=35.000 g/mol) and polycaprolactone (PCL) (average M_n=45.000 g/mol) homopolymers were purchased from Aldrich. β-cyclodextrin (≥97%, Aldrich), tetrabutylammonium fluoride (TBAF, 1 M in THF, Aldrich), and CuBr (99.9%, Aldrich) were used as received. *N,N,N',N'',N''*-pentamethyldiethylenetriamine (PMDETA, Aldrich) was distilled over NaOH prior to use. Dichloromethane (CH_2Cl_2) was purchased from Aldrich and used after distillation over P_2O_5. Tetrahydrofuran (THF; 99.8%, J.T. Baker) and *N,N*-dimethylformamide (DMF, 99.8%, Aldrich) were all purchased from Aldrich and used as received. The mono-6-deoxy-6-azido-β-cyclodextrin (β-CD-N_3) was synthesized according to our previously published procedure [27]. 3-(Trimethylsilyl)prop-2-ynyl 2-bromo-2-methylpropanoate and α-silyl protected alkyne polystyrene (α-silyl-alkyne-PS) were prepared according to literature procedures [28].

2.2 Instrumentation

^{1}H NMR measurements at a frequency of 500 MHz were conducted using $CDCl_3$ as the solvent and $Si(CH_3)_4$ as the internal standard, employing an Agilent VNMRS 500 instrument. 2D NOESY measurement was performed on an Agilent VNMRS 500 instrument in DMSO-d_6 as the solvent. Conventional gel permeation chromatography (GPC) measurements were performed using an Agilent instrument (Model 1100) equipped with a pump, refractive index (RI), and ultraviolet (UV) detectors. The GPC system utilized a series of four Waters Styragel columns (guard, HR 5E, HR 4E, HR 3, HR 2) with dimensions of 4.6 mm internal diameter and 300 mm length, packed with 5 µm particles. The effective molecular weight ranges for the columns were 2000-4,000,000, 50-100,000, 500-30,000, and 500-20,000, respectively. Elution was carried out using THF as the mobile phase at a flow rate of 0.3 mL/min at 30 °C, while toluene was employed as the internal standard. FT-IR spectra were obtained with an Agilent Technologies Cary 630 FTIR instrument over the range of 4000–500 cm^{-1}. DSC scans were carried out by using a Seiko DSC-7020 under a nitrogen atmosphere as the purge gas. The samples were heated from 25 ^{o}C to 300 ^{o}C (heating rate: 10 °C/min) with a weight of about 3-5 mg. Optical microscope micrographs were taken by using YAMER at 10X magnification.

2.3 Preparation of Compatibilizer

2.3.1 Hydrolysis of a-silyl protected alkyne polystyrene (a-Silyl-Alkyne-PS) and preparation of alkyne-end functionalized PS (Alkyne-PS)

The protective silyl group of α-silyl-alkyne-PS (1.5 g, 0.75 mmol, $M_{n,theo}$ =2000 g/mol) was removed using TBAF (1.1 mL, 3.75 mmol) dissolved in THF (20 mL). The reaction mixture was stirred at room temperature for 2 hours, followed by concentration under reduced pressure and precipitation in methanol. The resulting polymer was then dried under a vacuum at 40°C for 24 hours. The ^{1}H NMR analysis (in $CDCl_3$, δ) revealed peaks at 7.5–6.5 (ArH), 4.4 (CHBr), 4.1 (C[equiv]CCH$_2$O), and 2.0– 0.9 (CH$_2$ and CH).

2.3.2 CuAAC click reaction of Alkyne-PS with β-CD-N_3 (β-CD-PS)

In a Schlenk tube containing a magnetic stirring bar, Alkyne-PS (1.3 g, 0.67 mmol, $M_{n,theo}$ =1930 g/mol) and β-CD-N_3 (1.16 g, 1.00 mmol) were dissolved in DMF (10 mL). To ensure protection from air, CuBr (0.143 g, 1.00 mmol) and PMDETA (195.0 μL, 1.00 mmol) were added under a nitrogen flow. The reaction tube was degassed by three cycles of degassing using FPT (freeze-pump-thaw) method and was then placed in an oil bath set to a constant temperature of 60 °C for a period of 2 days. When the reaction was completed, it was dissolved in CH_2Cl_2 (no need to remove the DMF) and passed through an alumina column to eliminate copper catalysts. Next, the mixture was evaporated until completely dry, and then redissolved in CH_2Cl_2, and precipitated in methanol. The blueish solid was subjected to washing with (10 mL x 2) and methanol (10 mL) to remove any excess β-CD-N_3. Finally, the white precipitate was dried in a vacuum oven at 40 °C for 24 hours. Yield = 1.48 g (74 %). The ^{1}H NMR spectrum (in $CDCl_3$, δ) displayed peaks at 7.79 (br, CH of triazole), 7.4–6.4 (ArH), 5.70 (br, 14H, OH-2,3), 5.01-4.83 (m, 6H, H-1), 4.55-4.48 (br, 6H, OH-6), 3.76-3.50 (br, 28H, H-3,5,6,6'), 3.49-3.23 (br, 14H, H-2,4 overlapping with H_2O), 2.0– 1.1 (CH_2 and CH).

2.4 Preparation of Solution-Cast Films

Solutions containing PS (average M_n=35.000 g/mol) and PCL (average M_n=45.000 g/mol) both with and without β-CD-PS were prepared at a total solids concentration of 20% (w/v) in THF/DMF (4:1) mixture. The solutions were vigorously stirred using a Teflon-coated magnetic stir bar in an appropriately sized beaker, and the beaker was covered to minimize solvent evaporation. The magnetic stirring was conducted at 60 °C and 350 rpm for 1 day. Solution casting was performed in a glass petri dish. To establish controlled evaporation, a glass dish was placed over the films and sealed along the edges using a paper towel to prevent solvent evaporation and eliminate bubble formation. After controlled evaporation, the films were first dried in a fume hood for up to a week, followed by additional drying in a vacuum oven at 40°C for one day.

III. RESULTS AND DISCUSSIONS

To begin with, we synthesized and characterized the β-CD-PS to investigate its miscibility behavior in immiscible PCL/PS blends. Mono azide functional β-cyclodextrin (β-CD-N_3) was prepared according to our previously published paper [26]. The preparation of silly protected polystyrene (α-silyl-alkyne-PS) was well described by Durmaz [27] and the same route was adopted to synthesize α-silyl-alkyne-PS via atom transfer radical polymerization (ATRP). Subsequently, the deprotection of α-silyl-alkyne-PS was successfully achieved using TBAF, resulting in the formation of the corresponding alkyne-PS as outlined in Scheme 1.

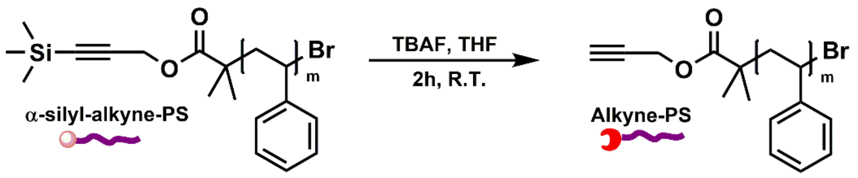

Scheme 1. Synthetic pathway for the deprotection of trimethyl silyl group ($(CH_3)_3Si$-).

The absence of the signal at 0.18 ppm, attributed to $(CH_3)_3Si$-, provided confirmation of the structure of alkyne-PS, as depicted in Figure 1.

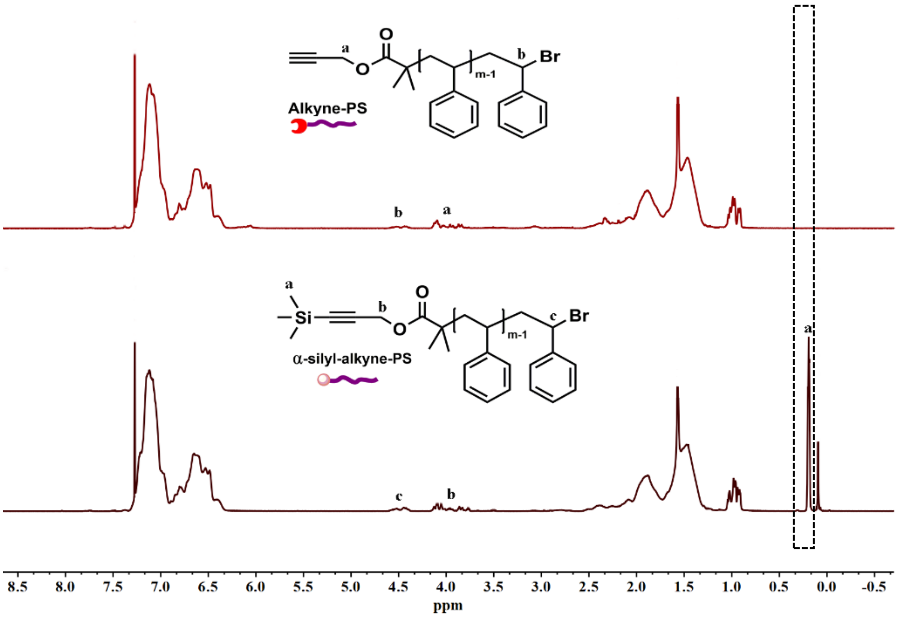

Figure 1. ^{1}H NMR spectra of α-silyl-alkyne-PS (bottom spectra) and alkyne-PS (upper spectra) in $CDCl_3$.

A single-peaked GPC trace and a low-molecular-weight distribution were observed for α-silyl-alkyne-PS and alkyne-PS, which aligned with the theoretical molecular weight ($M_{n,theo}$) values as presented in Table 1.

Table 1. The results of polymers used in the synthesis of compatibilizer

Polymer	$M_{n,GPC}^{b}$ (g/mol)	$M_{w,GPC}^{b}$ (g/mol)	M_w/M_n	$M_{n,theo}^{c}$ (g/mol)
a-Silyl-Alkyne-PS[a]	2080	2310	1.11	2000[c]
Alkyne-PS	1450	1970	1.35	1930[d]
β-CD-PS	3060	4980	1.62	3090[e]

[a] $[M]_0:[I]_0:[CuBr]:[PMDETA] = 200:1:1:1$; polymerization process was conducted at a temperature of 110 °C.

[b] Determined through conventional GPC, calibrated with respect to linear PS standards in THF at 30 °C.

[c] $M_{n,theo} = ([M]_o/[I]_o)$ x conversion % x molecular weight (MW) of monomer + MW of initiator.

[d] $M_{n,theo} = M_{n,theo}$ of α-silyl-alkyne-PS (2000) – M_w of trimethyl silyl group.

[e] $M_{n,theo}$ = sum of ESI-MS of β-CD-N_3 (1160 g/mol) and $M_{n,theo}$ of the alkyne-PS.

As a compatibilizer, β-CD-PS is simply prepared from copper(I) catalyzed azide-alkyne click reaction (CuAAC) of alkyne-PS with β-CD-N_3 concurrently in the CuBr/PMDETA in DMF at 60 °C for two days (Scheme 2). 1.5 equiv. of β-CD-N_3 to that of alkyne-PS was used in the reaction. Again, unreacted β-CD-N_3 was eliminated from the reaction mixture by employing a dissolution-reprecipitation method and washing with water and methanol, respectively.

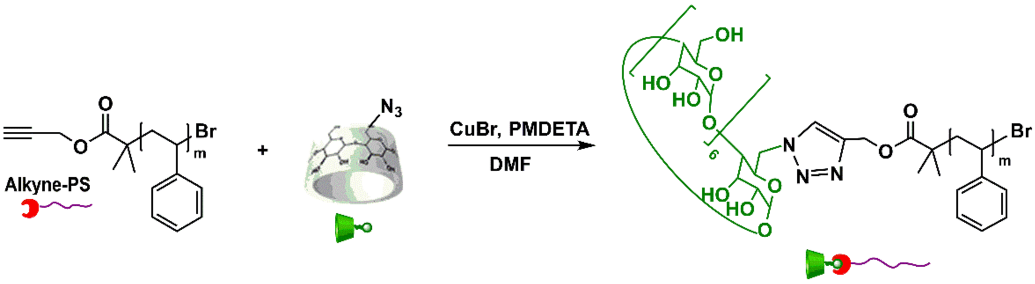

Scheme 2. Synthetic route for the synthesis of β-CD-PS as a compatibilizer

The synthesized β-CD-PS was subjected to characterization using ^{1}H NMR and GPC techniques. In the ^{1}H NMR spectrum, distinctive signals corresponding to the PS and β-CD segments were observed at 7.4–6.4 (ArH) and 5.70-3.23 ppm (methylene protons and hydroxyl groups of the β-CD ring). The peak at 7.79 ppm was attributed to the proton of the 1,2,3-triazole ring. The integration ratio of these peaks, compared to the aromatic hydrogen protons of PS at 7.4-6.4 ppm and 1-positioned CH peaks of β-CD at 5.01-4.83 ppm, was found to be 16.86:1. This ratio indicates a high click efficiency (74%) in the formation of β-CD-PEG, as determined using the theoretical molecular weight ($M_{n,theo}$) value of alkyne PS for the calculation (Figure 2).

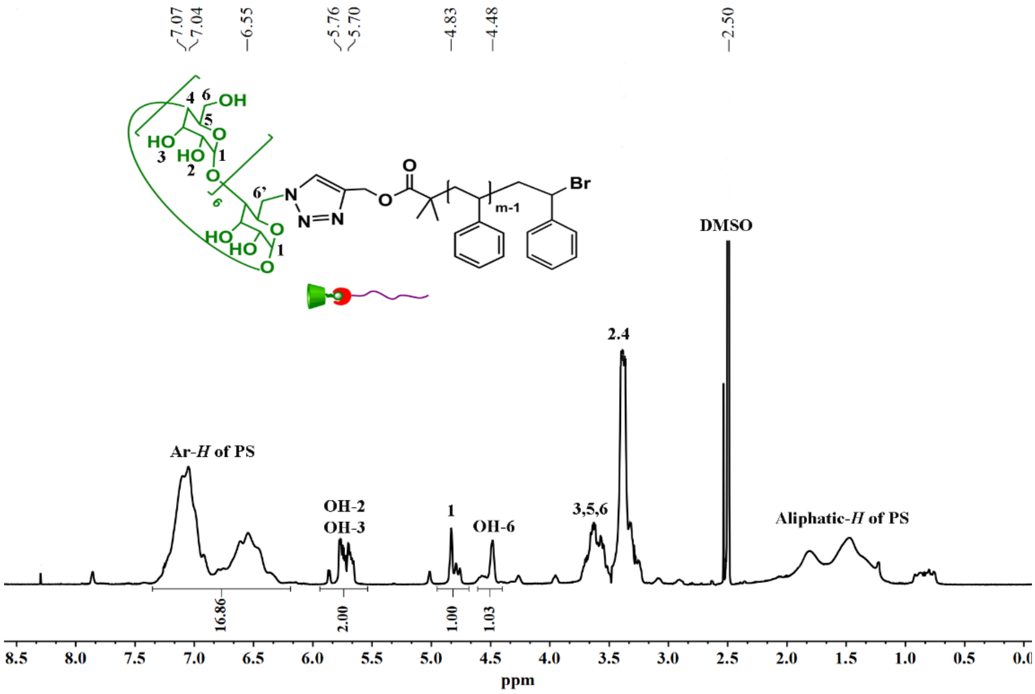

Figure 2. ^{1}H NMR spectrum of β-CD-PS in DMSO-d$_6$ at room temperature

GPC measurement was taken to see the change in molecular weight after the click reaction (Figure 3). According to GPC, M_n: 3060 g/mol (PDI: 1.62) was found, as listed in Table 1. The β-CD-PS exhibited a noticeable shift towards the higher molecular weight region; however, a necked chromatogram was obtained. It is more appropriate to use DMF instead of THF in the analysis of such CD-based polymers. THF may not have shown steady flow through the column because it is not a suitable solvent for CDs.

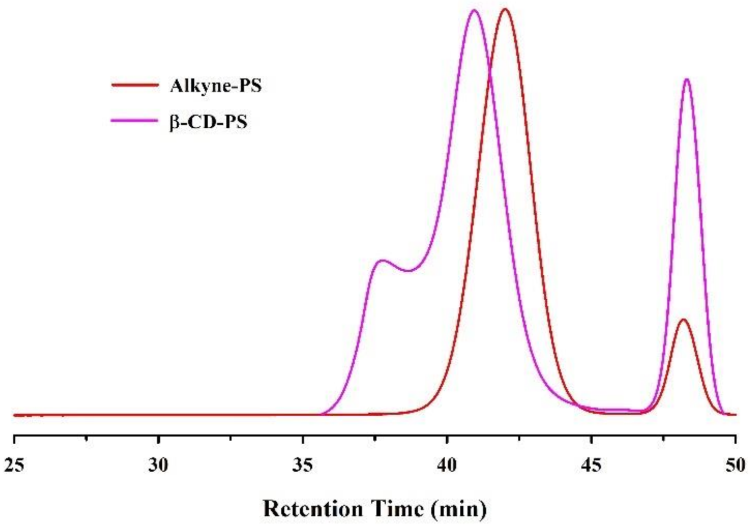

Figure 3. Evaluation of GPC traces of alkyne-PS and β-CD-PS, monitored using an RI detector in THF at 30 ºC

Additionally, the efficiency of the click reaction was confirmed using FT-IR spectroscopy. From the FT-IR spectra taken before and after the CuAAC click reaction, it is seen that the azide peak of β-CD-N_3 (2100 cm^{-1}) disappeared after the click reaction (Figure 4). These FT-IR findings further prove the successful click reaction and the complete removal of the excess β-CD-N_3.

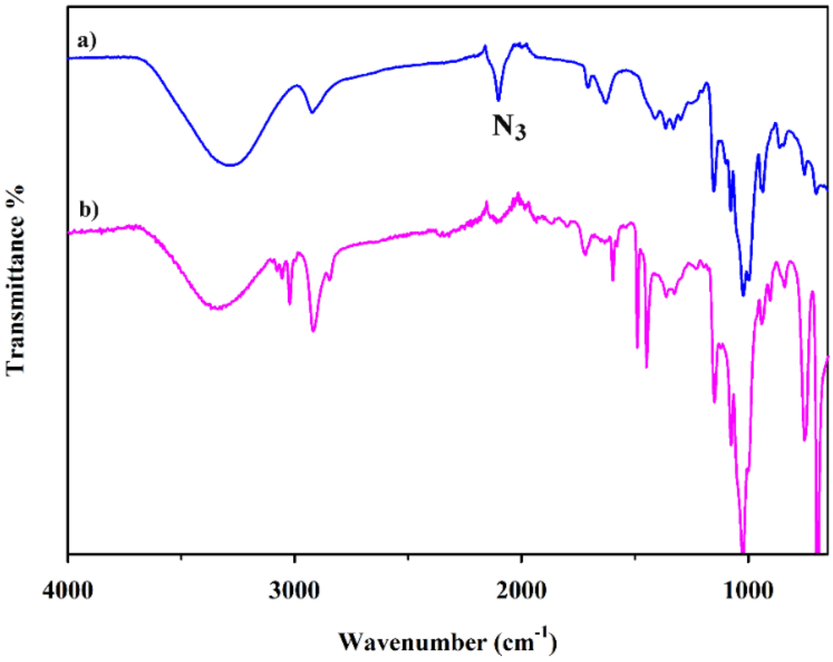

Figure 4. FT-IR spectra of β-CD-N_3 (blue) **(a)** and β-CD-PS (pink) **(b)**

Several solutions were prepared with PCL/PS contents ranging from 100/0, 70/30, 50/50, and 30/70 (wt%) with β-CD-PS contents (equivalent to PCL moles). Table 2 shows the compositions of PCL/PS blends with the compatibilizer (β-CD-PS) used in this work. The total solids concentration was 20% (w/v) in THF/DMF (4:1) mixture. The amount of β-CD-PS in the blends excludes the total mass of the PCL/PS amounts.

The compatibilizing effect of adding β-CD-PS to solutions of PCL and PS in the THF/DMF mixture can be seen in Figure 5. PCL and PLA were solubilized in THF (in different glass containers) and kept under stirring (350 rpm) and once completely dissolved, both solutions were mixed, and β-CD-PS in DMF was added by droplets during stirring. The blends with different compositions were carried out by magnetic stirring at 60 ºC for one day. Upon preparation, all solutions exhibited turbidity; however, they gradually became clear (indicating compatibility) after being stirred for one day at 60 °C, as depicted in Figure 5.

Table 2. Composition of blends initially containing various amounts of β-CD-PS (equal moles of PCL to β-CD-PS)

Composition of PCL/PS	**β-CD-PS** (mg)	**PCL** (g)	**PS** (g)
100/0	68.6	1.0	-
70/30	48.1	0.7	0.3
50/50	34.3	0.5	0.5
30/70	20.6	0.3	0.7

Polymer blends were performed in a glass petri dish by a solvent-cast technique. To control the evaporation process, the solutions were subjected to a controlled two-day evaporation by covering the films with a glass dish, which was sealed along the edges using a paper towel to slow down solvent evaporation and prevent bubble formation. Subsequently, the films were dried in a fume hood for a period of up to one week, followed by an additional drying step in a vacuum oven at 40 °C for one day. Photographs are shown in Figure 6 of the appearance of a polymer blend with and without β-CD-PS. As is easily observed, polymer blends without compatibilizers are white and opaque, and polymer blends with compatibilizers are yellowish and transparent. In addition, all blends which contain more PS are brittle and breakable. However, all blends which contain more PCL are flexible and easily removable from glass Petri dishes. The observed characteristics of the films suggest variations in their morphology.

The presence of an inclusion complex between β-CD and PCL was verified using 2D NOESY NMR, a technique commonly employed by researchers to investigate localized interactions within cyclodextrins. Figure 7 shows the 2D NOESY NMR spectrum of the 1:1 mixture of PCL and β-CD-PS, obtained using the same solution preparation steps to confirm the formation of the inclusion complex. The hydrophobic PCL block has gone through the hydrophobic cavity of β-CD to yield an inclusion compound. In this particular sample, the concentration of PCL and β-CD-PS is relatively low, leading to weak interactions between them, evident in the rectangular region of Figure 7a. Upon magnification of this region in Figure 7b, the proton signals of β-CD-PS can be discerned above the noise and exhibit cross-peaks with the methyl groups of PCL. Notably, cross-peaks arise from dipolar interactions between the signals at 4.5-5.9 ppm, assigned to protons located in the cavities of β-CD (such as C2, C3 secondary hydroxyl group, primary C6 hydroxyl group, and 1-H protons), and the signals at 3.8-3.5 ppm, attributed to methylene protons adjacent to oxygen atoms on PCL. These cross-peaks confirm that methyl groups have been deeply embedded in the cavities of β-CD via host-guest interactions.

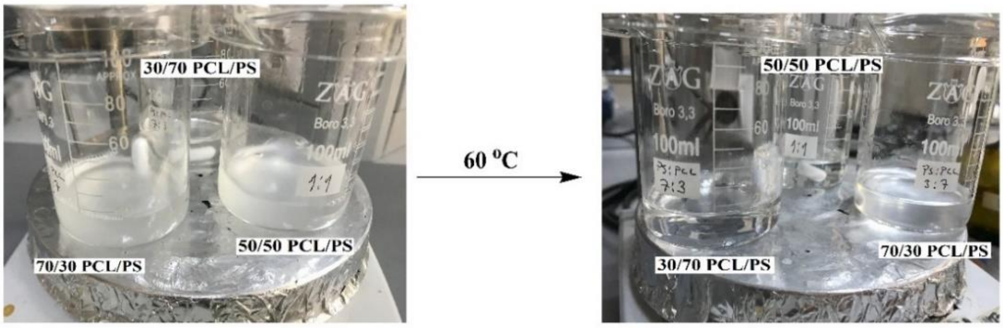

Figure 5. Three different solutions of PCL and PS in THF: DMF mixture with β-CD-PS before and after stirring at 60 °C for 1 day

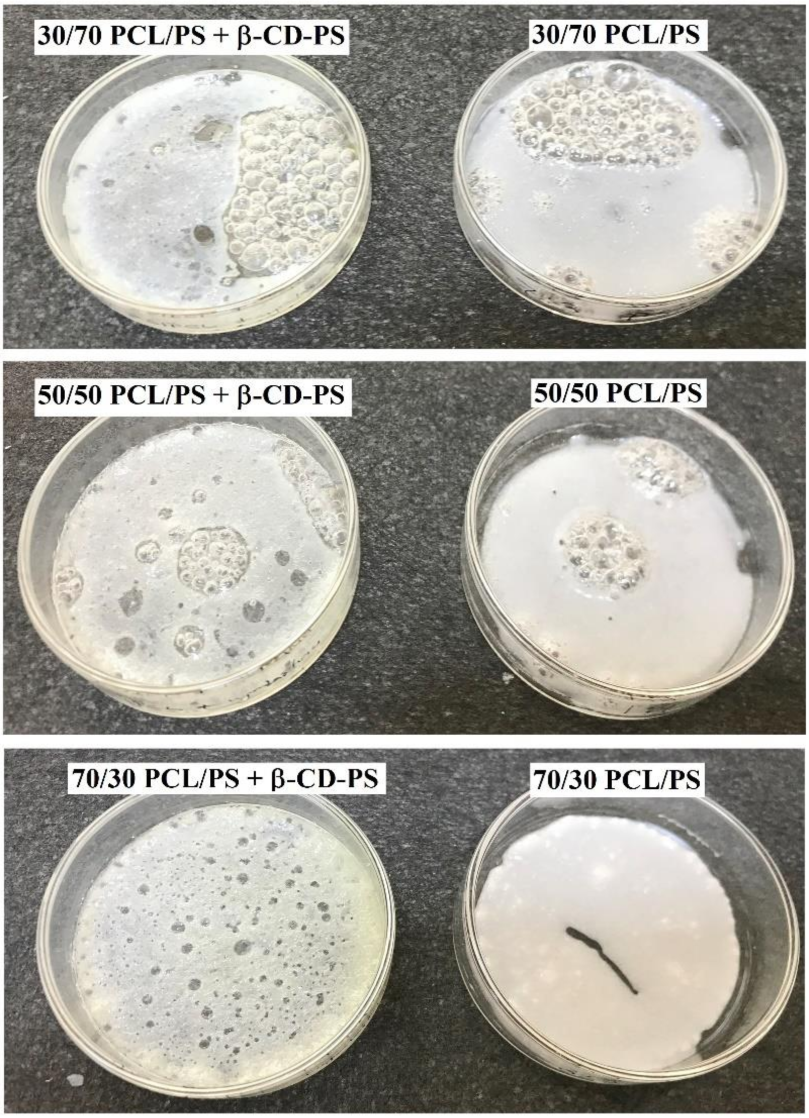

Figure 6. The appearance of solvent-cast films prepared with different ratios of PCL/PS with and without compatibilizer

Figure 8 presents the DSC thermograms of the individual components that constitute the solution-cast films. The homopolymer PCL (average M_n=45.000 g/mol) used in these samples shows a sharp melting point (T_m) 60.2 °C. The homopolymer PS (average M_n=35.000 g/mol) exhibits T_g of 17.9 and T_m 66.6 °C. The DSC analysis of β-CD-PS shows no distinctive features except for the T_g associated with the PS arms at 17.8 °C.

While the literature reports [5] the T_g of PCL to be around -61.5 °C, we did not measure the T_g of PCL in this particular experiment. Therefore, no crystallization peak associated with PCL is observed in our findings.

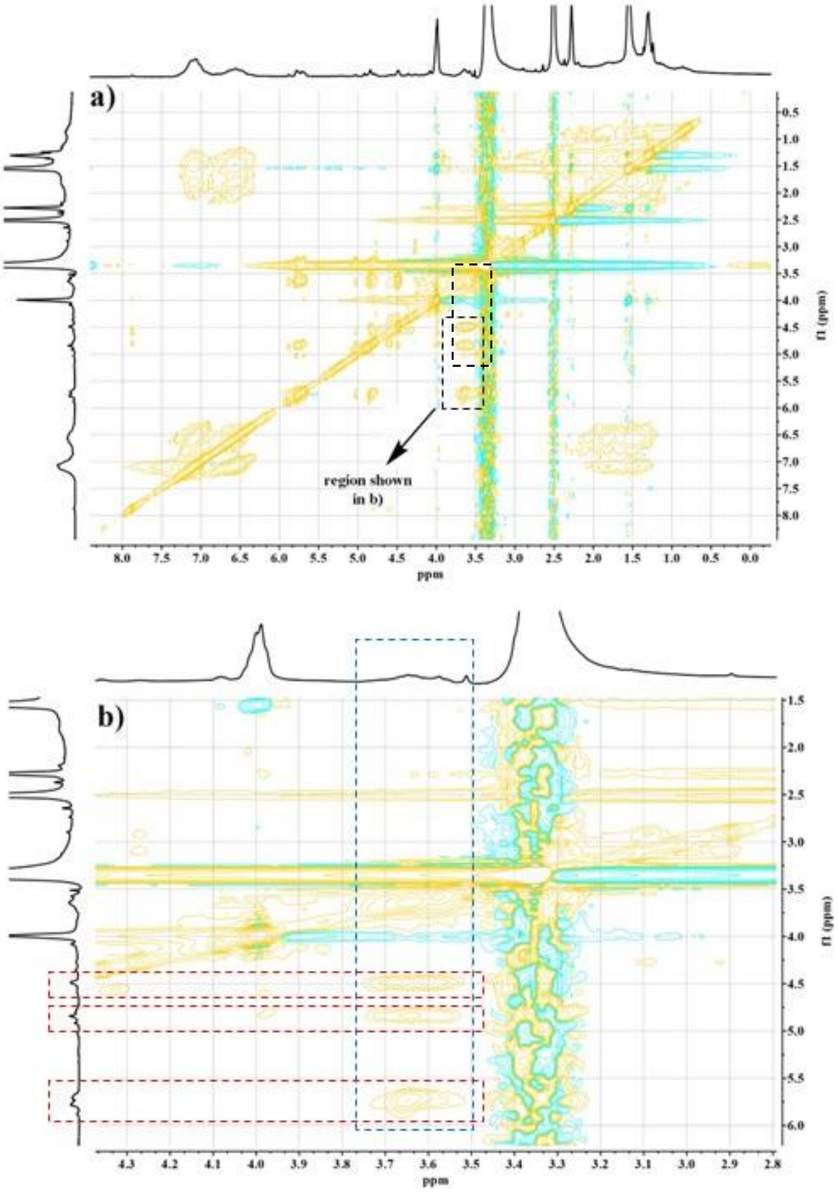

Figure 7. a) 2D NOESY NMR spectrum of 1:1 mol/mol of PCL/β-CD-PS solutions in DMSO-d_6 at room temperature, **b)** Magnified view of the rectangular circle in a)

Figure 8 presents the DSC thermograms of the individual components that constitute the solution-cast films. The homopolymer PCL (average M_n=45.000 g/mol) used in these samples shows a sharp melting point (T_m) 60.2 °C.

The homopolymer PS (average M_n=35.000 g/mol) exhibits T_g of 17.9 and T_m 66.6 ^oC. The DSC analysis of β-CD-PS shows no distinctive features except for the T_g associated with the PS arms at 17.8 ^oC.

While the literature reports [5] the T_g of PCL to be around -61.5 °C, we did not measure the T_g of PCL in this particular experiment. Therefore, no crystallization peak associated with PCL is observed in our findings.

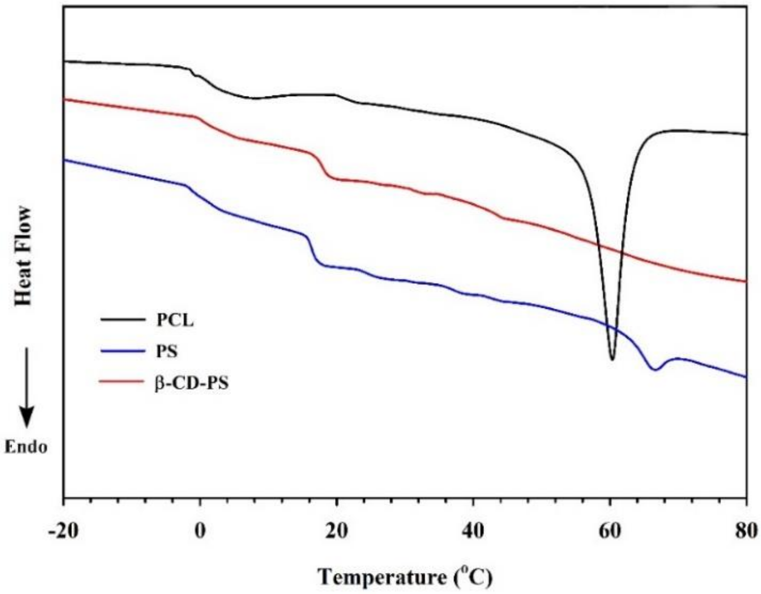

Figure 8. DSC thermograms of the constituent elements comprising the solution-cast films are depicted, with the curves being vertically displaced for better visibility

DSC scans of a series of PCL/PS (30/70, 50/50, and 70/30) blends with and without various amounts of β-CD-PS are shown in Figure 9. A significant change in the T_g value was observed for the 30/70 PCL/PS blend. The T_g of the 30/70 PCL/PS blend shifted to 21°C and 30.5 °C (with β-CD-PS) (left graph (2)) from 18.8 °C (without β-CD-PS) (left graph (1)). In addition, in another series of PCL/PS blends, the T_g values were slightly changed. T_ms of PCL were observed to undergo slight alterations in the presence of β-CD-PS. This may be attributed to forming a crystalline structure that differs from the previous system. Figure 9, the right graph, shows the results of the cooling cycle from DSC analysis for all samples. The PCL crystallization of the β-CD-PS containing 30/70 PCL/PS blend significantly declined to 14 °C from 24.6 °C with an exothermic peak. It is possible to conclude that adding β-CD-PS as a compatibilizer causes changes in some of the thermal properties of the 30/70 PCL/PS blend. Specifically, the addition of β-CD-PS does not significantly impact the glass temperature or the melting temperature, as anticipated.

The amount of compatibilizer (β-CD-PS) added to PCL/PS blends for miscibility was also investigated. The films of 50/50 PCL/PS blends and 2-fold and 4-fold β-CD-PS contents are clearly in Figure 10a. When β-CD-PS is increased, more homogenously mixed film is obtained. Moreover, from DSC cooling thermograms of 50/50 PCL/PS blends, show that T_c of PCL is remarkably decreased due to the inclusion complexation of β-CD:PCL (Figure 10b).

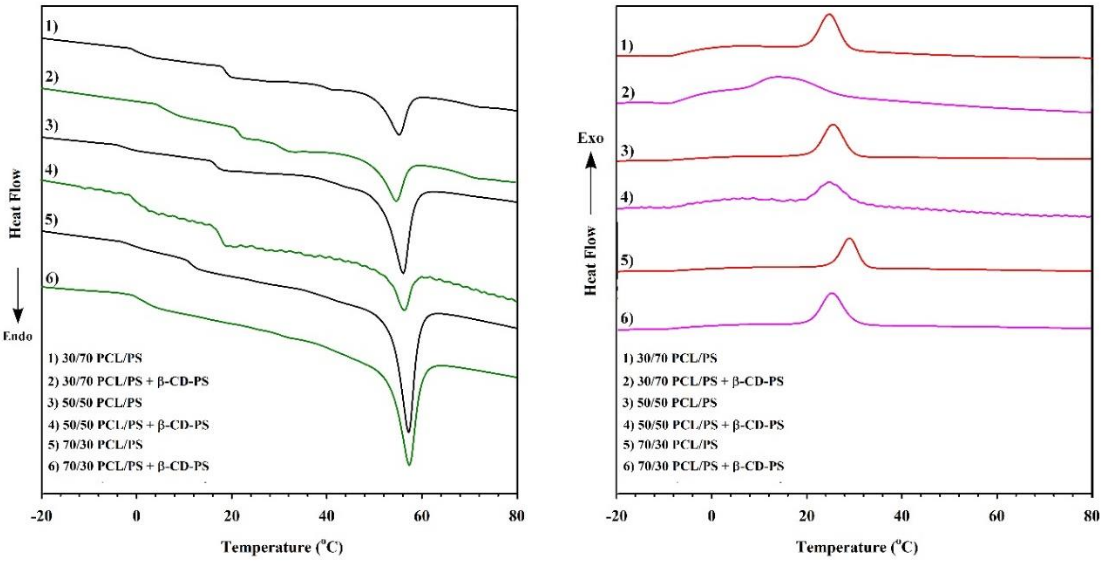

Figure 9. DSC thermograms of films containing different concentrations of β-CD-PS are presented, with the vertical shift applied to enhance clarity (left graph). The cooling cycle of the same samples (right graph)

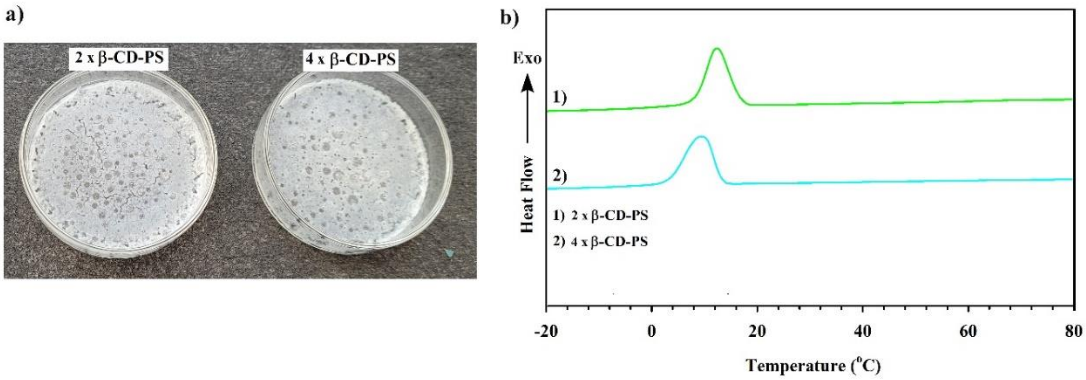

Figure 10. a) Appearance of solvent-cast films prepared with 50/50 PCL/PS blend with 2-fold and 4-fold β-CD-PS. **b)** DSC thermograms of 50/50 PCL/PS blend with 2 fold and 4 fold of β-CD-PS

The surface morphology of 50/50 PCL/PS blends containing various amounts of β-CD-PS was studied through an optical microscope to observe the miscibility of blends. The casting films were subsequently hot pressed for 3 min at 195 °C under the pressure of 5 Mpa between Teflon sheets to produce film samples of uniform thickness (~50 μm). Figure 11 presents the optical microscope micrographs of 50/50 PCL/PS blends with different ratios of β-CD-PS at 10X magnification to evaluate the morphological surfaces of the blends. Figure 11a has significant phase separation on the surface. Figure 11d seems to have one uniform phase. Figure 11c showed better homogeneously dispersed droplets than Figure 11b. The morphologies of these binary blend films changed depending on the amount of β-CD-PS as compatibilizer. Additional techniques such as scanning electron microscopy (SEM) or atomic force microscopy (AFM) may be employed to get information about the nanoscale or detect slight phase separations for further studies.

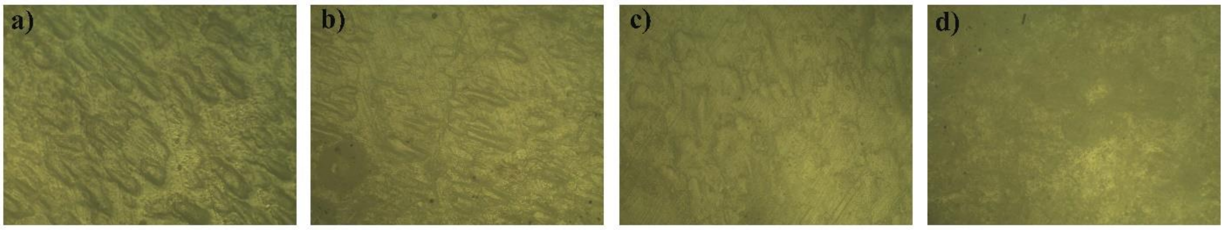

Figure 11. Optical microscopy micrographs of 50/50 PCL/PS blends **a)** without β-CD-PS, **b)** equimolar β-CD-PS to PCL, **c)** 2-fold of β-CD-PS to PCL, and **d)** 4 fold of β-CD-PS to PCL

IV. CONCLUSIONS

Compatibilization of PCL and PS in THF/DMF (4:1) is achieved by the addition of β-CD end-functionalized PS (β-CD-PS) (equimolar to PCL) by solution-cast technique. The β-CD-PS was obtained via CuAAC click reaction of mono azide functional β-CD (β-CD-N_3) and previously synthesized PS via ATRP. The 1:1 inclusion complexation was driven by β-CD and PCL by host-guest interaction. The process of compatibilization is visually evident as the initially cloudy solutions become clear when heated and stirred for an extended period. The mechanism underlying compatibilization is attributed to the threading of the β-CD-PS by PCL, which reduces the interfaces between different components. This threading phenomenon of the β-CD ring by PCL is supported by evidence obtained from 2D NOESY NMR analysis. A significant change in the T_g value was observed for the β-CD-PS containing a 30/70 PCL/PS blend. In addition, PCL crystallization was significantly shifted for the same blend. Moreover, the amount of compatibilizer (β-CD-PS) added to PCL/PS blends for miscibility was also investigated. The films of 50/50 PCL/PS blends with 2-fold and 4-fold β-CD-PS contents gave homogenously mixed films via optical microscope observations. The morphological properties showed that the PCL/PS mixtures were miscible when the amount of β-CD-PS was increased. In conclusion, for inclusion complexation 1:1 β-CD:PCL mole ratio is enough; however, β-CD can be increased for good miscibility of blends.

ACKNOWLEDGMENT

The author is grateful to Prof. Dr. Gürkan Hızal, Prof. Dr. Ümit Tunca, and Prof. Dr. Hakan Durmaz to provide the laboratory facilities during the synthesis of the compatibilizer (β-CD-PS).

This study was supported by Yalova University Scientific Research Unit (Project No: 2019/AP/0020).

REFERENCES

[1] Rameshwaram J, Yang Y-S, Jeon H (2005) Structure–property relationships of nanocomposite-like polymer blends with ultrahigh viscosity ratios. Polymer 46 (15):5569-5579. https://doi.org/10.1016/j.polymer.2005.05.033
[2] Ajitha A, Thomas S (2020) Compatibilization of polymer blends, Compatibilization of Polymer Blends, Elsevier, 640.
[3] Holsti-Miettinen R, Seppälä J, Ikkala O (1992) Effects of compatibilizers on the properties of polyamide/polypropylene blends. Polymer Eng Sci 32(13):868-877. https://doi.org/10.1002/pen.760321306
[4] DeLeo C L, Velankar S S (2008) Morphology and rheology of compatibilized polymer blends: Diblock compatibilizers vs crosslinked reactive compatibilizers. Journal of Rheology 52(6):1385-1404. https://doi.org/10.1122/1.2995857

[5] Koning C, Van Duin M, Pagnoulle C, Jerome R (1998) Strategies for compatibilization of polymer blends. Progress in Polymer Science 23(4):707-757. https://doi.org/10.1016/S0079-6700(97)00054-3

[6] Patrício T, Bártolo P (2013) Thermal stability of PCL/PLA blends produced by physical blending process. Procedia Engineering 59:292-297. https://doi.org/10.1016/j.proeng.2013.05.124

[7] Wang H, Dong W, Li Y (2015) Compatibilization of immiscible polymer blends using in situ formed janus nanomicelles by reactive blending. ACS Macro Letters 4(12):1398-1403. https://doi.org/10.1021/acsmacrolett.5b00763

[8] Lokensgard E (2016) Industrial plastics: theory and applications: Cengage Learning.

[9] Zhang Y, Huang Y, Mai K (2005) Crystallization and dynamic mechanical properties of polypropylene/polystyrene blends modified with maleic anhydride and styrene. Journal of Applied Polymer Science 96(6):2038-2045. https://doi.org/10.1002/app.21658

[10] Lv Q, Wu D, Xie H, Peng S, Chen Y, Xu C (2016) Crystallization of poly (ε-caprolactone) in its immiscible blend with polylactide: insight into the role of annealing histories. RSC Advances 6(44):37721-37730. https://doi.org/10.1039/C6RA07752H

[11] Na Y-H, He Y, Shuai X, Kikkawa Y, Doi Y, Inoue Y (2002) Compatibilization effect of poly (ε-caprolactone)-b-poly (ethylene glycol) block copolymers and phase morphology analysis in immiscible poly (lactide)/poly (ε-caprolactone) blends. Biomacromolecules 3(6):1179-1186. https://doi.org/10.1021/bm020050r

[12] Chun Y, Kyung Y, Jung H, Kim W (2000) Thermal and rheological properties of poly (ϵ-caprolactone) and polystyrene blends. Polymer 41(24):8729-8733. https://doi.org/10.1016/S0032-3861(00)00263-9

[13] Shabana H, Olley R, Bassett D, Jungnickel B-J (2000) Phase separation induced by crystallization in blends of polycaprolactone and polystyrene: an investigation by etching and electron microscopy. Polymer 41(14):5513-5523. https://doi.org/10.1016/S0032-3861(99)00713-2

[14] Ma M, He Z, Yang J, Wang Q, Chen F, Wang K, Zhang Q, Deng H, Fu Q (2011) Vertical phase separation and liquid-liquid dewetting of thin PS/PCL blend films during spin coating. Langmuir 27(3):1056-1063. https://doi.org/10.1021/la104003p

[15] Ma M, He Z, Li Y, Chen F, Wang K, Zhang Q, Deng H, Fu Q (2012) Surface phase separation, dewetting feature size, and crystal morphology in thin films of polystyrene/poly (ε-caprolactone) blend. Journal of Colloid Interface Science 387(1):262-269. https://doi.org/10.1016/j.jcis.2012.07.087

[16] Silva L I, Montoya Rojo U M, Riccardi C C (2017) Phase separation and segregation morphology of PCL/PS blends: Quantitative effect of the crystallization temperature, composition, and molecular weight of PS. Polymer Engineering Science 57(10):1062-1072. https://doi.org/10.1002/pen.24480

[17] Ho R-M, Chiang Y-W, Lin C-C, Bai S (2002) Block copolymer self-assembly ınduced compatibilization of PCL/PS− PEP blends. Macromolecules 35(4):1299-1306. https://doi.org/10.1021/ma011381j

[18] Harada A, Takashima Y, Yamaguchi H (2009) Cyclodextrin-based supramolecular polymers. Chemical Society Reviews 38(4):875-882. https://doi.org/10.1039/B705458K

[19] Poulson B G, Alsulami Q A, Sharfalddin A, El Agammy E F, Mouffouk F, Emwas A-H, Jaremko L, Jaremko M (2022) Cyclodextrins: structural, chemical, and physical properties, and applications. Polysaccharides 3(1):1-31. https://doi.org/10.3390/polysaccharides3010001

[20] Cakir Yigit N, Hızal G, Tunca U (2022) Synthesis of multiarm star block copolymer based on host-guest inclusion complexation. Journal of Innovative Engineering and Natural Science 2(1):1-16. https://doi.org/10.29228/JIENS.54191

[21] Okumura H, Kawaguchi Y, Harada A (2001) Preparation and characterization of inclusion complexes of poly (dimethylsiloxane)s with cyclodextrins. Macromolecules 34(18):6338-6343. https://doi.org/10.1021/ma010516i

[22] Kawaguchi Y, Nishiyama T, Okada M, Kamachi M, Harada A (2000) Complex formation of poly (ε-caprolactone) with cyclodextrins. Macromolecules 33(12):4472-4477. https://doi.org/10.1021/ma992103b

[23] Busche B J, Tonelli A E, Balik C M (2010) Morphology of polystyrene/poly (dimethyl siloxane) blends compatibilized with star polymers containing a γ–cyclodextrin core and polystyrene arms. Polymer 51(6):1465-1471. https://doi.org/10.1016/j.polymer.2010.01.019

[24] Balik C, Tonelli A, Libert R (2012) Compatibilization of polymer blends with star polymers containing a gamma-cyclodextrin core and polystyrene arms. APS March Meeting Abstracts 2012:Q48. 005.

[25] Sharma D, Dhingra S, Banerjee A, Saha S, Bhattacharyya J, Satapathy B K (2022) Designing suture-proof cell-attachable copolymer-mediated and curcumin-β-cyclodextrin inclusion complex loaded aliphatic polyester-based electrospun antibacterial constructs. International Journal of Biological Macromolecules 216:397-413.

[26] Busche B J, Tonelli A E, Balik C M (2010) Compatibilization of polystyrene/poly (dimethyl siloxane) solutions with star polymers containing a γ-cyclodextrin core and polystyrene arms. Polymer 51(2):454-462. https://doi.org/10.1016/j.polymer.2009.11.069

[27] Cakir N, Hizal G, Becer C R (2015) Supramolecular glycopolymers with thermo-responsive self-assembly and lectin binding. Polymer Chemistry 6(37):6623-6631. https://doi.org/10.1039/C5PY00939A

[28] Durmaz H, Dag A, Erdogan E, Demirel A L, Hizal G, Tunca U (2010) Multiarm star block and multiarm star mixed-block copolymers via azide-alkyne click reaction. Journal of Polymer Science Part A: Polymer Chemistry 48(1):99-108. https://doi.org/10.1002/pola.23765

J. Innovative Eng. Nat. Sci., vol. 3, no. 2, pp. 127-136, 2023.
http://dx.doi.org/10.29228/JIENS.70020

JIENS

Journal of Innovative Engineering and Natural Science
(Yenilikçi Mühendislik ve Doğa Bilimleri Dergisi)
journal homepage: https://jiens.org

Original Paper

Development of reactive digital printing process for cellulosic fabrics

Halil İbrahim Turgut[a,*], Aslı Balçak Girgin[a] and Özlem Yarar[a]

[a]*Harput Tekstil San. ve Tic. A.Ş.-R&D Center, Bursa and 16140, Turkiye.*

ARTICLE INFO

Article history:
Received 12 May 2023
Received in revised form 20 June 2023
Accepted 05 July 2023

Available online

Keywords:
Digital printing
Reactive dyeing
Cellulosic fabrics

ABSTRACT

In this study, the development processes of reactive digital printing for cellulosic fabrics are discussed. In the study, viscose fabric qualities were evaluated with the same content and different impregnation process numbers, according to pH value, washing fastness, rubbing fastness, water fastness, and perspiration fastness tests, after digital printing application under the same conditions. In addition, print patterns were visually examined. It has been determined that the visual quality of the fabrics with one pass impregnation is better than two passes impregnations and the test results have similar values for all samples. Viscose fabric qualities, with one pass application, were tested by applying different recipes and the optimum recipe was determined by making a cost analysis and sustainability aspect. It was determined that the wet rubbing fastness values were low. Fabric pH test results were determined to be in the range of 5.5-7.5, as expected. Washing, water, and perspiration fastness values were determined to be in the range of 4-5 as expected.

I. INTRODUCTION

The foundations of digital printing technology date back to 1878. The continuous ink jet printing method, which is widely used in today's printing technology, was invented by Sweet in 1965. It was developed by Hertz in 1967. Another important step in this field was taken in 1979 when HP and Canon found DOD (drop-on-demand) technologies. This invention has enabled the printing of dots in the desired color at the desired point [1]. Inkjet printing systems have had an extremely important area of use in offices, homes, and the advertising sector in the last 20 years. This technology, which developed primarily in the direction of printing on paper in the 1980s, has advanced considerably, especially with the developments in dye chemistry, digital printing is widely used in the textile industry today. Since the first systems used in production had a very low resolution (12–20 doi), they were only used for printing suitable products such as carpets and blankets, where the patterns are of low resolution. Since the early 1990s, high resolution inkjet printing systems have been used for printing on fabrics. Although the first applications were for sample purposes, today there is a trend towards printing in smaller quantities. Most recently, Reggiani Company launched a machine with a speed of 150 m^2/hour [2]. Digital printing technology is applied in the textile industry, which provides green production processes with smart equipment and saves a lot of water. The products produced with this technology in the textile sector have high quality and high resolution [3]. The printing process on the fabric can be finished in a short time, it is not limited to the pattern size, and it provides repeatability advantages. Another advantage is fast production, sensitivity, and no waste paint released into the environment [4]. In recent years, the application of digital inkjet printing on textiles has attracted increasing attention at both the academic and industrial levels due to its flexibility, cleanliness, versatility, and competitiveness [5-7]. Reactive printing ink is most commonly used in digital printing for cellulose-fiber fabrics

*Corresponding author. Tel.: +90-551-245-0061; e-mail: halil.turgut@harputholding.com

such as cotton and linen. But reactive dye is very easy to hydrolyze. Dye fixation rate and color strength are low during steaming. Hydrolyzed reactive dyes in wastewater can also pose an environmental hazard [8-13]. The viscosity of digital printing inks is low. For this reason, without applying printing paste, the penetration of the printing ink into the fabric cannot be controlled, and it spreads on the fabric surface. This prevents the acquisition of clear patterns. Therefore, printing paste is required as a pre-treatment in digital printing. With digital printing paste, thickeners, fixing agents, and auxiliary materials are applied to the fabric [14].

The pastes used in digital printing are prepared like the printing pastes used in conventional printing. Since digital printing is not widespread yet, it is not preferred for expensive long-length prints. Digital prints are commonly made on cotton, viscose, and polyamide fabrics in the textile sector. Therefore, reactive and acid dyestuffs are used in printing, and printing pastes of these dyestuffs are prepared [15].

Covalent bonds between the dye and the cellulose are created by reactive dyes reacting with each other in an alkaline environment. Sodium bicarbonate is often recommended because is affordable, provides adequate pretreatment, and stabilizes print paste while causing the least amount of hydrolysis. Oxidizing agent is used for avoid the risk of reduction, and decolourisation, of the dye during steaming. Urea is mainly used to swell cotton fibers during the steaming process. It also acts as a moisture absorbing agent. Urea accelerates the transfer of dye to cotton fiber and urea also reduces yellowing of cotton under warm, dry alkaline conditions [16-20].

Printing pastes; contain monomers that can cause air emissions, such as ammonia, formaldehyde, methanol, alcohols, esters, aliphatic hydrocarbons, acrylates, vinyl acetate, styrene, and acrylnitrile. In addition, reactive printing pastes can contain up to 150 g/kg of urea. Urea causes eutrophication in wastewater.

It has been observed that digital printing is cleaner than rotary screen printing in terms of depletion of natural resources and the environmental effects of acidification. The environmental impact of rotary printing (such as the Global warming effect, eutrophication, ozone depletion, and photochemical oxidation) increases, as the number of colors used in rotary screen printing increases [21]. Complex multi-color printing patterns make digital printing more advantageous. In addition, optimization of the digital printing preparation process and reducing its environmental load have been recognized as important work areas.

Digital and conventional printing pastes are prepared differently. In conventional printing, it is difficult to measure the amount of dye applied to the fabric. More dye is used than necessary to ensure sufficient dye penetration into the fabric. For this reason, the dyestuffs used in general are fixed at a rate of 65-70% in fabric. In digital printing, the amount of dye applied to the fabric can be precisely controlled, and the fixation rates are over 90%. In conventional printing, thickeners and carriers are used in printing paste for both reactive and disperse dyes. After the dyeing process, these substances are removed from the fabric by washing. These chemicals are not used in digital printing [22, 23] While there is an optimized recipe for rotational printing, the digital printing recipe needs to be optimized at the plant.

Harput Tekstil has invested in a digital printing machine both to gain a place in the clothing market and to build up a sustainable alternative to the rotary printing process. With this investment, both an alternative printing method in small quantities and an environmentally friendly process that generates less waste have been reached. Since the digital printing machine investment was made for the first time in this study, the need for process optimization before and after digital printing in the enterprise was determined, and this need was met with recipe optimizations.

The aim of this study is to reduce the amount of chemicals released into the environment and reduce the process cost by optimizing the paste content and amount in the digital printing process. In this study, the reactive digital printing process was optimized with paste impregnation studies before reactive digital printing, and the cost has been reduced. Reactive digital printing applications were carried out by working on three different preferred qualities. In addition, with the optimizations made, the amount of chemicals in the paste recipe has been reduced, and the process's environmental load has been reduced.

II. EXPERIMENTAL METHOD

2.1. Materials

Paste auxiliary chemicals (touching and color efficiency enhancer, thickener, reduction inhibitor) were supplied from Setas. Sodium bicarbonate, sodium sulfate, and urea chemicals were supplied by Ozan Kimya. Viscose fabric qualities were supplied from the company's own resources. Printing design was chosen for reactive digital printing, and recipe optimization was carried out for paste impregnations. The paste recipe is given in Table 1.

Table 1. Quantity of Chemicals in Digital Paste Recipe

Chemicals	**Quantity** *(g/L)*
Sodium bicarbonate	35
Paste Auxiliary Chemicals (3 different chemicals)	36
Urea	200

2.2. Method

Viscose fabrics have been made ready for the digital printing process by applying one or two layers of paste impregnation. Visual quality control, pH, washing fastness, rubbing fastness, water fastness, and perspiration fastness tests were performed on fabrics that were digitally printed at the same conditions. Fabrics were compared after application. After the paste impregnation applications, different sustainable paste recipes were determined, a cost analysis was performed, and the most suitable paste recipe was determined. Old and new paste recipes were applied to different commercially preferred cellulosic fabric qualities. In addition, fabric qualities were compared by pH, washing fastness, rubbing fastness, water fastness, and perspiration fastness tests.

2.3 Characterization

The pH value was calculated, according to the TS ISO 3801 test standard. Color fastness to rubbing was determined according to the ISO 105-X16:2016 test standard. Color fastness to perspiration was determined according to the TS EN ISO 105-E04 test standard. Color fastness to water was determined according to the TS EN ISO 105-E01 test standard. Color fastness to washing was determined according to the TS EN ISO 105-C06 test standard. Paste impregnation applications were carried out in a stenter machine at 120 ºC at a speed of 40 m/min. Digital printing applications were carried out at 90 ºC at a speed of 5 m/min. After digital printing, viscose fabrics were fixed at 1200 kg of steam and 102 ºC for 12 minutes then washing and drying processes occured.

III. RESULTS AND DISCUSSIONS

3.1. Fabric Analysis

At first, three different cellulosic fabric analyses, which are more preferred in the market, were made (Table 2). The process was optimized with paste applications on viscose fabric quality before digital reactive printing. Viscose fabrics are made ready for digital printing application by impregnating the paste once and twice in the stenter machine. Front and back side images of viscose fabric qualities with digital reactive printing are given in Figure 1.

Table 2. Fabric Analysis

	30/1 Viscose		**50/1 Poplin**		**Cotton + Elastane**	
	115 *(g/m^2)*		108 *(g/m^2)*		144 *(g/m^2)*	
	Yarn Type	**Density** *(w/cm)*	**Yarn Type**	**Density** *(w/cm)*	**Yarn Type**	**Density** *(w/cm)*
Weft	Ne 30/1 Viscose	21	Ne 50/1 Cotton	32	Ne 30/1 Cotton	23
Warp	Ne 30/1 Viscose	26	Ne 50/1 Cotton	56	Ne 40/1 Cotton + Elastane	53
	Plain		Plain		Twill	

3.2. Paste Impregnations

As a result of the paste impregnations, it has been determined that there is a difference in handle and color between the viscose fabric qualities. When we look at the fabrics that have been impregnated twice, it has been determined that the applied dyestuff has more transitions to the back surface, but in visual quality control, the colors are more dull and the handle is harder. In addition, it has been observed that the colors of the fabrics that have been impregnated with the paste at one time are more vivid, and the handle is softer and more draped.

3.3. Test Results

After digital reactive printing applications, the visual quality control, pH, washing fastness, rubbing fastness, water fastness, and perspiration fastness tests were performed, and paste impregnations were compared. Washing fastness, perspiration fastness, and water fastness test results are given in Table 3. In this context, the fastness test results of the sample fabrics, which were applied once and twice, were almost the same and also desired values. The visual quality of one and double pass impregnation studies is similar.

Wet and dry rubbing fastnesses and pH values of viscose fabric qualities are given in Table 4. The pH test range, which is determined as the acceptance criterion for garments according to DIN EN/ISO 3071 is between 4 and 7.5, and the pH value of the sample fabrics was determined as 5.5-5.6 in the tests. In lighter tones, the wet rub test was 3-4 and the dry rub test was 4-5, while the pH was 6-6.5. In this study, the rubbing fastness values of cellulosic fabrics were compared over dark colors. Other fastness values were higher for all colors.

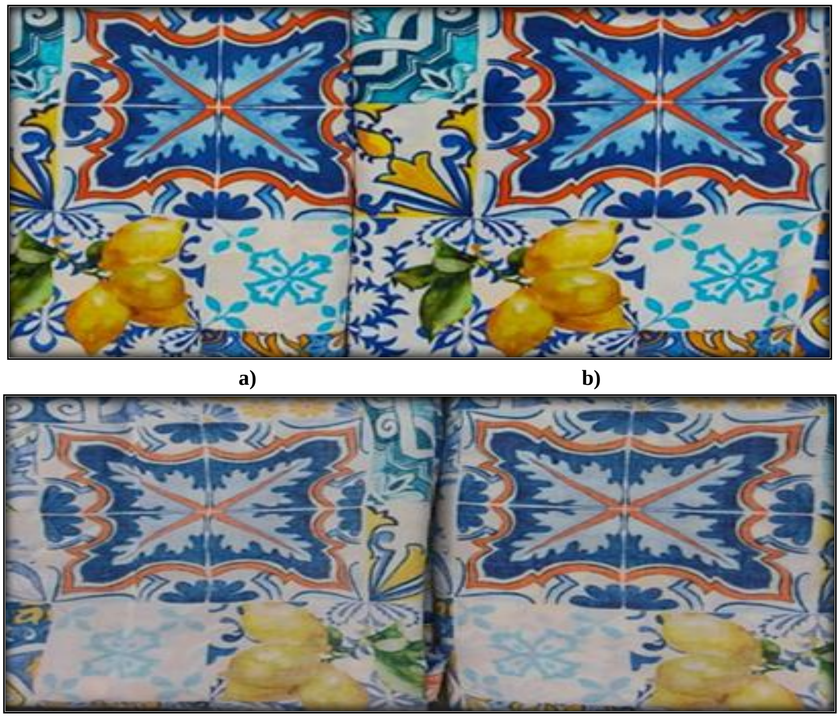

a) **b)**

c) **d)**

Figure 1. The front and back side images of digital printed fabrics **(a)** Front side image of one pass application **(b)** Front side image of two passes application **(c)** Back side image of one pass application **(d)** Back side image of two passes application

Table 3. Fastness test results of 30/1 viscose fabric qualities

	Wool	Acrylic	Polyester	Polyamide	Cotton	Acetate
			Fastness to Washing			
One pass	5	5	4-5	5	4-5	4
Two passes	5	5	4-5	4-5	4-5	4-5
			Fastness to Perspiration (Acid)			
One pass	5	5	4-5	4-5	4-5	4-5
Two passes	5	5	4-5	4-5	4-5	4-5
			Fastness to Perspiration (Alkali)			
One pass	5	5	4-5	4-5	4-5	4-5
Two passes	5	5	4-5	4-5	4-5	4-5
			Fastness to Water			
One pass	5	5	4-5	4-5	4-5	4-5
Two passes	5	5	4-5	4-5	4-5	4-5

Table 4. Wet and dry rubbing fastnesses and pH values of 30/1 viscose fabric qualities

	Wet Rubbing Fastness	**Dry Rubbing Fastness**	**pH**
One pass	2	3-4	5.6
Two passes	2	4	5.5

With the paste impregnation study, it has been determined that impregnations with one paste are more suitable for digital printing processes. For comparison of viscose qualities with different cellulosic fabric qualities, comparisons were made on three different fabric qualities preferred in the garment sector. Fastness tests and pH tests were carried out to compare the fabric qualities with reactive digital printing under the same conditions. Rubbing fastness test results and pH values are given in Table 5. Washing, water, and perspiration fastness test results are given in Table 6. Reactive digital print images of viscose, poplin, and cotton fabric qualities are given in Figure 2.

Table 5. Rubbing fastness test results and pH results

Fabric Quality	Wet Rubbing Fastness	Dry Rubbing Fastness	pH
Viscose	2	4	6.9
Poplin	2-3	3-4	6.5
Cotton + Elastane	1-2	3-4	6.9

Wet color fastnesses are at least one point lower than dry color fastnesses, especially in dark tones, consistent with studies on reactive digital printing on cellulosic materials in the literature [24].

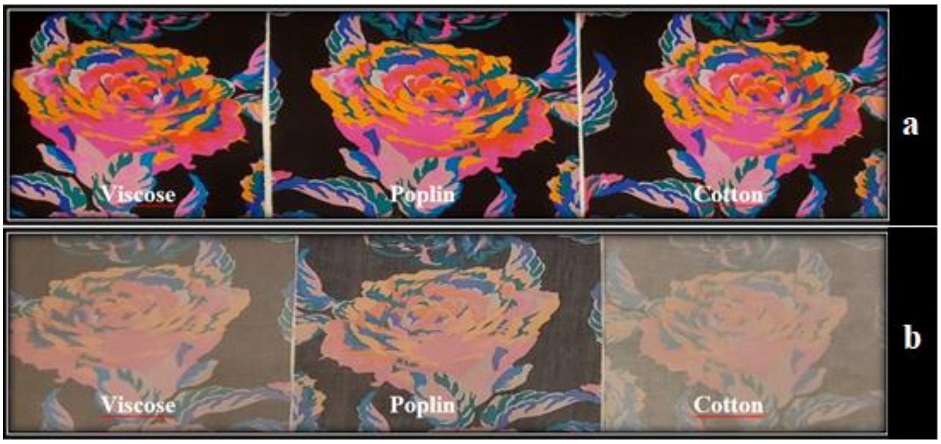

Figure 2. Reactive digital printing images of viscose, poplin and cotton fabrics (a: front side, b: back side)

According to visual quality control, the best performance with the most vivid color tones was seen in viscose fabric. The lowest performance was seen in poplin due to the paste passing to the back side of the fabric.

Table 6. Washing, water and perspiration fastness test results

	Wool	Acrylic	Polyester	Polyamide	Cotton	Acetate
Fabric Quality			**Fastness to Washing**			
Viscose	5	5	5	5	4-5	5
Poplin	4-5	5	4-5	4-5	4-5	5
Cotton + Elastane	5	5	5	5	5	5
Fabric Quality			**Fastness to Perspiration (Acid)**			
Viscose	4-5	4-5	4-5	4-5	4-5	5
Poplin	4-5	4-5	4-5y	4-5	4-5	5
Cotton + Elastane	4-5	4-5	5	5	4-5	5
Fabric Quality			**Fastness to Perspiration (Alkali)**			
Viscose	4-5	4-5	4-5	4-5	4-5	5
Poplin	4-5	4-5	4-5	4-5	4-5	5
Cotton + Elastane	4-5	4-5	5	5	4-5	5
Fabric Quality			**Fastness to Water**			
Viscose	5	5	5	5	4-5	5
Poplin	4-5	4-5	4-5	4-5	4-5	5
Cotton + Elastane	4-5	4-5	5	5	4-5	5

When the obtained fastness data were compared to the literature regarding reactive digital printing on cellulosic materials, it was discovered that the results were consistent with the literature [24].

3.4. Optimization of the Pat Recipe

The current recipe for different fabric qualities preferred in the market has been optimized. Samples that were impregnated once, under the same conditions were compared. Costs were reduced by changing the type of paste auxiliary chemicals (different commercial product with similar chemical properties) and the amounts of urea chemicals in the existing recipes (the old recipe).The current paste recipe and the developed paste recipe are given in Table 7.

Table 7. Paste recipes developed for cost reduction

Chemical	**Old recipes** *(g)*	**New recipes 1** *(g)*	**New recipes 2** *(g)*
Sodium bicarbonate	35	35	35
Paste Auxiliary Chemicals (3 different chemicals)	36	36	36
Urea	200	200	100
Total Cost *(€/kg)*	**0.330**	**0.292**	**0.229**

With the new recipes, digital printing was applied, and as a result of the fastness tests, the values were close to the quality of the old recipe. New Recipe 1 was developed for viscose and cotton qualities. Recipe 2 is developed for poplin grades. The cost of paste in poplin grades has been reduced from 0.33 €/kg to 0.229 €/kg. In viscose and cotton qualities, the cost of paste has been reduced from 0.33 €/kg to 0.292 €/kg. A new recipe has started to be used in the enterprise. After the study, the fabric qualities were tested and evaluated. The data for the test results are given in Table 8. Washing, water, and perspiration fastness test results are given in Table 9.

Table 8. Rubbing fastness test results and pH values of old and new recipes

Fabric Quality	**Wet Rubbing Fastness**	**Dry Rubbing Fastness**	**pH**
Viscose (Old recipes)	2-3	4-5	6.7
Viscose (New recipes)	2-3	4	6.6
Poplin (Old recipes)	2-3	4	6.5
Poplin (New recipes)	2	4	6.5
Cotton + Elastane **(Old recipes)**	2	3-4	6.9
Cotton + Elastane **(New recipes)**	1-2	3-4	6.8

All the pH values remained in the range of 6.5-6.9, ensuring DIN EN/ISO 3071 (the standard range is between 4 and 7.5). Wet rubbing test values of cellulosic fabrics are quite low, dry rubbing test values are at a medium level, and other fastness values are high and at desired values.

In this study, for the digital printing preparation phase, a more sustainable process was achieved by obtaining 50% less chemical urea waste for viscose, poplin, and cotton qualities. Water consumption was reduced by 50% with one pass applications.

Table 9. Washing, water and perspiration fastness test results

	Wool	Acrylic	Polyester	Polyamide	Cotton	Acetate
Fabric Quality	**Fastness to Washing**					
Viscose (Old recipes)	5	5	5	5	5	5
Viscose (New recipes)	5	4-5	5	5	4-5	5
Poplin (Old recipes)	5	5	4-5	4-5	4-5	5
Poplin (New recipes)	5	4-5	4-5	4-5	4-5	5
Cotton + Elastane **(Old recipes)**	5	5	5	5	5	5
Cotton + Elastane **(New recipes)**	5	4-5	5	4-5	4-5	5
Fabric Quality	**Fastness to Perspiration (Acid)**					
Viscose (Old recipes)	4-5	4-5	5	5	4-5	5
Viscose (New recipes)	4-5	4-5	5	5	4	4-5
Poplin (Old recipes)	4-5	4-5	4-5	4-5	4-5	5
Poplin (New recipes)	4-5	4-5	4-5	4-5	4-5	5
Cotton + Elastane **(Old recipes)**	4-5	4-5	5	5	4-5	5
Cotton + Elastane **(New recipes)**	4-5	4-5	5	4-5	4-5	5
Fabric Quality	**Fastness to Perspiration (Alkali)**					
Viscose (Old recipes)	4-5	4-5	5	5	4-5	5
Viscose (New recipes)	4-5	4-5	5	5	4	4-5
Poplin (Old recipes)	4-5	4-5	4-5	4-5	4-5	5
Poplin (New recipes)	4-5	4-5	4-5	4-5	4-5	5
Cotton + Elastane **(Old recipes)**	4-5	4-5	5	5	4-5	5
Cotton + Elastane **(New recipes)**	4-5	4-5	5	4-5	4-5	5
Fabric Quality	**Fastness to Water**					
Viscose (Old recipes)	4-5	4-5	5	5	4-5	5
Viscose (New recipes)	4-5	4-5	5	5	4	4-5
Poplin (Old recipes)	4-5	4-5	4-5	4-5	4-5	5
Poplin (New recipes)	4-5	4-5	4-5	4-5	4-5	5
Cotton + Elastane **(Old recipes)**	4-5	4-5	5	5	4-5	5
Cotton + Elastane **(New recipes)**	4-5	4-5	5	4-5	4-5	5

IV. CONCLUSIONS

Reactive digital printing paste impregnation processes were optimized for cellulosic fabric qualities. With the optimized paste recipe, more efficient results were obtained in the viscose fabric qualities that were impregnated once. Thus, the study was continued with one layer of paste impregnation. The visual quality, pH, and fastness values of three different cellulozic fabric qualities (viscose, poplin, and cotton + elastane fabrics), which were impregnated once with paste, met expectations. After reactive digital printing, rubbing, washing, water, pH tests, and visual quality controls were performed on three different fabric qualities. When the obtained fastness results were compared to the research on reactive digital printing on cellulosic materials, the results were found to be consistent.

Viscose fabrics have been found to have more vibrant colors than other fabric types. It has been found that the dye penetrates up to the rear surface of the fabric because poplin fabric qualities have a lighter and tighter structure than viscose fabric qualities. As a result, it has been found that viscose fabrics have better visual quality than poplin materials. In addition, it was predicted that the dye could not form integrity on the fabric surface due to the different weave structure of the cotton + elastane fabric, and the visual quality decreased compared to other fabric qualities. It was determined that the optimized paste recipe was costly, and the existing recipe was improved again for three different cellulosic fabric qualities. In cost reduction studies, low-cost recipes have been obtained by changing the high-cost paste auxiliary chemicals and amounts of urea chemicals. Fastness tests, fabric pH tests, and visual quality controls were performed in all studies.

While the fastness values were high for all color tones, the rubbing fastness values were observed lower. Especially the wet rubbing fastness values are quite low for dark tones. This shows that more studies are needed to improve the wet rubbing fastness of reactive digital printing processes, especially in dark tones. The developed process provided a significant reduction in water and chemical consumption, enabling the application of a more sustainable process.

ACKNOWLEDGMENT

This work was supported by the Harput Tekstil R&D Center with the equity project numbered HRPT-PR-K55

REFERENCES

[1] Ujiie H (2006) Digital printing of textiles. The Woodhead Publishing Ltd., Cambridge p.202-204
[2] Kanık M (2004) Tekstil teknolojisi ve kimyasındaki son gelişmeler sempozyumu. s.191-203
[3] Leelajariyakul S, Noguchi H, Kiatkamjornwong S (2008) Surface-modified and micro-encapsulated pigmented inks for ink jet printing on textile fabrics. Progress in Organic Coatings. 62:145-161. https://doi.org/10.1016/j.porgcoat.2007.10.005
[4] Kuo CH, Shiu JW, Rwei SP (2022) Preparation and characterization of PMMA encapsulated carbon black for water-based digital jet printing ink on different fibers of cotton and PET. Colloids and Surfaces A: Physicochemical and Engineering Aspects, 648, 129450.
[5] Kuang M, Wang L, Song Y (2014) Controllable printing droplets for high-resolution patterns. Advanced materials (Deerfield Beach, Fla.). 26. 10. https://doi.org/1002/adma.201305416.
[6] Menard E, Meitl MA, Sun Y, Park JU, Shir DJ, Nam YS, Jeon S, Rogers JA (2007) Micro- and nanopatterning techniques for organic electronic and optoelectronic systems. Chem Rev 107(4):1117-60. https://doi.org/10.1021/cr050139y.
[7] Nie Z, Kumacheva E (2008) Patterning surfaces with functional polymers. Nature Materials 7:277-90. https://doi.org/10.1038/nmat2109
[8] Hauser P, Tabba AH (2001). Improving the environmental and economic aspects of cotton dyeing using a cationised cotton. Review of Progress in Coloration and Related Topics 117:282-288.
[9] Khatri A, Peerzada M, Mohsin M, White M (2015) A review on developments in dyeing cotton fabrics with reactive dyes for reducing effluent pollution. Journal of Cleaner Production 87:50-57. https://doi.org/10.1016/j.jclepro.2014.09.017
[10] Montazer M, Malek MAR, Rahimi A. (2007) Salt free reactive dyeing of cationized cotton. Fibers and Polymers 8:608-612. https://doi.org/10.1007/BF02875997
[11] Nallathambi A, Rengaswami GDV (2016) Salt-free reactive dyeing of cotton hosiery fabrics by exhaust application of cationic agent. Carbohydr Polym 5(152):1-11. https://doi.org/10.1016/j.carbpol.2016.06.087
[12] Wang L, Ma W, Zhang S, Teng X, Yang J (2009) Preparation of cationic cotton with two-bath pad-bake process and its application in salt-free dyeing. Carbohydrate Polymers 78:602-608. https://doi.org/10.1016/j.carbpol.2009.05.022
[13] Aston SO, Provost JR, Masselink H. (2008) Jet printing with reactive dyes. Journal of the Society of Dyers and Colourists 109(4):147–152. https://doi.org/10.1111/J.1478-4408.1993.TB01546.X
[14] Tyler DJ (2005) Textile digital printing technologies. Textile Progress 37(4):1-65.
[15] T.C. Millî Eğitim Bakanlığı (2013) Tekstil teknolojisi, dijital baskıya hazırlık, Ankara, 2013.
[16] Eser B, Ozguney A, Ozerdem A (2012) Investigation of the usage of different thickening agents in ink-jet printing with reactive dyes. Industria textilă 63:85-90.
[17] Choi PSR, Yuen CWM, Ku SKA, Kan CW (2005) Digital ınk-jet printing for chitosan-treated cotton fabric. In: Fibers and Polymers 6(3):229-234. https://doi.org/10.1007/BF02875647
[18] Gutjahr H, Koch RR (1994) Direct print coloration. Textile Printing, 2nd Edn., Ed. Miles, L.W.C., Bradford: SDC, pp 139-195.
[19] Achwal W. B (2002) Textile chemical principle of digital textile printing. Colourage, 49(12):33.
[20] Chen W, Wang G, Bai Y (2002) Best for wool fabricprinting – digital inkjet. Textile Asia 33(12):37.

[21] Rüzgar A (2019) Rotasyon ve dijital reaktif baskıların çevresel etkilerinin yaşam döngüsü analizi tekniğiyle karşılaştırılması, Yüksek Lisans Tezi, Tekstil Mühendisliği Anabilim Dalı, Fen Bilimleri Enstitüsü, Bursa Uludağ Üniversitesi, Bursa, Türkiye.

[22] Marianofreire E (2006) Ink jet printing technology (CIJ/DOD): Digital Printing of Textiles, Editor: Ujiie, H Woodhead Publishing Limited, Cambridge, England, pp 29- 52.

[23] Kanık M (2013) Dijital baskı teknolojileri ve tekstil sanayindeki uygulamaları ders notları. Uludağ Üniversitesi, Fen Bilimleri Enstitüsü, Tekstil Mühendisliği, Bursa, Türkiye.

[24] Acar S (2020) Viskon ve viskon elastan karışım kumaşlarının dijital inkjet baskısına yeni bir yaklaşım, Yüksek Lisans Tezi, Fen Bilimleri Enstitüsü, Tekstil Eğitimi Anabilim Dalı, Tekstil Eğitimi Programı, Marmara Üniversitesi, İstanbul, Türkiye.

J. Innovative Eng. Nat. Sci., vol. 3, no. 2, pp. 137-152, 2023.
http://dx.doi.org/10.29228/JIENS.70166

JIENS
Journal of Innovative Engineering and Natural Science
(Yenilikçi Mühendislik ve Doğa Bilimleri Dergisi)
Original Paper
journal homepage: https://jiens.org

Effect of PVDF content on the filtration performance and mechanical properties of melt-blown PP fibrous webs

Andinet Kumella Eticha[a,b], Yasin Akgül[c,d,*], Ayben Pakolpakçil[c,e], Oğuz Kağan Ünlü[c,f], Harun Cüğ[b], and Ali Kiliç[c,f]

[a] *School of Mechanical and Industrial Engineering, Addis Ababa Institute of Technology, Addis Ababa University, Addis Ababa 385, Ethiopia.*
[b] *Mechanical Engineering Department, Karabuk University, Karabuk 78050, Türkiye.*
[c] *Temag Labs, Faculty of Textile Technology and Design, Istanbul Technical University, Istanbul 34437, Türkiye.*
[d] *Iron and Steel Institute, Karabuk University, Karabuk 78050, Türkiye.*
[e] *Textile and Fashion Design Department, Faculty of Art and Design, Istanbul Nişantaşı University, Türkiye.*
[f] *R&D Department, Areka Group LLC, Istanbul, Türkiye.*

ARTICLE INFO

Article history:
Received 19 May 2023
Received in revised form 03 July 2023
Accepted 05 July 2023

Available online

Keywords:
Polypropylene
Polyvinylidene fluoride
Melt-blown
Filtration performance
Mechanical properties

ABSTRACT

Particulate matter (PM0.3) aerosols are the most penetrating particles, which pose a serious health threat to humans. Therefore, mechanical filtration alone is insufficient to effectively filter 0.3 µm aerosols from a polluted environment. Thus, the need for electrostatic filtration is undeniable. This study aims to investigate the effect of incorporating 10 wt.% and 20 wt.% mass fractions of Polyvinylidene fluoride (PVDF) on the filtration performance and mechanical properties of polypropylene (PP)-based melt-blown (MB) nonwoven filter webs for air filtration applications. Morphological tests, fiber diameter measurements, filtration tests, mechanical tests, contact angle tests, etc., were conducted for each filter web to characterize its properties. The test results revealed that PP/PVDF fibrous webs exhibited thicker micro-fibers in the range of 1.0 to 1.32 µm and rough surface morphologies (beads and droplets) compared to MB PP, which can be attributed to the incorporation of PVDF. Consequently, the introduction of 10 wt.% and 20 wt.% PVDF into PP resulted in the creation of super-hydrophobic MB nonwoven webs, as evidenced by their resistance to water droplets. However, the study also demonstrated that the incorporation of 10 wt.% and 20 wt.% PVDF into PP reduced the tensile strength of PP nonwoven filters by approximately 5.55% and 8.33%, respectively. Furthermore, the addition of 20 wt.% PVDF into PP, along with corona charging, induced a quality factor (QF) of 0.11 mmH2O-1 for the 80PP-20PVDF sample. A similar QF was observed for corona-charged MB PP, which exhibited a filtration efficiency of 99.01% against 0.3 µm aerosol particles, at the expense of a pressure drop of 427 Pa.

I. INTRODUCTION

Micro/nanofibrous webs emerge as prominent filtering techniques for separating aerosol pollutants of various sizes from polluted environments. These aerosols, in the form of solid and liquid droplets, including toxic PM particles, pose a serious threat to human health [1]. Particles with diameters less than 2.5 µm are particularly hazardous to the respiratory system [2]. Therefore, there is a need for fibrous webs with high filtration performance to improve the quality of inhaled air [3].

Various methods, including electrospinning (ES), solution blow spinning (SBS), centrifugal spinning (CS), and melt-blowing, are used to produce polymeric micro/nanofibrous webs. While ES is low-cost and suitable for lab-scale production [4], it has limitations and is not suitable for industrial-scale manufacturing [3-5]. On the other

---

*Corresponding author. Tel.: +90-533-671-7361; e-mail: yasinakgul@karabuk.edu.tr side, SBS and CS, driven by air pressure and centrifugal forces respectively, have higher production capacities compared to ES [4, 5]. However, melt-blowing technology surpasses them in terms of production capacity.

Melt-blown nonwovens, known for their high surface area per unit weight, high porosities, and barrier characteristics, are widely used for air filtration. During corona charging, these nonwovens can hold an abundant amount of charges on the fiber periphery, creating a quasi-permanent electric field that attracts negatively charged PM aerosols [6]. Polymers such as polyethylene (PE), polyamide (PA), polyurethane (PUR), poly (ethylene terephthalate) (PET), polystyrene, and poly (butylene terephthalate) (PBT) are suitable polymers types for MB applications [7]. Polypropylene (PP) is commonly used for melt-blown applications due to its versatility, availability, and relatively low cost [8, 9].

Pu et al. [10], studied MB PP using a novel approach of electrostatic-assisted melt-blown technology. In the study, it was found that the average fiber diameter (AFD) obtained from the electrostatic-assisted melt-blown techniques was reduced approximately by 43.19%. Also, the new approach leads to a better filtration efficiency of 50.826% in contrast to the conventional MB method (40.651%) against 0.3 μm aerosol. In another MB PP study, a QF of 1.69×10^{-3} Pa^{-1} and a pressure drop of 173 Pa were found by Alberta et al. [11]. Although the filtration efficiency of MB PP filter fabrics increased when thinner fibers were used during the filtration process, there are limitations in the capacity of the device.

Aerosol sizes of 0.3 μm are characterized by the most penetrating particles which cannot be fully filtered by mechanical filtration [12]. To enhance the filtration efficiency of most penetrating small aerosols the need for an electrostatic capturing mechanism along with mechanical filtration is inevitable. Thus, numerous types of research have been done by blending PP with other polymers and electret additives to see their effects on the characteristics of MB nonwoven filter webs. In 2018 Zhang et al. studied MB nonwoven filter webs in detail by preparing PP blended with magnesium stearate (MgSt) as the charge enhancement [6]. The study showed a high filtration efficiency of 99.22% and a low-pressure drop of 92 Pa were achieved with the help of the electret additive. In another research work by Zhang et al. [13], corona-charged MB PP filters exhibit a high filtration efficiency of 99.65% and a pressure drop of 120 Pa. The MB study using Ag@ZIF-8 PP resulted in a filtration efficiency of 88 ± 2.2% and a pressure drop of 51 ± 3.6 Pa against 0.3 μm aerosols [14]. Brochocka et al. [15] studied improving the filtration efficiency of MB PP filters with the effect of electret additives perlite beads (positive charge) and amber (negative charge). An electret perlite-modified PP MB nonwovens exhibit a filtration efficiency of 99.56% and a pressure drop of 290 Pa against sodium chloride aerosols. Previous studies have explored the use of PP and various additives to enhance the filtration efficiency of melt-blown nonwoven filter webs. Some studies have shown promising results by incorporating electret additives or optimizing the fiber web morphology [6, 13, 15]. However, achieving higher filtration efficiency with lower pressure drop remains a challenge.

Piezoelectric polymers such as polyvinylidene fluoride (PVDF) can be used to fabricate melt-blown fibers that exhibit self-polarized electret properties, thus enhancing aerosol filtration [16]. PVDF is known for its low cost, excellent hydrophobicity, and good impact strength [17]. However, there is limited research on melt-blown PP/PVDF filter webs, making it a promising alternative for efficiently filtering 0.3 μm aerosols from polluted environments.

In this study, the effect of different amounts of PVDF on the filtration performance and mechanical behavior of melt-blown PP fibrous webs would be investigated. Additionally, the influence of corona charging on the filtration capacity of PP and PP/PVDF filter webs with the addition of the electret additive zinc stearate (ZnSt) would be examined. Various characterization tests were conducted to gain a better understanding of the behavior of the fabricated filter webs.

II. EXPERIMENTAL METHOD

2.1 Materials

Polypropylene granules with a melt flow index (MFI) of 1800 g/10 min were purchased from TEKNOMELT. Whereas, *Kynar® MG15 resin*-PVDF powder with a density of 1.78 g/cm^3 was purchased from ARKEMA. Irgafos-168 powder was purchased from BASF. Maleic anhydride grafted polypropylene (PP-G-mA, MFI = 8 g/10 min) was supplied from DuPont. An electret additive zinc stearate was purchased from BASF.

2.2 Methods

2.2.1. Preparation of MB nonwoven filter webs

PVDF fine powders get dried in the vacuum furnace for 2 hrs at 80 °C. Then, as per the DOE presented in Table 1, each composition of MB samples was prepared by blending the dried PVDF powders with other granules. Afterward, sample codes were assigned namely PP, 90PP-10PVDF, and 80PP-20PVDF. The blended compositions for each sample were fed into the extruded compounder (Figure 1) with a twin screw speed of 9 rpm. The compounding process was performed using the process parameter specified in Table 2. For each composition, the extruded compounding process was performed successfully. Subsequently, the MILLER device is used for cutting the compounded PP/PVDF samples into granules. The compounded granules of each sample were again left to dry in a vacuum furnace at 80 °C for another 2 hr to completely remove the presence of any moisture. Later, using the dried compounded granules the MB process for each sample is performed as indicated schematically in Figure 2. Eventually, after the MB process PP, 90PP-10PVDF, and 80PP-20PVDF nonwoven fibrous webs were fabricated. During the fibrous webs production process parameters including screw speed of 12 rpm, die tip-to-collector distance (DCD) of 25 cm, die temperature of 275 °C, hot air pressure of 3 bar, and hot air temperature of 350 °C were used to produce all the nonwoven filter webs.

Table 1. Design of experiment (DOE) for MB fiber preparation

Sample Code	**PP** *(wt.%)*	**PVDF** *(wt.%)*	**Irgafos-168** *(wt.%)*	**ZnSt** *(wt.%)*	**PP-G-mA** *(wt.%)*
PP	100	0	1	1	1.5
90PP-10PVDF	90	10	1	1	1.5
80PP-20PVDF	80	20	1	1	1.5

Table 2. The temperature profile of the twin screw compound extruder

Heating zone	1	2	3	4	5	6	7
Temperature *(°C)*	100	150	190	200	210	180	130

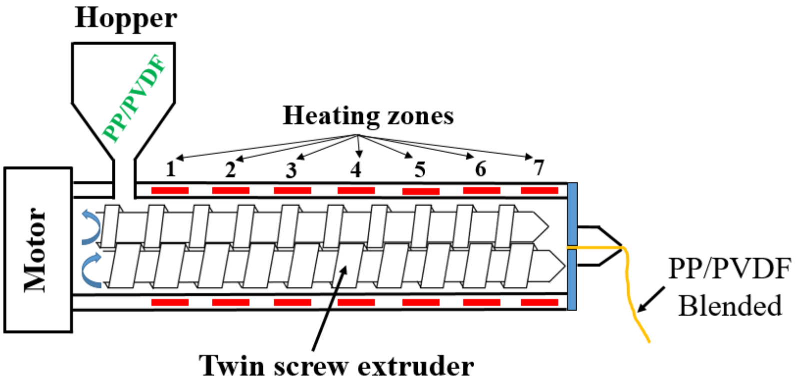

Figure 1. Schematic drawing of twin screw compound extruder

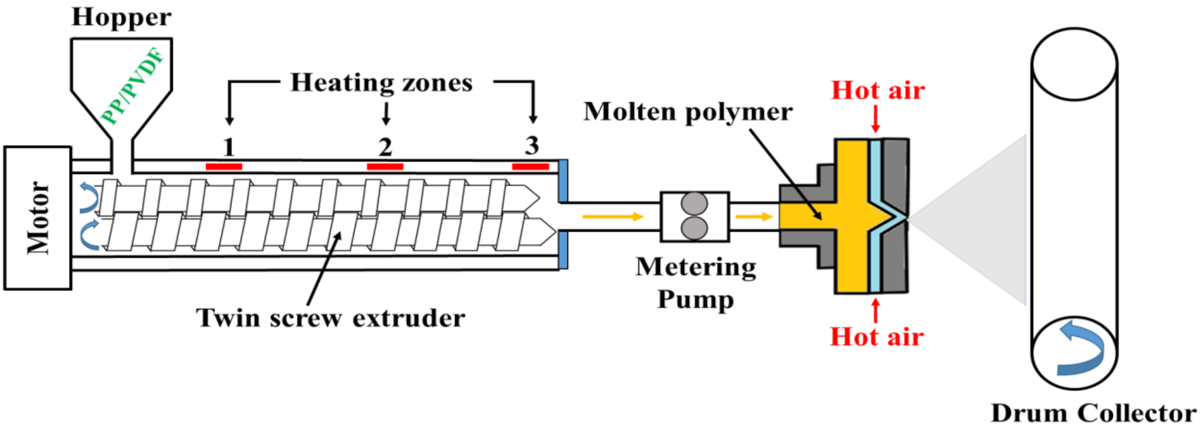

Figure 2. Schematic drawing of the MB process

2.2.2. Corona charging

The corona charging apparatus schematically represented in Figure 3(a) consists of a high-voltage power supply, two cylindrical rollers separated approximately by 1 mm, a manually rotating handle, and a grounding electrode. Because of the high potential difference between the high-voltage power and the roller-shaped electrode, corona discharge arises, causing the deposition of the positively charged ions on the electret MB fibrous webs. All single-layer samples were charged via a voltage of 2 kV for a charging time of 30 sec. On the contrary, as shown in Figure 3(b) all double-layer nonwoven samples were placed on a plate 5 cm away from the electrode represented by pink color. And for each double-layer MB nonwoven, corona charging is taking place at a higher-voltage power supply of 12.4 kV for 1 min.

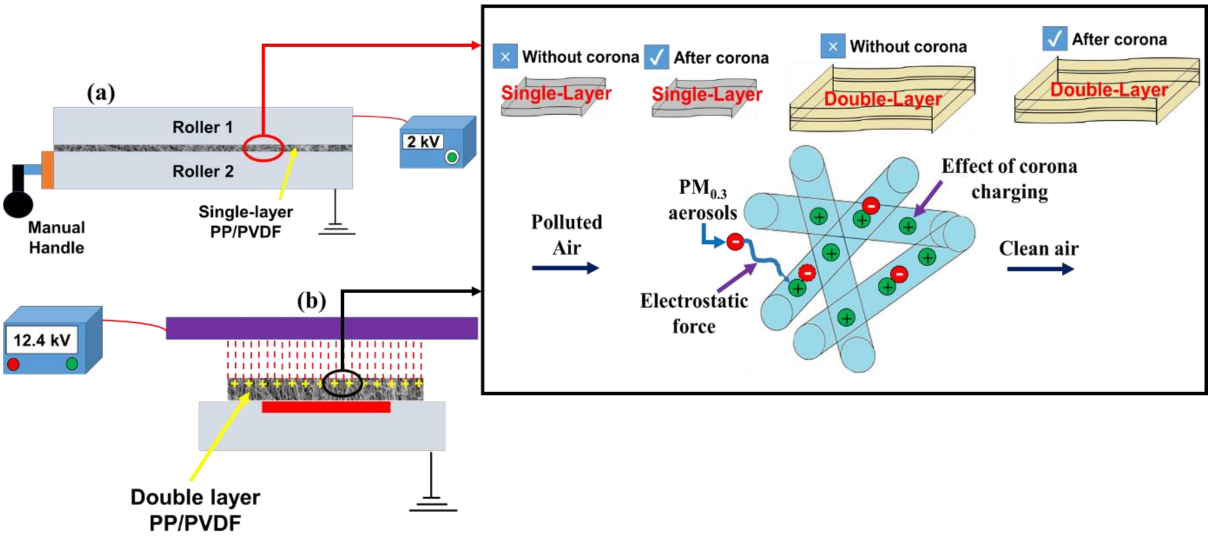

Figure 3. Schematic drawing for corona charging of (**a**) single-layer filter webs and (**b**) double-layer filter webs.

2.3 Characterization

2.3.1. Scanning electron microscope (SEM)

PP and PP/PVDF MB samples were coated with gold via a sputter coater (Quorum, Q150R ES Plus model) and then, fiber morphologies were investigated via Zeiss Ultra Plus scanning electron microscope (SEM). Fiber diameters were determined with the help of ImageJ software. During the fiber diameter determination, a total of 100 random fiber diameter measurements were taken from each sample. Subsequently, for each sample, the measured 100-fiber diameter data would be exported to Origin software for determining the AFD based on the Gaussian approach.

2.3.2. Air filtration

The filtration efficiency (η) and pressure drop (ΔP) of MB PP and PP/PVDF filter webs were measured by an automated air filter tester (8130A model, TSI Inc.). Mathematically the filtration efficiency of filter webs was determined by using Eq. 1. On the other side, the filtration performance or QF of each MB filter web is theoretically calculated via Eq. 2. All air filtration tests took place at a 95 l/min flow rate with the help of solid salt (NaCl) particles with a diameter of 0.26 ± 0.07 µm at a face velocity of 15.83 cm/s. The tests were conducted three times on each filter sample with an effective area of 100 cm^2 to challenge $PM_{0.3}$ NaCl aerosol particles. Each sample's filtration efficiency (η), and pressure drop (ΔP) value is the average of the three individual tests.

$$\eta = 1 - \frac{\text{Cdown}}{\text{Cup}} \tag{1}$$

where, Cdown and Cup are the captured particles concentration at the downstream and upstream sides, respectively [18].

$$\mathrm{QF} = -\frac{\ln(1-\eta)}{\Delta \mathrm{P}} \tag{2}$$

where QF is the representation of the quality factor and ΔP is the short-hand form of pressure drop [19].

2.3.3. Air permeability

PP and PP/PVDF fibrous webs air permeability test was performed according to ISO standards with the help of the Prowhite Airtest II device. The test was performed at room temperature using a fiber filter measuring an area of 38 cm^2 and at a constant applied air pressure load of 100 Pa. For each MB filter web air permeability test is conducted five times and the mean of all five tests will be assigned as the air permeability value for each PP and PP/PVDF sample. The air permeability of nonwoven webs is theoretically calculated based on the Darcy equation (Eq. 3).

$$\mathrm{q} = \frac{k_p \times \Delta \mathrm{P}}{\mu \times \mathrm{L}} \tag{3}$$

where q is the representation of air permeability (m/s), k_p is the air permeability coefficient (m^2), ΔP is the short-hand form of pressure drop (Pa), L is samples thickness (m), and μ is the viscosity of the flow (Pa.s) [20]. Moreover, the air permeability of porous materials can also be computed using Eq. 4.

$$\mathrm{q} = \frac{1}{9.4} \times \frac{\Delta \mathrm{P}}{\mu \times \mathrm{L}} \times \frac{(\rho_f - \rho_n) \times d^2}{\rho_n} \times \frac{2 - lnR_e}{2.4 - lnR_e} \tag{4}$$

where q represents air permeability (m/s), ΔP is pressure drop (Pa), μ is flow viscosity (Pa.s), L is the thickness of samples (m), ρ_f and ρ_n are fibers and nonwoven webs densities (kg/m^3), d is the diameter of fiber (m), and R_e is the representation of Reynolds number [20].

2.3.4. Basis weight measurement

The weight of 10 cm × 10 cm square-shaped MB fibrous webs was measured by KERN ACJ 220-4M. The basis weight for PP, 90PP-10PVDF, and 80PP-20PVDF samples was determined by dividing the weight of fibrous webs by their effective area as expressed in Eq. 5.

$$BW = \frac{\text{Mass of samples}}{\text{Effective area}} \tag{5}$$

where BW is the designation of samples basis weight.

On the other hand, solidity also known as packing density affects air permeability. Basis weight, the thickness of the filter web, and the density of the fiber material are the major factors that govern solidity. Theoretically, the solidity value of PP, 90PP-10PVDF, and 80PP-20PVDF webs are calculated using the formula given in Eq. 6 [21].

$$Solidity = \frac{\mathrm{BW}}{\mathrm{t} \times \rho} \tag{6}$$

where t represents the thickness of filter webs and the density of the material, fiber webs are made designated by ρ.

2.3.5. Filter web thickness measurement

The thickness of each MB filter web was measured at three different points using LOYKA digital micrometer with a 1 µm measurement resolution. And the mean value was computed and assigned for each sample.

2.3.6. Water contact angle (WCA) measurement

To investigate the surface hydrophobicity of filter samples contact angle measurements (Theta Lite) against a drop of nearly 0.0062 ml of pure water at room temperature and pressures were measured by the sessile drop method. For this analysis, samples were prepared with a dimension of 10 mm × 40 mm. Then, three contact angle data at different locations on one surface were averaged to get a reliable value for each sample.

2.3.7. Mechanical properties

The mechanical properties of MB fibrous webs with a dimension of 5 cm × 25 cm were investigated according to DIN EN ISO 7198 standard via INSTRON tensile testing device. The test is conducted three times for each MB sample and a mean value was assigned for each PP and PP/PVDF fibrous web. During the test, tensile strength, elongation modulus, and strains were examined under a fiber gauge length of 200 mm and speed of 2 mm/min.

III. RESULTS AND DISCUSSIONS

3.1. SEM morphologies and fiber diameters

In MB technology high-speed hot air stretches the molten polymer to form fine fibers with high porosity. In this study, all nonwoven filter samples were produced under the same MB processing parameters. Figure 4 indicates the MB web morphologies and fiber diameters of PP and PP/PVDF micro/nanofibrous examined under SEM. Although the presence of beads was tremendously high, droplet-free MB filter webs were fabricated for PP (Figure 4(a)). These beads are attributed to the effect of high turbulence of air during MB production [22]. For other nonwoven filters such as 90PP-10PVDF and 80PP-20PVDF randomly distributed fibers with a relatively small number of droplets were fabricated. But, there were more beaded morphologies were also noticed in 80PP-20PVDF. On the other hand, fibrous webs of AFD 0.62 ± 0.03 μm were examined for melt-spun PP. From the literature survey, it was investigated that by adjusting the MB process parameters such as low screw speed (i.e., low feed rate) and low hot air pressure it can be possible to produce thinner fibers [23]. However, thicker fibers in micro-scale of 1.0 ± 0.03 μm and 1.32 ± 0.07 μm were observed for 90PP-10PVDF and 80PP-20PVDF, respectively. This tells that fiber diameter increases with the increment addition of the content of PVDF into PP. This is attributed to the increment in the viscosity of molten PP/PVDF polymer as compared to PP. Furthermore, fiber diameter distribution for MB samples was considerably influenced by MB process parameters. Also, the amount of blended material PVDF into the host polymer (PP) had a significant effect on fiber diameter distribution. So, PP blended with 10 wt.% PVDF produces narrow fiber distribution with lower fiber diameter as illustrated in Figure 4(b). On the contrary, as indicated in SEM images of Figure 4(c) 20 wt.% PVDF incorporated into PP produces MB webs with higher fiber diameter and wider fiber distribution.

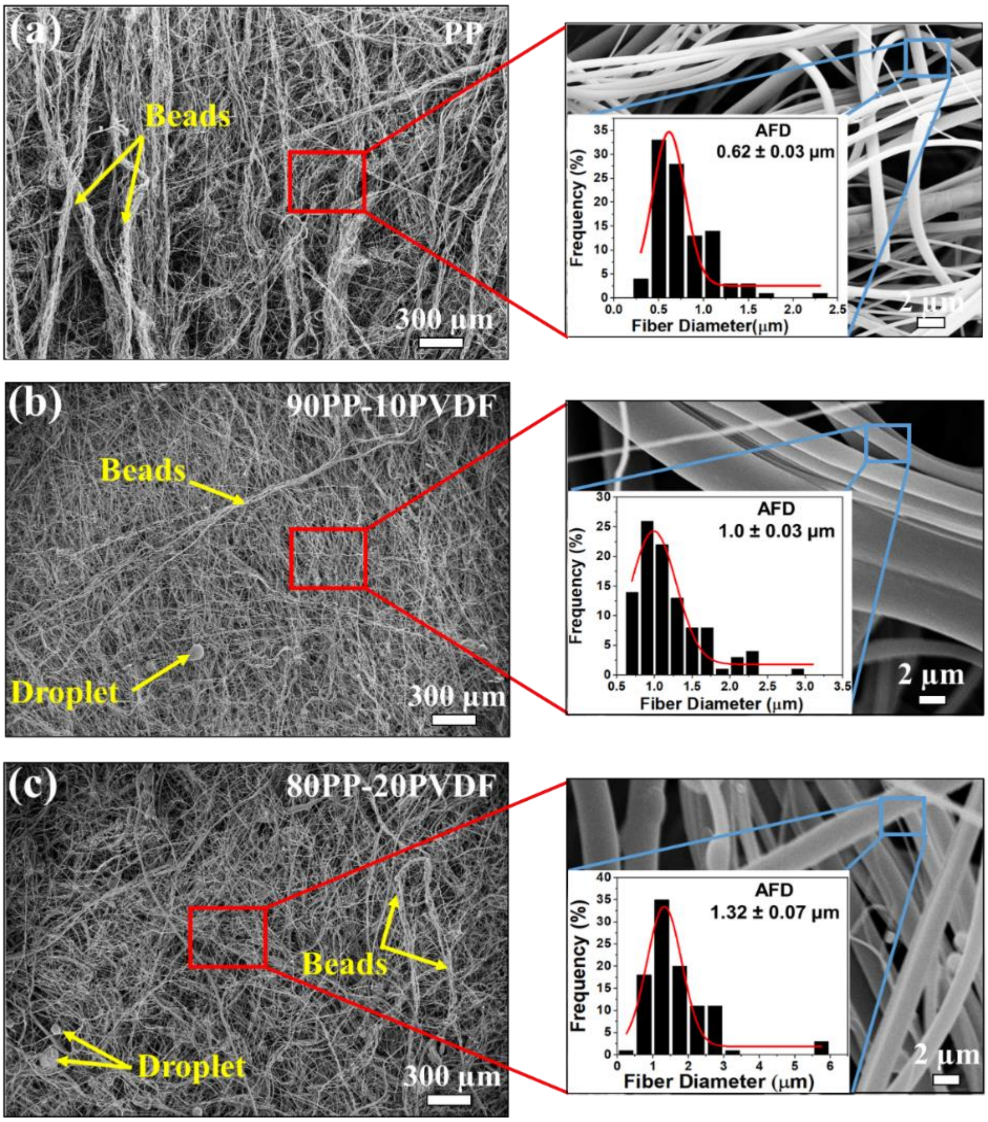

Figure 4. Fiber morphologies of MB fibrous webs

3.2. Basis weight and air permeability

The basis weight, solidity, and air permeability of single-and-double-layer filter samples were presented in Figures 5(a) and 5(b), respectively. As shown in Figure 5(a) the basis weight for single-layer PP, 90PP-10PVDF, and 80PP-20PVDF was measured as 58.47, 38.96, and 49.62 g/m^2, respectively. Similarly, a basis weight value in the range between 77.98 to 116.94 g/m^2 was measured for double-layer filter webs as depicted below in Figure 5(b). Compared to MB PP filter webs, PP/PVDF samples blended with 10 and 20 wt.% PVDF showed better air permeability properties. Among single-layer filter webs the highest air permeability of 101.8 mm/s was investigated for the 90PP-10PVDF nonwoven filter, but the lowest is for PP with 81 mm/s. This shows that there exists an indirect relationship between basis weight and air permeability. Looking at Figure 5(a), adding 10 wt.% PVDF into PP results in a 33.37% reduction of basis weight conversely 25.68% improvements were noted in air permeability. Furthermore, the study observed that there were no significant differences were noticed in the air permeability values for filter webs before and after electrification treatment via corona charging. Likewise, a resemble results were noted in the study of Yang et al. [17]. In their study, it was found that filter webs before and after electrification treatment have relatively similar air permeability values. Thickness, density, and fiber diameters are other structural parameters of nonwoven webs which influences filter air permeability. Also, in the literature, it was revealed porosity is another factor that changes the air permeability of MB PP/PVDF nonwoven webs. However, weight is the dominant factor in the determination of air permeability compared to thickness, fiber diameter, and density of fibrous webs [24]. In the study, it was also noted that corona charging had insignificant influence on the air permeability of MB webs.

Similarly, the air permeability test for double-layer filters gives in the range of 16.2 to 39.2 mm/s. The decrement in air permeability values for double-layer MB samples was related to their thickness value in contrast to single-layer filters. Thus, the study showed filter webs thickness had also an influence on their air permeability behavior. The thickness of single-layer nonwoven webs such as PP, 90PP-10PVDF, and 80PP-20PVDF measured as 0.22, 0.72, and 0.74 mm, respectively. On the other hand, thickness values of 0.286, 0.899, and 0.970 mm were reported for double-layer PP, 90PP-10PVDF, and 80PP-20PVDF, respectively. For instance, when filter web thickness was increased from 0.72 to 0.899 mm between single and double layers of 90PP-10PVDF this resulted in an approximately 72.1% reduction in air permeability. Air permeability decrement as a result of increment in filter webs thickness was also noticed in the study of air permeability of Polyester nonwoven fabrics [20]. Generally, due to the less torturous path encountered lower thickness nonwoven webs result in higher air permeability [25]. It was indicated in Figure 5(b) adding 20 wt.% PVDF into PP causes a decrement in basis weight (15.12%) however, the air permeability was enhanced by (142%). The fiber collection time is also another factor that affects fibrous web parameters namely basis weight and thickness but here during fiber production; the collection time for all samples was identical. Basis weight, web thickness, and density of fiber material are the main factors of solidity. An increment in basis weight results in simultaneous enhancement in filter webs solidity but a considerable decrement in air permeability.

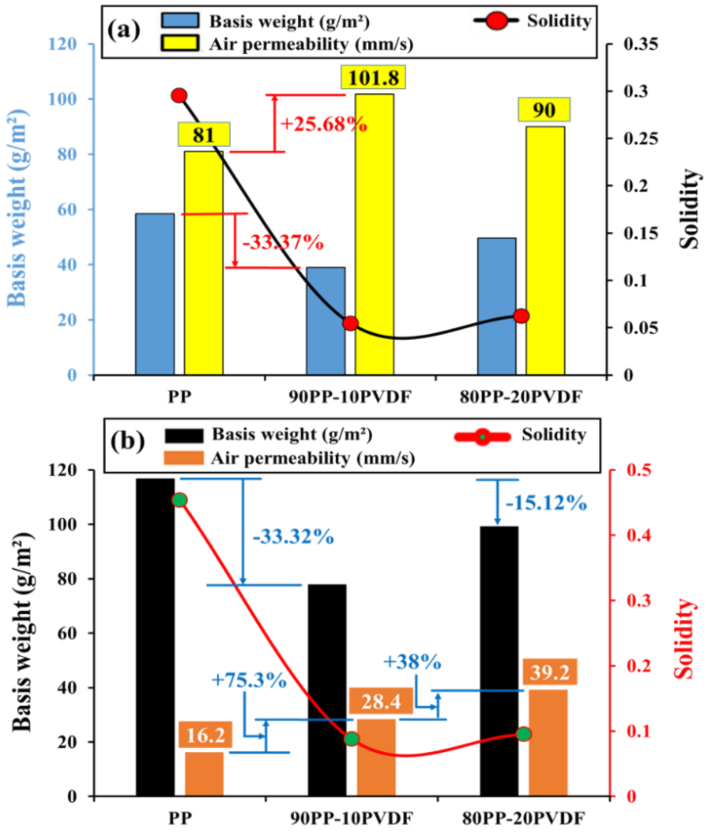

Figure 5. Basis weight and air permeability of (**a**) single-layer and (**b**) double-layer MB fibrous webs (where the "+" and "-" signs ahead of the number indicate percentage increment and decrement, respectively)

3.3. Filtration Efficiency of MB filter webs

The filtration efficiency test is conducted in single-layer PP, 90PP-10PVDF, and 80PP-20PVDF nonwoven MB filter samples as illustrated in Figure 6(a). Here for each MB sample, the test was performed before and after corona charging. So, from Figure 6(a) it was seen that maximum filtration efficiency of 83.88% and 85.28% were investigated for the PP filter web without corona and after corona charging, respectively. In addition, the maximum pressure drop was also observed for this MB PP sample. This might be due to the effect of beaded morphologies plays a crucial role in enhancing the air resistance properties of the MB PP sample. The highest basis weight for PP samples shows the highest filtration efficiency and pressure drop. The increment in filtration efficiency and pressure drop as a result of enhancement in basis weight was also observed in the study of Liu et al. [26]. On the other side, introducing PVDF into PP-based fibrous webs had considerable effects on reducing the filtration efficiency of PP/PVDF nonwoven filters. Thus, the lowest filtration efficiency of 48.64% was noted for the sample (80PP-20PVDF) produced from the addition of a maximum amount of PVDF (20 wt.%). This might be due to the presence of thicker fiber diameters observed in SEM images and also morphological defects (i.e., droplets and beads) resulting from the addition of PVDF. The reduction in filtration efficiency due to the presence of many thicker fibers was reported in previous research works and hence, this result is supported by past findings. For instance, Eticha et al. showed that the addition of thermoplastic polyurethane (TPU) into electrically assisted solution blow spun PVDF nonwovens results in the reduction of the filtration efficiency of PVDF nanofibrous mats due to the increment in fibers diameter [18].

Furthermore, together with mechanical filtration to enhance filtering of the most penetrating particle size of 0.3 μm corona charging technology was adopted on both single-layer (Figure 6(a)) and double-layer (Figure 6(b)) nonwovens. As demonstrated in both Figure 6(a) and 6(b) corona charged samples have shown better filtration efficiency than the uncharged filter webs. This is probably due to charged fibers capturing both charged and neutral aerosol particles with the help of electrostatic force [6]. While considering double-layer fibrous webs before the corona and after corona charging (Figure 6(b)) have exhibited higher filtering efficiency compared to single-layer MB webs (Figure 6(a). This might be due to the increment in the thickness of filter samples. Also, it might be related to because of the higher-voltage power supply and more charging time as compared to single-layer filters. Moreover, in double-layer MB samples, the electret nature of fibers was higher since more charges will be created and stored on the MB webs. Thus, a higher coulomb attraction force is created between charged aerosols and charged fibers, and the electrostatic capturing mechanism will be conducted. On top of that, for neutral aerosols the electric field created by the electret fibers will going to charge the neutral $PM_{0.3}$ aerosols, and filtering action is executed via an electrostatic filtration mechanism. It was also observed that for each corona-charged and uncharged sample, the pressure drop remained relatively the same. This indicates that corona charging does not have remarkable effects on the morphologies of MB nonwoven webs.,

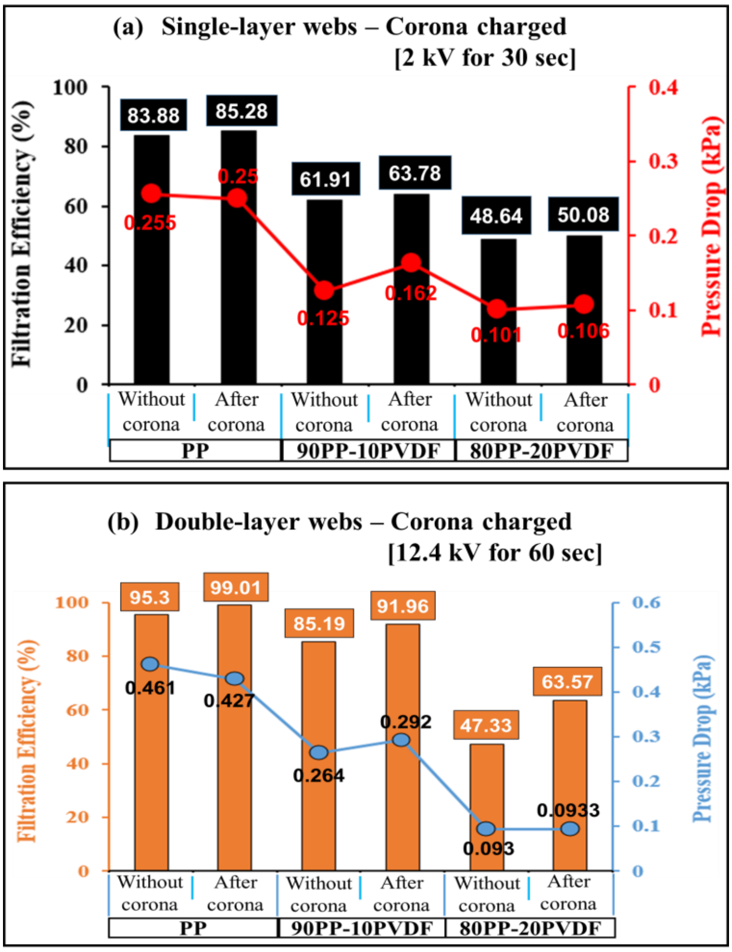

Figure 6. Filtration properties of MB filter webs

3.4. Filtration performance of MB filter webs

The filtration performance of both single and double-layer MB nonwoven samples PP, 90PP-10PVDF, and 80PP-20PVDF was depicted below in Figure 7. The lowest QF has been noticed for all non-corona-charged MB samples. In addition, as shown in Figure 7(a) blending of PP by a low amount (10 wt.%) of PVDF and without any charging causes a slight improvement in the QF of filter webs than uncharged PP filter samples. But, as the PVDF content increased to 20 wt.% the QF behaves a slight decrement compared to 90PP-10PVDF. This might be related to fiber morphologies (presence of more beads and droplets) responsible for the rising of filters air resistance behavior and an increment in fiber diameter lowers filtration efficiency, the combination of these two scenarios together leads to QF reduction. On the contrary, non-corona charged double-layer MB nonwovens (Figure 7(b)) show the addition of 10 and 20 wt.% PVDF into PP brings about higher QF as compared to PP filters. According to Figure 7(b), corona-charged samples have better QF as compared to uncharged nonwovens. Hence, as indicated in Figure 7(b) the study founds the maximum QF for double-layer corona-charged 80PP-20PVDF samples of 0.11 mmH_2O^{-1} at a lower pressure drop of 93.3 Pa. Although corona-charged double-layer PP filter webs have similar QF to double-layer corona-charged 80PP-20PVDF filter sample, it was seen that the measured pressure drop (427 Pa) was remarkably high.

Furthermore, looking at Figures 7(a) and 7(b), generally, the QF value of PP, 90PP-10PVDF, and 80PP-20PVDF is improved by blending PP with 10 and 20 wt.% PVDF contents. Before and after corona charging the QF values for each sample displayed by the bar graph behaves a similar increment trend as represented in Figure 7(b), which shows that the electrostatic force enhances the filtration efficiency without affecting filter webs pressure drop.

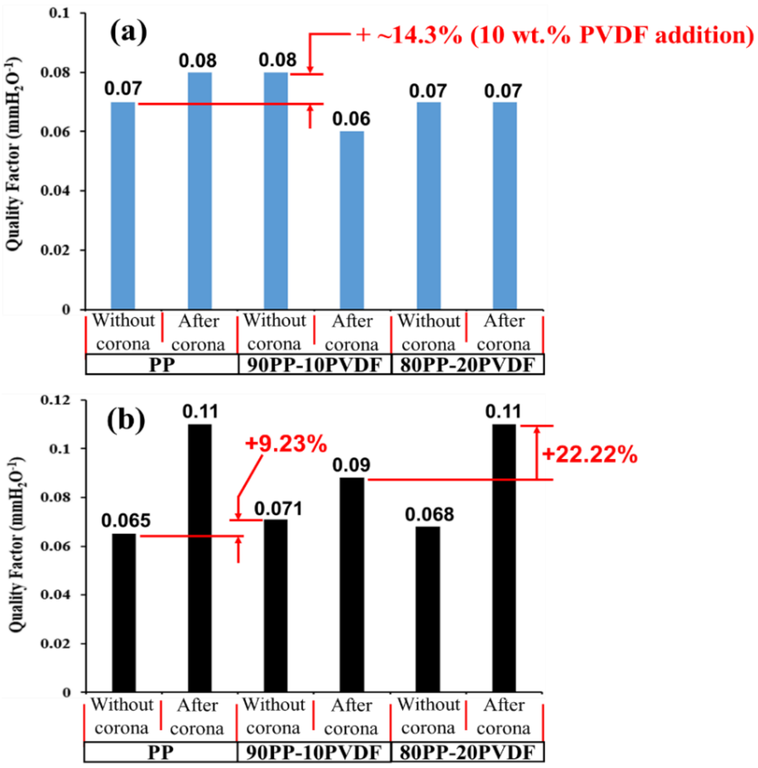

Figure 7. Filtration performance of (**a**) single-layer filter webs and (**b**) double-layer filter webs (where the "+" sign ahead of numbers indicates percentage increment)

3.5. Contact angle measurements

For each MB filter web sample, the hydrophobicity/hydrophilicity tests were conducted, and their water contact angle values were indicated in Figure 8. Contact angle values of 127.16 ± 1.52°, 133.53 ± 1.52°, and 134.22 ± 0.96° were measured for PP, 90PP-10PVDF, and 80PP-20PVDF samples, respectively. As per the results, a hydrophobic surface was noticed for all samples. Further, the addition of 10 and 20 wt.% PVDF contents into PP improves the surface hydrophobic character of MB PP nonwoven webs. This is because of the intrinsic hydrophobic characteristics of PVDF [27, 28]. Therefore, the hydrophobic properties of fibrous webs increased with PVDF addition to the PP morphology, and hence, the contact angles increased. In addition to the hydrophobicity of the blended polymer, the surface roughness of filter webs is also another factor that affects the WCA. As shown in SEM images, the introduction of 20 wt.% PVDF results in a large number of beads on the PP/PVDF surface of MB filter webs. So, compared to MB 90PP-10PVDF, SEM images revealed the surface roughness is greater for 80PP-20PVDF, and hence, the surface experience better hydrophobicity properties. This result was in complete agreement with Li et al. [29]. In their study, the addition of PVDF layers into PP shows superior hydrophobicity behavior. A contact angle of 96.96 ° was noted for PP nanofibrous layers, but the WCA value between 100 to 140.5 ° was noted for PVDF-coated PP nanofibrous layers.

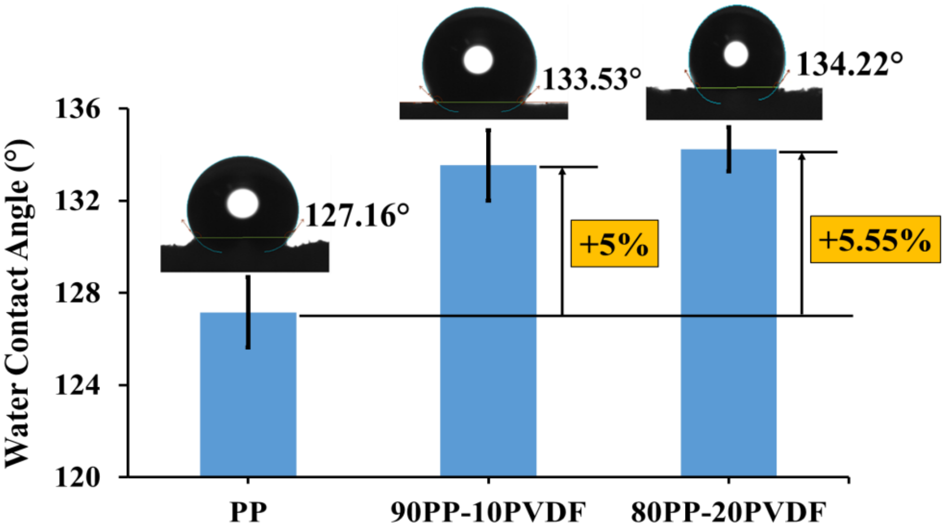

Figure 8. MB filter samples with their contact angle values (where the "+" sign ahead of numbers indicates percentage increment)

3.6. Mechanical properties

Figure 9 shows the mechanical properties of single-layer MB PP, 90PP-10PVDF, and 80PP-20PVDF fibrous webs. As can be seen in Figure 9(a), the tensile strength slightly decreases with the increment of PVDF content. On the contrary, the addition of 10 wt.% and 20 wt.% PVDF contents into PP notably affect the elastic modulus of the MB PP sample. The maximum tensile strength and elastic modulus were determined for PP with 0.18 ± 0.05 MPa and 2.68 ± 1.08 MPa, respectively. As the mass fraction of PVDF added to PP is 20 wt.%, the tensile strength and elastic modulus become 0.165 ± 0.06 MPa and 1.29 ± 0.43 MPa, respectively. The decrement in tensile strength might be attributed to the formation of weak bonds between fibers. Similar mechanical properties were observed in the studies of PPS/PVDF by Xing et al. [30]. In their study, it was shown that until the content of PVDF reaches 40 wt.% the tensile strength and tensile modulus of PPS/PVDF initially increase for low content of PVDF and then gradually decrease. When the tensile load escalates the nonwoven filter webs begin to fracture gradually as a result of random entanglements of fiber. Strain at break of PP/PVDF MB samples was indicated in Figure 9(b). Incorporation of PVDF (10 and 20 wt.%) into PP reduced the tensile strength and elastic modulus of PP and increased its strain at break. These results were in complete agreement with previous studies by Khakestani et al. [31].

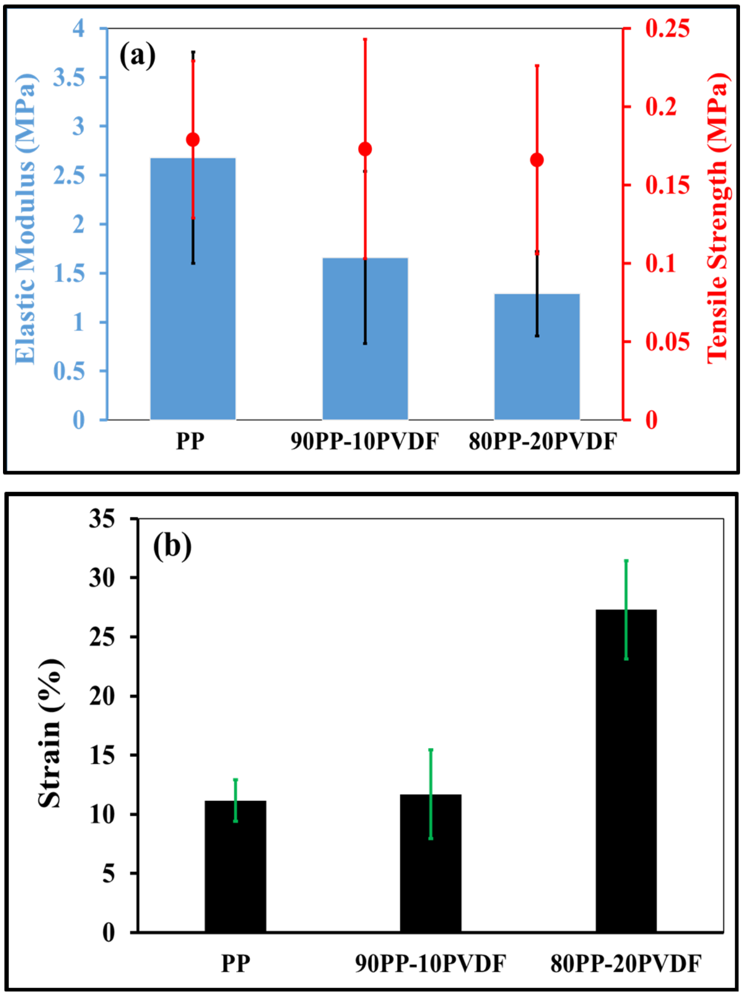

Figure 9. Mechanical properties of MB filter webs (**a**) tensile and elastic modulus and (**b**) strain value

IV. CONCLUSIONS

The fabrication of PP and PP/PVDF nonwoven filter webs using MB technology was successfully achieved. SEM analysis revealed that introducing 20 wt.% PVDF into PP resulted in the production of thicker micro-scale fibers, increased bead formation, and a relatively lower number of droplets compared to the 10 wt.% PVDF composition. The addition of PVDF had a significant advantage in reducing the basis weight of the filter webs, leading to improved air permeability in PP/PVDF samples compared to pure PP filter webs. The piezoelectric properties of

PVDF polymers likely played a crucial role in enhancing the electret characteristics of PP/PVDF filter webs by improving their charge storage capacity after corona charging. Moreover, the incorporation of zinc stearate electret additive in the MB PP and PP/PVDF fibers further enhanced the electrostatic attraction properties of the filter webs. This enhancement was evident in the filtration efficiency results, where the corona-charged PP double-layer filter web exhibited the highest filtration efficiency of 99.01% with a pressure drop of 427 Pa. Corona charging had a remarkable impact on improving PM0.3 aerosol filtration through electrostatic attraction, while not significantly affecting the pressure drops. However, relatively higher pressure drops were observed for the MB samples in this study. On the other hand, the addition of 20 wt.% PVDF significantly improved the hydrophobicity of PP/PVDF nonwovens. Nevertheless, mechanical tests revealed a slight decrease in the tensile and elongation modulus properties of PP-based fibrous webs with the addition of 10 wt.% and 20 wt.% PVDF.

ACKNOWLEDGMENT

The authors highly appreciated and thank Karabuk University Iron and Steel Laboratory and TEMAG Laboratory of Istanbul Technique University for their support for the characterization. Also, the authors would like to thank DuPont for the supply of Maleic anhydride grafted polypropylene.

REFERENCES

[1] Deng Y, Lu T, Cui J, Samal SK, Xiong R, and Huang C (2021) Bio-based electrospun nanofiber as building blocks for a novel eco-friendly air filtration membrane: A review. Separation and Purification Technology 277:119623. https://doi.org/10.1016/j.*seppur*.2021.119623
[2] Mamun A, Blachowicz T, and Sabantina L (2021) Electrospun nanofiber mats for filtering applications—Technology, structure and materials. Polymers 13(9):1368. https://doi.org/10.3390/polym13091368
[3] Zhang X et al. (2021) Multi-layered, corona charged melt blown nonwovens as high performance PM0. 3 air filters. Polymers 13(4):485. https://doi.org/10.3390/polym13040485
[4] Doğan C, Doğan N, Gungor M, Eticha AK, and Akgul Y (2022) Novel active food packaging based on centrifugally spun nanofibers containing lavender essential oil: Rapid fabrication, characterization, and application to preserve of minced lamb meat. Food Packaging and Shelf Life 34:100942. https://doi.org/10.1016/j.fpsl.20222.100942
[5] Doğan N, Doğan C, Eticha AK, Gungor M, and Akgul Y (2022) Centrifugally spun micro-nanofibers based on lemon peel oil/gelatin as novel edible active food packaging: Fabrication, characterization, and application to prevent foodborne pathogens E. coli and S. aureus in cheese. Food Control 139:109081. https://doi.org/10.1016/j.foodcont.2022.109081
[6] Zhang H, Liu J, Zhang X, Huang C, and Jin X (2018) Design of electret polypropylene melt blown air filtration material containing nucleating agent for effective PM2. 5 capture. RSC advances 8(15):7932–7941. https://doi.org/10.1039/c7ra10916d
[7] Bhat G (2015) Meltblown submicron fibers for filter media and other applications. International fiber journal: 20–23.
[8] Duran K, Duran D, OYMAK G, Kilic K, Ezgi Ö, and Mehmet K (2013) Investigation of the physical properties of meltblown nonwovens for air filtration. Textile and Apparel 23(2):136–142.
[9] Han MC et al. (2022) High-performance electret and antibacterial polypropylene meltblown nonwoven materials doped with boehmite and ZnO nanoparticles for air filtration. Fibers and Polymers 23(7):1947–1955. https://doi.org/10.1007/s12221-022-4786-8
[10] Pu Y et al. (2018) Preparation of polypropylene micro and nanofibers by electrostatic-assisted melt blown and their application. Polymers 10(9):959. https://doi.org/10.3390/polym10090959
[11] Podgórski A, Ba\lazy A, and Gradoń L (2006) Application of nanofibers to improve the filtration efficiency of the most penetrating aerosol particles in fibrous filters. Chemical Engineering Science 61(20):6804–6815. https://doi.org/10.1016/j.ces.2006.07.022

[12] Matulevicius J, Kliucininkas L, Martuzevicius D, Krugly E, Tichonovas M, and Baltrusaitis J (2014) Design and characterization of electrospun polyamide nanofiber media for air filtration applications. Journal of nanomaterials. https://doi.org/10.1155/2014/859656
[13] Zhang H et al. (2020) Design of polypropylene electret melt blown nonwovens with superior filtration efficiency stability through thermally stimulated charging. Polymers 12(10):2341. https://doi.org/10.3390/polym12102341
[14] Shiu BC, Zhang Y, Yuan Q, Lin JH, Lou CW, and Li Y (2021) Preparation of Ag@ ZIF-8@ PP melt-blown nonwoven fabrics: air filter efficacy and antibacterial effect. Polymers 13(21):3773. https://doi.org/10.3390/polym13213773
[15] Brochocka A, Majchrzycka K, and Makowski K (2013) Modified melt-blown nonwovens for respiratory protective devices against nanoparticles. Fibres & Textiles in Eastern Europe.
[16] Sanyal A and Sinha-Ray S (2021) Ultrafine PVDF nanofibers for filtration of air-borne particulate matters: A comprehensive review. Polymers 13(11):1864. https://doi.org/10.3390/polym13111864
[17] Yang B, Hao M, Huang Z, Chen Z, and Liu Y (2023) High Filterable Electrospun Nanofibrous Membrane with Charged Electret After Electrification Treatment for Air Filtration. Fibers and Polymers. https://doi.org/10.1007/s12221-023-00110-1
[18] ETICHA AK, TOPTAŞ A, AKGÜL Y, and KILIÇ A (2023) Electrically assisted solution blow spinning of PVDF/TPU nanofibrous mats for air filtration applications. Turkish Journal of Chemistry 47(1):47–53. https://doi.org/10.55730/1300-0527.3515
[19] Gungor M, Toptas A, Calisir MD, and Kilic A (2021) Aerosol filtration performance of nanofibrous mats produced via electrically assisted industrial-scale solution blowing. Polymer Engineering & Science 61(10): 2557–2566. https://doi.org/10.1002/pen.25780
[20] Zhu G, Kremenakova D, Wang Y, and Militky J (2015) Air permeability of polyester nonwoven fabrics. Autex Research Journal 15(1):8–12. https://doi.org/ 10.2478/aut-2014-0019
[21] Leung WWF, Hung CH, and Yuen PT (2010) Effect of face velocity, nanofiber packing density and thickness on filtration performance of filters with nanofibers coated on a substrate. Separation and purification technology 71(1):30–37. https://doi.org/10.1016/j.seppur.2009.10.017
[22] Y. Polat et al. (2019) Solution blown nanofibrous air filters modified with glass microparticles. Journal of Industrial Textiles. https://doi.org/10.1177/1528083719888674
[23] Luiso S, Henry JJ, Pourdeyhimi B, and Fedkiw PS (2020) Fabrication and characterization of meltblown poly (vinylidene difluoride) membranes. ACS Applied Polymer Materials 2(7):2849–2857. https://doi.org/10.1021/acsapm.0c00395
[24] Abuzade RA, Zadhoush A, and Gharehaghaji AA (2012) Air permeability of electrospun polyacrylonitrile nanoweb. Journal of Applied Polymer Science 126(1):232–243. https://doi.org/10.1002/app.36774
[25] Naragund VS and Panda PK (2021) Electrospun polyacrylonitrile nanofiber membranes for air filtration application. International Journal of Environmental Science and Technology. https://doi.org/10.1007/s13762-021-03705-4
[26] Liu B, Zhang S, Wang X, Yu J, and Ding B (2015) Efficient and reusable polyamide-56 nanofiber/nets membrane with bimodal structures for air filtration. Journal of colloid and interface science 457:203–211. http://dx.doi.org/10.1016/j.jcis.2015.07.019
[27] Wu X et al. (2016) Hydrophobic PVDF/graphene hybrid membrane for CO2 absorption in membrane contactor. Journal of Membrane Science 520:120–129. https://doi.org/10.1016/j.memsci.2016.07.025
[28] Francis L, Ghaffour N, Alsaadi AS, Nunes SP, and Amy GL (2014) PVDF hollow fiber and nanofiber membranes for fresh water reclamation using membrane distillation. Journal of Materials Science 49:2045–2053. https://doi.org/10.1007/s10853-013-7894-4
[29] Li H, Shi W, Zeng X, Huang S, Zhang H, and Qin X (2020) Improved desalination properties of hydrophobic GO-incorporated PVDF electrospun nanofibrous composites for vacuum membrane distillation. Separation and Purification Technology 230:115889. https://doi.org/10.1016/j.seppur.2019.115889
[30] Xing J, Ni QQ, Deng B, and Liu Q (2016) Morphology and properties of polyphenylene sulfide (PPS)/polyvinylidene fluoride (PVDF) polymer alloys by melt blending. Composites Science and Technology 134:184–190. https://doi.org/10.1016/j.compscitech.2016.08.020
[31] Khakestani M, Jafari SH, Zahedi P, Bagheri R, and Hajiaghaee R (2017) Physical, morphological, and biological studies on PLA/n HA composite nanofibrous webs containing E quisetum arvense herbal extract for bone tissue engineering. Journal of Applied Polymer Science 134(39):45343. https://doi.org/10.1002/app.45343

J. Innovative Eng. Nat. Sci., vol. 3, no. 2, pp. 153-166, 2023.
http://dx.doi.org/10.29228/JIENS.70059

Original Paper

Journal of Innovative Engineering and Natural Science
(Yenilikçi Mühendislik ve Doğa Bilimleri Dergisi)
journal homepage: https://jiens.org

Detecting acetone from breath using a $PrFeO_3$-doped PANi/TiO_2-coated PAN nanofiber sensor for non-invasive diabetic diagnosis

Nesibe Yeşildağ[a], Ömer Faruk Ünsal[a], Ramazan Gömeç[b] and Ayşe Çelik Bedeloğlu[a,*]

[a]*Department of Polymer Materials Engineering, Bursa Technical University, Eflak Str. No: 177 Yıldırım, Bursa, 16310, Turkey.*
[b]*Aydın Textile, İkitelli Organized Industrial Zone, Eski Turgut Özal Str. No: 38/3 Başakşehir, İstanbul, 34490, Turkey.*

ARTICLE INFO

Article history:
Received 15 May 2023
Received in revised form 4 July 2023
Accepted 6 July 2023

Available online

Keywords:
Nanofiber
Acetone
Gas sensor
Non-invasive
Diabetics
Perovskites

ABSTRACT

Polyacrylonitrile (PAN) nanofibers doped with varying concentrations of perovskite praseodymium ferrite ($PrFeO_3$) nanoparticles synthesized by calcination were successfully manufactured using a simple electrospinning process. The nanofibers were coated with layers of polyaniline-titanium dioxide (PANi-TiO_2) combination using an air brush. The structure, morphology, and electrical characteristics of the nanoparticles and nanofibers were characterized by SEM, FT-IR, and electrical measurement methods. The results indicated that the produced nanofibers exhibited a strong in vitro interaction and selectivity against acetone gas, a biomarker of diabetes. Perovskite nanoparticle doped PAN nanofibers have shown approximately 43% change in resistance with acetone gas exposure. These findings suggest that $PrFeO_3$-doped nanofibers hold promise as potential candidates for acetone gas sensors in non-invasive diabetes monitoring.

I. INTRODUCTION

According to reports from the International Diabetes Federation (IDF) [1], there are currently over 537 million adults living with diabetes worldwide, with one in every 10 individuals being affected by the disease. Reports from the World Health Organization (WHO) [2], estimate that there are 422 million adults with diabetes (ages 18-99), with an expected increase to 629 million by 2045 [3, 4]. The number of recorded deaths from diabetes is currently at 1.6 million annually [5]. The rising prevalence of diabetes highlights the increasing yearly medical and non-medical costs, as well as the growing number of diabetic fatalities [4, 6]. Diabetes Mellitus (DM) is a metabolic disorder characterized by hyperglycemia (blood glucose level greater than 230 mg/dL) or hypoglycemia (blood glucose level less than 65 mg/dL) caused by insulin hormone secretion or activation problems [4, 7]. Diabetes is caused by the pancreas's failure to produce enough insulin for the body or the body's inability to use the insulin produced by the pancreas effectively. Type 1 Diabetes Mellitus (T1DM) is a metabolic disorder caused by the destruction of cells in the pancreas as a result of the immune system recognizing and attacking the beta cells as foreign, resulting in insulin deficiency. Type 2 Diabetes Mellitus (T2DM) is caused by the body's inability to use insulin effectively. Other types of diabetes include genetic disorders, drug use, genetic syndromes, and gestational diabetes (GDM) [4, 8–12]. When T1DM and T2DM patients cannot effectively absorb glucose from circulation, the metabolic shift results in increased ketone synthesis in the blood (ketonemia), urine (ketonuria), and breath (ketosis) [13]. Acetone in the breath has been identified as an effective biomarker [5]. While it is evident that

---

*Corresponding author. Tel.: +90-224-300-3491; e-mail: ayse.bedeloglu@btu.edu.tr

T1DM patients have a high concentration of ketones in their breath, there is no universally accepted measure of the concentration of ketones in T2DM patients' breath [14–21].

Clinical investigations have demonstrated that the concentration of acetone in the breath of individuals with diabetes exceeds 1.8 ppm (with a range of 1.25-2.5 ppm), while healthy individuals exhibit acetone concentration below 0.9 ppm (with a range of 0.2-1.8 ppm) [22–27]. Moreover, the concentration of acetone in the breath of individuals with type 1 diabetes mellitus (T1DM) may reach up to 25 ppm [5, 24, 28–30]. In terms of age, healthy adults between the ages of 40-50 exhibit acetone concentration of 0.2-0.8 ppm in their breath, while adult diabetics aged 50 or older exhibit acetone concentration within the range of 1.8 ppm [3]. The significant difference in acetone concentration between healthy individuals and diabetics makes acetone in the breath a valuable biomarker for diabetes identification [26, 27, 29, 31]. The discovery of the odor of rotten apple breath by John Gallo in 1798 and the identification of this odor as acetone in 1857 led to the use of acetone as the first biomarker for diabetes [5, 24, 31]. In 1971, Linus Pauling presented a report proposing a study plan for differentiating 250 gases in human breath using gas chromatography [5, 32]. Since then, more than 3000 distinct volatile organic compounds (VOCs) and aerosolized particles have been identified in human breath [32–34]. These gases are produced as byproducts of metabolic reactions, for physiological functions such as cell-to-cell communication, or in infections and other pathological conditions in the body [32]. Diet [35, 36], exercise [37], and medical condition [5, 20, 38] all contribute to variations in breath acetone content. In addition to diabetes, intensive physical active ity and ketogenic diets may also cause an increase in breath acetone content. Therefore, the measurement of acetone in breath is critical for diabetes diagnosis and monitoring the efficacy of therapies in medical disorders [17]. is considered a hazardous gas as well as a breath biomarker for diabetes [3, 39, 40], as it can cause nausea in humans above 2000 ppm and respiratory irritation above 300-500 ppm [3, 40].

Elevated blood sugar levels in the body lead to several health complications, including hyperglycemia, cardiovascular disease, diabetic nephropathy, diabetic retinopathy, and diabetic neuropathy [41, 42]. Furthermore, diabetes can also result in heart attack, stroke, blindness, kidney failure, leg amputation, vision loss, and nerve damage [2, 5, 42]. These complications highlight the critical importance of controlling blood sugar levels [3, 43]. To diagnose diabetes, a Plasma Glucose Level test is necessary. Diabetics receiving insulin therapy for diabetes management need to test their blood glucose levels at least three times per day using the conventional finger prick method [32, 44, 45]. However, these tests have significant drawbacks such as being uneconomical, unsafe, impractical, painful, laborious, and susceptible to the risk of infection. These drawbacks can be eliminated by using the acetone analysis method from breath. Breath analysis is a powerful tool in medical diagnosis and disease research due to its noninvasive nature and real-time monitoring capability [16, 18, 24, 32–34, 46–48]. Various techniques have been employed to measure acetone concentration for breath analysis, including mass spectrometry (MS), proton transfer reaction by mass spectrometry (PTR-MS), gas chromatography (GC), flame ionization detector (FID), selected ion flow tube mass spectrometry, ion mobility spectrometry (IMS), among others [47, 49–51]. Nonetheless, these sensitive and reliable techniques have certain limitations such as bulky equipment size, high cost, and unsuitability for miniaturization, making them unsuitable for daily diabetes monitoring [52].

An alternative approach to the diagnosis and monitoring of diabetes is the use of sensors for non-invasive and continuous real-time measurement of acetone in breath. This method has the potential to facilitate early treatment and promote effective management of the disease [3, 32]. Chemical sensors have become increasingly popular for breath analysis due to their small size, portability, and ability to provide real-time monitoring at a low cost. In recent years, sensors that are selective, sensitive, stable, robust, and economical have been developed for breath analysis. The advantages of using chemical sensors include ease of use, ease of sampling, and the ability to obtain measurements from unconscious patients [32, 53].

Chemical gas sensors function by changing one or more physical properties, such as mass, electrical conductivity, or dielectric properties when exposed to gas molecules [5]. Chemical gas sensors operate by measuring the change in electrical resistance of the sensing material in the presence of target analytes and translating this chemical information by changing the electrical resistance [5, 54]. Recently, chemical-resistant gas sensors have been developed for the detection of acetone gas, a biomarker of diabetes, from breath [3, 55]. The detection mechanisms of these sensors based on change in electrical resistance of sensing material by the molecular and/or crystalline structure change. The basis for determining the presence of acetone is the reactions between surface oxygen and acetone gas [3, 56]. The performance of these sensors is affected by various features such as surface area, particle size, crystal defects, porous structures, stoichiometry, and morphology [56–58].

In recent years, there has been increasing interest in the development of chemical resistance gas sensors using semiconductor metal oxides for acetone detection. Among the most extensively studied materials for chemical resistance sensors are WO_3, ZnO, SnO_2, Fe_2O_3, In_2O_3, TiO_2, perovskites, and p-type metal oxides. TiO_2, in particular, has proven to be effective in sensing various gases [59]. Furthermore, environmentally friendly perovskites have demonstrated exceptional long-term stability and durability in the detection area due to their stable lattice structure [30, 60–63]. Perovskites such as Pd-doped $SmFeO_3$ [64], $SmFeO_3$/ZnO (p-$SmFeO_3$/n-ZnO) [64], Ni-doped $LaFeO_3$ [65] and Pd-doped $NdFeO_3$ [66] have been investigated, with the gas sensitivity performance of praseodymium ferrite ($PrFeO_3$) receiving particular attention. In one study, Ma et al. (2017) [67] investigated the structure, elemental composition, and morphology of $PrFeO_3$ hollow nanofibers. These nanofibers exhibited a low operating temperature (180 ℃), high response value, good selectivity, fast response recovery, and excellent long-term stability [67]. As such, $PrFeO_3$ hollow nanofibers have the potential to be used in the fabrication of high-performance acetone sensors and represent promising candidates for practical applications. In a subsequent study, Ma et al. (2020) [68] investigated Sm^{3+} doped $PrFeO_3$ to improve the response and recovery process of $PrFeO_3$ gas sensors. Nanofibers have become increasingly relevant in the sensing configuration of biosensors, as their use can reduce sensor size, increase surface energy, and improve sensitivity by increasing specific surface area [69–71]. Conducting polymers, such as polyaniline (PANi), can also be utilized in the sensing configuration of gas sensors [72], where their molecular and macroscopic properties can change when exposed to various chemicals [73]. PANi has been used as a sensing material for gases such as hydrogen (H_2), ammonia (NH_3), nitrogen oxide (NO_2), hydrogen sulfide (H_2S), dimethylamine (DMA), and liquid petroleum gas (LPG) in various forms [74]. Therefore, this study sought to combine conductive polymers, metal oxides, perovskites, and nanofibers to create a unique sensor structure with the advantages of ease of synthesis, good environmental and chemical stability, and improved sensing properties. Specifically, the study employed crystal lattice structured perovskite $PrFeO_3$ nanoparticles on PANi-TiO_2-coated PAN nanofibers to develop an efficient acetone sensor for diabetics, followed by structural, morphological, and electrochemical characterizations.

II. EXPERIMENTAL METHOD

2.1 Materials

Praseodymium (III) nitrate hydrate (99.9%, $Pr(NO_3)_3.H_2O$) (REO, Alfa Aesar, M=326.92 g/mol), Iron (III) nitrate nonahydrate ($Fe(NO_3)_3.9H_2O$) (Sigma Aldrich, Merk, M=403.95 g/mol), Citric acid monohydrate (98%, $C_6H_8O_7.H_2O$) (food grade, Aromel, M=210.14 g/mol) and urea (≥ 99.5%, CH_4N_2O) (Iso-lab) were used for synthesis of perovskite praseodymium ferrite ($PrFeO_3$). Aniline (99%, $C_6H_5NH_2$) (Sigma Aldrich), Ammonium persulfate (≥98%, APS) ($H_8N_2O_8S_2$) (Honeywell / Fluka, M=228.2 g/mol), extra pure hydrochloric acid (30-32%, HCl(aq)) (TEKKİM), Titanium (IV) oxide (≥99.5%, TiO_2) (particle size 21 nm, Sigma Aldrich, M=79.87 g/mol) and ethanol (C_2H_5OH) were used for synthesis of titanium dioxide-doped polyaniline (PANi). Polyacrylonitrile (PAN) (MW=150,000, JK Chemical) and N,N dimethyl formamide (99.9%, DMF) as solvent (Carlo Erba Reagents, M=73.1 g/mol) was used for preparation of PAN nanofiber.

2.2 Methods

2.2.1. Synthesis of Praseodymium Ferrite ($PrFeO_3$), Polyaniline (PANi) and Titanium (IV) oxide (TiO_2)

The $PrFeO_3$ nanoparticles were synthesized using the sol-gel process, which has been previously reported in the literature [75]. To prepare the growth solution at room temperature, a solution containing 0.1 M $Pr(NO_3)_3$ and 0.67 M citric acid was used, and a separate 0.1 M solution of iron (III) nitrate was prepared. $Fe(NO_3)_3$ solution was then added dropwise to the growth solution until the molar ratio of $Pr(NO_3)_3$ to $Fe(NO_3)_3$ in the solution became 1:1. To obtain a gel, 0.5 g of urea was added to the resulting solution, which was stirred in a 50°C water bath for 60 minutes. The gel was then kept at 80°C for 24 hours to obtain the xerogel, which was calcined at 800°C for 5 hours to produce the cinnamon-colored nanoparticles (Figure 1).

Figure 1. Picture of synthesized $PrFeO_3$

For the synthesis of PANi-TiO_2, 3.75 mL of aniline ($C_6H_5NH_2$) as the monomer and a desired amount of TiO_2 (30 wt.%) were added to the mixture and ultrasonicated until the TiO_2 nanoparticles were uniformly dispersed. Then, 2.360 g of ammonium persulfate ($(NH_4)_2S_2O_8$) prepared as an initiator was added dropwise in a cold water bath to the solution obtained by dissolving in 100 mL of 1 M hydrochloric acid (HCl). The solution was kept in a cold water bath under magnetic stirring condition for approximately 24 hours, until the polymerization was completed, resulting in a solution that changed from colorless to blue tones. The solution was filtered by vacuum filtration method, and the resulting PANi was washed twice with water (H_2O) and ethanol (C_2H_5OH), respectively [76]. The dark green precipitate obtained after washing was taken into ethanol, and the concentration of PANi obtained was determined to be 11mg/L. Titanium (IV) oxide was weighed to 30% by mass and added to PANi as a powder. The solid amount in 2.5 mL of PANi/ethanol solution was determined to be 25 mg.

2.2.2. Preparation of Nanofibers and Air-Brush Coating Process

To produce nanofiber solutions, 5% (w%) solid polymer was dissolved in DMF, and after adding $PrFeO_3$, a total of 10 g of polymer solution containing 0%, 5%, 10%, and 20% $PrFeO_3$ was sonicated for 20 minutes. The resultant colloidal solution was covered with aluminum (Al) foil and paraffin tape to protect it from light. The nanofibers were then electrospun in the Nanospinner 24 device (Inovenso, NS24) at 28 kV, 500 rpm, and 175 mm between the nozzle and the collector.

Undoped PAN nanofiber, 5% $PrFeO_3$-added PAN nanofiber, 10% $PrFeO_3$-added PAN nanofiber, and 20%-$PrFeO_3$ added PAN nanofiber were coated with layers of PANi/TiO_2 using an air-brush method to a thickness of a few tens of microns. The coating was carried out by spraying at a pressure of 1-1.5 bar from a distance of 3 cm. The coated nanofibers were dried in a desiccator for approximately 48 hours.

2.2.3. Device fabrication

To construct the acetone sensor, the PANi/TiO_2 layer was coated on electrospun PAN nanofibers doped with $PrFeO_3$. Two copper electrodes were placed on the surface of the nanofiber sensor that was coated with the PANi/TiO_2 layer, with a distance of 1 cm between them. The produced nanofiber sensor was then heated in an oven at 40°C overnight to ensure complete moisture evaporation. The acetone sensing measurement was performed by modifying the following reference [77] in the air. To measure the acetone sensing characteristics, the sensors (Figure 2) were positioned at a distance of 10 cm from the petri dish in the sample holder, with the coated surface facing the acetone. The gas response of the nanofibers, measured as electrical resistance, was used to evaluate the acetone-sensing properties. The initial resistance of the nanofiber sensor was measured without acetone evaporation using a two-probe technique. Subsequently, acetone gas was heated using a hot plate to control acetone evaporation by maintaining a temperature between 50-55 °C, which is close to the acetone evaporation temperature. After 10 seconds, the second electrical resistance was measured.

2.2.4. Characterization

The morphology of $PrFeO_3$ nanoparticles, as well as the undoped and $PrFeO_3$-doped PAN nanofibers, were examined using a scanning electron microscope (SEM) (Carl Zeiss/Gemini 300) at different distances ranging from 8-9 mm and under a voltage of 5 kV. The bound structures of $PrFeO_3$ nanoparticles, undoped and $PrFeO_3$-doped PAN nanofiber structures were analyzed using an FT-IR spectrophotometer (Thermofisher NICOLET–iS50). The sensing measurements of PANi/TiO_2-coated $PrFeO_3$-doped PAN nanofibers were conducted through a two-point resistance measurement test in vitro using a multimeter (Keithley 2400 device).

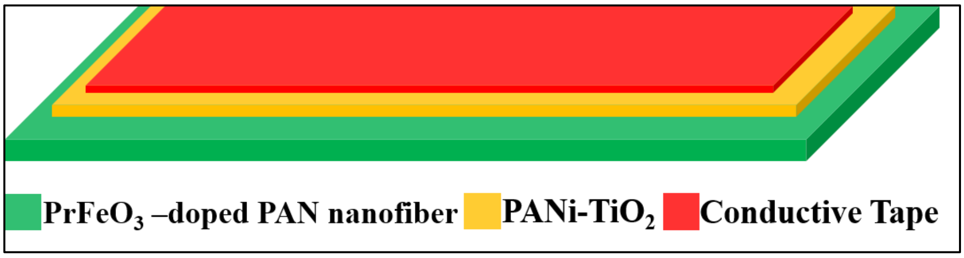

Figure 2. PrFeO3-doped PANi/TiO_2-coated PAN sensor

III. RESULTS AND DISCUSSIONS

3.1 FT-IR Results

The results of the FT-IR analysis of $PrFeO_3$ nanoparticles are presented in Figure 3a. The spectrum revealed prominent absorption peaks at 462 cm^{-1}, which correspond to O-Fe-O bending vibrations, and 530 cm^{-1}, which correspond to Fe-O stretching vibrations [78]. In Figure 3b, the FT-IR spectra of undoped and $PrFeO_3$-doped PAN nanofibers are presented.

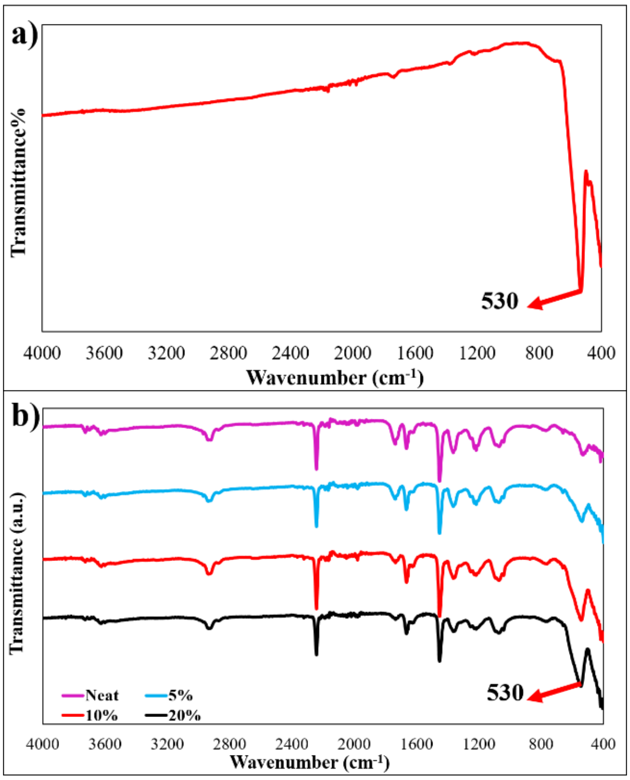

Figure 3. a) FT-IR results of $PrFeO_3$ nanoparticles and b) FT-IR results of undoped and $PrFeO_3$-doped PAN nanofiber structures

The Fe-O stretching peak of $PrFeO_3$ observed at 530 cm^{-1} became more prominent as the $PrFeO_3$ concentration increased, as seen from the FT-IR spectra of the undoped and $PrFeO_3$-doped PAN nanofiber structures. The effect of acetone treatment on powder $PrFeO_3$, undoped PAN nanofiber, and $PrFeO_3$-doped nanofiber was examined by

FT-IR analysis, and it was observed that the structure retained acetone (Figure 4). Although no significant change was observed in the FT-IR spectrum of powder $PrFeO_3$ after acetone treatment, the CO_2-induced peaks that appeared in the calcination range of 1200-1500 cm^{-1} disappeared [78]. In undoped PAN nanofiber, it was observed that the nanofiber porous structure held acetone, and the vibrations of the aliphatic -CH groups at 1217 and 1364 cm^{-1} of the PAN [79] were intensified by combining with the -CH vibrations of the acetone at the same points, indicating that the structure retained acetone.

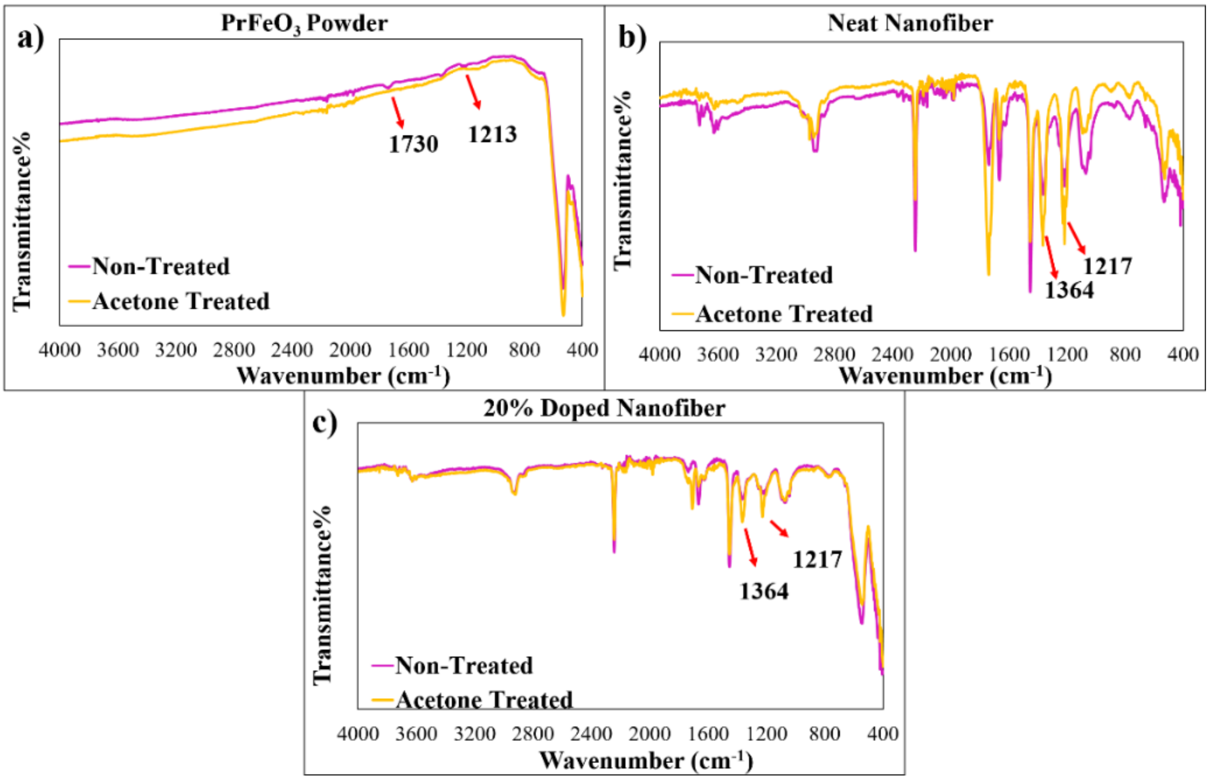

Figure 4. FT-IR spectra of undoped and $PrFeO_3$-doped PAN nanofiber structures

3.2 Morphology

Figure 5 displays SEM images of neat PAN nanofibers and $PrFeO_3$-doped PAN nanofibers before PANi-TiO_2 coating. The SEM images indicate that the nanofibers were formed uniformly with diameters ranging from 200 to 500 nm. Mean Diameters or neat nanofibers and 20% $PrFeO_3$ doped nanofibers were 336 nm and 216 nm, respectively (Figure 5a). Here, main reason that caused to thinning the fibres by nanoparticle loading into electrospinning solution was the decrease in polymer concentration. With the other words, while the polymer concentration was 5% by weight for neat PAN solution, the polymer concentration remained 4% since inorganic was loaded in 20% doped solution. Moreover, $PrFeO_3$ nanoparticles were observed to exist in the PAN nanofiber structure, with some embedded in the fibers and others protruding out of the fiber. The size of the nanoparticles was between 100 and 500 nanometers, and the addition of $PrFeO_3$ nanoparticles led to a decrease in the mean diameter of the PAN nanofibers (Figure 5b). The SEM images indicated that perovskite ($PrFeO_3$) nanoparticles were successfully produced using the sol-gel method. However, it was observed that the crystal particles were fused and sintered together during calcination, resembling coral (Figure 5c). Despite this, the heat treatment synthesis method offers several advantages such as low cost, simplicity, low reaction temperatures, and no waste by-product [63,64,80].

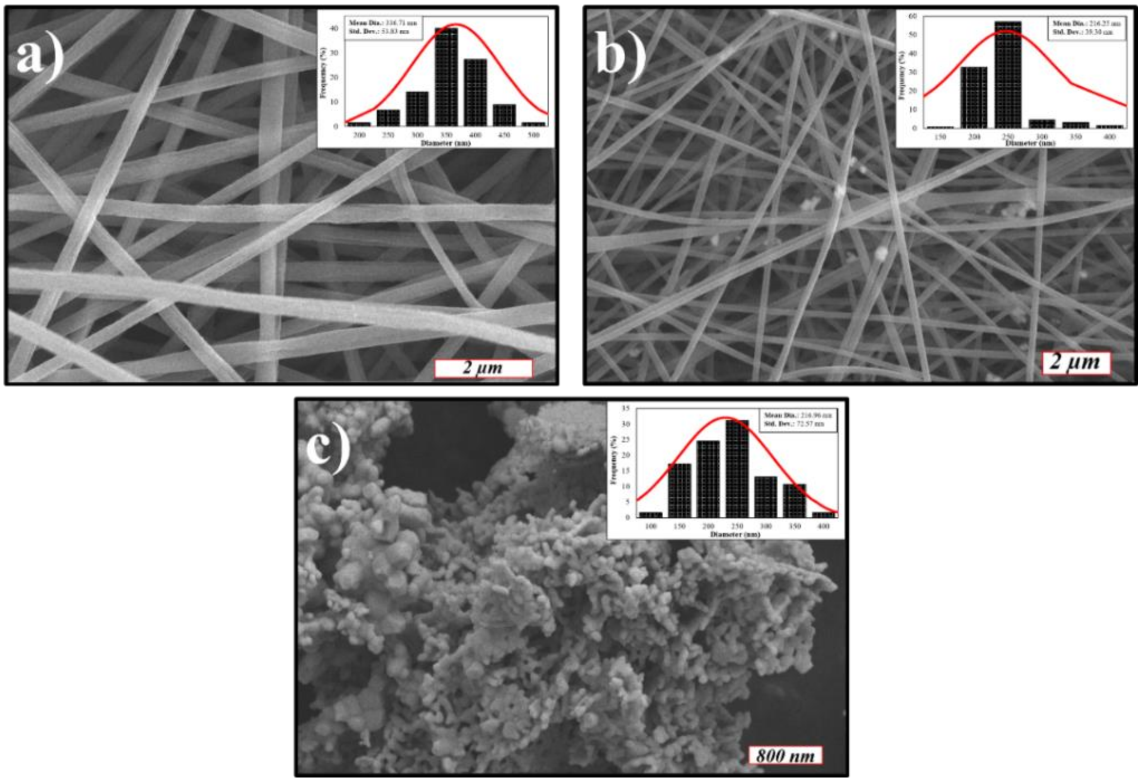

Figure 5. a) Undoped PAN nanofibers - b) 20% $PrFeO_3$-doped PAN nanofibers - c) $PrFeO_3$ nanoparticles

3.3 Sensing Measurements

Air-stable $PrFeO_3$, a perovskite material, possesses desirable sensing properties, including high response, good selectivity, and low operating temperatures, owing to its large specific surface area and abundance of active sites that facilitate gas molecule diffusion and adsorption, thereby enhancing its detection ability [81]. The gas sensing mechanism of $PrFeO_3$ is primarily based on the electrical resistance change before and after exposure to the test gas [67]. The use of electrospun nanofibers with high specific surface area and web-like morphology resulted in high sensing performance, as the target acetone gas molecules could diffuse efficiently into the nanofibers [82]. When the undoped PAN nanofiber sensor was exposed to acetone gas, its electrical resistance increased from 38.86 kΩ to 42 kΩ (Figure 6). Conversely, the electrical resistance of 5%, 10%, and 20% $PrFeO_3$-doped PAN nanofibers increased from 131.52 kΩ to 145.56 kΩ, 156.87 kΩ to 172.35 kΩ, and 508.5 kΩ to 726.6 kΩ, respectively, upon exposure to acetone gas (Figure 6). The observed increase in the ratio of $PrFeO_3$ in the nanofibers correspondingly increased the initial resistance of the sensors compared to the neat nanofibers. The results obtained are consistent with prior studies, which have shown that the electrical resistance of prepared sensors increases upon exposure to acetone gas [67]. Moreover, this increase is below 10% for undoped, 5%, and 10%-doped nanofibers, while the increase is approximately 30% for 20%-doped nanofiber sensors.

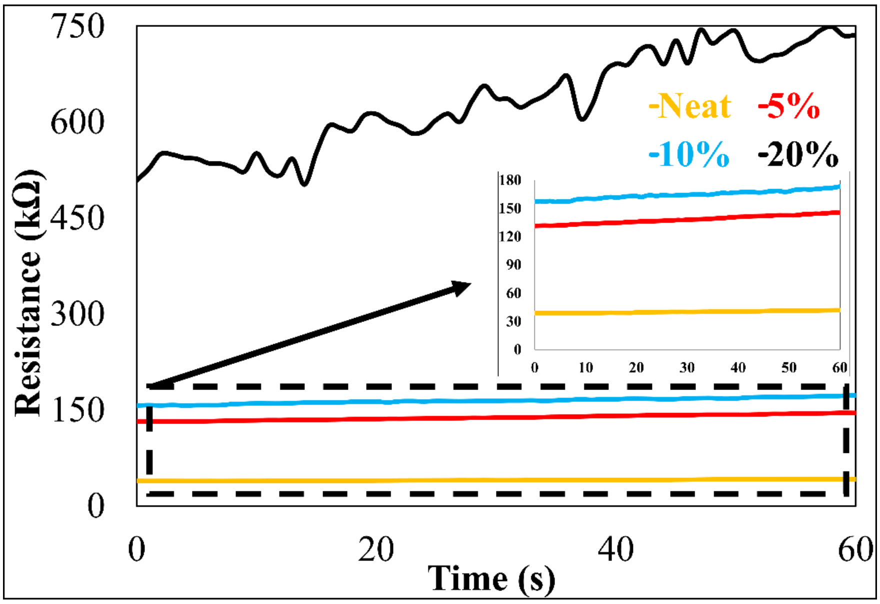

Figure 6. Electrical resistance change of PAN nanofiber sensors during acetone exposure

IV. CONCLUSIONS

In this study, $PrFeO_3$-doped PANi/TiO_2 coated PAN nanofibers were synthesized via a combination of $PrFeO_3$ synthesis, electrospinning of nanofibers, and air-brush coating. SEM images were obtained to confirm the successful synthesis and incorporation of $PrFeO_3$ nanoparticles into the PAN nanofiber structure. The electrical resistance of both doped and undoped nanofiber sensors increased when exposed to acetone gas, with the increase in resistance being more pronounced for doped nanofiber sensors as the amount of $PrFeO_3$ additive increased. Overall, these findings suggest that $PrFeO_3$-doped PANi/TiO_2 coated PAN nanofibers hold significant potential for use as high-performance acetone sensors, and may prove to be promising candidates for non-invasive detection of diabetes.

ACKNOWLEDGMENT

This project was supported under the project application number TUBITAK BIDEB 1139B411901869 within the scope of TUBITAK 2209-B Industry Oriented Research Project Support Programme for Undergraduate Students. This article is based upon work from COST Action “European Network to connect research and innovation efforts on advanced Smart Textiles” (CONTEXT, Ref. CA17107, https://www.context-cost.eu) supported by COST (European Cooperation in Science and Technology, https://www.cost.eu).

REFERENCES

[1] Webber S, International Diabetes Federation - Diabetes Atlas, 10th Edition 2021, 2013. https://doi.org/10.1016/j.diabres.2013.10.013.
[2] World Health Organization, Global Report on Diabetes, Isbn. 978 (2016) 88. https://doi.org/ISBN 978 92 4

156525 7.

[3] Baharuddin AA, Ang BC, Haseeb ASMA, Wong YC, Wong YH (2019) Advances in chemiresistive sensors for acetone gas detection. Materials Science in Semiconductor Processing 103 104616 https://doi.org/10.1016/j.mssp.2019.104616.

[4] Shokrekhodaei M and Quinones S (2020) Review of Non-Invasive Glucose Sensing Techniques. Sensors (Switzerland) 1251 https://sci-hub.scihubtw.tw/10.3390/s20051251

[5] Masikini M, Chowdhury M, Nemraoui O (2020) Review—Metal Oxides: Application in Exhaled Breath Acetone Chemiresistive Sensors. Journal of The Electrochemical Society 167 037537 https://doi.org/10.1149/1945-7111/ab64bc.

[6] Rowley WR, Bezold C, Arikan Y, Byrne E, Krohe S (2017) Diabetes 2030: Insights from Yesterday, Today, and Future Trends. Population Health Management 20 6–12 https://doi.org/10.1089/pop.2015.0181.

[7] Jang C, Park JK, Lee HJ, Yun GH, Yook JG (2018) Temperature-corrected fluidic glucose sensor based on microwave resonator. Sensors (Switzerland) 18 1–12 https://doi.org/10.3390/s18113850.

[8] Classification and diagnosis of diabetes: Standards of medical care in Diabetes-2018, Diabetes Care. 41 (2018) S13–S27. https://diabetesjournals.org/care/article/41/Supplement_1/S13/30088/2-Classification-and-Diagnosis-of-Diabetes

[9] Köksal Atış Ş and Önder A (2020) Yeni Tanı Diyabetes Mellitus Hastalarında Sınıflandırma ve Tedavi Yönetimi. Hitit Medical Journal 3 (2020) 62–66

[10] WHO, Use of Glycated Haemoglobin (HbA1c) in the Diagnosis of Diabetes Mellitus: Abbreviated Report of a WHO Consultation. Approved by the Guidelines Review Committee., World Health Organization. (2011) 299–309.

[11] I. Classification, Standards of medical care in diabetes-2014, Diabetes Care. 37 (2014) 14–80. https://doi.org/10.2337/dc14-S014.

[12] Abacı A, Böber E, Büyükgebiz A (2007) Tip 1 Diyabet. Güncel Pediatri 5 1–10 https://dergipark.org.tr/en/pub/pediatri/667492.

[13] Mishra BK (2013) Chemistry of Diabetes and its Impact. Academic Voices: A Multidisciplinary Journal 2 16–22 https://doi.org/10.3126/av.v2i1.8279.

[14] Yuan Y, Chen Z, Zhao X, Sun M, Li Y, Wang Z, Wang C (2017) Continuous Monitoring of Breath Acetone, Blood Glucose and Blood Ketone in 20 Type 1 Diabetic Outpatients Over 30 Days. Journal of Analytical & Bioanalytical Techniques 08 https://doi.org/10.4172/2155-9872.1000386.

[15] Güntner AT, Kompalla JF, Landis H, Theodore SJ, Geidl B, Sievi NA, Kohler M, Pratsinis SE, Gerber PA (2018) Guiding ketogenic diet with breath acetone sensors. Sensors (Switzerland) 18 1–12 https://doi.org/10.3390/s18113655

[16] Wang C, Mbi A, Shepherd M (2010)A study on breath acetone in diabetic patients using a cavity ringdown breath analyzer: Exploring correlations of breath acetone with blood glucose and glycohemoglobin A1C. IEEE Sensors Journal 10 54–63 https://doi.org/10.1109/JSEN.2009.2035730

[17] Musa-Veloso K, Likhodii SS, Rarama E, Benoit S, Liu YMC, Chartrand D, Curtis R, Carmant L, Lortie A, Comeau FJE, Cunnane SC (2006) Breath acetone predicts plasma ketone bodies in children with epilepsy on a ketogenic diet. Nutrition 22 1–8 https://doi.org/10.1016/j.nut.2005.04.008

[18] Puchalska P and Crawford PA (2017) Multi-dimensional Roles of Ketone Bodies in Fuel Metabolism, Signaling, and Therapeutics. Cell Metabolism 25 262–284 https://doi.org/10.1016/j.cmet.2016.12.022

[19] Güntner AT, Sievi NA, Theodore SJ, Gulich T, Kohler M, Pratsinis SE (2017) Noninvasive Body Fat Burn Monitoring from Exhaled Acetone with Si-doped WO3-sensing Nanoparticles. Analytical Chemistry 89 10578–10584 https://doi.org/10.1021/acs.analchem.7b02843

[20] Wang Z and Wang C (2013) Is breath acetone a biomarker of diabetes? A historical review on breath acetone measurements. Journal of Breath Research 7 https://doi.org/10.1088/1752-7155/7/3/037109

[21] Bovey F, Cros J, Tuzson B, Seyssel K, Schneiter P, Emmenegger L, Tappy L (2018) Breath acetone as a marker of energy balance: an exploratory study in healthy humans. Nutrition and Diabetes 8 https://doi.org/10.1038/s41387-018-0058-5

[22] Afreen S and Zhu JJ (2019) Rethinking EBAD: Evolution of smart noninvasive detection of diabetes. TrAC - Trends in Analytical Chemistry 118 477–487 https://doi.org/10.1016/j.trac.2019.06.011

[23] Konvalina G and Haick H (2014) Sensors for Breath Testing : From Nanomaterials to Comprehensive Disease Sensors for Breath Testing : From Nanomaterials to Comprehensive Disease Detection. Accounts of Chemical Research 47 1 66-76 https://doi.org/10.1021/ar400070m

[24] Rydosz A (2018) Sensors for enhanced detection of acetone as a potential tool for noninvasive diabetes monitoring. Sensors (Switzerland) 18 (2018) 1–14 https://doi.org/10.3390/s18072298

[25] Rydosz A (2015) A negative correlation between blood glucose and acetone measured in healthy and type 1 diabetes mellitus patient breath. Journal of Diabetes Science and Technology 9 881–884 https://doi.org/10.1177/1932296815572366

[26] Diskin AM, Španěl P, Smith D (2003) Time variation of ammonia, acetone, isoprene and ethanol in breath:

A quantitative SIFT-MS study over 30 days. Physiological Measurement 24 107–119 https://doi.org/10.1088/0967-3334/24/1/308

[27] Wang X, Qin H, Pei J, Chen Y, Li L, Xie J, Hu J (2016)Sensing performances to low concentration acetone for palladium doped LaFeO3 sensors. Journal of Rare Earths 34 704–710. https://doi.org/10.1016/S1002-0721(16)60082-0.

[28] Amann A and Smith D (2013) Volatile Biomarkers: Non-Invasive Diagnosis in Physiology and Medicine. Elsevier. https://doi.org/10.1016/C2012-0-01274-4

[29] Deng C, Zhang J, Yu X, Zhang W, Zhang X (2004) Determination of acetone in human breath by gas chromatography–mass spectrometry and solid-phase microextraction with on-fiber derivatization. Journal of Chromatography B 810 269–275 https://doi.org/10.1016/j.jchromb.2004.08.013

[30] Fergus JW, (2007)Perovskite oxides for semiconductor-based gas sensors. Sensors and Actuators B: Chemical 123 1169–1179 https://doi.org/10.1016/j.snb.2006.10.051

[31] Shankar P and Rayappan JBB (2015) Gas sensing mechanism of metal oxides: The role of ambient atmosphere, type of semiconductor and gases - A review. Science Letters Journal 4 126 http://www.cognizure.com/scilett.aspx?p=200638572

[32] Minh TDC, Blake DR, Galassetti PR (2012) The clinical potential of exhaled breath analysis for diabetes mellitus. Diabetes Research and Clinical Practice 97 195–205. https://doi.org/10.1016/j.diabres.2012.02.006

[33] Miekisch W, Schubert JK, Noeldge-Schomburg GFE (2004) Diagnostic potential of breath analysis - Focus on volatile organic compounds. Clinica Chimica Acta 347 25–39 https://doi.org/10.1016/j.cccn.2004.04.023

[34] Lourenço C and Turner C (2014) Breath Analysis in Disease Diagnosis: Methodological Considerations and Applications. Metabolites 4 465–498 https://doi.org/10.3390/metabo4020465

[35] Li J, Smeeton TM, Zanola M, Barrett J, Berryman-Bousquet V (2018) A compact breath acetone analyser based on an ultraviolet light emitting diode. Sensors and Actuators B: Chemical 273 76–82 https://doi.org/10.1016/j.snb.2018.05.114

[36] Prabhakar A, Quach A, Zhang H, Terrera M, Jackemeyer D, Xian X, Tsow F, Tao N, Forzani ES (2015) Acetone as biomarker for ketosis buildup capability - A study in healthy individuals under combined high fat and starvation diets. Nutrition Journal 14 https://doi.org/10.1186/s12937-015-0028-x

[37] King J, Kupferthaler A, Unterkofler K, Koc H, Teschl S, Teschl G, Miekisch W, Schubert J, Hinterhuber H, Amann A (2009) Isoprene and acetone concentration profiles during exercise on an ergometer Journal of Breath Research 3 027006 https://doi.org/10.1088/1752-7155/3/2/027006

[38] Blaikie TPJ, Edge JA, Hancock G, Lunn D, Megson C, Peverall R, Richmond G, Ritchie GAD, Taylor D (2014) Comparison of breath gases, including acetone, with blood glucose and blood ketones in children and adolescents with type 1 diabetes. Journal of Breath Research 8 046010 https://doi.org/10.1088/1752-7155/8/4/046010

[39] Do JS and Wang SH (2013) On the sensitivity of conductimetric acetone gas sensor based on polypyrrole and polyaniline conducting polymers. Sensors and Actuators B: Chemical 185 39–46 https://doi.org/10.1016/j.snb.2013.04.080

[40] Liu S, Zhang F, Li H, Chen T, Wang Y (2012) Acetone detection properties of single crystalline tungsten oxide plates synthesized by hydrothermal method using cetyltrimethyl ammonium bromide supermolecular template. Sensors and Actuators B: Chemical 162 259–268 https://doi.org/10.1016/j.snb.2011.12.076

[41] Huang Z, Zhang A, Zhang Q, Pan S, Cui D (2019) Electrochemical Biosensor Based on Dewdrop-Like Platinum Nanoparticles-Decorated Silver Nanoflowers Nanocomposites for H 2 O 2 and Glucose Detection. Journal of The Electrochemical Society 166 B1138–B1145 https://doi.org/10.1149/2.0471913JES/XML

[42] Staden RIS, Popa-Tudor I, Ionescu-Tirgoviste C, Stoica RA, Magerusan L (2019) Molecular Enantiorecognition of D- and L-Glucose in Urine and Whole Blood Samples. Journal of The Electrochemical Society 166 B3109–B3115 https://doi.org/10.1149/2.0211909JES/XML

[43] IDF, Eighth edition 2017, 2017. https://www.idf.org/aboutdiabetes/type-2-diabetes.html.

[44] Makaram P, Owens D, Aceros J (2014) Trends in Nanomaterial-Based Non-Invasive Diabetes Sensing Technologies. Diagnostics 4 27–46 https://doi.org/10.3390/diagnostics4020027

[45] Standards of medical care in diabetes-2010, Diabetes Care. 33 (2010). https://doi.org/10.2337/dc10-S011.

[46] Alonso M and Sanchez JM (2013) Analytical challenges in breath analysis and its application to exposure monitoring. TrAC - Trends in Analytical Chemistry 44 78–89 https://doi.org/10.1016/j.trac.2012.11.011

[47] Rooth G and Ostenson S (1966) Acetone in alveolar air, and the control of diabetes. Lancet 2 1102–1105. https://doi.org/10.1016/s0140-6736(66)92194-5

[48] Tassopoulos CN, Barnett D, Fraser TR (1969) Breath-acetone and blood-sugar measurements in diabetes. Lancet 293 1282–1286 https://doi.org/10.1016/s0140-6736(69)92222-3

[49] Kim KH, Jahan SA, Kabir E (2012) A review of breath analysis for diagnosis of human health. TrAC - Trends in Analytical Chemistry 33 1–8 https://doi.org/10.1016/j.trac.2011.09.013

[50] Kupferthaler A, King J, Amann A, Hinterhuber H, Hackner H, Hogl B (2010) Acetone and isoprene concentration profiles in normal human sleep. Memo - Magazine of European Medical Oncology 3 6–7

http://ovidsp.ovid.com/ovidweb.cgi?T=JS&PAGE=reference&D=emed11&NEWS=N&AN=70264318

[51] Saasa V, Malwela V, Beukes M, Mokgotho M, Liu CP, Mwakikunga B (2018) Sensing Technologies for Detection of Acetone in Human Breath for Diabetes Diagnosis and Monitoring. Diagnostics 8 12 https://doi.org/10.3390/diagnostics8010012

[52] Tomer VK, Singh K, Kaur H, Shorie M, Sabherwal P (2017) Rapid acetone detection using indium loaded WO3/SnO2 nanohybrid sensor. Sensors and Actuators B: Chemical 253 703–713 https://doi.org/10.1016/j.snb.2017.06.179

[53] Hung CM, Le DTT, Van Hieu N (2017) On-chip growth of semiconductor metal oxide nanowires for gas sensors: A review. Journal of Science: Advanced Materials and Devices 2 263–285 https://doi.org/10.1016/j.jsamd.2017.07.009

[54] Wong YC, Ang BC, Haseeb ASMA, Baharuddin AA, Wong YH (2020) Review—Conducting Polymers as Chemiresistive Gas Sensing Materials: A Review. Journal of The Electrochemical Society 167 037503 https://doi.org/10.1149/2.0032003jes

[55] Righettoni M, Amann A, Pratsinis SE (2015) Breath analysis by nanostructured metal oxides as chemo-resistive gas sensors. Materials Today 18 163–171 https://doi.org/10.1016/j.mattod.2014.08.017

[56] Korotcenkov G (2007) Metal oxides for solid-state gas sensors: What determines our choice?. Materials Science and Engineering B: Solid-State Materials for Advanced Technology 139 1–23 https://doi.org/10.1016/j.mseb.2007.01.044

[57] Wetchakun K, Samerjai T, Tamaekong N, Liewhiran C, Siriwong C, Kruefu V, Wisitsoraat A, Tuantranont A, Phanichphant S (2011) Semiconducting metal oxides as sensors for environmentally hazardous gases. Sensors and Actuators B: Chemical 160 580–591 https://doi.org/10.1016/j.snb.2011.08.032

[58] Li SM, Zhang LX, Zhu MY, Ji GJ, Zhao LX, Yin J, Bie LJ (2017) Acetone sensing of ZnO nanosheets synthesized using room-temperature precipitation. Sensors and Actuators B: Chemical 249 611–623 https://doi.org/10.1016/j.snb.2017.04.007

[59] Navale ST, Yang ZB, Liu C, Cao PJ, Patil VB, Ramgir NS, Mane RS, Stadler FJ (2018) Enhanced acetone sensing properties of titanium dioxide nanoparticles with a sub-ppm detection limit. Sensors and Actuators B: Chemical 255 1701–1710 https://doi.org/10.1016/j.snb.2017.08.186

[60] Giang HT, Duy HT, Ngan PQ, Thai GH, Thu DTA, Thu DT, Toan NN (2011) Hydrocarbon gas sensing of nano-crystalline perovskite oxides LnFeO 3 (Ln = La, Nd and Sm). Sensors and Actuators B: Chemical 158 246–251 https://doi.org/10.1016/j.snb.2011.06.013

[61] Song P, Wang Q, Zhang Z, Yang Z (2010) Synthesis and gas sensing properties of biomorphic LaFeO3 hollow fibers templated from cotton. Sensors and Actuators B: Chemical 147 248–254 https://doi.org/10.1016/j.snb.2010.03.006

[62] Fan K, Qin H, Wang L, Ju L, Hu J (2013) CO2 gas sensors based on La1-xSrxFeO 3 nanocrystalline powders. Sensors and Actuators B: Chemical 177 265–269 https://doi.org/10.1016/j.snb.2012.11.004

[63] Naseri M and Ghasemi R (2016) Structure and physical properties of Fe6 O8/ba Fe6 O11 nanostructure. Journal of Magnetism and Magnetic Materials 406 200–206 https://doi.org/10.1016/j.jmmm.2016.01.019

[64] Anajafi Z, Naseri M, Neri G (2020) Acetone sensing behavior of p-SmFeO3/n-ZnO nanocomposite synthesized by thermal treatment method. Sensors and Actuators B: Chemical 304 https://doi.org/10.1016/j.snb.2019.127252

[65] Hao P, Lin Z, Song P, Yang Z, Wang Z (2020) Hydrothermal preparation and acetone-sensing properties of Ni-doped porous LaFeO3 microspheres. Journal of Materials Science: Materials in Electronics 31 6679–6689 https://doi.org/10.1007/s10854-020-03224-x

[66] Zhang YH, Li YL, Gong FL, Xie KF, Liu M, Zhang HL, Fang SM (2020) Al doped narcissus-like ZnO for enhanced NO2 sensing performance: An experimental and DFT investigation. Sensors and Actuators B: Chemical 305 127489 https://doi.org/10.1016/j.snb.2019.127489

[67] Ma L, Ma SY, Shen XF, Wang TT, Jiang XH, Chen Q, Qiang Z, Yang HM, Chen H (2018) PrFeO3 hollow nanofibers as a highly efficient gas sensor for acetone detection. Sensors and Actuators B: Chemical 255 2546–2554 https://doi.org/10.1016/j.snb.2017.09.060

[68] Pei S, Ma S, Xu X, Xu X, Almamoun O (2021) Modulated PrFeO3 by doping Sm3+ for enhanced acetone sensing properties. Journal of Alloys and Compounds 856 158274 https://doi.org/10.1016/j.jallcom.2020.158274

[69] Bulut U, Oyku Sayin V, Altin Y, Can Cevher S, Cirpan A, Celik Bedeloglu A, Soylemez S (2023) A flexible carbon nanofiber and conjugated polymer-based electrode for glucose sensing. Microchemical Journal 184 108148. https://doi.org/10.1016/j.microc.2022.108148

[70] Virji S, Huang J, Kaner RB, Weiller BH (2004) Polyaniline nanofiber gas sensors: Examination of response mechanisms. Nano Letters 4 491–496 https://doi.org/10.1021/nl035122e

[71] Ding B, Wang M, Yu J, Sun G (2009) Gas sensors based on electrospun nanofibers. Sensors 9 1609–1624 https://doi.org/10.3390/s90301609

[72] Gupta N, Sharma S, Mir IA, Kumar D (2006) Advances in sensors based on conducting polymers. Journal

of Scientific and Industrial Research 65 549–557

[73] Wang Y, Liu A, Han Y, Li T (2020) Sensors based on conductive polymers and their composites: a review. Polymer International 69 7–17 https://doi.org/10.1002/pi.5907

[74] Pirsa S (2017) Chemiresistive gas sensors based on conducting polymers. In Khosrow-Pour M (ed) Materials Science and Engineering: Concepts, Methodologies, Tools, and Applications, Engineering Science Reference, 1–3, pp. 543–574 https://doi.org/10.4018/978-1-5225-1798-6.ch022

[75] Tang P, Xie X, Chen H, Lv C, Ding Y (2019) Synthesis of Nanoparticulate PrFeO3 by Sol–Gel Method and its Visible-Light Photocatalytic Activity. Ferroelectrics 546 181–187 https://doi.org/10.1080/00150193.2019.1592470

[76] Jin LN, Shao F, Jin C, Zhang JN, Liu P, Guo MX, Bian SW (2017) High-performance textile supercapacitor electrode materials enhanced with three-dimensional carbon nanotubes/graphene conductive network and in situ polymerized polyaniline. Electrochimica Acta 249 387–394 https://doi.org/10.1016/j.electacta.2017.08.035

[77] Kim NH, Choi SJ, Kim SJ, Cho HJ, Jang JS, Koo WT, Kim M, Kim ID (2016) Highly sensitive and selective acetone sensing performance of WO3 nanofibers functionalized by Rh2O3 nanoparticles. Sensors and Actuators B: Chemical 224 185–192 https://doi.org/10.1016/j.snb.2015.10.021

[78] Tijare SN, Bakardjieva S, Subrt S, Joshi MV, Rayalu SS, Hishita S, Labhsetwar N (2014) Synthesis and visible light photocatalytic activity of nanocrystalline PrFeO 3 perovskite for hydrogen generation in ethanol-water system. Journal of Chemical Sciences 126 517–525 https://doi.org/10.1007/s12039-014-0596-x

[79] Altin Y and Celik Bedeloglu (2021) A Polyacrylonitrile/polyvinyl alcohol-based porous carbon nanofiber electrodes for supercapacitor applications. International Journal of Energy Research 45 16497–16510 https://doi.org/10.1002/ER.6896

[80] Chireh M and Naseri M (2019) Effect of calcination temperature on the physical properties of LiFe 5 O 8 nanostructures. Advanced Powder Technology 30 952–960 https://doi.org/10.1016/j.apt.2019.02.009

[81] Zhang H, Xiao J, Chen J, Zhang L, Zhang Y, Jin P (2022) Au modified PrFeO3 with hollow tubular structure can be efficient sensing material for H2S detection. Frontiers in Bioengineering and Biotechnology 10 1–12 https://doi.org/10.3389/fbioe.2022.969870

[82] Mirzaei A, Majhi SM, Kim HW, Kim SS (2022) Metal oxide-based nanofibers and their gas-sensing applications. In Esposito V and MArani D (ed) Metal Oxide-Based Nanofibers and Their Applications, Elsevier, pp. 139–158 https://doi.org/10.1016/B978-0-12-820629-4.00008-4

J. Innovative Eng. Nat. Sci., c. 3, s. 2, ss. 167-190, 2023.
http://dx.doi.org/10.29228/JIENS.70514

Journal of Innovative Engineering and Natural Science
(Yenilikçi Mühendislik ve Doğa Bilimleri Dergisi)
journal homepage: https://jiens.org

Araştırma Makalesi

Gaziantep banliyö projesi (Gaziray) raylı sistem hattı tünellerinde olası tren yangını durumunda tünel acil durum havalandırma sisteminin simülasyonu

Çiğdem Avcı Karataş[a,*]

[a] *Department of Transportation Engineering, Faculty of Engineering, Yalova University, 77200, Yalova, Turkey*

MAKELE BİLGİSİ

Makale Geçmişi:
Geliş 07 Haziran 2023
Düzeltme 20 Haziran 2023
Kabul 10 Temmuz 2023

Çevrimiçi mevcut

Anahtar Kelimeler:
Raylı sistemler
Tüneller
Yapısal yangın güvenliği
Gaziray
Simülasyon
CFD Modelleme
Risk analizi

ÖZET

Raylı sistemler, hızlı, güvenli ve çevre dostu bir toplu taşıma seçeneği olarak dünya genelinde aktif olarak kullanılmaktadırlar. Gaziantep banliyö projesi (Gaziray) Raylı Sistem Hattı, Türkiye'nin Gaziantep şehrinde, toplu taşıma ihtiyacını karşılamak amacıyla planlanan bir proje olarak büyük önem taşımaktadır. Raylı sistem hatlarında, tren yangınları gibi potansiyel olası tehlikelerin dikkate alınması ve yangının etkilerinin değerlendirilmesi çok önemlidir. Yangınlar, trenlerin elektrikli ve mekanik bileşenlerinde, örneğin; elektrik kablolarının aşırı ısınması, fren sistemlerinde arızalar, yakıt sızıntıları gibi sebeplerle çeşitli nedenlerle ortaya çıkabilmektedirler. Bu tür yangınlar, tünellerde, tünelin duvar, tavan, taban ve diğer yapısal elemanlara zarar verebilecek özellikte tehlikeli sonuçlara yol açabileceğinden, tünel yapısının yangından etkilenme seviyesi ve böylelikle yangının tünel yapısına verdiği zararın dikkatlice değerlendirilmesi gerekmektedir. Yangın sonrası, tünelin kullanılabilirliğini, güvenliğini ve yapısal bütünlüğünü etkileyen yapısal hasarlar, tünelin onarım maliyetlerini ve işletme süreçlerini de etkileyebilmektedir. Tünel yangınlarının etkilerini değerlendirmek için yangın testleri, modelleme ve benzetimler/simülasyonlar gibi yöntemler kullanılmaktadır. Yangın testleri, gerçek yangın senaryolarını taklit ederek tünel yapısının yangına karşı tepkisini belirleyebilmekte, modelleme ve simülasyonlar ise tünel yapısının yangından etkilenme seviyesini belirlemektedir. Bu çalışmanın amacı, Gaziray Raylı Sistem Hattında bulunan tünellerde meydana gelebilecek olası tren yangını durumunda, tünel yapısının yangından etkilenme seviyesi ve bu etkinin değerlendirilmesidir. Kritik hız; yangın esnasında ortaya çıkan duman ve yanma ürünü zehirli gazların ters katmanlaşmadan istenilen yöne itilmesi için gerekli olan minimum hava hızıdır. Çalışmada, yapısal bütünlüğün bozulmadan, çevresel kontrol sistemlerinin çalışmasına olanak sağlayarak ve insan tahliye yönünün ters yönünde kritik hava hızı sağlanarak; gerekli havalandırma stratejisi ve kapasitesinin belirlenmesi hedefi gerçekleştirilmiştir.

Simulation of the tunnel emergency ventilation system in the event of a potential train fire in the tunnels of the Gaziray Railway System Line

ARTICLE INFO

Article history:
Received
Received in revised form
Accepted

Available online

Keywords:
Railway systems
Tunnels
Structural fire safety
Gaziray
Simulation
CFD Modeling
Risk analysis

ABSTRACT

Rail systems are actively used worldwide as a fast, safe, and environmentally friendly public transportation option. The Gaziray Rail System Line is a project of great importance planned to meet the public transportation needs in Gaziantep, Turkey. In rail system lines, it is crucial to consider potential hazards such as train fires and evaluate the effects of fire. Fires can occur for various reasons in the electrical and mechanical components of trains, such as overheating of electrical cables, malfunctions in braking systems, fuel leaks, and so on. Such fires can cause dangerous consequences that can damage the tunnel's walls, ceiling, floor, and other structural elements, so the level of the tunnel's susceptibility to fire and the damage it causes to the tunnel structure must be carefully evaluated. Structural damages that affect the tunnel's usability, safety, and integrity after a fire can also affect repair costs and operational processes. Methods such as fire tests, modelling, and simulations are used to assess the effects of tunnel fires. Fire tests can determine the tunnel structure's response to fire by simulating real fire scenarios, while modelling and simulations determine the level of the tunnel structure's susceptibility to fire. The purpose of this study is to evaluate the level of damage to the tunnel structure and its effects in the event of a possible train fire in the tunnels of the Gaziray Rail System Line. The critical speed is the minimum airspeed required to push smoke and toxic combustion products in the desired direction without stratification during a fire. The study aims to determine the necessary ventilation strategy and capacity to provide critical airspeed in the opposite direction of human evacuation while enabling the environmental control systems to operate without compromising the structural integrity.

---

*Sorumlu yazar. Tel.: +90-226-815-5963; e-mail: cigdem.karatas@yalova.edu.tr

I. GİRİŞ

Toplu taşıma sektöründe özellikle büyük şehirlerdeki trafik sorunlarını çözmede, raylı sistemler önemli bir rol oynamaktadır. Raylı sistemler, insanları ve yükleri hızlı, güvenli, konforlu ve çevre dostu bir şekilde taşımak için kullanılan toplu taşıma araçları olup, modern şehirlerin ulaşım ihtiyaçlarını karşılamak için son derece önemli bir ulaşım bileşenidir. Raylı sistemlerin birçok avantajı bulunmaktadır. Bu sistemler, öncelikle, bu sistemler yüksek hızlı ve düzenli bir hizmet sunarken, kara yolu trafiği sorunlarından kaynaklanan gecikmelerin ve zaman kayıplarının önüne geçmektedirler. Ayrıca, bu sistemlerin düşük maliyetli işletme ve bakım maliyetleri bulunmaktadır. Çevreye duyarlı bir ulaşım seçeneği olmaları nedeniyle raylı sistemler, aynı zamanda, karbon ayak izini azaltmaya yardımcı olmaktadırlar. Farklı türlerde raylı sistemler mevcuttur; hafif raylı sistemler, metro hatları, tramvaylar ve tren hatları, vb. Her bir tür, farklı özellikleri ve avantajları ile birbirinden farklıdır. Örneğin, hafif raylı sistemler, düşük maliyetli bir seçenek olarak bilinirken, metro hatları yüksek kapasiteli ve yüksek hızlı bir hizmet sunmaktadırlar.

Raylı sistem tünelleri/demiryolu tünelleri, modern şehirlerde toplu taşıma araçlarının güvenli bir şekilde seyahat etmesini sağlayan kritik bir altyapı bileşenidir. Tünellerin bir ülkenin ulaşım altyapı ağının ayrılmaz bir bileşeni olduğu, bu nedenle tünellerin iyi durumda çalışmasının yaşamı, çevreyi tehdit edebilecek her türlü etkiye karşı düzenli olarak kesintisiz olarak sürekli bakımlarının yapılması gerekmektedir. Tünellerin tasarımı ve inşası zorlu bir süreç olup şehirlerde trafik akışını düzenlemek ve toplu taşıma hizmetlerini daha güvenli ve verimli hale getirmek için önem arz etmektedir. Demiryolu ve karayolu tünelleri arasında dikkate alınması gereken önemli farklılıklar bulunmaktadır [1]. Tünelin uzunluğu, derinliği, eğimi ve yönü gibi faktörler, inşaat maliyetleri ve tünelin dayanıklılığı açısından önemliyken, tünellerin tasarımı, tünelin içindeki hava kalitesini ve havalandırma sistemlerini de dikkate almaktadır. Tünellerdeki yangın riski, hava kalitesi ve güvenliği açısından önemli bir faktördür ve bu nedenle tünellerde yangın önleme ve söndürme sistemleri dikkatle tasarlanmalıdır.

Tüneller, kaza ve olağanüstü yük olayları gibi istisnai yükleme olaylarına maruz kalabileceği 120 yıl boyunca hizmet vermek üzere tasarlanmıştır [2]. Tünel hattı boyunca meydana gelebilecek risk seviyesi en yüksek kazalardan biri olan yangın insan kaynaklı bir felakettir [3-8]. Yangın durumunda, tünel içindeki sıcaklık çok kısa bir süre içinde hızlı bir şekilde artabilmektedir. Bir yangın tarafından üretilen ısı, doğrudan yangın kaynağında 1200 °C'ye, tünelin üst kısmındaki havada 900 °C'ye ve en sıcak duman bölümlerinde 500–600 °C'ye kadar ulaşabildiği gözlemlenmiştir [9, 10]. Kaplama ve zeminin (özellikle yer altı suyu mevcutsa) ısı akış özellikleri, kaplamadaki gerçek sıcaklık dağılımını büyük ölçüde etkileyecektir. Yanma, ısı, yakıt ve oksijenin doğru oranlarda birleşmesiyle başlayan bir reaksiyondur. Kontrolsüz yanma ise yangın olarak adlandırılır. Yanma sırasında, alevin, yakıtın ve çevrenin etkileşimi esasen doğrusal değildir. Malzeme tünel gibi kapalı bir ortamda yanarsa, iki ana parametre yangın gücünü ve yangın hızını etkileyecektir. Bunlardan ilk parametre; kapalı ortamın ısınmasıdır. Bu durum, kapalı ortamda yükselen sıcak hava birikmesine neden olacaktır. Böylece, yüzeyler ve sıcak gaz tabakası ışınım yoluyla yakıt yüzeyine ısı transferi yaparak yanmayı hızlandıracaktır. İkinci parametre; ortam havasının girebileceği sınırlı alanlardan dolayı yanma için gereken oksijenin kısıtlanmasıdır. Böylece, maddenin yanma hızı ve çevreye verdiği ısı miktarı azalacak ve gazın yanma hızı artacaktır. "Kapalı alan yangını" terimi, kapalı bir alanda meydana gelen yangın için kullanılan bir terimdir. Tünelde meydana gelen yangınlar kapalı alan yangınları olarak sınıflandırılmaktadır (Şekil 1). Tünellerin kapalı yapısı, raylı sistem araçlarının doğal engellerden etkilenmesini ve hava koşullarından zarar görmesini önlerken, diğer taraftan, olası bir yangın durumunda meydana gelebilecek tüm olumsuzluklara karşın gerekli tedbirlerin alınması son derece önemlidir.

Şekil 1. Bolu Dağı Tüneli içerisindeki yangın [11]

Tünel yangınlarına karşı yangın algılama ve alarm sistemleri 1960'lardan bu yana kullanılmaktadır, ancak özellikle 1999–2001 yılları arasında Avrupa'da meydana gelen tünel kazaları, tünel güvenlik sistemlerinin önemini artırmıştır. Özellikle son yıllarda, teknolojinin gelişmesiyle birlikte, olası bir yangını erken teşhis edebilen ve acil durum yönetimini eşzamanlı olarak sağlayabilen yangın algılama sistemleri üretilmiş ve kullanılmaktadır [12]. Öte yandan tünel yangınlarının erken teşhisi ve kontrolü, tünel yangın direnci ve teknik altyapının iyileştirilmesi gibi konularda gerekli çalışmalar hızlandırılmıştır [13-17]. Tünel güvenliği konusu, dünya çapında meydana gelen bir dizi büyük yangın nedeniyle de acil eylem planı içerisine alınmıştır. 1996, 2006 ve 2008 yıllarında üç büyük önemli yangın geçiren "*The Channel Tunnel*"-Fransa [18], yaşanan bu yangınlardan dolayı önemli yapısal hasarlar almıştır. Diğer demiryolu tünel yangınları arasında "*The Summit Tunnel*"-İngiltere yangını (1984), "*The Great Belt Tunnel*"-Danimarka TBM yangını (1994), Daegu metrosu-Güney Kore yangını (182 ölü), ve 2000 yılında Avusturya'nın Kaprun'daki füniküler demiryolu tünel yangını (155 ölü) yer almaktadır [19]. Meydana gelen bu yangınlara yanıt olarak, tünel yangını güvenliği konularının araştırılarak, yeni uygulama konuları önermek için bir dizi uluslararası girişimler başlatılmıştır [20].

Tünel yangınlarıyla ilgili olarak birçok araştırma yapılmış ve bu konuda literatür oldukça geniş bir yelpazede sunulmaktadır [21-29]. Ingason vd. [7], yangınlar sırasında tüneldeki hava akışı, sıcaklık, basınç ve duman üretimi gibi faktörleri inceleyerek, tünel yangınlarına karşı alınacak önlemleri belirlemişlerdir. Kodur ve Naser [30] çalışmalarında, köprüler ve tüneller gibi kritik ulaşım altyapılarında yangın sorununu ele alan yapılan son araştırmaları incelemişler ve bu yapıların performansını etkileyen kritik faktörleri çalışma kapsamında tartışmışlardır. Köprü ve tünellerdeki yangın tehlikelerini azaltmak için önerilen ana stratejileri sunarak, pratik bir vaka çalışması aracılığıyla uygulanabilirliklerini göstermişlerdir. Demiryolu tünellerinde yangınların risk ve sonuçlarını değerlendirmede normal olarak kullanılan kriterleri ve "en kötü senaryo" yangınların evrimini tanımlayan uygun zaman-sıcaklık eğrilerinin seçimini gözden geçiren çalışmalarında Tarada ve King [1], püskürtme yangın koruma malzemeleri, çimento kaplamaları ve polipropilen liflerin eklenmesi vb. alternatif yangın koruma yöntemlerinin avantajları ve dezavantajları incelemişlerdir ve ayrıca, sabit yangın söndürme sistemleri konusu ve bunların pasif yangın koruma önlemlerine bir alternatif veya ek olarak görülebilecekleri konusu tartışılmıştır.

Tüneli yangınlarında, risk değerlendirmesi için kullanılan modelleme teknikleriyle yangının boyutu hakkında bilgi edinilmesi ve tahliye prosedürleri ve güvenlik önlemlerinin geliştirilerek oluşabilecek hasarların minimize edilmesi hedeflenmektedir. Son yıllarda tünel yüzey sıcaklıklarının analizi, duman ve zararlı gaz etkileri/çeşitleri, yapı malzemelerinin davranışının modellenmesi ve yangın söndürme sistemleri konusunda ilerleme kaydedilmiştir. Tünel yangınlarının en önemli güvenlik yönlerinden biri, tasarım aşamasında duman yoğunluğunun/dispersiyonunun doğru tahmin edilebilmesidir [31]. Birçok tünel projesine yangın güvenliği açısından katkı sağlayan “Computational Fluid Dynamics” (CFD) analizi, yangın durumunda ısı ve duman emisyonlarının, kirlenmiş/zehirli gazların dağılımı ve yoğunluğunun hesaplanması, duman besleme elemanlarının ve rüzgârın etkilerinin de hesaba katılması için kullanılmaktadır. Bir tünelden yangın çıktığında, duman havalandırma hava akışının yönünde geniş bir alana yayılır ve yangın olayı sırasında tahliye ortamı yeterince güvenli olmayabilir. Bir tüneldeki havalandırma ekipmanı değiştirildiğinde, yeni havalandırma ekipmanının güvenliği ve ekonomik verimliliği önceden değerlendirilmelidir [32]. Ancak, deney yaparak yeni havalandırma ekipmanının doğrulanması maliyetli ve kullanışlı olmaması nedeniyle uygun değildir. Bu nedenle, sayısal bir simülasyon gerçekleştirerek bir tünelden yangın çıktığında tahliye durumunu tahmin etmek ve tünelin tahliye güvenliğini incelemek faydalı olabilmektedir [33, 34]. Yamamoto vd. [35] çalışmalarında, “Fire Dynamics Simulator” (FDS) [36, 37] yangın simülasyon yazılımını kullanarak, olası yangını yeniden oluşturmuşlardır. FDS bir tür akışkanlar dinamiği yazılımı olup, bu yöntemle; (i) tünel içi alev yayılması, (ii) yangının büyümesi, (iii) nesneler arasındaki (gaz-katı) ısı transferi, (iv) tünelde kullanılan yangın söndürme sistemlerinin aktivasyonu ve (v) geliştirilen sistemle yangının söndürülmesi gibi konularda doğru tahminler yapılabilmektedir [25, 26, 32, 38]:

FDS programı hesaplarını her sayısal ızgaradaki her ayrık zaman adımında, her bir sayısal ızgara hücresi içindeki sıcaklık, yoğunluk, basınç, hız ve kimyasal bileşimi şeklinde gerçekleştirmektedir. Aynı zamanda, program kapalı katı yüzeylerin sıcaklığını, ısı akısını ve kütlesel kayıplarını da hesaplamaktadır. FDS kodu, yangın akışı ile yönlendirilen CFD temelinde formüle edilmiştir [10].

Smokeview (SMW), üç boyutlu (3D) modelleme, zamanla değişen yangınların sayısal hesaplaması ve duman yayılmasının görselleştirilmesi sağlamaktadır. SMV, FDS ve “Consolidated Fire and Smoke Transport” (CFAST) [39] simülasyonlarının çıktılarını görüntülemek için kullanılan bir görselleştirme programıdır. Geliştirilen yazılım, sadece tünel yangın modellemesi için değil, aynı zamanda tüneldeki toksik gaz akışını ve insanların tahliyesini de kapsamaktadır. Tünel yangını: yanma maddesi ve yanma yöntemi gibi birçok bilinmeyeni içeren karmaşık bir süreçtir. Önceki deneyimlere ve tam ölçekli yangın testlerine dayanarak, yangının büyüme ve azalma hızları, ateşleme yerleri ve yangın boyutu vb. gibi bazı varsayımlar yapılabilmektedir. Bu analiz yöntemleriyle, tünelin yangın davranışını incelenerek, elde edilen veriler, tünelde olası bir yangın durumunda alınacak önlemleri belirlemek için kullanılabilmektedir. Böylelikle, yolcuların güvenli şekilde tahliyesi için acil çıkış merdivenleri ve havalandırma açıklıklarının yeterliliği de belirlenebilmektedir.

Gaziantep banliyö projesi (Gaziray) Raylı Sistem Hattı, Türkiye Cumhuriyeti Devlet Demiryolları (TCDD) ile Gaziantep Büyükşehir Belediyesi arasında ortak bir girişim olup, Türkiye'nin Gaziantep şehrinde hizmet veren çevre dostu bir toplu taşıma sistemidir. Gaziantep şehir merkezinden yaklaşık 25 km uzaklıktaki Gaziantep-Nizip ilçesi arasında, raylı sistem kullanarak banliyö taşımacılığı hizmeti sunan bir ulaşım projesidir. Projenin amacı, kentsel ulaşımı kolaylaştırmak ve trafiği azaltmak için modern bir toplu taşıma sistemi sağlamaktır. Toplam uzunluğu 25.532 km olan hatta ve Gaziray hattı üzerinde tamamı engelli erişimine uygun olan ikisi yer altında olmak üzere toplam 16 istasyonu olan hat, 5 Kasım 2022'de hizmete girmiştir (Tablo 1). İZBAN, Marmaray ve Başkentray'dan sonra Türkiye'nin dördüncü banliyö treni sistemidir [40]. Hattın tüm araçları elektrikle çalışmakta ve çevreye hiçbir zararlı gaz salınımı yapmamaktadır. Hattın işletmesi, enerji tasarrufu sağlamak amacıyla akıllı sistemler kullanmaktadır. Hat, modern bir güvenlik sistemi ile donatılmıştır. Tüm istasyonlarda "Closed-Circuit Television" (CCTV) kameralar, yangın algılama ve söndürme sistemleri, acil durum anonsları ve acil durum çıkışları bulunmaktadır. Ayrıca, hattın güvenliğini sağlamak için her vagonun kapıları ve pencereleri alarm sistemleri ile donatılmıştır.

Tablo 1. Gaziray istasyon bilgileri [40]

Sıra	İstasyon	İlçe	Tür	İstasyonlar arası uzaklık	İlk istasyona olan uzaklık
1	Başpınar	Şehitkamil	Hemzemin	0+00 km	Başlangıç
2	OSB-3		Hemzemin	0+73 km	0+73 km
3	OSB-4		Hemzemin	1+01 km	1+74 km
4	Dülük		Hemzemin	2+37 km	4+11 km
5	Stadyum		Hemzemin	3+27 km	7+38 Km
6	Beylerbeyi		Hemzemin	0+91 km	8+29 km
7	Fıstıklık		Hemzemin	0+93 km	9+22 km
8	Selimiye		Hemzemin	1+64 km	10+86 km
9	Adliye		Yeraltı	1+85 km	12+71 km
10	Topraklık		Yeraltı	1+71 km	14+42 km
11	Mücahitler		Hemzemin	0+83 km	15+25 km
12	Gaziantep Garı		Hemzemin	1+07 km	16+32 km
13	Göllüce		Hemzemin	2+02 km	18+34 km
14	Seyrantepe		Hemzemin	2+13 km	20+47 km
15	Mustafa Yavuz		Hemzemin	0+79 km	21+26 km
16	Taşlıca		Hemzemin	2+28 km	23+54 km

Gaziray Raylı Sistem Hattı, yer altında 3.634,000 km uzunluğunda bir güzergaha sahip olup projesinde iki adet yer altı istasyonu bulunmaktadır (Adliye ve Topraklık İstasyonları). Tünel yapısı aç-kapa şekilde tasarlanmıştır ve her iki uçta da yüzeye açık portallar mevcuttur. Aç-kapa tünel yapısında 14 adet 4.8 m^2 (1.2 x 4 m) havalandırma açıklığı yer almaktadır. Ayrıca, tünelde 9 adet acil çıkış merdiveni de bulunmaktadır. Gaziray Raylı Sistem Hattı boyunca yer alan tünellerden, yolcuların tamamının, "*National fire protection association*" (NFPA) 130 [41] kurallarına uygun olarak, 4 dakika içinde perondan tahliye edilebildiği ve 6 dakikada güvenli bir noktaya ulaşılabildiği varsayılmaktadır. Bu çalışmanın amacı, Gaziray Raylı Sistem Hattında bulunan tünellerde meydana gelebilecek olası tren yangını durumunda, tünel yapısının yangından etkilenme seviyesi ve bu etkinin değerlendirilmesidir. Kritik hız; yangın esnasında ortaya çıkan duman ve yanma ürünü zehirli gazların ters katmanlaşmadan istenilen yöne itilmesi için gerekli olan minimum hava hızıdır. Yapısal bütünlüğün bozulmadan, çevresel kontrol sistemlerinin çalışmasına olanak sağlayarak ve insan tahliye yönünün ters yönünde kritik hava hızı sağlanarak; gerekli havalandırma stratejisi ve kapasitesinin belirlenmesi hedefi çalışma kapsamında gerçekleştirilmiştir. “Subway Environmental Simulation” (SES) [42] paket programı kullanılarak, hat bilgisi, tren ve yangın bilgileri tanımlanarak, yangın bölgesinde tünel içyapısının ulaştığı süreye bağlı sıcaklık tayin gerçekleştirilmiştir. Çalışma kapsamında, öncelikle tünelde yer alan havalandırma açıklıklarına yerleştirilecek tünel havalandırma fanlarının efektif kullanılmasının mümkünlüğü irdelenmiştir. Bunun yanında tünellere yerleştirilen jet fanların kullanımı değerlendirilmiştir. CFD simülasyonu sınır değerleri, bu çalışmada verilen fan adet kapasiteleri kullanılarak hazırlanan SES simülasyonu analizinden alınmıştır. CFD simülasyonu ile zamana bağlı olarak sıcaklık, görüş mesafesi ve hava hızı dağılımları gösterilerek, sunulan bu araştırma makalesi ile belirlenen havalandırma fan kapasitelerin yeterliliği incelenerek değerlendirilmiştir.

II. MODELLEME

2.1 Trenlerin Modellenmesi

Tünel havalandırma sistemi kapasitelerinin belirlenmesi için yapılan yangın simülasyonlarında, yolcu ve yük trenlerinin, simülasyon yapılabilmesi için belirlenen tünel, makas veya geceleme hattı bölgelerinde sabit durdukları varsayılmaktadır. Tek boyutlu olarak modellenen trenler, bu bölgelerde, zamana bağlı olmayan ısı kaynakları olarak düşünülmektedir. Simülasyonlarda kullanılan trenlere ait özellikler Tablo 2’de ve araç ön görünümü Şekil 2’de verilmiştir.

2.1 Analiz Programı

Bu çalışmada, tünel havalandırma simülasyonları SES v4.1 programı [42] kullanılarak gerçekleştirilmiştir. SES programı tek boyutlu bir analiz programı olup, metro ve yeraltı ulaşım sistemlerinin tünel havalandırması tasarımlarına yardımcı olmak amacıyla kullanılan bir paket programdır. SES programının tek boyutlu analiz diye nitelendirilmesinin sebebi ise, hava hızı ve sıcaklığı gibi parametrelerin tünellerin eninde ($y-$ doğrultusunda) ve düşey yönde ($z-$ doğrultusunda) değişmediği, sadece tünel boyunca ($x-$ doğrultusunda) değiştiğinin varsayılmasıdır. Tünelin eni ve yüksekliği genelde tünellerin boyuna oranla çok daha kısa olduğu için parametrelerin hacimsel olarak değiştiği varsayılmaktadır. Dolayısıyla, 3D analizlere göre, SES programı basitleştirilmiş sonuçlar verebilmektedir. SES programının 3D analizlere karşı bir başka avantajı ise, uzun bir tünel sistemini bir arada çözebilmesinin mümkün olabilmesi ve zamansal tasarruf sağlanmaktadır.

Tablo 2. Yolcu ve yük trenlerinin özellikleri

Özellik	**Değer**
Yolcu treni yangın yükü	12 Mw
Yük treni yangın yükü	100 Mw
Konvektif ısı katsayısı	0.8
Konvektif ısı transferi (yolcu treni)	9.6 Mw
Konvektif ısı transferi (yük treni)	80 Mw
Tren kesit alanı	10.7 m^2
Tren uzunluğu (yük treni)	460 m
Tren uzunluğu (yolcu treni)	180 m
Tren çevre uzunluğu	-
Trenin yüzeysel sürtünme katsayısı (yolcu treni)	0.023
Trenin yüzeysel sürtünme katsayısı (yük treni)	0.1
Sürüklenme katsayısı (yolcu treni)	0.55
Sürüklenme katsayısı (yük treni)	0.56

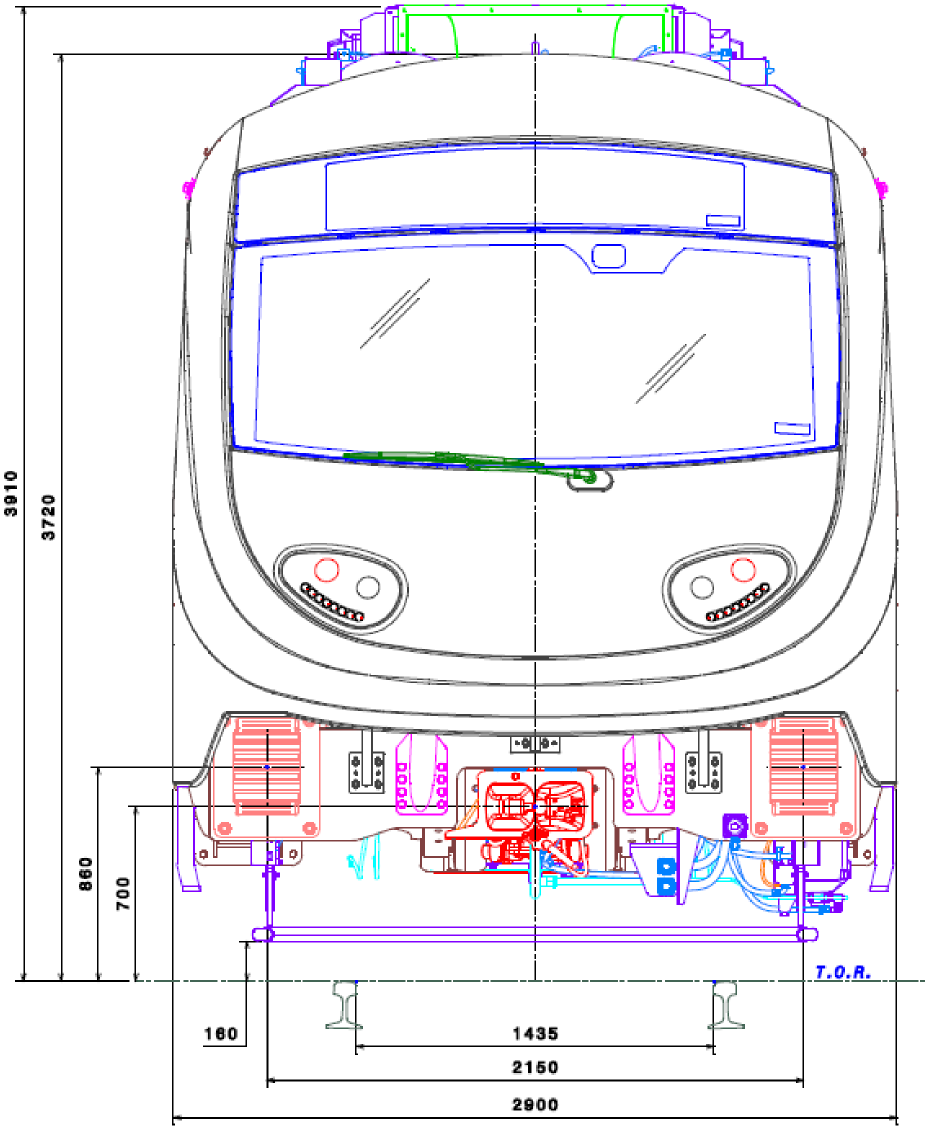

Şekil 2. Araç ön görünümü

III. TÜNEL HAVALANDIRMA SİSTEMİ TASARIMI

3.1 SES Modeli

Simülasyon modelinin oluşturulması aşamasında, tünel ve istasyon mimari projeleri basitleştirilerek, bu alanlar SES programında kullanılacak olan tek boyutlu elemanlar halinde ifade edilmiştir. Ray üstü kot değerlerinin, demiryolu hatlarında belirli sınırlarla sınırlanmasının ana nedenleri, yolcu konforunu ve seyir güvenliğini sağlamaktır. EN 13848-Hat Geometrik Kalitesi şartnamesi [43], hat profilinde meydana gelen kot değişikliklerinin belirli bir hat uzunluğu boyunca sınırlamaları konusunda öneriler sunmaktadır. Hat profilindeki değişiklikler, tren hızına, değişimin büyüklüğüne ve bu değişimin meydana geldiği hat uzunluğuna bağlı olarak hat üzerinde farklı kuvvetlerin oluşmasına neden olur. Bu değişikliklerin sınırlanması, yolcu konforunu etkileyen titreşimleri azaltmayı ve seyir güvenliğini sağlamayı amaçlamaktadır. Tünel kesitleri ve ray üstü kot değerleri Tablo 3'te gösterilmiştir. Tablodaki değerler ortalama deniz seviyesine göre yükseklik değerleri olup, Gaziantep ili merkez rakım değeri ~850 m olması durumu göz önünde bulundurulmuştur. Senaryo oluşturulurken tünelin, 15.827,700 km konumundan, hattın Mücahitler istasyonu yönüne doğru değişken olmak üzere 15.827,700 km~15.920,000 km arası M-M ve N-N kesitleri dikkate alınmıştır. Hazırlanan simülasyon modelinin ağ şeması mimik diyagramı (MD) Şekil 3'te verilmiştir.

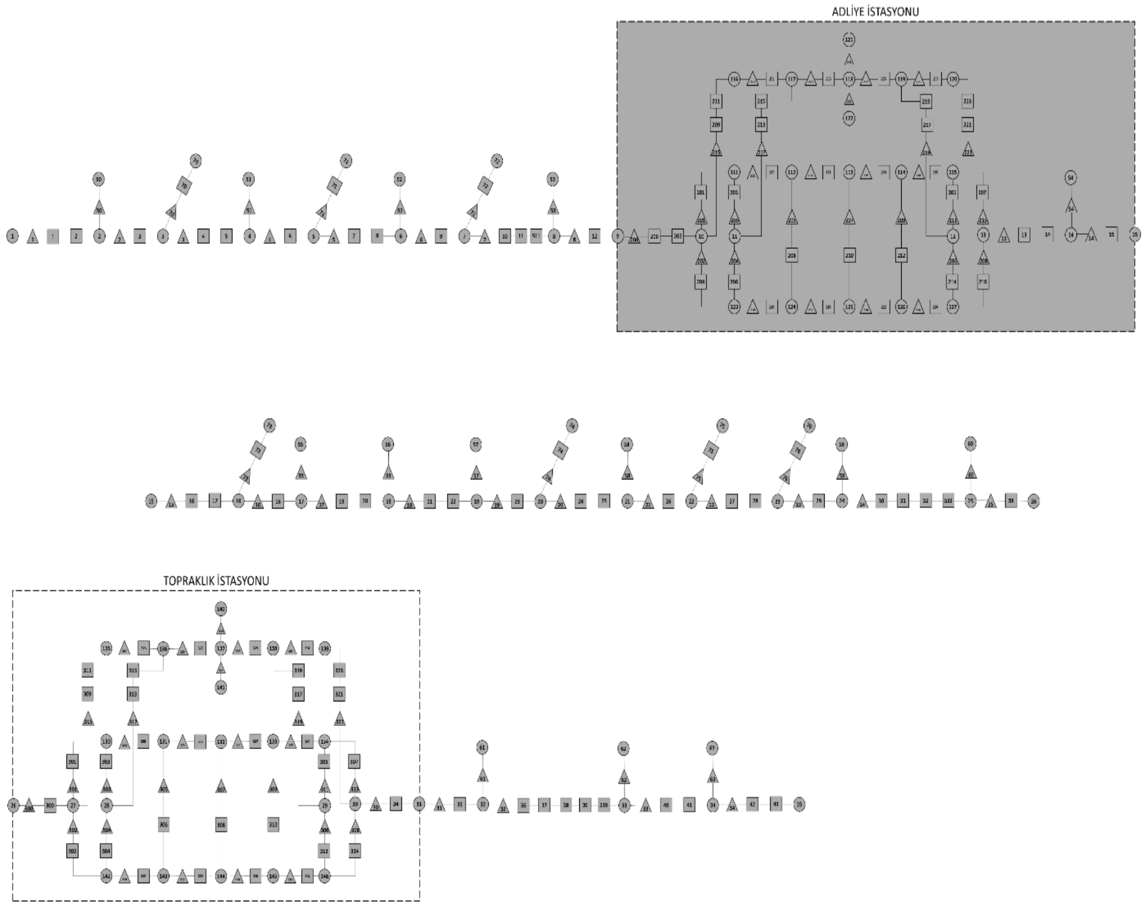

Şekil 3. SES simülasyon modelinin ağ şeması MD

Tablo 3. Tünel kesitleri ve ray üstü kot değerleri

Kesitler	Ray üstü kot değerleri (m)
C-C	1.086,100
D-D	979,600
E-E	882,300
F-F	803,600
G-G	819,000
H-H	915,00
I-I	1.008,100
J-J	763,100
K-K	757,600
L-L	757,600
M-M	757,600
N-N	757,600
O-O	757,600
P-P	753,400
R-R	752,300
S-S	752,800

3.2 Sıcaklık Kriterleri

Yolcuların bulunduğu alanlar ve tahliye güzergahında, NFPA 130, Tablo B.2.1.1'e [41] göre 60 °C den düşük olması durumu dikkate alınarak tünel tahliye yönünde maksimum sıcaklık 50 °C olarak belirtilmiş olsa da NFPA 130 standardı gereğince, tahliye yollarında insanların maruz kalınan sıcaklığa bağlı olarak belirli bir süre içerisinde tahliyeyi sürdürebilmesi mümkündür. Bu çalışmada, Tablo 4'te belirtilen aralıklar göz önünde bulundurmuş olup dumansız bir sıcaklık koşulu olduğu dikkate alınmıştır.

Tablo 4. Acil durum tahliye esnasında süreye bağlı maksimum maruz kalınan süresi

Maruz kalınan sıcaklık (℃)	Maruz kalınan süre (dakika)
80	3.8
75	4.7
70	6.0
65	7.7
60	10.1
55	13.6
50	18.8
45	26.9
40	40.2

3.2.1. Yapısal sıcaklık kriterleri

Sıcaklık-süre bazlı grafikler, genellikle iki bileşenden; i) sıcaklık süresi eğrisi, ii) malzeme performans eğrisi, oluşmakta olup, yapının yangın durumunda sıcaklığa maruz kalma süresini ve yapının bu sıcaklık profil seviyelerine karşı gösterdiği performansı gösteren bir araçtır. Bu grafik, yangın mühendisliği ve yapısal tasarım alanlarında yaygın olarak kullanılan bir yöntemdir. Değerler, genellikle ısı yayılımına dayalı yangın testlerinden elde edilen verilere dayanmaktadır. Yapının sıcaklık-süre bazlı performansı, malzemelerin yangın sırasında yapının işlevselliğini sürdürme kapasitesini belirlemektedir.

3.3 Hava Hızı Kriterleri

Amerika Birleşik Devletleri hava bürosu tarafından, rüzgâr kuvvetini göstermek için kullanılan Beaufort ölçeği, 0'dan 12'ye kadar kademelendirilmiş bir tablodur ve Subway Environmental Design Handbook'ta, Tablo 2.13'te verilmektedir [44]. Beaufort ölçeğinde tavsiye edilen acil durumdaki maksimum hava hızı 2500 fpm (12.700 m/s) olarak ifade edilmektedir. Normal koşulların üst limiti, 2200 fpm (11.176 m/s) hava hızı acil durum koşullarında alt limit olarak kabul edildiği için, acil durum koşullarında insanların maruz kalacağı maksimum hava hızı 11 m/s olarak kabul edilmiştir. Tahliye süresi boyunca havalandırma tasarımının, yolcu tahliyesini mümkün kılmasıyla birlikte tünel çeperine gelen sıcaklığın yapı formuna zarar vermemesi ve formunu en az 1 saat boyunca koruyabilmesi, havalandırma sisteminin işlevini yerine getirme olanağı sağlayacaktır. Yolcu güvenliği mutlak öncelik olmasıyla birlikte tesisin kısa bir süre sonra yeniden işletilebilir olması amaçlanarak, yapı güvenliğinin korunması dikkate alınmıştır. Bu çalışmada ele alınan konuya ilişkin hava hızı kriterleri Tablo 5’te verilmektedir.

Tablo 5. İstasyon ve tünel bölgesi yangın durumu hava hızı kriterleri

Konum	Minimum	Ortalama	Azami
Platform (yatay)	-	3 m/s	11 m/s
Merdivenler	-	1.8 m/s	11 m/s
Tüneller	0.75 m/s	-	11 m/s
İstasyon girişi	-	-	11 m/s
Havalandırma bacaları	-	5 m/s	11 m/s
Kaldırım ızgaraları	-	2.5 m/s	11 m/s
Kaldırımdan 3 m ve daha yüksekteki menfezler	-	5 m/s	11 m/s

3.4 Yangın Senaryoları

Acil durum havalandırma sistemi, tünelde veya istasyonda yangın gibi olası bir acil durum koşulunda yolcuların güvenli bir biçimde tahliye edilmesini ve itfaiyenin yangınla mücadele ekipleri ile arama kurtarma ekiplerinin müdahalelerini yapabilecek ortam koşullarını sağlamak için tasarlanmaktadır. Yapısal formun, sıcaklık karşısında dayanımı bu sistemlerin sağlıklı çalışabilmesi için önemlidir. Acil durum havalandırma sisteminin kapasitesine; (i) tünel içi tren yangını senaryosu ve (ii) istasyon içi tren yangını senaryosu olmak üzere toplam iki tip senaryo etki etmektedir:

İşletim sırasında, olası bir tren yangınının gerçekleşmesi durumunda, eğer tren halen hareket edebilir durumda ise, ilk tercih bu trenin bir sonraki istasyona kadar gitmesini sağlamak ve yolcu tahliyesini burada gerçekleştirmektir. Fakat bazı durumlarda, yanmakta olan tren tünelde hareketsiz kalabilmektedir. Bu durumda insanlar; yangının tüneldeki konumuna ve yanan vagonun trendeki konumuna göre en yakın istasyon, tünel portalı veya acil kaçış merdivenlerine doğru yürümesi ve tahliyesi gerekmektedir. Trende yangın çıkması ve yanan trenin tünelde durması çok küçük bir olasılık olsa da sonuçları can ve mal güvenliği açısından büyük olacağından, uluslararası standartlar gereğince dikkate alınması zorunlu kılınmıştır.

Bu makale kapsamında verilen yangın senaryosu çalışmalarında, yangının yalnızca bir trende ortaya çıktığı ve işletmede olan diğer trenlerin yangın bölgesinden uzaklaştığı varsayımı yapılmıştır. Yangının konumuna göre, portalda olan yangın vakasının dışındaki trenler tünelde ise yangından uzaklaşarak en yakın istasyonda tahliyenin gerçekleştiği veya tünel dışına çıktığı kabulü yapılmaktadır. Ayrıca henüz tünele giriş yapmamış trenlerin ise hareket doğrultusunu ters istikamete doğru yönlendirdiği ve yangından uzaklaştığı kabulü yapılmıştır. Tünel içi araç yangınlarında en kritik senaryo, özellikle kesit alanın, hat eğiminin ve yangın yükünün yüksek olduğu konumlarda meydana gelmektedir. Tünel içi tren yangınlarında, tünel havalandırma fanları devreye girerek; “itme-çekme” prensibi ile dumanı bir yönde iterken, yolcular/personeller diğer yönde dumandan etkilenmeden tünelden çıkabilmesi hedeflenmektedir. Yanan vagonun trendeki konumu ve tahliye yönü havalandırma fanlarının yönünü etkilemektedir. Tünel acil durum havalandırma simülasyon analizinde; yük treni yangın yükü (Tablo 2, 100 Mw), yolcu treni yangın yükünden (Tablo 2, 12 Mw) fazla olması sebebiyle öncelikle yük treni dikkate alınmıştır. Yük treni yangın senaryo simülasyon analizleri, tünel havalandırma fanlarının kapasitesini belirlemede yeterli olsa da ilave olarak yolcu treni için de simülasyon analizleri yapılmıştır. Tünel havalandırma senaryoları, üç bölgeye; (i) Tünel Portalı-Adliye, (ii) Adliye-Topraklık ve (iii)Topraklık-Tünel Portalı, ayrılmış ve her bir bölge için tahliye yönlerine göre iki farklı senaryo olmak üzere, yük ve yolcu trenleri için ayrı ayrı toplam 6 senaryo oluşturulmuştur. Analiz edilen yangın senaryoları Tablo 6'da verilmiştir.

Tablo 6. Yangın senaryoları

Senaryo No	Tren	Bölge	Konumu (km)	Tahliye yönü
SN-01	Yük	Tünel Portalı-Adliye	13.900	Tünel Portalı
SN-02	Yük	Tünel Portalı-Adliye	13.453	Adliye
SN-03	Yük	Adliye-Topraklık	15.209	Adliye
SN-04	Yük	Adliye–Topraklık	14.775	Topraklık
SN-05	Yük	Topraklık-Tünel Portalı	15.708	Tünel Portalı
SN-06	Yük	Topraklık-Tünel Portalı	16.196	Topraklık
SN-07	Yolcu	Tünel Portalı-Adliye	13.900	Tünel Portalı
SN-08	Yolcu	Tünel Portalı-Adliye	13.453	Adliye
SN-09	Yolcu	Adliye-Topraklık	15.209	Adliye
SN-10	Yolcu	Adliye-Topraklık	14.775	Topraklık
SN-11	Yolcu	Topraklık-Tünel Portalı	15.708	Tünel Portalı
SN-12	Yolcu	Topraklık-Tünel Portalı	16.196	Topraklık

Bu çalışmada, yanan trenin bulunduğu bölgedeki fanların, yüksek ısı sebebiyle iptal durumu SN-13 ve SN-18 arasındaki senaryolarda irdelenmiştir. Yangın bölgesine denk gelen fanların hizmet dışı tutularak, diğer fanlarla sağlanan hava hızları da detaylı bir şekilde gösterilmiştir.

3.5 Havalandırma Fanları

Tünel havalandırma sistemi, yangının tren üzerindeki yerine ve trenin tünel içerisindeki yerine bağlı olarak dumanı her iki yönde de (tersinir) itebilme kapasitesine sahip olmalıdır. Dolayısıyla, tünel havalandırma fanları tersinir olmalı ve emme yönündeki hava debi değeri ile basma yönündeki hava debi değerleri olabildiğince birbirine eşit performansta olmalıdır. Çalışmada, jet fanların verimliliği %90 olarak ve havalandırma fanları 1 saat ve 250 °C sıcaklığa kadar dayanıklı olduğu kabulü yapılmıştır.

3.6 Kritik Hız

Tünel içerisinde oluşabilecek olası bir tren yangını durumunda, trenden duman ve zehirli gazlar tüm tünele yayılacak şekilde açığa çıkmaktadır. Eğer tünel havalandırma sistemleri, trenden yayılan dumanı tünel içerisinde bir yöne doğru yönlendirmede yeterli olamazsa, duman ve gazlar tüm tüneli sararak yolcuların güvenliğini tehdit edebilmektedirler. Kritik hız, trenden yayılmakta olan sıcak ve zehirli gazları, tünel içerisinde sadece bir yöne doğru yönlendirmek için, dolayısıyla diğer yönde yolcular için güvenli bir kaçış yolu sağlamak için, gerekli olan en düşük hava hızı değeridir (Şekil 4). Fanlı/Cebri havalandırma ile kritik hızın sağlanması durumunda, dumanın geri katmanlaşması oluşmayacaktır.

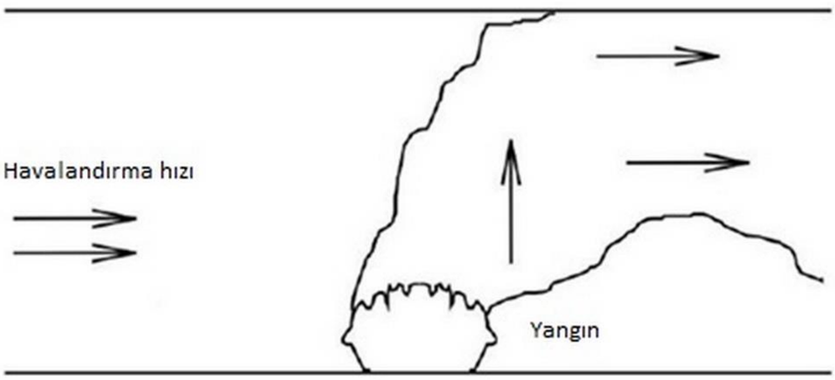

Şekil 4. Kritik hızın sağlanması durumundaki duman ve sıcak gazın dağılımı

Kritik hız değeri; (V_c), yangın yükü; (Q), ortam sıcaklığı; (T), tünel kesit alanı; (A), tünel eğimi; ($grade$), tünel yüksekliği; (H), ve tren kesit alanı gibi birçok değişkene bağlıdır. Eş. (1) bağıntısıyla verilen kritik hız değeri kritik hız ve yangın bölgesindeki duman sıcaklığı denklemlerinin eş zamanlı olarak çözülmesi sonucunda elde edilir:

$$V_c = K_1\, K_g \left(\frac{g\, H\, Q}{\rho\, C_p\, A\, T_f}\right)^{1/3} \tag{1}$$

Burada, $K_1 =$ birimsiz sabit olup değeri 0.606'dır. $K_g =$ eğim düzeltme katsayısını, $C_p =$ sabit basınçlı havanın özgül ısı katsayısını, $T_f =$ yangın bölgesi duman sıcaklığını göstermektedir. T_f ve K_g'nin formülleri aşağıda Eş. (2) ve Eş. (3) bağıntılarıyla verilmektedir:

$$T_f = \frac{Q}{\rho\, C_p\, A\, V_c} + T \tag{2}$$

$$K_g = 1 + 0.0374(grade)^{0.8} \tag{3}$$

Burada, $\rho =$ havanın yoğunluğunu, $grade$ =yüzde cinsinden tünelin eğimini vermektedir. Eğer tünel içerisinde yangın olan bölgede havalandırma yönü yokuş yukarı veya tünel eğimi düz ($= \%0$) ise $K_g = 1'dir.$ Havalandırma yönü yokuş aşağı ise K_g değişkeni için Eş. 3 denklemi kullanılarak değer birden büyük bulunur. Bunun gerekçesi, sıcak gazların tünelin tavanına doğru yükselecek olması, hatta eğimli olan tünellerde daha fazla yükselecek şekilde eğimi kullanarak yayılmasıdır. Dolayısıyla yokuş aşağı yapılacak olan havalandırma durumunda, yükselen sıcak gazları da yokuş aşağı süpürmek için daha yüksek havalandırma hızına ihtiyaç duyulmaktadır. Bu da kritik hız için daha yüksek bir değer hesaplanmasını açıklamaktadır. Şekil 5'te eğim düzeltme katsayısının eğimle değişim grafiği verilmektedir [45].

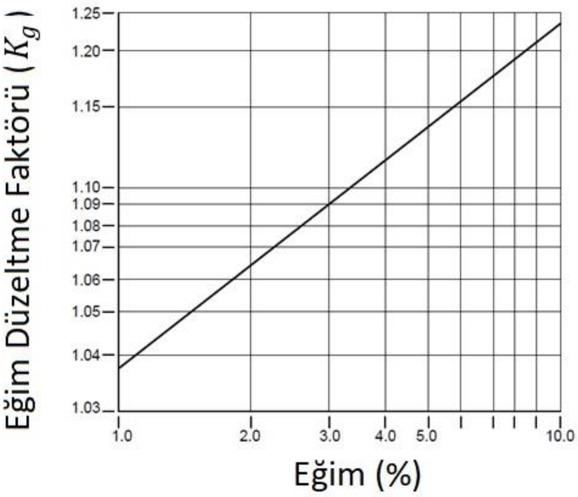

Şekil 5. Eğim düzeltme katsayısının eğimle değişim grafiği [45]

IV. ANALİZ BULGULARI VE TARTIŞMA

Başarılı/geçerli senaryo sonuçlarının elde edildiği nihai fan adedi ve kapasitesi ile gerçekleştirilen simülasyon sonuçları bu bölüm kapsamında incelenmiştir. Sonuçlarda belirli bölgeler için hava hızı ve sıcaklık bilgisi verilmiştir. Acil kaçış yönünün tersi yönünde kritik havalandırma hızı sağlanması durumunda, jet fan kapasiteleri yeterli görülmüştür. Böylece, tahliye yönüne doğru, duman ve sıcak gazların ilerlemesi mümkün olmayacaktır. Tahliye yönünde yer alan acil kaçış merdivenleri için bu bölgelere duman yönelimi olmaması sebebiyle ilave bir basınçlandırma gereksinimi bulunmamaktadır. Normal işletme ve trafik sirkülasyonunun fazla olduğu sıkışık işletme durumlarında tünel sıcaklıklarını bertaraf etmek adına ve tünellerde oluşan kirli havanın veya yangınla mücadele sonunda tünellerde kalan soğuk dumanın deşarj edilmesi için tünel havalandırma fanlarının (TVF) şaftlarına toplamda 36 m^3/s kapasiteli aksiyel fanlar yerleştirilerek bu aşamalarda çalıştırılacaktır. Üstün performanslı bir hava akışı işlemini yerine getirerek, ortamdaki havanın kontrolünü en iyi biçimde sağlayan aksiyel fanlar, ilgili alanda aktive olduklarında, basınç farkının yardımıyla eksenel yönde bir hava dengesi oluştururlar. Ele alınan makale çalışmasında, elde edilen analiz sonuçlarındaki yangın konumuna ve tahliye yönlerine göre havalandırma ekipmanlarının pozisyonları Tablo 7’ de verilmektedir. Yangın bölgesinde fanların iptal olması durumunda yük treni kritik hız analizi yangın senaryolarına göre sonuçları Şekiller 6−17 arasında verilmekte olup havalandırma tasarımı için yolcu tahliyesini ve oluşun hava gazlarına ait sıcaklık ve hız bilgilerini göstermektedirler.

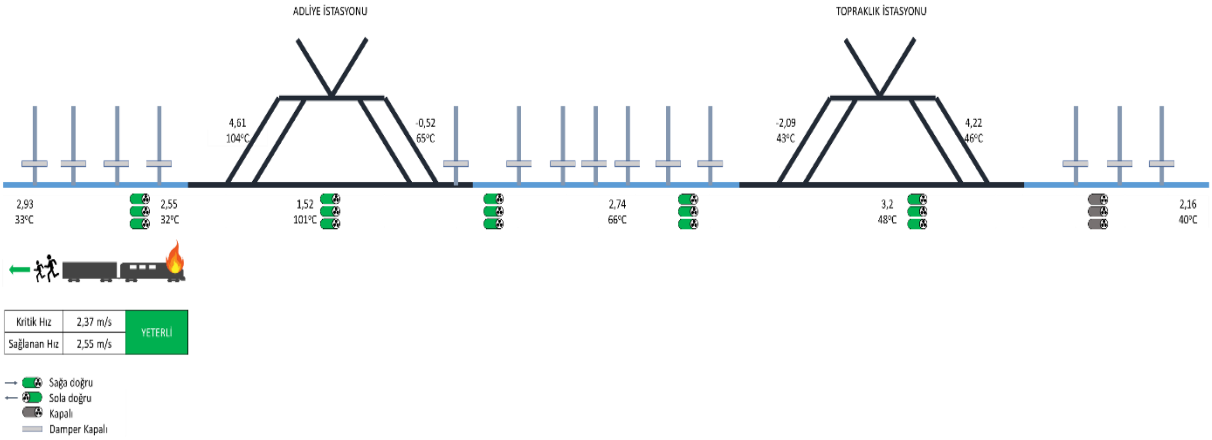

Şekil 6. SN-01: Tünel Portalı - Adliye İstasyonu Arası Yük Treni Yangını - Tahliye Yönü: Tünel Portalı

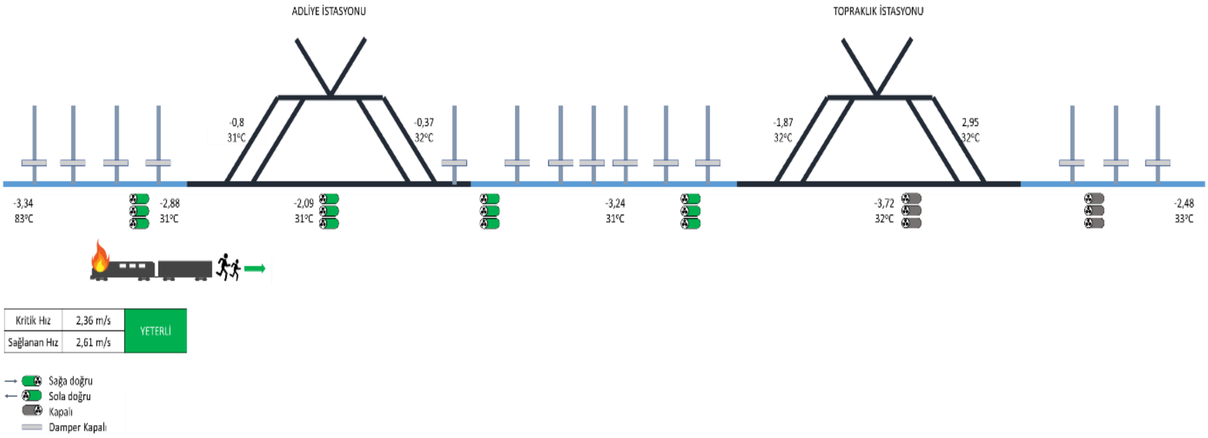

Şekil 7. SN-02: Tünel Portalı - Adliye İstasyonu Arası Yük Treni Yangını - Tahliye Yönü: Adliye İstasyonu

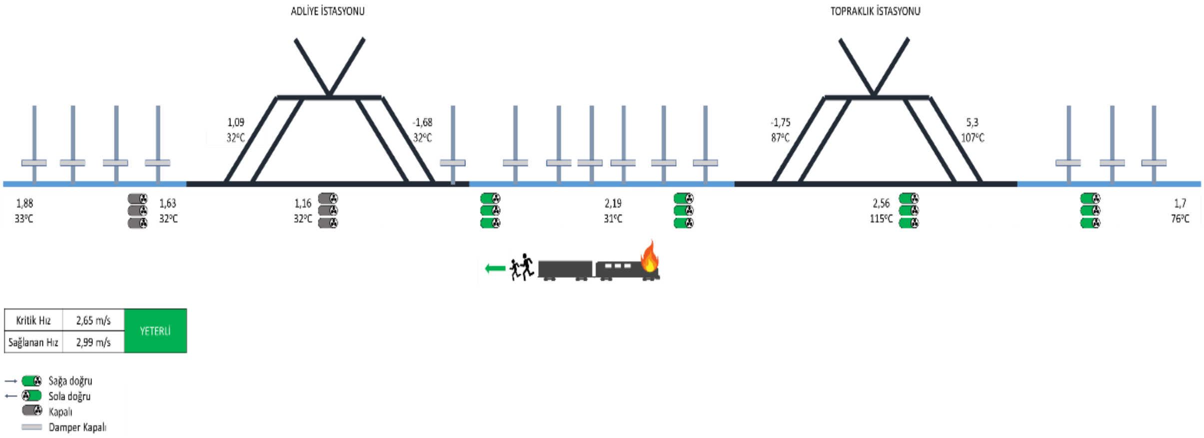

Şekil 8. SN-03: Adliye – Topraklık İstasyonları Arası Yük Treni Yangını - Tahliye Yönü: Adliye İstasyonu

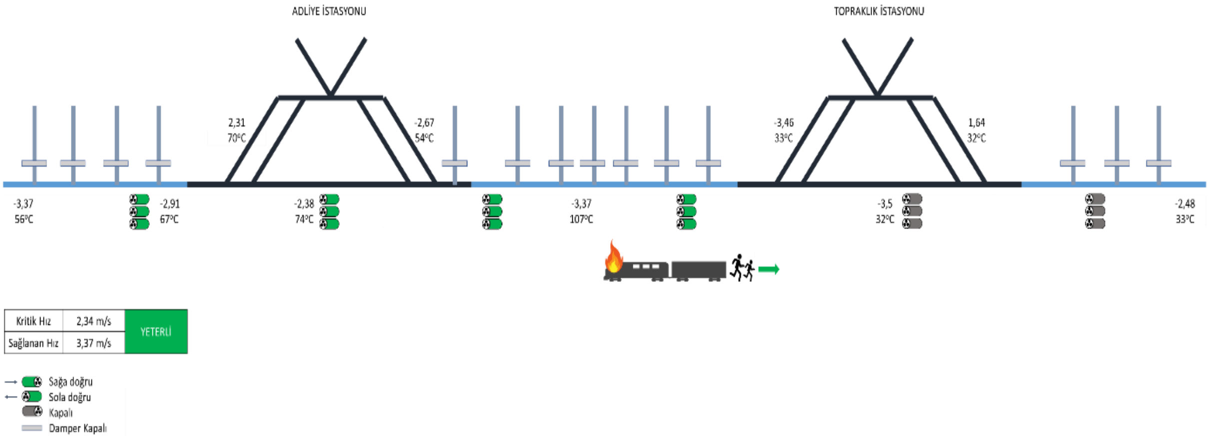

Şekil 9. SN-04: Adliye – Topraklık İstasyonları Arası Yük Treni Yangını - Tahliye Yönü: Topraklık İstasyonu

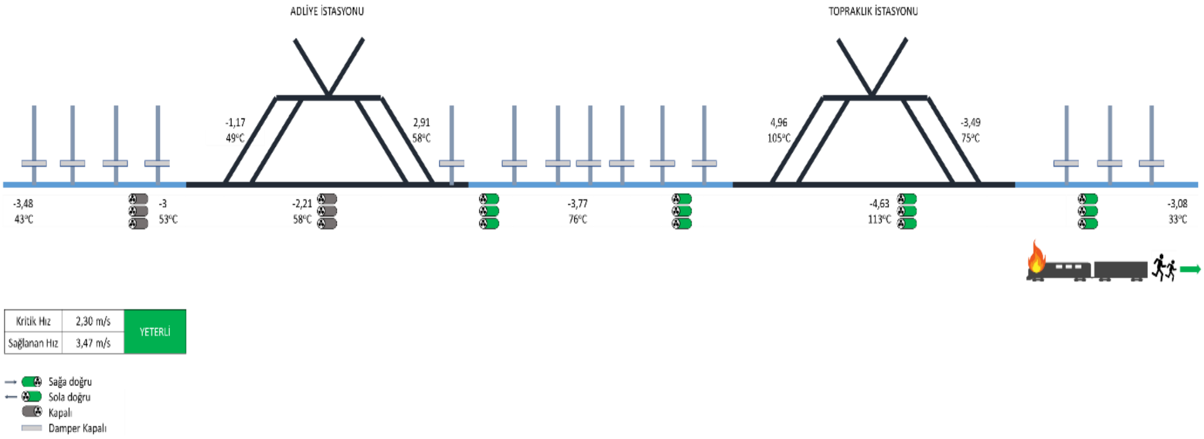

Şekil 10. SN-05: Topraklık İstasyonu - Tünel Portalı Arası Yük Treni Yangını - Tahliye Yönü: Tünel Portalı

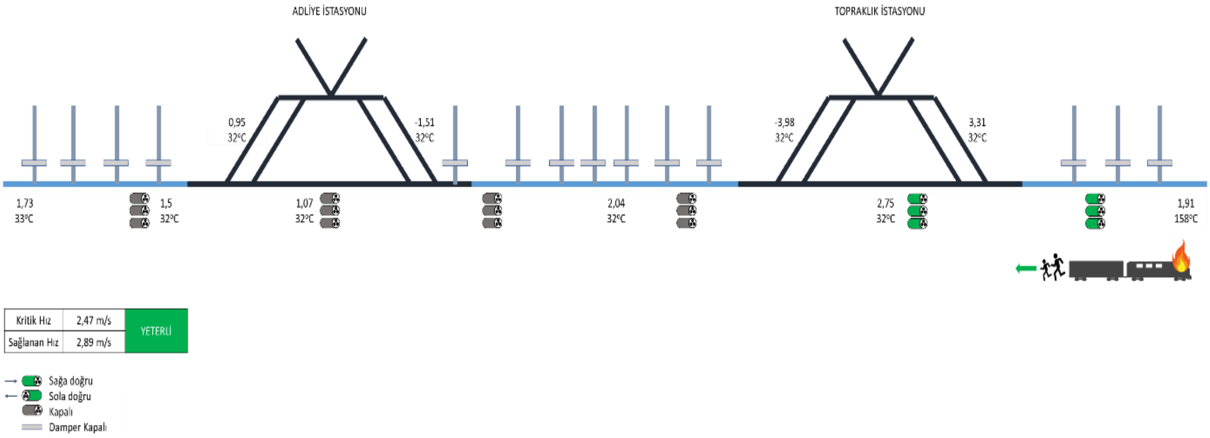

Şekil 11. SN-06: Topraklık İstasyonu - Tünel Portalı Arası Yük Treni Yangını - Tahliye Yönü: Topraklık İstasyonu

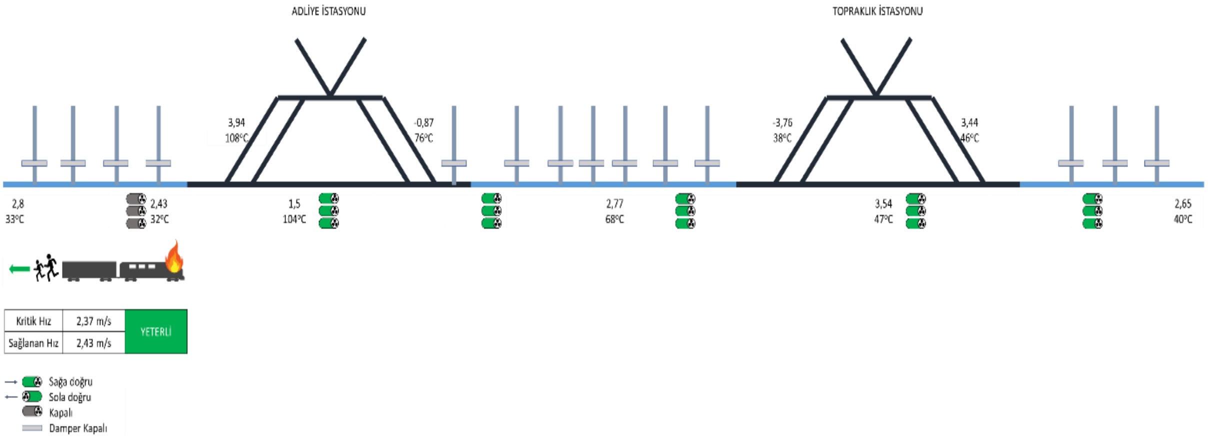

Şekil 12. SN-07: Tünel Portalı - Adliye İstasyonu Arası Yolcu Treni Yangını - Tahliye Yönü: Tünel Portalı

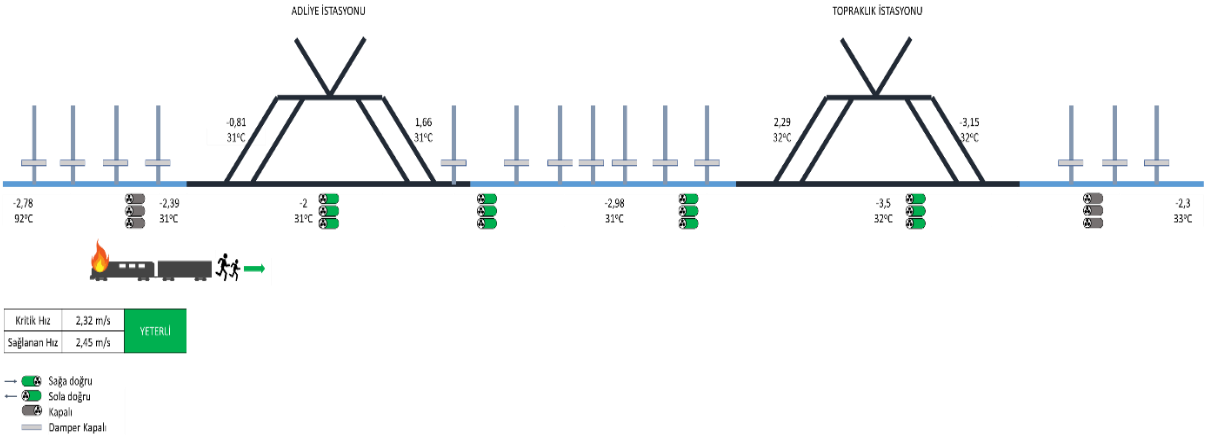

Şekil 13. SN-08: Tünel Portalı - Adliye İstasyonu Arası Yolcu Treni Yangını - Tahliye Yönü: Adliye İstasyonu

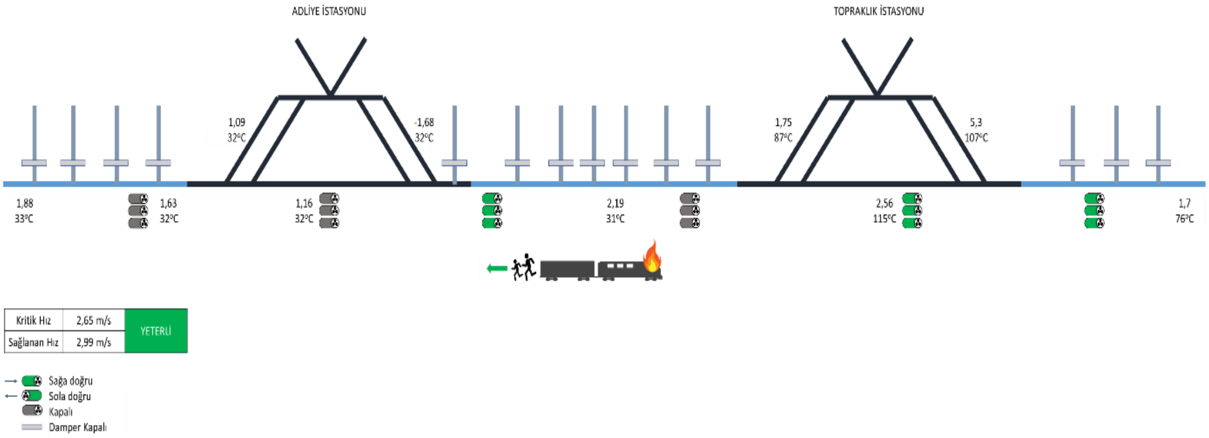

Şekil 14. SN-09: Adliye – Topraklık İstasyonları Arası Yolcu Treni Yangını - Tahliye Yönü: Adliye İstasyonu

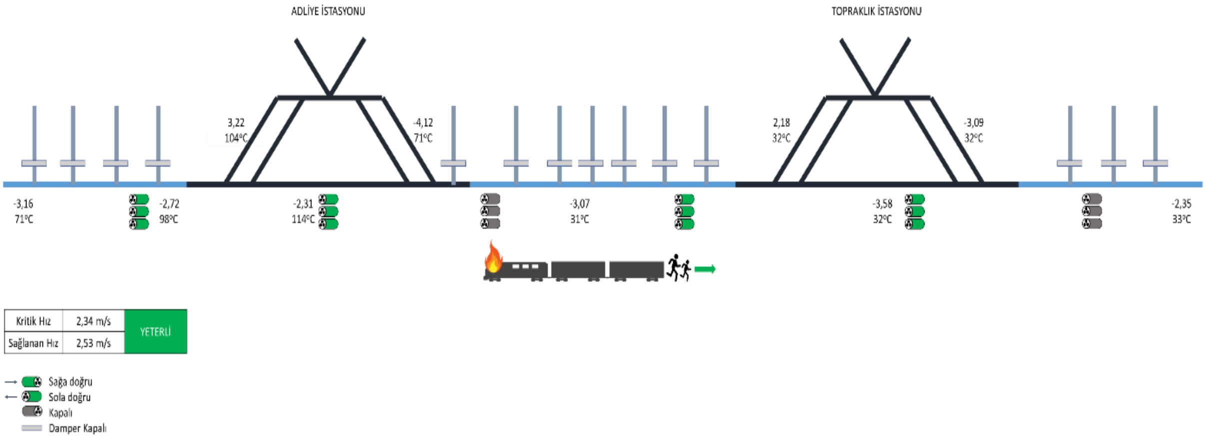

Şekil 15. SN-10: Adliye – Topraklık İstasyonları Arası Yolcu Treni Yangını - Tahliye Yönü: Topraklık İstasyonu

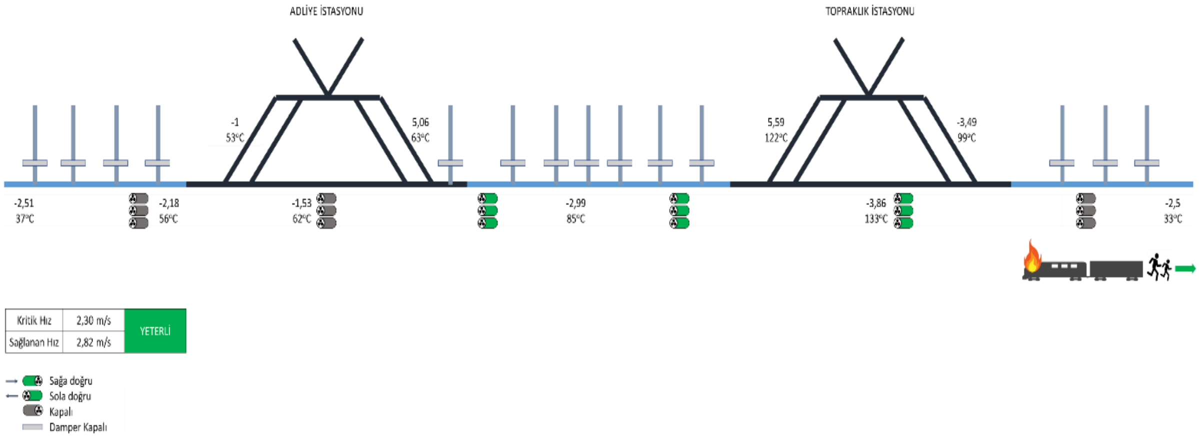

Şekil 16. SN-11: Topraklık İstasyonu - Tünel Portalı Arası Yolcu Treni Yangını - Tahliye Yönü: Tünel Portalı

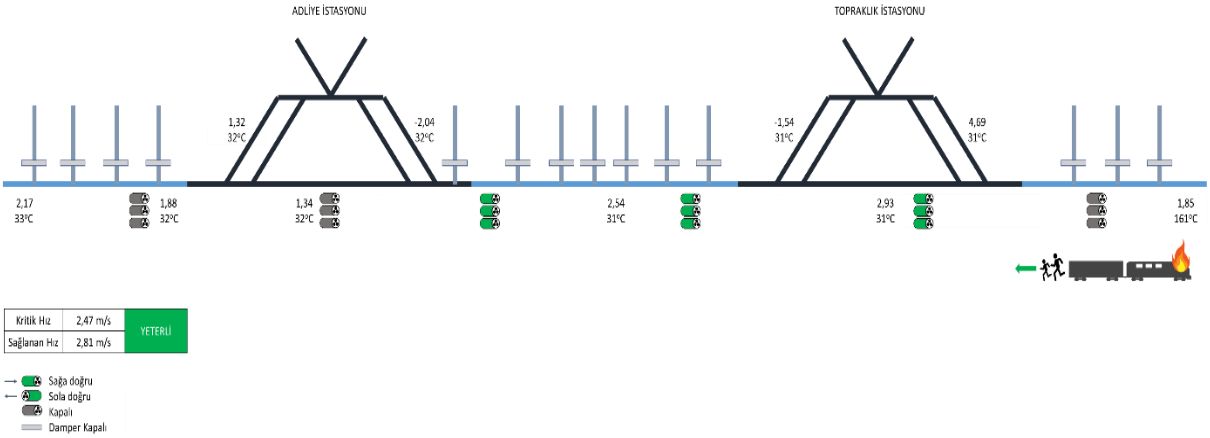

Şekil 17. SN-12: Topraklık İstasyonu - Tünel Portalı Arası Yolcu Treni Yangını - Tahliye Yönü: Topraklık İstasyonu

Tablo 7. Yangın senaryoları ve oluşturulan havalandırma stratejileri

Yangın Konumu	**Tünel Portalı–Adliye İstasyonu**		**Adliye İstasyonu–Topraklık İstasyonu**		**Topraklık İstasyonu–Tünel Portalı**	
Yolcu/Personel Tahliye Yönü	Tünel Portalı ←	Adliye İstasyonu →	Adliye İstasyonu ←	Topraklık İstasyonu →	Topraklık İstasyonu ←	Tünel Portalı →
Havalandırma açıklıklarındaki damperler	Kapalı	Kapalı	Kapalı	Kapalı	Kapalı	Kapalı
Jet Fan-01-02-03	→	←	—	←	—	—
Jet Fan-04-05	→	←	—	←	—	—
Jet Fan-06	→	←	—	←	—	—
Jet Fan-07-08-09	→	←	→	←	—	←
Jet Fan-10-11-12	→	—	→	←	→	←
Jet Fan-13-14	→	—	→	—	→	←
Jet Fan-15	→	—	→	—	→	←
Jet Fan-16-17-18	→	—	→	—	→	←

Yapılan analizler sonucunda, Tünel Portalı – Adliye İstasyonu – Topraklık İstasyonu – Tünel Portalı bölgesinde yer altı tünellerindeki toplam 12 yangın senaryosu için yapılan analizde (bkz. Tablo 6), gerekli kritik hızın sağlanması için toplam 18 adet jet fan ihtiyacı olduğu görülmüştür. Tablo 8'de belirtilen değerler, yapısal formun zarar görmemesi durumu kabul edilerek ekipmanların çalışma yeterliliğidir. Ancak, ilgili senaryolarda tünel iç çeperinin maruz kaldığı sıcaklıklarında ortaya konularak gerekli önlemlerin alınması gerekmektedir. Tüneldeki güvenli tahliye için gereken kritik hızı sağlayan jet fanlara ait konum ve kapasite bilgileri Tablo 9'da verilmektedir.

Tablo 8. Yangın senaryoları ve sağlanan hızlar

Senaryo No	**Kritik hız (m/s)**	**Sağlanan hız (m/s)**	**Açıklama**
SN-01	2.37	2.61	√ Yeterli
SN-01	2.32	2.38	√ Yeterli
SN-02	2.65	3.41	√ Yeterli
SN-03	2.34	3.34	√ Yeterli
SN-04	2.30	3.54	√ Yeterli
SN-05	2.47	2.47	√ Yeterli
SN-06	2.37	2.62	√ Yeterli
SN-07	2.32	2.52	√ Yeterli
SN-08	2.65	3.15	√ Yeterli
SN-09	2.34	3.20	√ Yeterli
SN-10	2.30	3.12	√ Yeterli
SN-11	2.47	2.68	√ Yeterli
SN-12	2.37	2.61	√ Yeterli

Tablo 9. Jet Fan konum ve kapasiteleri

Konum	Fan adedi	Çıkış hava hızı (m/s)	Çıkış hava debisi (m^3/s)	İtki kuvveti (N)
13.670	3	35.7	40.4	1730
13.960	1	35.7	40.4	1730
13.960	2	35.7	40.4	1730
14.100	3	35.7	40.4	1730
15.480	3	35.7	40.4	1730
15.685	1	35.7	40.4	1730
15.685	2	35.7	40.4	1730
15.955	3	35.7	40.4	1730
13.670	3	35.7	40.4	1730
13.960	1	35.7	40.4	1730
13.960	2	35.7	40.4	1730
14.100	3	35.7	40.4	1730
15.480	3	35.7	40.4	1730

Yangın senaryolarına bağlı olarak, yangın çıkan bölümde maksimum duvar sıcaklıkları Tablo 10'da verilmektedir Bu sıcaklık değerleri, yük trenin yangın başlamasından 1 saat sonraki durumunu göstermektedir. Ayrıca, yük trenine ait yüksek yangın yükünden (~100 Mw) dolayı çıkan yangına ait duman ve sıcak havanın; istasyon merdiven yapılarından veya tünel portallarından atıldığı görülmektedir. Yangın senaryo analiz sonuçlarından, merdiven ve peron bölgesine ait sıcaklık verilerinden de anlaşılan bu durum, istasyon peronlarında bekleyen/tahliye olan yolcular açısından can güvenliğini tehlikeye atmaktadır. Sonuçta, Marmaray hattında da olduğu üzere, yüksek yangın yüküne sahip yük tren işletmeciliği, yolcu tren işletim saatlerinde yapılmaması büyük önem taşımaktadır [46].

Tablo 10. Yangın bölgesinde oluşan maksimum duvar sıcaklıkları

Senaryo No	Maksimum duvar sıcaklıkları (°C)
SN-01	774
SN-01	802
SN-02	894
SN-03	846
SN-04	776
SN-05	923
SN-06	774

V. SONUÇLAR VE ÖNERİLER

Raylı sistemler, hızlı, güvenli ve çevre dostu bir toplu taşıma seçeneği olarak dünya genelinde kullanılmaktadır. Gaziray Raylı Sistem Hattı, Türkiye'nin Gaziantep şehrinde toplu taşıma ihtiyacını karşılamak amacıyla planlanan bir proje olarak büyük önem taşımaktadır. Tren yangınları, raylı sistem hatlarında nadir olsa da meydana gelebilecek potansiyel tehlikelerden biri olsa da, tehlike riski dikkate alınması ve tünel yapısının yangından etkilenme seviyesinin değerlendirilmesi çok önemlidir. Yangınlar, trenlerin elektrikli ve mekanik bileşenlerinde çeşitli nedenlerle ortaya çıkabilmekte, örneğin elektrik kablolarının aşırı ısınması, fren sistemlerinde arızalar, yakıt sızıntıları gibi sebeplerle yangınlar meydana gelebilmektedir. Tünel yapısının yangından etkilenme seviyesi, yangının tünel yapısına verdiği zararın değerlendirilmesini ifade etmektedir. Tünelde meydana gelen yangınlar, tünel duvarlarına, tavanına, tabanına ve diğer yapısal elemanlara zarar verebilmekte ve bu zararlar, tünelin kullanılabilirliğini, güvenliğini ve yapısal bütünlüğünü etkileyebilmektedir. Yangın sonrası yapısal hasar, tünelin onarım maliyetlerini ve işletme süreçlerini de etkiler. Tünel yangınlarının etkilerini değerlendirmek için yangın testleri, modelleme ve simülasyonlar gibi yöntemler kullanılmaktadır. Yangın testleri, gerçek yangın senaryolarını taklit ederek tünel yapısının yangına karşı tepkisini belirlemektedir. Modelleme ve simülasyonlar ise tünel yapısının yangından etkilenme seviyesini belirlemek için kullanılmaktadır.

Bu makalede sunulan analiz çalışması, Gaziray Raylı Sistem Hattı'nın güvenliğini ve yangın durumlarında tahliye süreçlerini değerlendirmek amacıyla gerçekleştirilmiştir. Çalışmanın temel hedefi, tünel yapısının yangından etkilenme seviyesini belirlemek ve gerekli önlemleri alarak güvenli bir işletme ortamı sağlamaktır. Analizde, tünelde oluşabilecek yangın senaryoları ele alınmış ve bu senaryolara yönelik havalandırma stratejileri geliştirilmiştir. Tahliye yönlerine göre hava akışı, sıcaklık ve hız bilgileri incelenmiştir. Yapılan analizler ve simülasyonlar sonucunda, yer altı tünellerinde gerçekleştirilen yangın senaryoları için havalandırma tasarımının başarılı ve geçerli olduğu sonucuna varılmıştır. Acil kaçış yönünün tersi yönünde kritik havalandırma hızının sağlanması için jet fan kapasiteleri yeterli tespit edilmiştir. Bu sayede tahliye yönüne doğru duman ve sıcak gazların ilerlemesi engellenerek güvenli bir tahliye sağlanabilecektir. Tahliye yönünde bulunan acil kaçış merdivenleri için duman yönelimi olmaması nedeniyle ilave bir basınçlandırma gereksinimi bulunmamaktadır. Ayrıca, tünelde normal işletme ve yoğun trafik durumlarında oluşabilecek sıcaklık artışları ve kirli hava problemlerini çözmek için TVF kullanılmıştır. Bu 36 m^3/s kapasiteli aksiyel fanlar, tüneldeki havanın kontrolünü sağlamak ve kirli havayı dışarıya atmak için kullanılmaktadır. Fanların konumu ve kapasiteleri yangın senaryolarına bağlı olarak belirlenmiştir. Analiz sonuçlarına göre, Tünel Portalı - Adliye İstasyonu - Topraklık İstasyonu - Tünel Portalı bölgesinde yer alan yer altı tünellerindeki toplamda 12 yangın senaryosu için 18 adet jet fan gerektiği tespit edilmiştir. Jet fanların çıkış hızı 35.7 m/s ve çıkış debisi 40.4 m^3/s olarak belirlenmiştir. Yangın senaryolarına bağlı olarak, yangın bölgesindeki duvar sıcaklıkları maksimum olarak ölçülmüştür. Bu sıcaklıklar, yük treninin yangın başlamasından 1 saat sonra ulaşılan değerlerdir. Yangın çıkan bölümdeki duvarlarda maksimum 774 °C ile 923 °C arasında sıcaklıklar kaydedilmiştir. Bu bilgiler, yangının şiddetini ve yayılma potansiyelini belirlemek için önemli veriler sağlamaktadır. Örneğin, yüksek yangın yüküne sahip yük trenlerinin işletimi, yolcu trenlerinin işletim saatleriyle çakışmaması önerilmektedir. Yük trenleri, yolcu trenlerinden farklı bir risk potansiyeli taşımaktadır ve yangın durumunda yolcuların güvenliğini tehlikeye atabilmektedirler. Bu nedenle, işletim saatlerinin düzenlenmesi ve gerektiğinde ayrı bir tren hattının kullanılması önerilmektedir.

Bu çalışma, Gaziray Raylı Sistem Hattı'ndaki tünellerin yangın güvenliği açısından kapsamlı bir değerlendirme sunmakta ve proje için özelleştirilmiş çözümler önermektedir. Çalışmanın sonuçlarının, tünelin yangın güvenliği ve acil durum yönetimi konularında tasarımcılara, işletmecilere ve karar vericilere rehberlik etmek amacıyla kullanılabileceği düşünülmektedir. Gaziray Raylı Sistem Hattı'ndaki tünellerde meydana gelebilecek olası tren yangını durumunda tünel yapısının yangından etkilenme seviyesini değerlendirmek amacıyla gerçekleştirilen bu makale çalışması, diğer benzer çalışmalardan farklılık gösteren başlıca hususları aşağıda sıralanmıştır:

- İncelenen çalışma konusu, Gaziantep şehrinde gerçekleştirilen Gaziray Raylı Sistem Hattı projesine odaklanmaktadır. Bu nedenle, tünel yapılarının yangın güvenliği için özel olarak bu projeye yönelik analizler yapılmış ve öneriler sunulmuştur.
- Tünel yangınlarından etkilenen bölgelerde etkili havalandırma stratejilerinin belirlenmesi konusu çalışmanın odakladığı bir diğer husustur. Yangın sırasında oluşan dumanın ve sıcak gazın hızlı bir şekilde tahliyesi, insanların güvenli bir şekilde tahliye edilmesi için hayati öneme sahiptir. Bu yönüyle çalışma,

jet fanların doğru konumlandırılması ve kapasitelerinin belirlenmesi gibi havalandırma stratejilerine yönelik detaylı analizler içermektedir.

- Çalışmada, kritik hava hızının sağlanması ve dumanın tahliye yönüne doğru yönlendirilmesi için gerekli havalandırma stratejileri belirlenmektedir. Yangın senaryolarına bağlı olarak, jet fanların çıkış hızı ve debisi gibi parametreleri ile birlikte tünelin güvenli bir şekilde tahliye edilmesi için gerekli olan jet fan sayısı ve performansı da belirlemektedir.
- Yangın sonrası yapısal hasarın minimize edilmesi için yangın dayanıklı malzemelerin kullanımı, yangın sırasında yapısal deformasyonları önlemek için stratejik destek elemanlarının yerleştirilmesi gibi öneriler sunulan bu makele çalışmasında değerlendirilmektedir.

Yangınların yol açabileceği yapısal hasarlar da dikkate alınarak gerekli önlemlerin alınması önerilmiştir. Çalışma kapsamında, yangınların tünel yapısına ve yapısal elemanlara verdiği zararlar da değerlendirilmiştir. Gaziray Raylı Sistem Hattı gibi kritik ağlar için yangın güvenliği önlemlerini iyileştirmede aşağıdaki genel önlemler önerilmektedir:

- **Yangına dayanıklı malzemelerin kullanımı:** Tünel yapısının yangına dayanıklı malzemelerle güçlendirilmesi, yangının tünel içindeki yapısal elemanlara verdiği zararı en aza indirecektir. Bu sayede tünelin yangın sonrası onarım maliyetleri azalacak ve işletme süreçleri daha hızlı bir şekilde normale dönebilecektir.
- **Duman tahliyesi ve havalandırma sistemlerinin optimize edilmesi:** Yangın sırasında oluşan dumanın ve sıcak gazın tünel içinden hızlı bir şekilde tahliye edilmesi önemlidir. Jet fanların doğru konumlandırılması ve kapasitelerinin uygun şekilde belirlenmesi, etkin bir duman tahliye sistemi oluşturulmasını sağlayacaktır.
- **Acil tahliye önlemlerinin güçlendirilmesi:** Tüneldeki acil kaçış merdivenlerinin konumları ve erişilebilirlikleri, güvenli tahliye için büyük önem taşmaktadır. Bu önlemlerin güçlendirilmesi, yangın durumunda insanların hızlı ve güvenli bir şekilde tünelden çıkmasını sağlayacaktır.
- **Yangın alarm ve söndürme sistemlerinin iyileştirilmesi:** Yangınların erken tespiti ve hızlı müdahale için etkili bir yangın alarm ve söndürme sistemi kurulmalıdır. Bu sistemlerin sürekli olarak bakımı ve test edilmesi, güvenliğin sürdürülebilirliği açısından büyük önem taşımaktadır.
- **Eğitim ve farkındalık:** Tünel kullanıcıları, çalışanları ve güvenlik personeli arasında yangın güvenliği konusunda düzenli eğitimler düzenlenmelidir. Yangın durumunda yapılması gerekenlerin bilinmesi ve farkındalığın artırılması, güvenli tahliyenin sağlanması açısından kritik öneme sahiptir.

Sonuç olarak, bu analiz çalışması Gaziray Raylı Sistem Hattı'nın güvenliğini sağlamak amacıyla yapılmıştır. Yangın senaryoları ve tahliye yönleri göz önünde bulundurularak havalandırma stratejileri geliştirilmiş ve gerekli ekipmanların konumu ve kapasiteleri belirlenmiştir. Bu çalışma, tünel yapısının yangından etkilenme seviyesini değerlendirmek ve güvenli bir işletme ortamı sağlamak için önemli bir adımdır.

TEŞEKKÜR

Yazar, bu makale çalışmasının hazırlanmasında teknik desteği için Makine Mühendisi Davut Belkızoğlu’na teşekkür eder.

KAYNAKLAR

[1] Tarada F, King M (2009) Structural fire protection of railway tunnels. Railway Engineering Conference, University of Westminster, UK, June 24-25.

[2] Wang H, Binder E, Mang H, Yuan Y, Pichler B (2018) Multiscale structural analysis inspired by exceptional load cases concerning the immersed tunnel of the Hong Kong-Zhuhai-Macao Bridge. Underground Space 3(4):252–267. https://doi.org/10.1016/j.undsp.2018.02.001

[3] Feist C, Aschaber M, Hofstetter G (2009) Numerical simulation of the load-carrying behavior of RC tunnel structures exposed to fire. Finite Elements in Analysis and Design 45(12):958–965. https://doi.org/10.1016/j.finel.2009.09.010

[4] Long X, Guo H (2016) Fire Resistance study of concrete in the application of tunnel-like structures. 2nd International Symposium on Submerged Floating Tunnels and Underwater Tunnel Structures, Procedia Engineering 166:13–18.

[5] Avcı-Karataş Ç (2022) Yalova il afet risk azaltma planının (İRAP) hazırlanması konusunda ön çalışmaların incelenmesi. 8. Uluslararası Mühendislik ve Teknoloji Yönetimi Kongresi, İstanbul, Türkiye, 8-9 Aralık.

[6] Krausmann E, Mushtaq F (2008) A qualitative Natech damage scale for the impact of floods on selected industrial facilities. Nat Hazards 46:179–197. https://doi.org/10.1007/s11069-007-9203-5

[7] Ingason H, Li YZ, Lönnermark A (2014) Tunnel Fire Dynamics. Springer, New York.

[8] PIARC. (1999). Fire and Smoke Control in Road Tunnels. Technical Committee 5 Road Tunnels (C5). PIARC-World Road Association, France.

[9] EI-Arabi IA, Duddeck H, Ahrens H (1992) Structural analysis for tunnels exposed to fire temperatures. Tunelling and Underground Space Technology 7(1):19–24. https://doi.org/10.1016/0886-7798(92)90109-U

[10] Davidy A (2016) CFD studies of tunnel fire growth on composite lining materials. International Refereed Journal of Engineering and Science, 5(4):1-6.

[11] Avci-Karatas C, Taşkin K (2023) Current modeling techniques for reviewing fire safety in road/highway tunnels. 5th International Congress on Engineering Sciences and Multidisciplinary approaches. Istanbul, Turkey, Feb. 25-26.

[12] AASHTO-LRFD (2010). Bridge Design Specifications. American Association of State Highway and Transportation Officials. 5th Edition. ISBN: 978-1-56051-451-0. 444 North Capitol Street, Washington DC, USA.

[13] Directive (EU) (2004). 2004/54/EC of the European Parliament and of the Council of 29 April 2004 on minimum safety requirements for tunnels in the Trans-European Road Network. Luxembourg, Belgium.

[14] Directive (EU) (2019). 2019/1936 of the European Parliament and of the Council of 23 October 2019 amending Directive 2008/96/EC on road infrastructure safety management, OJ L 305, 26.11.2019, p.1. Luxembourg, Belgium.

[15] ITA-Working Group No.6 (2004). Maintenance and Repair. Guidelines for Structural Fire Resistance for Road Tunnels. International Tunneling Association (ITA). Châtelaine, Switzerland.

[16] EN 1991-1-2 (2002). (English): Eurocode 1: Actions on structures - Part 1-2: General actions - Actions on structures exposed to fire [Authority: The European Union Per Regulation 305/2011, Directive 98/34/EC, Directive 2004/18/EC]. Plzen, Czech Republic.

[17] EU (2021). Report - A9-0211/2021. REPORT on the EU Road Safety Policy Framework 2021-2030– Recommendations on next steps towards “Vision Zero”.

[18] Channel Tunnel. https://en.wikipedia.org/wiki/Channel_Tunnel. Erişim tarihi: 16 Mayıs 2023.

[19] Stucchi R, Amberg F (2020) A practical approach for tunnel fire verification. Structural Engineering International 30(4):515–529. https://doi.org/10.1080/10168664.2020.1772697

[20] Tarada F (2007) Improving road tunnel safety. Eurotransport 5:35–39.

[21] Seike M, Ejiri Y, Kawabata N, Hasegawa M (2014) Suggestion of estimation method of smoke generation rate by CFD simulation and fire experiments in full-scale tunnels. J Fluid Sci Technol 9:1–11. https://doi.org/10.1299/JFST.2014JFST0018

[22] Seike M, Kawabata N, Hasegawa M (2016) Experiments of evacuation speed in smoke-filled tunnel. Tunn Undergr Space Technol 53:61–67. https://doi.org/10.1016/j.tust.2016.01.003

[23] Thomas PH (1958) The movement of buoyant fluid against a stream and the venting of underground fires. Fire Safety Science 351:1–7.

[24] Oka Y, Atkinson GT (1995) Control of smoke flow in tunnel fires. Fire Safety Journal 25(4):305–322. https://doi.org/10.1016/0379-7112(96)00007-0

[25] Hwang CC, Edwards JC (2005) The critical ventilation velocity in tunnel fires—A computer simulation. Fire Safety Journal 40(3):213–244. https://doi.org/10.1016/j.firesaf.2004.11.001

[26] Hu LH, Peng W, Huo R (2008) Critical wind velocity for arresting upwind gas and smoke dispersion induced by near-wall fire in a road tunnel. Journal of Hazardous Materials 150(1):68–75. https://doi.org/10.1016/j.jhazmat.2007.04.094

[27] Ingason H, Lönnermark A (2004) Recent achievements regarding measuring of time-heat and time-temperature development in tunnels. In Proceedings of the 1st International Symposium on Safe & Reliable Tunnels, Innovative European Achievements, pp.87–96, Prague, Czech Republic, Feb 4–6.
[28] Li YZ, Ingason H (2016) Influence of ventilation on road tunnel fires with and without water-based suppression systems. SP Technical Research Institute of Sweden: Boras, Sweden, 36:1–58.
[29] Nakahori I, Sakaguchi T, Kohl B, Forster C, Vardy A (2015) Risk assessment of zero-flow ventilation strategy for fires in bidirectional tunnels with longitudinal ventilation. In Proceedings of the 16th International Symposium on Aerodynamics, Ventilation and Fire in Tunnels, Seattle, WA, USA, Sept. 15–17.
[30] Kodur, Naser MZ (2021) Fire hazard in transportation infrastructure: Review, assessment, and mitigation strategies. Frontiers of Structural and Civil Engineering 15:46–60. https://doi.org/10.1007/s11709-020-0676-6
[31] Isıkan MO, Kaya O (2019) Yüksek kamu binalarında duman tahliyesinin simülasyon metoduyla incelenmesi. International Journal of Advances in Engineering and Pure Sciences, 3:223–231. https://doi.org/10.7240/jeps.512479
[32] Nishiki S (2013) Numerical study of the effect of water mist spray in tunnel fire using FDS. In Proceedings of the 5th Japan/Taiwan/Korea Joint Seminar for Tunnel Fire and Management, pp.42084–42087, Tokyo, Japan, Nov. 7.
[33] Yamamoto K, Kokubo S, Nishinari K (2006) New approach for pedestrian dynamics by Real-Coded Cellular Automata (RCA). In Cellular Automata; Yacoubi, S.E., Chopard, B., Bandini, S., Eds.; Lecture Notes in Computer Science; Springer: Berlin/Heidelberg, Germany Vol. 4173, pp.728–731.
[34] Yamamoto K, Kokubo S, Nishinari K (2007) Simulation for pedestrian dynamics by real-coded cellular automata (RCA). Physica A 379(2):654–660. https://doi.org/10.1016/j.physa.2007.02.040
[35] Yamamoto K, Sawaguchi Y, Nishiki S (2018) Simulation of tunnel fire for evacuation safety assessment. Safety 4(2):12. https://doi.org/10.3390/safety4020012
[36] McGRATTAN K (2010) Fire Dynamics Simulator (Version 5) - Technical Reference Guide. NIST Special Publication 1018, NIST.
[37] McGrattan K, Forney GP (2010) Fire Dynamics Simulator (Version 5) - User's Guide. NIST Special Publication 1019, NIST.
[38] Wang HY, Sahraoui H (2014) Mathematical modelling of pool fire burning rates in a full-scale ventilated tunnel. Fire Saf Sci 11:361–375. http://dx.doi.org/10.3801/IAFSS.FSS.11-361
[39] CFAST (2023). National Institute of Standards and Technology (NIST),The United States Department of Commerce. 17/105, Middletown, CT.
[40] Gaziray. https://tr.wikipedia.org/wiki/Gaziray. Erişim tarihi: 16 Mayıs 2023.
[41] National Fire Protection Association (NFPA) 130 (2023). Standard for Fixed Guideway Transit and Passenger Rail Systems. Avon, Massachusetts.
[42] Subway Environmental Design Handbook, Volume II, Subway Environment Simulation Computer Program, Version 4, Part 1, User's Manual.
[43] UNE EN 13848-1:2020. Railway applications - Track - Track geometry quality - Part 1: Characterization of track geometry.
[44] Subway Environmental Design Handbook. (1976). Volume I. Principles and Applications. Second Edition. Technical rept. NTIS Issue Number: 197619.
[45] Bakke A, Safety in Mines Research Establishment (Great Britain), Leach SJ (1960) Methane Roof Layers, Ministry of Power, Safety in Mines Research Establishment.
[46] Marmaray Project – Detailed Design Report for Tunnel Ventilation Analysis and Design.

J. Innovative Eng. Nat. Sci., c. 3, s. 2, ss. 191-204, 2023.
http://dx.doi.org/10.29228/JIENS.70384

Journal of Innovative Engineering and Natural Science
(Yenilikçi Mühendislik ve Doğa Bilimleri Dergisi)
journal homepage: https://jiens.org

Araştırma Makalesi

Eksik tahrikli döner ters sarkaç sisteminin geribeslemeli doğrusallaştırma tabanlı kademeli kontrolü

Aykut Kocaoğlu[a],*

[a]*Elektrik ve Enerji Bölümü, İzmir Meslek Yüksekokulu, Dokuz Eylül Üniversitesi, İzmir, 35380, TÜRKİYE.*

MAKALE BİLGİSİ

Makale Geçmişi:
Geliş 31 Mayıs 2023
Düzeltme 27 Haziran 2023
Kabul 10 Temmuz 2023

Çevrimiçi mevcut

Anahtar Kelimeler:
Kademeli kontrol
Geribeslemeli doğrusallaştırma
Döner ters sarkaç
Eksik tahrik
Doğrusal olmayan sistem

ÖZET

Kademeli kontrol, özellikle bozanetkenlere karşı performansı iyileştirmek için tercih edilen çok döngülü bir kontrol yapısıdır. Genellikle, iç döngü kontrolü (bağımlı kontrolör) ve dış döngü kontrolünden (ana kontrolör) oluşan ve bağımlı kontrolörün ayar noktasının, bu ana kontrolör tarafından ayarlandığı bir geri besleme kontroldür. Bu çalışmada, üzerine etki eden yerçekimi kuvvetleri, Coriolis ve merkezcil kuvvetlerden dolayı doğrusal olmayan dinamiğe sahip döner ters sarkaç sisteminin denetlenmesinde kademeli kontrol kullanılmıştır. Burada, bağımlı kontrolcü için geribeslemeli doğrusallaştırma tabanlı oransal-türevsel *(PD)* denetleyici ve ana kontrolcü içinse doğrusal karesel düzenleyici (DKD) kullanılmıştır. İç döngüde kullanılan geri beslemeli doğrusallaştırmanın bağıl derecesi ikidir ve kararsız sıfır dinamiklere sahiptir. Bu kararsız dinamikler ana kontrolcü tasarımında ele alınmış ve kademeli kontrolün kararlı olması sağlanmıştır. Ters sarkacın doğrusal olmayan dinamik denkleminde sarkaca uygulanabilen tork bozanetken olarak formüle edilmiştir. Önerilen geribeslemeli doğrusallaştırma tabanlı kademeli denetleyici, bozan etken varlığında iki farklı denetleyici ile karşılaştırılmış ve daha iyi performans sergilediği gösterilmiştir.

Feedback linearization-based cascade control of an underactuated rotary inverted pendulum system

ARTICLE INFO

Article history:
Received 31 May 2023
Received in revised form 27 Jun 2023
Accepted 10 July 2023

Available online

Keywords:
Cascaded control
Feedback linearization
Rotary inverted pendulum
Underactuated
Nonlinear System

ABSTRACT

The cascaded control is a multi-loop control structure that is particularly favored to improve performance against disturbances. It is usually a feedback control consisting of an inner loop (slave controller) and an outer loop (master controller), where the set point of the slave controller is set by this master controller. In this paper, a cascaded control strategy is employed to control a rotary inverted pendulum system with nonlinear dynamics due to gravitational, Coriolis and centripetal forces acting on it. Herein, a feedback linearization-based Proportional-Derivative (PD) controller is used for the slave controller and a linear quadratic regulator is used for the master controller. The feedback linearization employed in the inner loop has a relative degree of two and has unstable zero dynamics. These unstable dynamics are addressed in the main controller design and the whole cascaded control becomes stable. In the nonlinear dynamic equation of the inverted pendulum, the torque applied to the pendulum is formulated as a disturbance factor. The proposed feedback linearization-based cascade controller is compared with two different controllers in the presence of disturbances and shown to perform better.

---

* Sorumlu yazar. Tel.: +90-232-301-2641; e-mail: aykut.kocaoglu@deu.edu.tr

I. GİRİŞ

Her biri kendine özgü özelliklere ve uygulamalara sahip çeşitli ters sarkaç sistemleri vardır. Araba üzerindeki ters sarkaç çeşidinde sistem, arabaya bağlı serbest bir direk ile bir ray üzerinde bir arabadan oluşur [1, 2]. Amaç, direği dikey konumda dengede tutmak için arabanın hareketini kontrol etmektir. Çift ters sarkaç [3, 4] ise uç uca eklenmiş iki sarkaçtan oluşur ve amaç sistemi dikey konumda dengede tutmak için her iki sarkacın hareketini kontrol etmektir. Bir diğer ters sarkaç çeşidi ise, dikey eksende yer çekimine karşı koymaya çalışan iki bağlantılı bir sistemdir [3, 5]. Sadece, ikinci bağlantı noktasında aktüatör bulunmaktadır. Bu çalışmada kullandığımız döner ters sarkaç (Furuta sarkacı olarak da bilinir) ise en yaygın olan ters sarkaç çeşitleri arasında yer almaktadır ve dikey eksen etrafında her iki yönde de dönebilen motorlu bir pivota bağlı olan ve yatay bir eksen etrafında dönebilen bir sarkaçtan oluşur [6-8]. Amaç, sarkacı dikey konumda dengede tutmak için motor tahriki ile pivotu kontrol etmektir. Sarkaç tipik olarak döner kola uygulanan bir tork aracılığıyla dolaylı olarak kontrol edilir, bu da onu eksik tahrikli bir sistem yapar. Sistemin dinamikleri oldukça karmaşıktır ve çoklu denge noktasının varlığı ve salınımlar gibi birçok doğrusal olmayan davranış sergiler. Döner ters sarkacının kontrolü, doğrusal olmayan doğası ve sistemin eksik tahrikle çalıştırılması nedeniyle zorlu bir problemdir, bu da sistemi stabilize etmek ve istenen yörüngeleri elde etmek için gelişmiş kontrol stratejileri gerektirir. Bu zorluklara rağmen, döner ters sarkaç, yeni kontrol algoritmaları ve tekniklerinin geliştirilmesi için yararlı bir test ortamı sağladığından, kontrol teorisi ve robotikte kapsamlı bir şekilde incelenmiştir.

Klasik Kontrol Yaklaşımı olan PID kontrolü, basitliği ve etkinliği nedeniyle döner ters sarkacı stabilize etmek için yaygın olarak uygulanmıştır. [9-11] gibi çalışmalar farklı yaklaşımlarla PID kontrolörlerini uygulamış ve tatmin edici performans elde etmişlerdir. Kutup yerleştirme ve DKD gibi durum geri beslemeli kontrol teknikleri de döner ters sarkacı kontrol etmek için kullanılmıştır [12-14]. Yapılan çalışmalar, DKD tabanlı durum geri beslemeli kontrolün başarılı bir şekilde uygulandığını, gelişmiş stabilizasyon ve kontrol performansı elde edildiğini göstermektedir [13, 14]. Bulanık mantık kontrolü [15-16], döner ters sarkaç da dahil olmak üzere doğrusal olmayan ve karmaşık sistemlerin kontrolünde popülerlik kazanmıştır. Oh ve ark. [15] tarafından yapılan çalışmada kontrolör parametreleri hiyerarşik adil rekabet tabanlı genetik algoritma ile belirlenmiştir. Nguyen ve ark. [16] tarafından ise kayan kipli kontrol esnasında oluşan çatırdama etkisini azaltabilen ve kontrol performansını artırabilen bulanık tabanlı bir üstün burulma stabilizasyon algoritması önerilmiştir. Döner ters sarkacın kontrolü için sinir ağlarının kullanımı umut verici sonuçlar göstermiştir. Soydemir ve ark. [7] ve Bulucu ve ark. [8] tarafından yapılan çalışmalarda, sistem dinamikleri içerisinde doğrusal olmayan kısımları öğrenmek ve uygun kontrol girişini elde etmek için sinir ağı kontrolörleri kullanılmıştır. Kayan kipli kontrol, bozanetken ve belirsizliklere karşı sağlamlığı ile bilinir. Birçok çalışmada, döner ters sarkacı stabilize etmek için kayan kipli kontrolünü başarıyla kullanılmış ve bozanetken reddi gösterilmiştir [16, 17]. Kademeli kontrol, iç içe geçmiş bir yapıda iki veya daha fazla kontrolörün kullanılmasını içerir; burada dış döngü kontrolörünün çıkışı, iç döngü kontrolörü için ayar noktası haline gelir. Akhtaruzzaman ve Shafie [9] tarafından yapılan çalışmada iki PID kontrolörü ile kademeli kontrol yapılmıştır. Güneş ve ark. [6] tarafından ise geribeslemeli doğrusallaştırmayla beraber iki PID kontrolör kademeli olarak uygulanmıştır.

Bu çalışmada döner ters sarkaç sisteminin stabilizasyonu için geribeslemeli doğrusallaştırma tabanlı kademeli kontrolü önerilmiştir. Önerilen bu yöntemde, iç döngü kontrolörü olarak geribeslemeli doğrusallaştırma ve PD kontrolör kullanılırken, dış döngü kontrolörü olarak da DKD kullanılmıştır. İç döngü kontrolörü döner kolu kontrol etmekten sorumluyken, dış döngü kontrolörü sarkacı stabilize etmeye odaklanmaktadır. Güneş ve ark. [6] tarafından bağımlı kontrol için sarkaç açısı geri beslenmiştir. Fakat kademeli kontrol tasarımında iç döngü dış döngüden daha hızlı çalışmalı ve ana kontrolörün belirlediği ayar değerine hızlı tepki vererek sistemi kontrol etmelidir. Bu sebeple, önerilen yöntemde Güneş ve ark. [6] tarafından yapılan çalışmadan farklı olarak kademeli kontrolör tasarlama gereksinimlerini karşılayacak şekilde bağımlı kontrol için döner kol açısı geri beslenmiştir. Ayrıca, önerilen yöntemde, kontrol parametrelerini belirlemek için genetik algoritma gibi yüksek işlem yükü gerektiren bir yöntem [6] yerine, kontrol parametrelerinin doğrudan hesaplanabildiği işlem yükü daha az yöntemler kullanılmıştır. Önerilen yöntem, standart DKD ve Güneş ve ark. [6] yaptığı çalışmadaki kademeli kontrolör ile karşılaştırılmış ve daha iyi performans sergilediği gösterilmiştir. Ek olarak, önerilen geri besleme tabanlı kademeli kontrol yaklaşımı bozanetken varlığında da daha iyi performans göstermektedir.

II. DÖNER TERS SARKAÇ SİSTEMİ VE MATEMATİKSEL MODELİ

Ters sarkaç sistemleri üzerine etki eden kuvvetler hesaba katıldığında doğrusal olmayan sistemlerdir. Her ters sarkaç sistemi kontrol etmek istenildiğinde farklı zorluklara sahiptir ve sistemi dengede tutmak için farklı kontrol stratejileri gerekmektedir. Döner ters sarkaç, serbestlik derecesinden daha az kontrol girdisine sahip bir dinamik sistem olduğu için eksik tahrikli bir sistemdir. Şekil 1'de döner sarkaç sisteminin temsili bir görseli verilmiştir. Burada, döner kol bir motora bağlı iken sarkaç serbesttir ve hareketi dolaylı olarak döner kol üzerinden sağlanmaktadır.

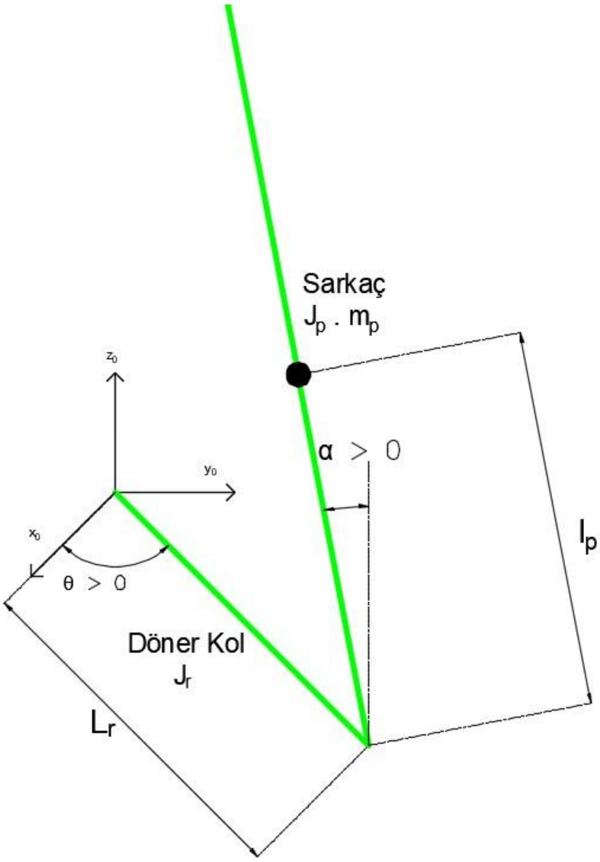

Şekil 1. Döner ters sarkacın basitleştirilmiş çizimi

2.1 Döner Ters Sarkaç Sistemine ait Hareket Denklemleri

Döner ters sarkaç sisteminde hareket denklemleri, detaylarına Balula [18] tarafından yapılan çalışmadan ulaşılabileceği şekilde Lagrange mekaniği kullanarak aşağıdaki gibi türetilebilir.

$$\begin{aligned}&\ddot{\theta}\big(J_0+J_2\sin^2(\alpha)\big)+\dot{\alpha}\dot{\theta}J_2\sin(2\alpha)+\dot{\alpha}^2m_pl_pL_r\sin(\alpha)-\ddot{\alpha}m_pl_pL_r\cos(\alpha)=\tau_1-B_1\dot{\theta}\\&-\ddot{\theta}m_pl_pL_r\cos(\alpha)-\dot{\theta}^2\frac{1}{2}J_2\sin(2\alpha)+\ddot{\alpha}J_2-m_pl_pg\sin(\alpha)=\tau_2-B_2\dot{\alpha}\end{aligned}\tag{1}$$

Burada θ döner kol açısı, $\dot{\theta}$ bu kolun açısal hızı, $\ddot{\theta}$ döner kola ait açısal ivme, α sarkaç açısı, $\dot{\alpha}$ sarkacın açısal hızı, $\ddot{\alpha}$ sarkaca ait açısal ivme ve g yerçekiminden kaynaklanan ivmedir. m_p, l_p ve L_r'de Şekil 1'de gösterildiği gibi sırasıyla sarkacın kütlesini, sarkacın kütle merkezinin bağlantı noktasına olan uzaklığını ve döner kolun uzunluğunu temsil etmektedir. B_1 taban ve döner kol arasındaki sürtünme katsayısıdır. B_2 döner kol ve sarkaç arasındaki sürtünme katsayısıdır. Ayrıca, J_0 döner kolun ve sarkacın ana eklemdeki atalet momentini ifade etmektedir ve döner kolun kütle merkezindeki atalet momenti bileşeni J_r cinsinden $J_0=J_r+m_p{L_r}^2$ olarak tanımlanabilir. J_2 sarkaç eklemindeki atalet momentini ifade etmektedir ve sarkacın kütle merkezindeki atalet momenti bileşeni J_p cinsinden $J_2=J_p+m_p{l_p}^2$ olarak tanımlanabilir. τ_1, motor tarafından uygulanan torktur. τ_2 ise sarkaca uygulanan bozanetkene ait torku ifade etmektedir.

2.2 Döner Ters Sarkacının Doğrusal Olmayan Durum Uzay Gösterimi

(1)'deki denklemler döner kol ve sarkaç arasındaki sürtünmenin ihmal edildiği durumda $(B_2=0)$ açısal ivmeler yalnız bırakılarak aşağıdaki gibi yazılabilir.

$$\begin{bmatrix}\ddot{\theta}\\\ddot{\alpha}\end{bmatrix}=\begin{bmatrix}J_0+J_2\sin^2(\alpha) & -m_pl_pL_r\cos(\alpha)\\-m_pl_pL_r\cos(\alpha) & J_2\end{bmatrix}^{-1}\begin{bmatrix}\tau_1-B_1\dot{\theta}-\dot{\alpha}\dot{\theta}J_2\sin(2\alpha)-\dot{\alpha}^2m_pl_pL_r\sin(\alpha)\\\tau_2+\dot{\theta}^2\frac{1}{2}J_2\sin(2\alpha)+m_pl_pg\sin(\alpha)\end{bmatrix}\tag{2}$$

Burada, durum uzay değişkenleri $x_1=\theta,\ x_2=\dot{\theta},\ x_3=\alpha$ ve $x_4=\dot{\alpha}$ olarak tanımlanarak ve (2)'deki denklem kullanılarak aşağıdaki durum uzay denklemi elde edilebilir.

$$\begin{aligned}\dot{x}_1&=x_3\\\dot{x}_2&=x_4\end{aligned}\tag{3}$$

$$\dot{x}_3 = \frac{m_p l_p L_r \cos(x_2)\left(\frac{J_2 \sin(2x_2){x_3}^3}{2} + \tau_2 + m_p l_p g \sin(x_2)\right)}{{J_2}^2 \sin^2(x_2) + J_0 J_2 - \left(m_p l_p L_r \cos(x_2)\right)^2} - \frac{J_2\left(m_p l_p L_r \sin(x_2){x_4}^2 + J_2 x_3 x_4 \sin(2x_2) - \tau_1 + B_1 x_3\right)}{{J_2}^2 \sin^2(x_2) + J_0 J_2 - \left(m_p l_p L_r \cos(x_2)\right)^2}$$

$$\dot{x}_4 = \frac{\left(J_0 + J_2 \sin^2(x_2)\right)\left(\frac{J_2 \sin(2x_2){x_3}^2}{2} + \tau_2 + m_p l_p g \sin(x_2)\right)}{{J_2}^2 \sin^2(x_2) + J_0 J_2 - \left(m_p l_p L_r \cos(x_2)\right)^2} - \frac{m_p l_p L_r \cos(x_2)\left(m_p l_p L_r \sin(x_2){x_4}^2 + J_2 x_3 x_4 \sin(2x_2) - \tau_1 + B_1 x_3\right)}{{J_2}^2 \sin^2(x_2) + J_0 J_2 - \left(m_p l_p L_r \cos(x_2)\right)^2}$$

Döner ters sarkaç sisteminde DC motor kullanılmaktadır ve motor torkunun ifadesi $\tau_1 = \eta_m \eta_g K_t K_g \left(V_m - K_g K_m x_3\right)/R_m$ (3)'deki denklemde yerine koyularak durum uzay gösterimi motor voltajı V_m'in giriş olduğu durum için aşağıdaki gibi yazılabilir. Burada η_m motorun verimliliğini, η_g dişli kutusu verimliliği, K_t motor tork sabiti, K_g motor dişli oranı, K_m motor voltaj sabiti ve R_m motorun armatür direncidir. Motora ve döner ters sarkaca ait bu değerler Tablo 1'de verilmiştir.

$$\dot{x} = f(x) + g(x)V_m + d(x)\tau_2 \tag{4}$$

Burada, $x = [x_1\ x_2\ x_3\ x_4]^T$, $f(.): R^4 \to R^4$, $g(.): R^4 \to R^4$, $d(.): R^4 \to R^4$ olarak tanımlanan fonksiyonlardır ve aşağıda açık halleri verilmiştir:

$$f(x) = \begin{bmatrix} x_3 \\ x_4 \\ \dfrac{-J_2\left(J_2 x_3 x_4 \sin(2x_2) + \frac{K_m K_t n_g n_m {K_g}^2 x_3}{R_m} - m_p l_p L_r \sin(x_2)\cos^2(x_2){x_3}^2 + B_1 x_3 + m_p l_p L_r \sin(x_2){x_4}^2 - \frac{{m_p}^2 {l_p}^2 L_r g \sin(2x_2)}{2}\right)}{{J_2}^2 \sin^2(x_2) + J_0 J_2 - \left(m_p l_p L_r \cos(x_2)\right)^2} \\ \dfrac{{J_2}^2 x_3 x_4 \sin(2x_2) + \frac{K_m K_t n_g n_m J_2 {K_g}^2 x_3}{R_m} - m_p l_p L_r\left(\sin(x_2)\cos^2(x_2)\right)J_2 {x_3}^2 + B_1 J_2 x_3 + m_p l_p L_r \sin(x_2) J_2 {x_4}^2 - \frac{{m_p}^2 {l_p}^2 L_r g \sin(2x_2)}{2}}{-R_m\left({J_2}^2 \sin^2(x_2) + J_0 J_2 - \left(m_p l_p L_r \cos(x_2)\right)^2\right)} \end{bmatrix},$$

$$g(x) = \begin{bmatrix} 0 \\ 0 \\ \dfrac{J_2 K_g K_t n_g n_m}{R_m\left({J_2}^2 \sin^2(x_2) + J_0 J_2 - \left(m_p l_p L_r \cos(x_2)\right)^2\right)} \\ \dfrac{K_g K_t n_g n_m m_p l_p L_r \cos(x_2)}{R_m\left({J_2}^2 \sin^2(x_2) + J_0 J_2 - \left(m_p l_p L_r \cos(x_2)\right)^2\right)} \end{bmatrix}, \quad d(x) = \begin{bmatrix} 0 \\ 0 \\ \dfrac{m_p l_p L_r \cos(x_2)}{\left({J_2}^2 \sin^2(x_2) + J_0 J_2 - \left(m_p l_p L_r \cos(x_2)\right)^2\right)} \\ \dfrac{J_0 + J_2 \sin^2(x_2)}{\left({J_2}^2 \sin^2(x_2) + J_0 J_2 - \left(m_p l_p L_r \cos(x_2)\right)^2\right)} \end{bmatrix}.$$

Ayrıca, motor voltajı V_m kontrol girişini ve sarkaca uygulanan tork τ_2 bozanetkeni temsil etmektedir.

III. KONTROLÖR TASARIMI

(4)'deki denklemde ters sarkaca ait doğrusal olmayan dinamik denklem verilmiştir. Bu bölümde, bozanetken ihmal edilerek elde edilen (5)'te tanımlanan sistemin matematiksel modeli kullanılarak geribeslemeli doğrusallaştırma tabanlı kademeli kontrolü tasarlanmıştır.

$$\begin{aligned} \dot{x} &= f(x) + g(x)V_m \\ y &= h(x) = x_1 \end{aligned} \tag{5}$$

Bu kademeli kontrolde iç döngü kontrolü (bağımlı kontrolör) olarak döner kol açısının çıkış olarak alındığı giriş-çıkış geribeslemeli doğrusallaştırma ile birlikte PD kontrolör uygulanmıştır. İç döngüde kullanılan geri beslemeli doğrusallaştırmanın bağıl derecesi ikidir ve uygulanan PD kontrolör ile döner kol açısı ve hızının kontrolü amaçlanmıştır. Fakat, geribeslemeli doğrusallaştırma tabanlı bu iç döngü kontrol sistemi kararsız sıfır dinamiklere sahiptir. Bu sebeple ana kontrolcü olarak kullanılan doğrusal karesel düzenleyici ile iç döngüde bulunan kontrol sisteminin referans denge noktası civarında kararlı olması sağlanacak şekilde tasarlanmış ve bu sayede kararsız dinamikler ele alınarak kademeli kontrolün kararlı olması sağlanmıştır. Bu kontrolörlerin detayları aşağıdaki alt bölümlerde açıklanmıştır.

3.1 İç Döngü (Bağımlı) Kontrolör Tasarımı

Geribeslemeli doğrusallaştırma, doğrusal olmayan bir dinamik sistemi geri besleme kullanarak eşdeğer bir doğrusal sisteme dönüştüren bir kontrol sistemi tasarım tekniğidir. Bu çalışmada tek girişli tek çıkışlı ters sarkaç sisteminin (5)'deki doğrusal olmayan durum uzay gösterimi kullanılarak giriş-çıkış geribeslemeli doğrusallaştırma yapılmıştır. Bu sayede elde edilen doğrusal sisteme iyi tanımlı doğrusal kontrol yöntemleri uygulanabilmektedir.

Herhangi bir $\boldsymbol{x} \in D_0$ için aşağıdaki koşullar sağlanıyorsa (5) doğrusal olmayan sisteminin $D_0 \subset D$ bölgesinde r bağıl derecesine sahip olduğu söylenir [19]:

$$\begin{aligned} &L_g L_f^i h(x) = 0, \qquad i \in \{0,1,\cdots,r-2\} \\ &L_g L_f^{r-1} h(x) \neq 0 \end{aligned} \tag{6}$$

Burada, $L_f h(x)$ Lie türevi olarak adlandırılır ve $L_f^k h(x) = L_f L_f^{k-1} h(x) = \frac{\partial}{\partial x}\left(L_f^{k-1} h(x)\right) f(x)$ ve $L_g L_f^k h(x) = \frac{\partial}{\partial x}\left(L_f^k h(x)\right) g(x)$ olarak tanımlıdır. Eğer bir sistem r bağıl derecesine sahipse, çıkışın r'inci türevi aşağıdaki gibi yazılabilir.

$$y^{(r)} = L_f^r h(x) + L_g L_f^{r-1} h(x) u \tag{7}$$

Dolayısıyla, (7) aşağıdaki kontrol girişi ile giriş-çıkış doğrusallaştırılabilir

$$u = \frac{1}{L_g L_f^{r-1} h(x)} \left(-L_f^r h(x) + v\right) \tag{8}$$

ve (8)'deki kontrol girişinin (7)'ye uygulanmasıyla aşağıdaki doğrusallaştırılmış sistem elde edilir.

$$y^{(r)} = v \tag{9}$$

İç döngü kontrolcü tasarımında (5)'de gösterildiği gibi çıkış döner kol açısı olarak alınmış ve (6) kullanılarak bağıl derece 2 olarak hesaplanmıştır. Bu durumda bağımlı kontrol için geribeslemeli doğrusallaştırma girişi aşağıdaki gibi hesaplanmıştır.

$$\begin{aligned} u &= \frac{1}{L_g L_f^1 h(x)} \left(-L_f^2 h(x) + v\right) = \\ &= \frac{1}{g_3(x)} (-f_3(x) + v) \end{aligned} \tag{10}$$

Burada, v doğrusallaştırılmış sisteme ait yeni kontrol girişi, $f_3(x)$ (5)'deki $f(x)$ vektörel fonksiyonunun 3. elemanı ve $g_3(x)$ ise (5)'deki $g(x)$ vektörel fonksiyonunun 3. elemanıdır. (10)'daki kontrol girişi ile doğrusallaştırılan sisteminin kontrolü için Şekil 1'de gösterildiği gibi PD kontrolü seçilmiş ve yeni giriş:

$$\begin{aligned} v &= K_{\boldsymbol{p}}(r - \theta) + K_d\left(r - \dot{\theta}\right) \\ &= K_{\boldsymbol{p}}(r - x_1) + K_d(\dot{r} - x_3) \end{aligned} \tag{11}$$

olmuştur.

3.2 Dış Döngü (Ana) Kontrolör Tasarımı

Bağımlı kontrolörde uygulanan geribeslemeli doğrusallaştırma tabanlı kontrolün referans girişi Şekil 2'de gösterildiği gibi ana kontrolör tarafından belirlenmektedir ve ana kontrolör olarak doğrusal karesel düzenleyici kullanılmıştır. Sürekli zamanlı sistemler için DKD, $\dot{\boldsymbol{x}} = \boldsymbol{A}\boldsymbol{x} + \boldsymbol{B}\boldsymbol{u}$ kısıtı altında $J(\boldsymbol{u}) = \int_0^\infty (\boldsymbol{x}^T\boldsymbol{Q}\boldsymbol{x} + \boldsymbol{u}^T\boldsymbol{R}\boldsymbol{u})dt$ ikinci dereceden bir maliyet fonksiyonunu en aza indirerek dinamik bir sistemi kontrol etmek için $u = -\boldsymbol{Kx}$ durum geribesleme kontrolündeki kazanç değerinin $(\boldsymbol{K})$ belirlenmesini sağlar [20]. DKD'nin uygulanabilmesi için (5)'teki sisteme bağımlı kontrolör tarafından uygulanan (10) ve (11)'deki kontrol girişleri ile elde edilen iç döngü kontrol sistemi, $[x_1 \quad x_2 \quad x_3 \quad x_4 \quad r \quad \dot{r}] = [0 \quad 0 \quad 0 \quad 0 \quad 0 \quad 0]$ denge noktası civarında aşağıda ifadesi verildiği üzere doğrusallaştırılmıştır:

$$\dot{x} = Ax + bv. \tag{12}$$

Burada $A = \begin{bmatrix} 0 & 0 & 1 & 0 \\ 0 & 0 & 0 & 1 \\ -K_{\boldsymbol{p}} & 0 & -K_d & 0 \\ \frac{-K_p m_p l_p L_r}{J_2} & \frac{m_p l_p g}{J_2} & \frac{-K_d m_p l_p L_r}{J_2} & 0 \end{bmatrix}$ ve $b = \begin{bmatrix} 0 \\ 0 \\ K_{\boldsymbol{p}} \\ \frac{K_p m_p l_p L_r}{J_2} \end{bmatrix}$'dir. Şekil 1'de DKD'nin ana kontrolör olarak uygulanması gösterilmiştir. Bu ana kontrol, iç döngü kontrol sisteminin dinamiklerini baz alarak tasarlandığı için bağımlı kontrolörde uygulanan geribeslemeli doğrusallaştırma tabanlı kontrol sonucu oluşan kararsız dinamiklerin toplam kademeli kontrolde kararlı olması sağlanmıştır.

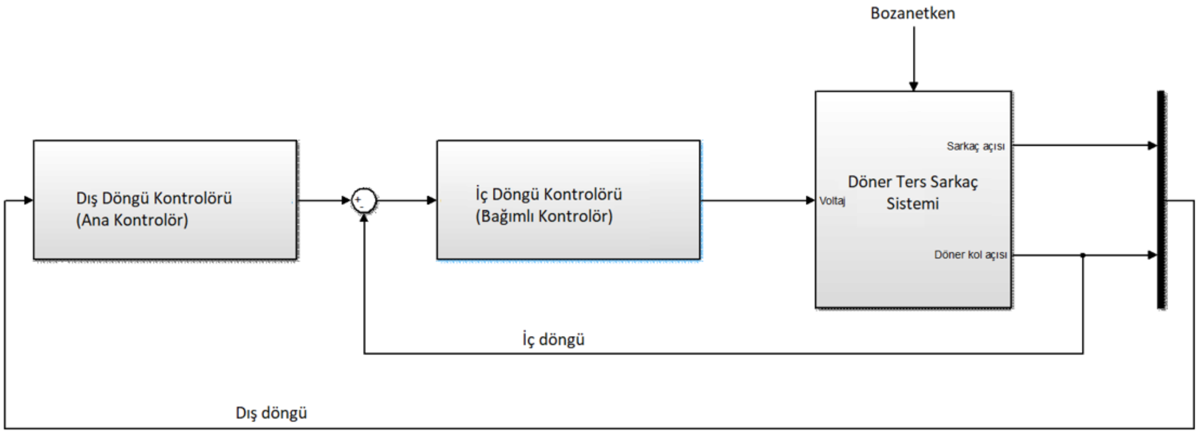

Şekil 2. Döner ters sarkaç sistemi için önerilen kademeli kontrolün blok diyagramı

IV. BENZETİM SONUÇLARI

Döner ters sarkacın kontrolü için şematik olarak Şekil 3'te önerilen geribesleme tabanlı kademeli kontrol yöntemi iki kontrol yöntemi ile karşılaştırılmıştır. Bunlardan biri Şekil 4'te gösterildiği gibi Güneş ve ark. [6] yaptığı çalışmadan alınan kademeli kontrol yöntemidir. Diğeri ise Şekil 5'teki standart kontrol yöntemi olan DKD'dir. Tablo 1'de döner ters sarkaç sistemine ait parametrelerin açıklamaları ve benzetimde kullanılan değerleri verilmiştir.

Tablo 1. Döner ters sarkaç sistemine ait parametrelerin açıklamaları ve benzetimde kullanılan değerler.

Sembol	Açıklama	Değerler
m_p	Sarkacın kütlesi	0.125 *kg*
l_p	Sarkacın kütle merkezinin bağlantı noktasına olan uzaklığı	0.1675 *m*
L_r	Döner kolun uzunluğunu	0.215 *m*
J_0	Döner kolun ve sarkacın ana eklemdeki atalet momenti	0.0091 $kg.m^2$
J_2	Sarkaç eklemindeki atalet momenti	0.0047 $kg.m^2$
g	Yer çekimi ivmesi	9.81 m/s^2
B_1	Taban ve döner kol arasındaki sürtünme katsayısı	0.0077 *N.m.s/rad*
η_m	Motor verimliliği	0.69
η_g	Dişli kutusu verimliliği	0.9
K_t	Motor tork sabiti	0.0077 *N.m/A*
K_g	Motor dişli oranı	70
K_m	Motor voltaj sabiti	0.0077 *V/(rad/s)*
R_m	Motor armatür direnci	2.6 *Ω*

Bu parametreler Güneş ve ark. [6] tarafından elde edilen sonuçla karşılaştırabilmek için bahsedilen bu çalışmadan alınmıştır. Benzetimler MATLAB R2022b ile Simulink kullanılarak yapılmıştır. Döner ters sarkaç sisteminin motor voltaj değerleri -12 V ve +12 V ile sınırlandırılmıştır. Bu yöntemler içerisinde bulunan DKD'nin tasarımında kullanılan **Q** ve **R** değerleri sırasıyla

$$\begin{bmatrix} 10 & 0 & 0 & 0 \\ 0 & 10 & 0 & 0 \\ 0 & 0 & 10 & 0 \\ 0 & 0 & 0 & 10 \end{bmatrix} \text{ ve 1 olarak seçilmiştir.}$$

Böylece önerilen yöntem için DKD kazancı $\boldsymbol{K} = [-4.3166 \quad 87.9655 \quad -5.9349 \quad 13.6371]$ ve karşılaştırılan DKD için ise $K = [-3.1623 \quad 60.98 \quad -4.81 \quad -9.4968]$ olarak bulunmuştur. Şekil 4'teki kademeli kontrolde iç ve dış döngülerde bulunan PID kontrolör parametreleri ise Güneş ve ark. [6] yaptığı çalışmadan alınmıştır. Önerilen yöntemde, bağıl derecesi 2 olan geribeslemeli doğrusallaştırma sonucu elde edilen (9)'daki sistem için iç döngüde kullanılan PD parametreleri $K_p = 3.1623$ ve $K_d = 4.04$, DKD tabanlı optimal değerler olarak hesaplanmıştır [21,22].

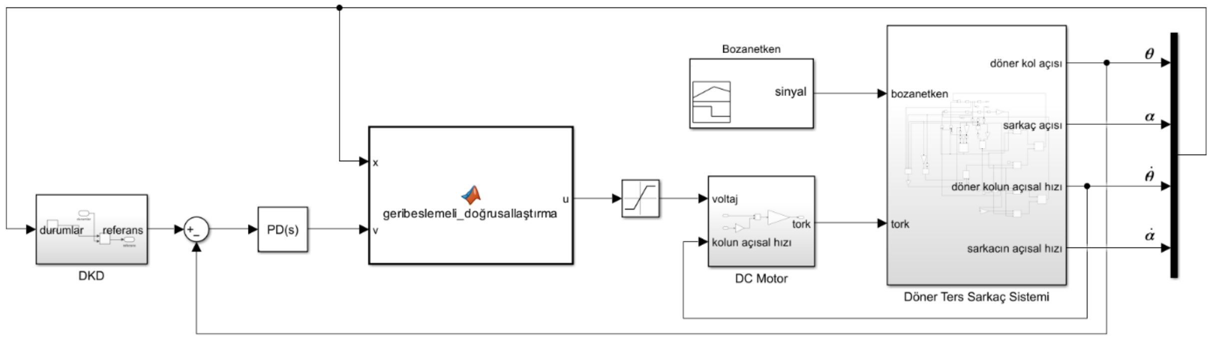

Şekil 3. Döner ters sarkacın önerilen geribesleme doğrusallaştırma tabanlı kademeli kontrolü

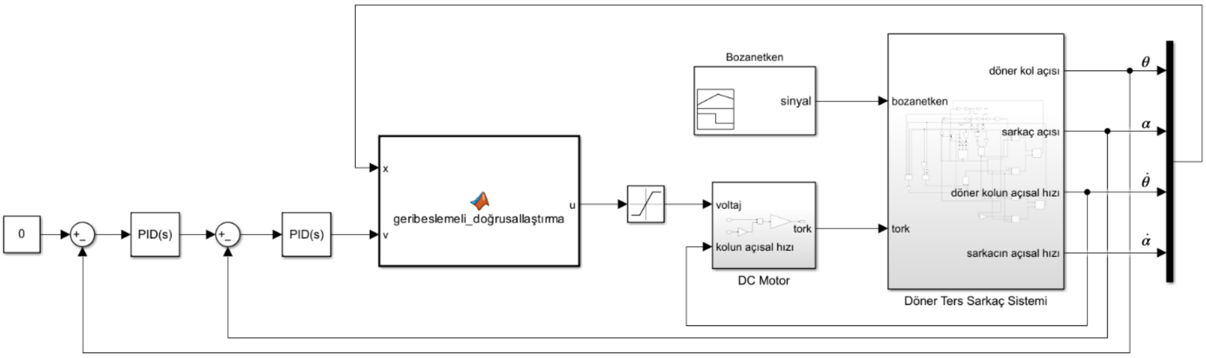

Şekil 4. Döner ters sarkacın Güneş ve ark. [6] yaptığı çalışmada tanıtılan kademeli kontrolü

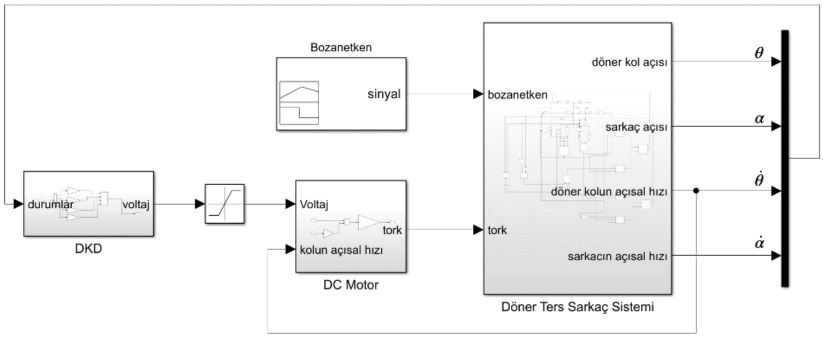

Şekil 5. Döner ters sarkacın doğrusal karesel düzenleyici ile kontrolü

Kademeli kontrolörde ana kontrolörün çıkışı, bağımlı kontrolörün referansıdır ve iç döngü kontrol değişkeninin dış döngü kontrol değişkeninden daha hızlı çalışması gerekir. Bu dış döngünün, iç döngü kontrol sistemindeki bozanetkeni telafi etmek için yeterli zamana sahip olmasını sağlar. Ayrıca, bu iç döngünün kontrol değişkeni dış döngünün kontrol değişkenini etkileyebilmelidir. Şekil 4'teki kademeli kontrolde iç döngü kontrolörü ile sarkaç açısı kontrol edilmekte ve bahsedilen koşullar sağlanmamaktadır. Şekil 3'te önerilen kademeli kontrolörde ise iç döngü kontrolörü ile döner kol açısı üzerinden PD kontrolü çalışmaktadır. Döner kolun daha hızlı çalışması ve sarkaçta oluşan bozanetkene karşı bu hızlı tepki, dış döngü kontrolörü ile sarkaç açısının Tablo 2'de gösterildiği gibi 5.1636x10^{-4} en düşük Ortalama Karesel Hata (OKH) değeri ile daha iyi bir performansla kontrol edilmesini sağlamaktadır. Şekil 6'daki bozanetken döner sarkaca (4)'deki matematiksel modelde gösterildiği gibi τ_2 üzerinden uygulanmıştır performans iyileştirilmesi Şekil 7'de gösterilmiştir. Burada karşılaştırılan kademeli kontrolörün bozanetkene karşı Tablo 2'de belirtilen 20x10^{-4} en yüksek OKH değeri ile sağlam olmadığı gözlenmektedir. Önerilen yöntem ise kademeli kontrolör gereksinimlerine uygun olarak tasarlanmasıyla bu bozanetkene karşı Şekil 7 ve Tablo 2'de gösterildiği gibi daha sağlam bir cevap sergilemiştir. Önerilen yöntem Şekil 5'teki standart DKD ile de karşılaştırılmış ve sarkaç açısının kontrolünde daha iyi performans gösterdiği Şekil 7'de gösterilmiştir. Sarkaç açısının OKH cinsinden elde edilen değerleri Tablo 2'de verilmiştir. Bu değerlere göre önerilen geribeslemeli doğrusallaştırma tabanlı kademeli kontrol yönteminin bozanetken olmadığı ve olduğu her iki durumda sırasıyla elde edilen 9.3066x10^{-5} ve 5.1636x10^{-4} OKH değerleriyle en iyi performansı sergilediği gözlenmiştir. Sarkacın stabilizasyonu esnasında döner kol açısının zamanla değişimi Şekil 8'de verilmiştir. Ayrıca, önerilen yöntemdeki iç döngüde kullanılan geribeslemeli doğrusallaştırma ile bağıl derecesi 2 olacak şekilde giriş-çıkış doğrusallaştırma yapılmış ve bu doğrusal sistem için iyi tanımlı bir PD kontrolör elde edilmesi sağlanmıştır. İç döngüdeki bağımlı kontrolörün döner kol açısını kontrol edecek şekilde ayarlanmasıyla, eksik tahrik olan sistem tek giriş-tek çıkış olacak şekilde bir iç döngü kontrol sistemi oluşturmuştur. Böylece, dış döngüde kullanılan DKD ile bu iç döngü kontrol sistemi ele alınmış ve iç döngü kontrol sistemindeki kararsız iç dinamiklerle birlikte toplam sistemin denge noktası civarında kararlı olması sağlanmıştır.

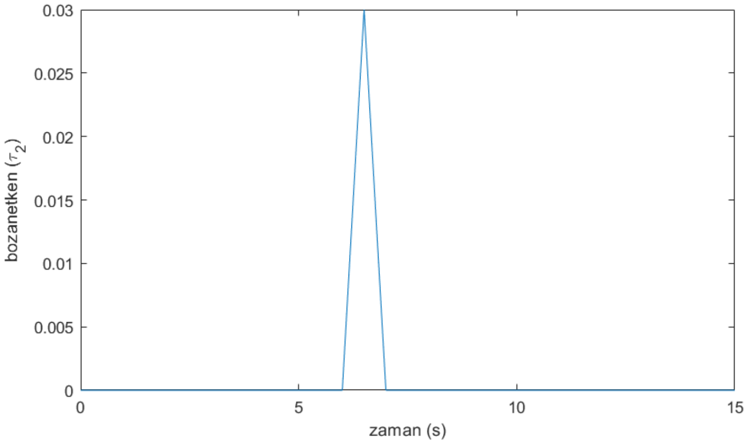

Şekil 6. Sarkaca uygulanan bozanetkene ait tork: (4)'teki sistem dinamiklerinde τ_2 olarak tanımlanmıştır.

Tablo 2. Döner ters sarkaç sisteminin stabilizasyonunda farklı kontrol sistemlerine ait sarkaç açısı için hesaplanan KOKH değerleri.

Kontrolör	Bozanetken olmadığında OKH	Bozanetken olduğunda OKH
Önerilen Kademeli Kontrolör	$9.3066\text{x}10^{-5}$	$5.1636\text{x}10^{-4}$
Kademeli Kontrolör	$26.421\text{x}10^{-5}$	$20\text{x}10^{-4}$
DKD	$9.6920\text{x}10^{-5}$	$5.8641\text{x}10^{-4}$

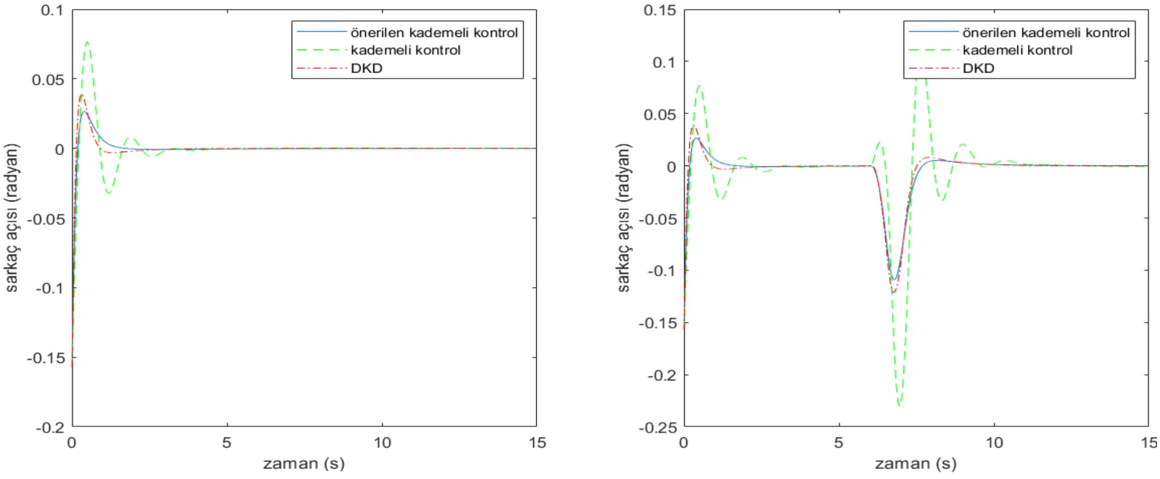

(a) **(b)**

Şekil 7. Döner ters sarkacın üç farklı kontrolör ile denge noktasında stabilizasyonunu esnasında sarkaç açısının zamanla değişimi **(a)** Sarkaçta bozanetken olmadığında **(b)** Sarkaçta bozanetken olduğunda

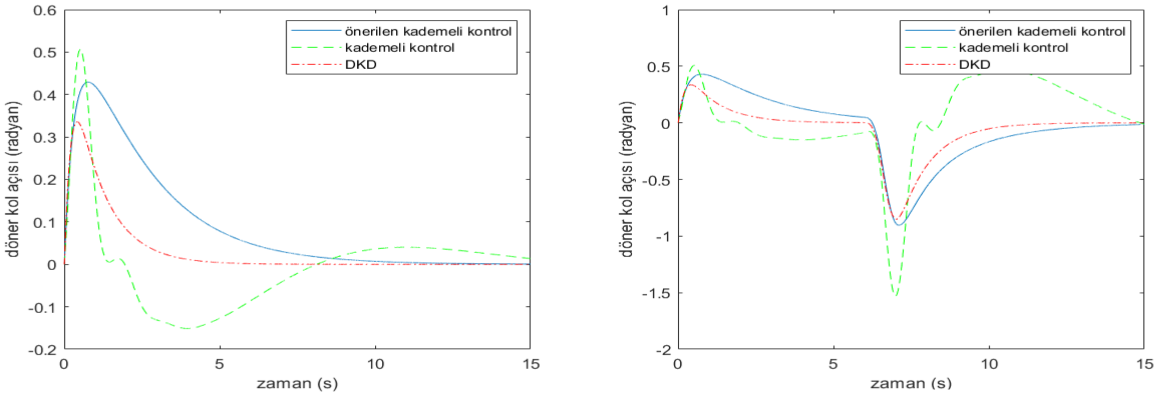

(a) **(b)**

Şekil 8. Döner ters sarkacın üç farklı kontrolör ile denge noktasında stabilizasyonunu esnasında döner kol açısının zamanla değişimi **(a)** Sarkaçta bozanetken olmadığında **(b)** Sarkaçta bozanetken olduğunda

IV. SONUÇLAR

Bu çalışmada, döner ters sarkaç sisteminin stabilizasyonu için geribeslemeli doğrusallaştırma tabanlı kademeli bir kontrol yöntemi önerilmiştir. Bu kontrol yöntemi, biri yine kademeli kontrolör diğeri ise standart DKD ile karşılaştırılmıştır. Önerilen kontrol, kademeli kontrolör tasarlama gereksinimlerini karşılamaktadır ve sarkaca uygulanan bozanetkene karşı daha sağlam olduğu gösterilmiştir. İki ayrı kontrolörle performansları karşılaştırılmış ve Tablo 2'de sunulan en düşük $9.3066x10^{-5}$ ve $5.1636x10^{-4}$ OKH değerleriyle daha iyi sonuçlar elde edilmiştir. Önerilen bu yöntemdeki iç döngü kontrolörü ile sistem bağıl derecesi 2 olacak şekilde doğrusallaştırılmış ve eksik tahrik olan sistem bu bağımlı kontrolör sayesinde tek giriş-tek çıkış olacak şekilde bir iç döngü kontrol sistemi oluşturmuştur. Böylece dış döngü kontrolörü için DKD yerine tek giriş-tek çıkış sistemler için özel olarak tasarlanan diğer kontrol yöntemleri uygulanabilir ve performans daha da iyileştirilebilir. Ayrıca, kademeli kontrol ile makine öğrenimi ve veri odaklı kontrol yaklaşımlarının entegrasyonu ve döner sarkaç için gelişmiş kontrol stratejileri geliştirmek üzere bu tekniklerin kombinasyonunu daha sonraki çalışmalarda keşfedebilir.

KAYNAKLAR

[1] Aguilar-Ibáñez C, Mendoza-Mendoza J, Dávila J (2014) Stabilization of the cart pole system: by sliding mode control. Nonlinear Dyn 78:2769–2777. https://doi.org/10.1007/s11071-014-1624-6

[2] Manrique Escobar CA, Pappalardo CM, Guida D (2020) A parametric study of a deep reinforcement learning control system applied to the swing-up problem of the cart-pole. Appl Sci-Basel 10(24):9013. https://doi.org/10.3390/app10249013

[3] Inoue A, Deng MC (2009) Non-linear control of under-actuated mechanical systems**.** Int J Modell Identif Control 6(1):32-39. https://doi.org/10.1504/IJMIC.2009.023528

[4] Mehedi IM, Al-Saggaf UM, Mansouri R, Bettayeb M (2019) Stabilization of a double inverted rotary pendulum through fractional order integral control scheme. Int J Adv Rob Syst 16(4). https://doi.org/10.1177/1729881419846741

[5] Peng Z, Xin X, Liu Y (2023) Energy-based swing-up control for a two-link underactuated robot with flexible first joint. Nonlinear Dyn 111:289–302. https://doi.org/10.1007/s11071-022-07831-7

[6] Güneş U, Sel A, Kürkçü B, Kasnakoğlu C (2020) A comparison of H-infinity-synthesis and feedback linearization for rotary inverted pendulum. 11th International Conference on Mechanical and Aerospace Engineering (ICMAE), Athens, GREECE, Jul. 14–17. https://doi.org/10.1109/ICMAE50897.2020.9178849

[7] Soydemir MU, Şahin S, Bulucu P, Kocaoğlu A, Güzeliş C (2019) Learning feedback linearization based stable robust adaptive NARMA controller design for rotary inverted pendulum. 11th International Conference on Electrical and Electronics Engineering (ELECO), Bursa, Turkey, 795-799. https://doi.org/10.23919/ELECO47770.2019.8990417
[8] Bulucu P, Soydemir MU, Şahin S, Kocaoğlu A, Güzeliş C (2019) Performance analysis of stable adaptive NARMA controller scheme for furuta pendulum. 23rd International Conference on System Theory, Control and Computing (ICSTCC), Sinaia, Romania, 350-354. https://doi.org/10.1109/ICSTCC.2019.8885779
[9] Akhtaruzzaman M, Shafie AA (2010) Modeling and control of a rotary inverted pendulum using various methods, comparative assessment and result analysis. IEEE International Conference on Mechatronics and Automation, Xi'an, China, 1342-1347. https://doi.org/10.1109/ICMA.2010.5589450
[10] Demirtaş M, Altun Y, İstanbullu A (2013) Virtual laboratory for sliding mode and PID control of rotary inverted pendulum. Comput Appl Eng Educ 21: 400-409. https://doi.org/10.1002/cae.20484
[11] Tang TF, Chong SH, Pang KK (2019) Stabilisation of a rotary inverted pendulum system with double-PID and LQR control: experimental verification. Int J Autom Control 14(1):18. https://doi.org/10.1504/IJAAC.2020.103799
[12] Nath V and Mitra R (2014) Swing-up and control of rotary inverted pendulum using pole placement with integrator. Recent Advances in Engineering and Computational Sciences (RAECS), Chandigarh, India, 1-5. https://doi.org/10.1109/RAECS.2014.6799545.
[13] Park M, Kim YJ, Lee JJ (2011) Swing-up and LQR stabilization of a rotary inverted pendulum. Artif Life Rob 16, 94–97. https://doi.org/10.1007/s10015-011-0897-9
[14] Nghi HV, Nhien DP, Ba DX (2022) A LQR neural network control approach for fast stabilizing rotary inverted pendulums. Int J Precis Eng Manuf 23:45–56. https://doi.org/10.1007/s12541-021-00606-x
[15] Oh SK, Jung SH, Pedrycz W (2009) Design of optimized fuzzy cascade controllers by means of hierarchical fair competition-based genetic algorithms. Expert Syst Appl 36(9):11641-11651. https://doi.org/10.1016/j.eswa.2009.03.027
[16] Nguyen NP, Oh H, Kim Y, Moon J, Yang J, Chen WH (2020) Fuzzy-based super-twisting sliding mode stabilization control for under-actuated rotary inverted pendulum systems. IEEE Access 8:185079-185092. https://doi.org/10.1109/ACCESS.2020.3029095
[17] Yiğit İ (2017) Model free sliding mode stabilizing control of a real rotary inverted pendulum. J Vib Control 23(10):1645–1662. https://doi.org/10.1177/1077546315598031
[18] Balula S (2016) Nonlinear control of an inverted pendulum. Dissertation, Tecnico Lisboa
[19] Khalil HK (2015) Nonlinear control. Pearson Educ., New York, USA
[20] Lewis FL, Vrabie D, Syrmos VL (2012) Optimal control. Wiley, New York, USA
[21] Das S, Pan I, Halder K, Das S, Gupta A (2013) LQR based improved discrete PID controller design via optimum selection of weighting matrices using fractional order integral performance index. Appl Math Modell 37(6):4253-4268. https://doi.org/10.1016/j.apm.2012.09.022
[22] Kumar EV, Jerome J (2013) LQR based optimal tuning of PID controller for trajectory tracking of magnetic levitation system. Procedia Eng 64:254-264. https://doi.org/10.1016/j.proeng.2013.09.097

J. Innovative Eng. Nat. Sci., vol. 3, no. 2, pp. 205-218, 2023.
http://dx.doi.org/10.29228/JIENS.70524

JIENS
Journal of Innovative Engineering and Natural Science
Yenilikçi Mühendislik ve Doğa Bilimleri Dergisi

Original Paper

Journal of Innovative Engineering and Natural Science
(Yenilikçi Mühendislik ve Doğa Bilimleri Dergisi)
journal homepage: https://jiens.org

The economic potentials of reclaimed asphalt pavements (RAP) in urban road infrastructure: a case study of Yalova city

Kader Fenerci[a], Merve Ceyhan Erdoğan[a,*] and Yavuz Abut[a]

[a] *Department of Transportation Engineering, Yalova University, Yalova 77200, Türkiye.*

ARTICLE INFO

Article history:
Received 07 June 2023
Received in revised form 08 July 2023
Accepted 20 July 2023

Available online

Keywords:
Reclaimed asphalt pavement
Sustainability
Cost-benefit analysis
Environmental protection
Hot mix asphalt

ABSTRACT

Due to population growth and technological development, consumption is rapidly increasing all over the world. Waste materials are not disposed of properly, resulting in environmental and visual pollution, health problems and economic disadvantages. Although recycling of waste materials has been given more importance in recent years than in the past, 100% recycling is not possible. Recycling asphalt pavements, protecting natural resources and reusing waste materials are very important to avoid the landfills they create in nature. In addition, the economic benefits of RAP (Reclaimed Asphalt Pavement) cannot be neglected. In this study, the significance of asphalt pavement recycling in the world, recycling methods and economic benefits are highlighted. In addition, the average annual amount of asphalt pavement excavated in Yalova was determined and the approximate cost of using different percentages of RAP was performed. For the construction of 1 km of asphalt pavement, the road construction costs were evaluated and compared using 30%, 50% and 70% RAP. Based on the findings, 6%, 11% and 15% of the initial costs could be saved, respectively. Although 70% RAP usage increased the recycling cost by 12%, it decreased the bitumen use by 7.2%, the aggregate use by 10.6%, and the operation cost by 11.1%.

I. INTRODUCTION

In recent years, there has been a significant increase in consumption worldwide, driven by the development of production technologies and growing human needs. Consequently, the production of waste materials has also increased. Globally, approximately 2.01 billion tons of municipal solid waste is generated annually, with at least 33 percent of this waste being improperly managed from an environmental standpoint [1]. The World Bank Group projects that waste generation will nearly double to reach 3.40 billion tons worldwide by 2050, with a particularly substantial increase expected in low and middle-income countries like Türkiye, nearly tripling compared to the present [2]. In order to prevent environmental damage caused by waste and to incorporate them into the economy, it is crucial to implement recycling methods across various sectors for our future well-being. Transportation and highway engineering have emerged as key areas where recycling methods have gained considerable importance in recent years. Hot mix asphalt layers, particularly the top layers, experience deterioration over time due to various factors. In some cases, pavements become completely unserviceable, leading to undesirable scenarios. It is imperative to address potential deformations before the end of the pavement's projected lifespan to ensure its longevity and functionality. To ensure a comfortable and safe driving surface, it may be necessary to modify the road profile and remove the existing pavement. However, with the right application method, the removed asphalt pavement waste can be recycled and reused. There are several available methods for pavement recycling. The

---

*Corresponding author. Tel.: +90-226-815-6176; e-mail: merve.ceyhan@yalova.edu.tr

Asphalt Recycling and Reclaiming Association (ARRA) categorizes them into five main groups: Cold Planning (CP), Hot In-Plant Recycling (HIPR), Hot In-Place Recycling (HIR), Full Depth Reclamation (FDR), and Cold Recycling (CR) [3]. Among these methods, HIPR is the most commonly used, involving the mixing of Reclaimed Asphalt Pavement (RAP) with new materials and the addition of additives if necessary. Another method is HIR, which involves the addition of pure asphalt and/or aggregate, mixing the materials with a recycling or rejuvenating agent without removing them from the pavement site [4]. The benefits of utilizing RAP extend beyond environmental protection and include reducing the consumption of new materials, minimizing transportation needs, saving energy, improving mixing properties, and, most importantly, achieving economic gains [5]. The objective of this study is to draw attention to the amount of waste generated globally, particularly asphalt waste, and highlight the benefits of utilizing these wastes in the construction of new roads. The aim is to emphasize the advantages that can be achieved by incorporating RAP into road construction, focusing on the economic benefits and sustainability aspects in Yalova City. Firstly, the annual quantity of excavated asphalt pavement in Yalova was determined. Subsequently, a cost-benefit analysis was conducted to investigate the economic implications associated with recycling the determined amount at specific rates. In the conclusion, the study not only highlights the benefits of employing RAP in Yalova but also emphasizes global research efforts and initiatives focused on recycling natural resources. Furthermore, the positive effects of RAP usage on the environment are presented. While there is significant emphasis on the use of Reclaimed Asphalt Pavement (RAP) in America and Europe, there have been relatively few studies conducted in Turkey. Therefore, this study will serve as a valuable resource, particularly in terms of literature review, for future research on this subject.

II. FINANCIAL SYNOPSIS OF THE RAP MARKET

2.1 Market Sizing for Recycling Asphalt

Various types of waste materials, such as Construction and Demolition Waste (CDW), steel slags, plastics, crumb rubber, glass, and RAP, have been successfully recycled in construction of pavement [1]. RAP, in particular, has been utilized in asphalt mixes since 1915 [6] , establishing itself as one of the most extensively recycled construction products worldwide, with an approximate recycling rate of 88% [7]. Additionally, according to The Federal Highway Administration (FHWA), asphalt concrete is the most recycled material worldwide [8]. The National Asphalt Pavement Association (NAPA) further asserts that the majority of reclaimed asphalt is either reused or recycled, solidifying asphalt pavement as the most recycled material [9]. In 2019, approximately 140 million tons of RAP were used in asphalt pavements [10]. In 2020, this figure amounted to 125 million tons (with the USA accounting for 88 million tons in 2019 and 85 million tons in 2020) [11].

Every year, approximately 1.5 billion tons of asphalt concrete are produced worldwide, consuming 1.425 billion tons of aggregate and 75 million tons of bitumen [12, 13]. Highways experience deterioration over time due to various factors such as traffic, climate change, poor design, inadequate maintenance, and weak soil. This deterioration results in a decrease in serviceability, which negatively impacts comfort and economic parameters. In more severe cases, pavements become completely unserviceable and require excavation and replacement with new ones. However, it is possible to recycle the removed asphalt pavements and transform them into economic value. Similarly, as shown in Figure 1, Türkiye produces an average of 37.9 million tons of asphalt annually, indicating that the cost of asphalt production amounts to approximately $34.5 billion* per year. By recycling only 1% of these excavation wastes, several benefits can be achieved. Specifically, 379 thousand tons less excavated asphalt pavement waste will be generated, 360 thousand tons less aggregate will be used, and an average of 19 thousand tons less bitumen will be consumed. This not only helps in preserving natural resources but also significantly reduces environmental pollution.

Recycling asphalt pavements is a widely adopted practice in Europe and America, with countries like the United States, France, and Germany leading the way in this regard [14]. In the United States, asphalt and asphalt pavements are among the most commonly recycled materials [15].

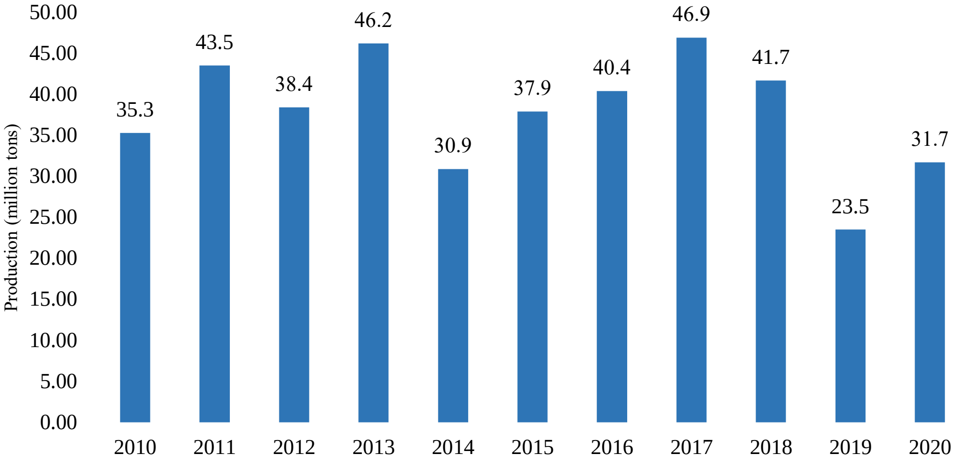

Figure 1. The total production of asphalt in Türkiye during the period of 2010-2020 [10], [11], [16]–[24]

*wearing course asphalt production cost is $91/tons [25]

Furthermore, according to NAPA, the majority of reclaimed asphalt in the United States is reused or recycled, making asphalt pavements the most extensively recycled material in the country [9, 26]. Additionally, EAPA reported that in 2020, 82.2 million tons of RAP and 1.05 million tons of recycled asphalt shingles (RAS) were utilized in the production of 370 million tons of new asphalt pavement mixes in the United States.

Table 1 presents the global quantities of reclaimed asphalt between 2010 and 2020. In the United States, in particular, an average of 74.6 million tons of reclaimed asphalt is generated annually, with 90-95% of this asphalt being effectively utilized in high-performance mixtures such as warm and hot mixes. Among European countries, several nations, including Germany, Italy, and France, demonstrate substantial amounts of reclaimed asphalt. Regarding Türkiye, as indicated once again in

Table 1, an average of 2.3 million tons of asphalt waste is removed annually over an eleven-year period.

Table 1. All available reclaimed asphalt in the World (in tons) [10], [11], [16]–[24]

Country	2010	2011	2012	2013	2014	2015	2016	2017	2018	2019	2020
Austria	500,000	550,000	750,000	750,000	1,500,000	1,350,000	1,400,000	1,650,000	1,900,000	1,800,000	1,260,000
Belgium	1,500,000	1,500,000	1,500,000	1,500,000	1,500,000	1,553,994	1,240,000	1,030	1,687,000	1,637,000	1,981,500
Croatia	75,000	No data	No data	No data	170,000	No data	80,000	No data	200,000	210,000	240,000
Czech Rep.	1,650,000	1,500,000	1,400,000	1,450,000	1,600,000	2,000,000	1,800,000	2,600,000	2,700,000	2,800,000	2,500,000
Denmark	350,000	600,000	580,000	790,000	1,300,000	1,300,000	1,150,000	1,165,000	1,185,000	1,255,000	1,160,000
Finland	1,000,000	1,000,000	1,000,000	860,000	1,000,000	1,160,000	1,150,000	1,200,000	1,300,000	1,500,000	No data
France	7,080,000	7,080,000	6,500,000	6,900,000	7,000,000	7,000,000	6,370,000	6,400,000	7,817,000	8,074,000	6,042,000
Germany	14,000,000	14,000,000	11,500,000	11,500,000	10,900,000	11,000,000	12,000,000	13,000,000	13,000,000	13,400,000	11,600,000
Great Britain	4,000,000	4,500,000	4,500,000	4,500,000*	3,350,000	3,500,000	3,250,000	3,400,000	6,100,000	6,050,000	4,973,106
Hungary	44,580	64,882	100,777	88,000	20,000	180,000	109,000	120,000	200,000	105,000	140,000
Italy	11,000,000	11,000,000	10,000,000	10,000,000	No data	9,000,000	9,000,000	9,000,000	9,000,000	9,500,000	9,500,000
Norway	750,000	726,000	787,689	686,268	834,410	932,049	1,112,000	No data	1,004,000	1,173,000	840,000
Romania	40,000	13,000	20,000	22,000	20,000	No data	No data	No data	No data	612,500	No data
Slovakia	No data	No data	33,000	26,000	30,000	75,000	54,000	50,000	150,966	165,600	135,846
Slovenia	26,160	10,000	10,000	26,000	40,000	37,000	56,000	84,000	106,200	150,000	170,000
Spain	1,590,000	1,350,000	368,000	205,000	390,000	410,000	490,000	494,000	1,165,000	1,486,000	1,900,000
Switzerland	1,450,000	1,750,000	1,575,000	1,370,000	1,000,000	No data	No data	No data	No data	1,650,000	No data
Türkiye	2,420,000	2,809,000	3,816,000	1,200,000	2,340,000	1,520,000	3,551,167	2,570,589	1,965,000	1,038,000	2,143,354
USA	66,500,000	71,400,000	64,000,000	69,000,000	68,700,000	69,700,000	74,200,000	72,500,000	91,700, 000	88,000,000	85,000,000
TOTAL	**113,975,740**	**119,852,882**	**108,440,466**	**110,873,268**	**101,697,410**	**110,718,043**	**117,012,167**	**114,234,619**	**141,180,166**	**140,606,100**	**129,585,806**

*(Continue to **Table 1**)*

As indicated in Table 2, among European countries, Italy and France rank highest in terms of the utilization of recycled asphalt in road construction, following Germany. RAP are commonly employed in the production of warm and hot mixed asphalt roads [11, 27]. Notably, Finland and Ireland achieved a remarkable 100% rate of reusing RAP in high-quality asphalt in 2020. In the United States, a substantial 85 million tons of asphalt pavement waste is utilized in the production of hot and warm mix asphalt, reaching an impressive rate of 93% by 2020. In Türkiye, the amount of reclaimed asphalt pavement utilized in 2020 reached 2,143,354 tons. According to EAPA, only 2% of this amount was used for hot and warm mix asphalt, while the remaining 98% was employed for unbound layers [11].

RAP has been the subject of numerous studies; however, only a few have compared the cost of recycled and virgin mixtures. An Illinois-based study evaluated the life-cycle cost and environmental impact of four pavement sections, each consisting of asphalt mixes with different RAP content: 0%, 30%, 40%, and 50%. The analysis conducted over a 45-year period demonstrated a significant cost reduction of up to $94,000 per mile, even with higher RAP content [14].

Table 2. Amount of available reclaimed asphalt in the World (in tons) and where to use in [11]

	Amount of reclaimed asphalt available to be used by the asphalt industry in 2020	**Hot and warm mix asphalt production**	**Half warm mix asphalt production**	**On-Site cold recycling**	**Plant cold recycling**	**Unbound road layers**	**Other civil eng. apps**	**Put to landfill/ Other Apps/ Unknown**
Austria	1,260,000	70	30					
Belgium	1,981,500	47	no data	no data	no data	no data	no data	no data
Croatia	240,000	33	0	0	2	no data	no data	no data
Czech Rep.	2,500,000	15	no data	25	no data	25	7	28
Denmark	1,160,000	85	no data	no data	no data	15	no data	no data
Finland	1,600,000*	100	0	0	0	0	0	0
France	6,042,000	76	10	no data	no data	no data	no data	no data
Germany	11,600,000	84	0	0	0	16	0	0
Great Britain	4,973,106	37	0	10	0	63		no data
Hungary	140,000	95	0	0	3	2	0	0
Ireland	220,000	100	0	0	0	0	0	0
Italy	9,500,000	25	75					
Norway	840,000	35	0	0	0	65	0	0
Romania	10,425*	0	0	100	0	0	0	0
Slovakia	135,846	53	0	30	0	17	0	0
Slovenia	170,000	29	0	10	1	25	10	25
Spain	1,900,000	72.7	0.2	0.2	0	24	3	0
Türkiye	2,143,354	2	0	0	0	98	0	0
USA	85,000,000	93	0	0	0.4	6.2	0.3	0

**there is no data about total amount of site-won asphalt generated*

RAP has been the subject of numerous studies; however, only a few have compared the cost of recycled and virgin mixtures. An Illinois-based study evaluated the life-cycle cost and environmental impact of four pavement sections, each consisting of asphalt mixes with different RAP content: 0%, 30%, 40%, and 50%. The analysis conducted over a 45-year period demonstrated a significant cost reduction of up to $94,000 per mile, even with higher RAP content [14]. Another case study focused on a 20% RAP content and performed a cost analysis, revealing a cost reduction of 14% compared to conventional materials [28]. Researchers also discovered that a mixture containing 40% RAP resulted in a 29% reduction in greenhouse gas emissions and a 26.2% decrease in life-cycle costs compared to a mixture without RAP additives [29]. Similar to various other examples worldwide, the idea of reusing asphalt pavements has gained prominence in Türkiye in recent years, driven by the crucial need for resource sustainability. The initial studies were conducted by ISFALT in 1996, where pavements excavated by the General Directorate of Highways (GDH) from the Çobançeşme-TEM connection road were applied at a 25% rate in a project in Bağcılar. However, certain issues arose during this application, requiring extensive laboratory testing. Recycling production of asphalt pavements gained momentum and significance from 2005 following partial trials conducted in 2001 [30]. Table 3 provides examples of recycling applications implemented in Türkiye.

Table 3. Recycling practices applied in Türkiye [31]

Region	Road Name	Firm	Application Layer	Recycle Type
GDH, 17th Regional Directorate	Sakarya Bridge Junction-Gümüşova Highway*	Gülsan	Binder, Bituminous Base	Cold in-Plant
DH, 3rd Regional Directorate	Şereflikoçhisar Aksaray-Ereğli road junction*	Fernas	Bituminous Base	Cold in-Plant
DH, 4th Regional Directorate	Bala road junction-Kulu road junction*	Fermak	Bituminous Base	Cold in-Plant
GDH, 9th Regional Directorate	Şanlıurfa Viranşehir Kızıltepe-Silopi Road*	Seza-DemyolACS	Binder, Bituminous Base	Cold in-Plant
GDH, 4th Regional Directorate	Ankara Kızılcahamam**	No data	All HMA Layers	Cold in-Place

2.2. European Green Deal and Circular Economy

Since our world is facing many problems such as climate change and environmental pollution, the European Union Commission has taken action on this issue. On December 11, 2019, the EU Commission released the European Green Deal which aims to make inhabited geography sensitive and harmless to the climate, environment, and nature until 2050 [32]. The concept of sustainability is key to achieving this goal. Sustainability creates and preserves conditions in which people and nature can exist in productive harmony, allowing present and future generations to fulfill their social, economic, and other needs [33]. Supporting biodiversity and public health, reducing carbon emissions and pollution, and preparing for a sustainable urban future not only benefit the global environment but also provide economic advantages. The three golden rules of sustainability—reduce, reuse, and recycle—can be applied to the asphalt industry [34].

Considering the impact of asphalt recycling on energy consumption, emissions, and the economy, it is concluded that studies on sustainable pavements should focus on minimizing energy usage and maximizing recycling efforts through the use of rapidly developing technology. This is essential to protect the environment and create a livable world for future generations [34]. Improving the performance of asphalt pavement materials is necessary to reduce energy consumption, greenhouse gas emissions, and associated costs for service, maintenance, and end-of-life projects. RAP materials offer an effective way to preserve natural resources and prevent the disposal of hazardous waste that harms the environment.

The long-term use of fuel, aggregate, and asphalt can be reduced by incorporating RAP. This leads to a reduction in greenhouse gas emissions, improved service quality, and support for sustainable practices. The greenhouse gas emissions and energy consumption levels associated with different percentages of RAP usage are illustrated in Figure 2 [35].

With a 50% RAP usage, greenhouse gas (CO_2) emissions decreased from 479,557 kg/km to 416,033 kg/km. Additionally, the amount of energy consumption, which was 6,543,635 MJ/km without the use of RAP material, was reduced to 5,672,810 MJ/km when 50% RAP was used. To achieve this reduction, it is crucial to recycle waste materials and prevent their accumulation in nature. Therefore, there should be an increase in RAP usage and recycling rates.

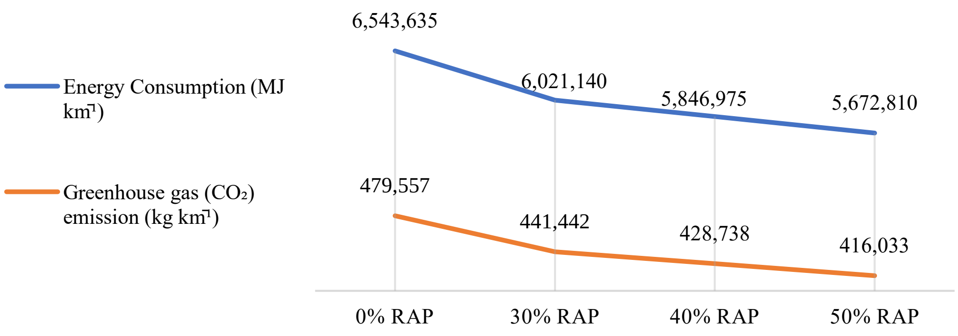

Figure 2. Greenhouse gas-CO2 emissions and energy consumption amounts due to using different RAP materials [35]

III. A CASE STUDY OF YALOVA CITY

Yalova, which is the smallest city in Türkiye in terms of surface area, has experienced a rapid increase in population due to immigration in recent years. When examining the geographical region of Yalova with a population of 276,050, it can be observed that the coastal areas, surrounded by the Marmara Sea, are flat, while the inland consists of elevated lands and maquis vegetation [36, 37]. The city is connected to surrounding provinces and districts through asphalt paved roads, and regular sea bus and ferryboat trips are organized to Istanbul due to its coastal location. Additionally, there has been significant development in freight transportation for national and international logistics, resulting in heavy vehicle traffic on the asphalt paved roads in these regions. Although Yalova lacks an airport, transportation is facilitated through the Yalova coach station, providing access to Istanbul Sabiha Gökçen Airport and Istanbul Airport. Asphalt pavement is extensively used for passenger and freight transport. However, the excavated asphalt pavement is not recycled and reused; instead, it is treated as waste material in various areas. This study aims to evaluate the feasibility of recycling asphalt in Yalova based on information obtained from Yalova Municipality and Yalova Special Provincial Administration.

3.1 Road Network and Construction Activities

In Yalova, four types of road surfaces are used: HMA (Hot Mix Asphalt) pavement, ICBP (Interlocking Concrete Block Pavement), chip seal, and dirt roads (unpaved roads). Among the surfaced roads, 65% are HMA and 5% are chip seal, with a total road length of 849,589 meters. On average, 10,000 tons of HMA are produced annually, with a production cost of $618,672.7. The annual average cost of road maintenance and repair for 5,000 tons of HMA is $281,214.8. Approximately 4,800 tons of excavated asphalt pavement waste are used annually in the construction of new stabilized roads, as part of the Granular Base Course and over the filling, as a fine material. Figure 3 illustrates the road construction, including 14,234 meters of chip seal, 3,846 meters of HMA, 143,026 meters of ICBP, and 14,011 meters of stabilized roads. Under the Special Provincial Administration, 1,232 tons of asphalt pavements are maintained and repaired at a cost of $35433.1. On average, 1,250 tons of asphalt pavement are excavated by the Special Provincial Administration. The waste materials are either taken to designated dumping areas as requested by the village headmen or used in areas within the villages where materials are needed.

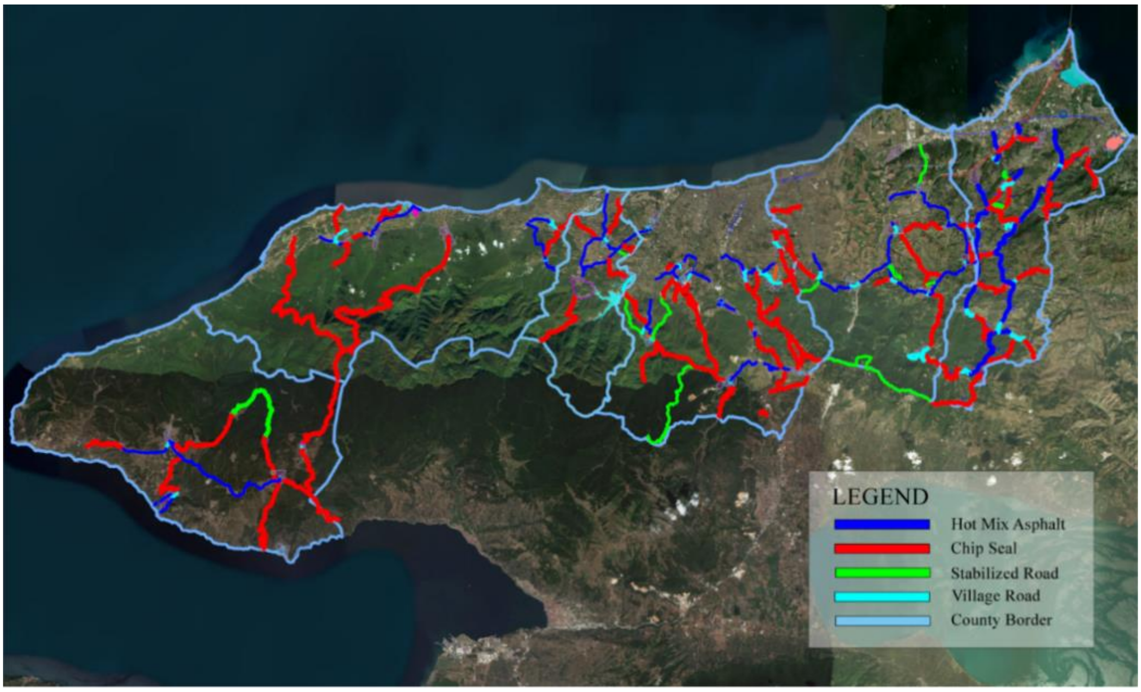

Figure 3. Distribution of Road Types under the Responsibility of Yalova Special Provincial Administration

3.2 Cost-Benefit Analysis

In this section, a cost-benefit analysis has been conducted for the implementation of a 1 km asphalt road in Yalova, considering the use of RAP instead of virgin aggregate. The analysis focuses on evaluating the cost and environmental benefits and opportunities associated with this approach.

Simge Group [13] conducted a study to examine the economic benefits of recycling the removed asphalt pavement waste and utilizing it in new pavements. Table 4 presents the results, indicating the gain rates for different RAP percentages: 6.7% for 30% RAP, 12.4% for 50% RAP, and 16.9% for 70% RAP. The cost comparisons were made by separately considering the parameters of *"Aggregate, Bitumen, Operating Expenses, and Recycling Expenses,"* and the differences and earnings ratios were evaluated. Also, considering the presence of bitumen in RAP, it is anticipated that incorporating RAP at rates of 30%, 50%, and 70% in the bitumen mixture, as indicated in the table, will result in respective increases of 4.2%, 8.2%, and 12%. In the first stage of the study, the annual amounts of excavated and constructed asphalt pavements in Yalova were determined. In the second stage, assuming the construction of a 1 km asphalt road, the initial construction cost was calculated without utilizing RAP material in this scenario. Subsequently, cost calculations were performed for using 30% RAP, 50% RAP, and 70% RAP on this 1 km road, respectively. Finally, a cost-benefit analysis was conducted to compare the different scenarios.

Table 4. Cost comparison asphalt production cost with and without using RAP [13]

Cost factors		**Without recycling**	**With recycling**		
		Aggregate Usage Rate	Reclaimed Asphalt Usage Rate		
		100%	30%	50%	70%
	Values mentioned on the chart are used as indicators of the content rates of unit cost				
Aggregate	Quarrying	3.7	2.6	1.8	1.1
	Back transport	3.4	2.4	1.7	1.0
	Crushing	3.1	2.2	1.5	0.9
	Carrying	5.1	3.5	2.5	1.5
	Total	15.2	10.6	7.6	4.6
	Difference		-30.0%	-50.0%	-70.0%
Bitumen	Bitumen Rate	5.0%	4.17%	3.70%	3.60%
	Bitumen	56.3	54.0	51.7	49.6
	Transport	0.8	0.8	0.8	0.7
	Heating	2.8	2.7	2.6	2.5
	Total	60.0	57.5	55.1	52.8
	Difference		-4.2%	-8.2%	-12.0%
Operating expenses	Electric	5.6	3.9	2.8	1.9
	Aggregate Heating cost of Asphalt Plant	11.3	7.9	5.5	3.9
	Labor Cost	5.6	5.6	5.6	5.6
	Total	22.5	17.5	13.9	11.4
	Difference		-22.5%	-38.3%	-49.3%
Cost For Reclamation	Electricity	0.0	1.3	2.2	3.1
	Aggregate heating costs	0.0	3.6	6.0	8.4
	Scrapping of Asphalt	1.1	1.1	1.1	1.1
	Transportation of Scrapped Asphalt	0.8	0.8	0.8	0.8
	Handling of Scrapped Asphalt	0.3	0.3	0.3	0.3
	Crushing and Screening of Scrapped Asphalt	0.0	0.6	0.6	0.6
	Total	2.3	7.7	11.0	14.3
	Difference		243.1%	388.4%	533.8%
	Total	**100**	**93.3**	**87.6**	**83.1**
			6.7%	**12.4%**	**16.9%**

IV. RESULTS AND DISCUSSIONS

Considering the components of HMA production costs without the use of RAP, as shown in Figure 4, the recovery costs of 2.3% are not associated with the utilization of RAP. This value solely represents the expenses related to scraping, transportation, and unloading of the removed pavement. When using 30% RAP, an increase of 1.3% in electricity costs, 3.6% in aggregate heating costs, and 0.6% in the crushing-sieving process of the removed asphalt pavement were observed as recovery costs. However, the reductions in aggregate and bitumen production, as well as operating costs, result in an overall gain of 6.9%. With 50% RAP material, an average gain of 12.4% was achieved, along with a 2.2% increase in electricity costs, a 6.0% increase in aggregate heating costs, and a 0.6% increase in the crushing-sieving process of the removed asphalt pavement. Nevertheless, the reductions in aggregate and bitumen production, as well as operating costs, make it economically beneficial when considering the total benefit.

Using 70% RAP material, an increase of 3.1% in electricity costs, an 8.4% increase in aggregate heating costs, and a 0.6% increase in the crushing-sieving process of the removed asphalt pavement were observed as recovery costs. However, the reductions in aggregate production, bitumen production, and operating costs result in a significant profit of 16.9% when considering the total benefit. Based on the research conducted by Yalova Municipality and Special Provincial Administration, it is determined that an average of 6,000 tons of asphalt pavement is excavated annually.

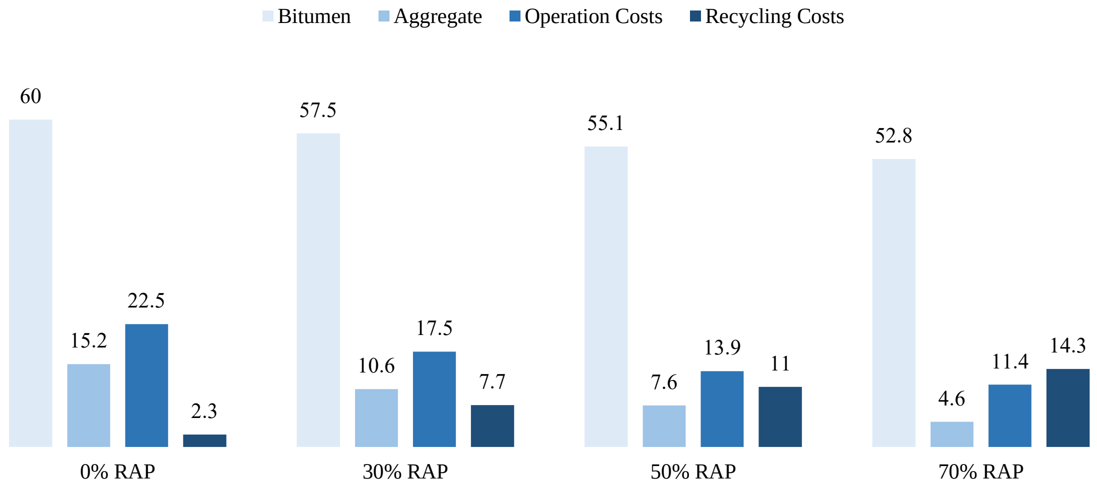

Figure 4. Cost components depending on the use of RAP at different rates (%)

As shown in Table 5, it is estimated that by recycling 30%, 50%, and 70% of the excavated asphalt pavement, gains of $4,341.1 to $25,549.6 can be achieved for 1,800, 3,000, and 4,200 tons of RAP, respectively. Apart from the financial benefits, recycling waste materials will protect the environment by preventing the creation of waste sites, reduce the use of natural resources, and significantly decrease greenhouse gas emissions associated with production and transportation. Cost-benefit analyses have been conducted in Table 6 and Table 7, considering the use of RAP at rates of 30%, 50%, and 70%, respectively. These analyses only include on-site production costs, and additional costs per ton, such as transportation, paving, compaction (labor), should be taken into account. Labor costs for paving and compaction, depending on the distance from the site, are typically around $1.7-$2.8 per ton. Moreover, expenses related to drainage works and horizontal and vertical marking should also be added.

Table 5. Comparison of recycling costs of asphalt pavements excavated in Yalova

Annual Average Amount of Asphalt Pavement Excavated (tons)	RAP Usage Rate (%)	RAP Amount (tons)	Initial Cost without using RAP ($)	Initial Cost with using RAP ($)	Profit ($)	Profit (%)
6000	30	1,800	64,791.9	60,450.8	4,341.1	6.7
6000	50	3,000	107,986.5	94,596.2	13,390.3	12.4
6000	70	4,200	151,181.1	125,631.5	25,549.6	16.9

Table 6. Asphalt pavement road construction cost without recycling for 1 km

Pavement Courses	Layer Thickness (m)	Density (tons m^{-3})	Road width (m)	Road length (m)	Amount (m^3)	Unit Cost ($)	Total Cost ($)
Excavation	0.15	1.60	7.00	1,000	1,050	3.4	3,543.3
PMB	0.15	1.60	7.00	1,000	1,050	5.6	5,905.5
						Subtotal	9,448.8
Wearing Course	0.05	2.40	7.00	1,000	840	36	30,236.2
Binder Course	0.08	2.40	7.00	1,000	1,344	33.2	44,598.4
						Subtotal	74,834.6
						TOTAL	84,283.5
Unit cost (per 1 m^2)							**12.04**

According to Table 6, the construction cost of a 1 km asphalt road is approximately $84,283.5. In this section, the use of RAP in the wearing and binder courses and the resulting savings in asphalt road costs were evaluated. It was planned to use 70% RAP in the wearing and binder courses, and as shown in Table 7, a cost saving was determined. Consequently, the total cost, which was $84,283.5, decreased by 15% to $71,636.4. By performing the same assessments, the use of 30% and 50% RAP in the wearing and binder courses was planned, and the cost saving was calculated. The total cost decreased by 6% from $84,283.5 to $75,004 with the use of 30% RAP, and it decreased by 11% from $84,283.5 to $79,269.5 with the use of 50% RAP. The increase in the utilization percentage of RAP to levels of 50-70% can potentially introduce challenges related to strength and durability [38, 39]. However, considering in terms of cost-effectiveness, environmental impact, and human well-being, usage of RAP in low-traffic volume road construction or as road maintenance material can still be advantageous along with a balance between the potential drawbacks and overall benefits [39].

Table 7. Asphalt pavement road construction cost with 30%,50% and 70% RAP for 1 km

Pavement Courses	Layer Thickness (m)	Density (tons m^{-3})	Road width (m)	Road length (m)	Amount (m^3)	Total Cost based on RAP usage ($)		
						30%	**50%**	**70%**
Excavation	0.15	1.60	7.00	1,000	1,050	3,543.3	3,543.3	3,543.3
PMB	0.15	1.60	7.00	1,000	1,050	5,905.5	5,905.5	5,905.5
					Subtotal	9,448.8	84,000	9,448.8
Pavement Courses	**Layer Thickness (m)**	**Density (tons m^{-3})**	**Road width (m)**	**Road length (m)**	**Amount (tons)**	**Total Cost based on RAP usage ($)***		
						30%	**50%**	**70%**
Wearing	0.05	2.40	7.00	1,000	840	28,210.3	26,487.0	25,126.3
Binder	0.08	2.40	7.00	1,000	1,344	41,610.3	39,068.3	37,061.3
					Subtotal	69,820.7	65,555.2	62,187.6
					TOTAL	79,269.5	75,004.0	71,636.4
Unit cost (per 1m^2)						**11.3**	**10.7**	**10.2**

**As mentioned before, for the calculations of asphalt production costs were decreased by 6.7% for 30% RAP, 12.4% for 50% RAP and 16.9% for 70% RAP.*

V. CONCLUSIONS

In this study, a cost-benefit analysis was conducted for the construction of a 1 km asphalt road in Yalova. The analysis focused on the benefits and opportunities of using RAP instead of virgin aggregate in asphalt pavements, considering cost and environmental factors. Based on the findings:

- It was observed that total production costs decreased by 6% to \$5,013.9 for 30% RAP usage, by 11% to \$9,279.4 for 50% RAP usage, and by 15% to \$12,647 for 70% RAP usage. These cost reductions indicate that recycling asphalt pavements can be a viable alternative for new road construction.
- Although energy consumption was not specifically addressed in this study for Yalova, references were made to existing literature. As previously mentioned in Figure 2, a study showed a decrease of approximately 7.6% in CO2 emissions, amounting to 63,524 kg per km, with the use of 50% RAP. Additionally, the use of 50% RAP resulted in an energy consumption reduction of 870,825 MJ per km. Despite the increase in recovery costs, the overall cost analysis favors the expansion of RAP usage due to the significant decrease in total production costs resulting from reductions in aggregate and bitumen production, as well as operating costs.
- Detailed life cycle cost analysis should be conducted to further explore the use of RAP in Yalova. To promote the recycling and reusability of pavement materials nationwide in Türkiye, an integrated management system could be established for recycling asphalt roads, which are classified as utilizable and recyclable waste. The government can incentivize municipalities and private entities to utilize RAP. Legislation must be enacted to mandate the use of recycled materials, and detailed regulations should be developed.
- The use of recycling methods and RAP in asphalt pavements not only helps preserve natural resources and prevent environmental damage but also offers significant financial gains. Non-recycled asphalt pavement waste poses significant harm to the environment when left untreated. Therefore, promoting the recycling and reusability of asphalt pavements is crucial not only in Türkiye but also worldwide. Taking steps to support the goals of the European Green Deal can contribute to creating a more sustainable world.

VI. RECOMMENDATIONS

- Conduct further research on different percentages of RAP usage: Although the study focused on 30%, 50%, and 70% RAP usage, it would be beneficial to explore the effects of other percentages as well. This can help identify the optimal balance between cost reduction and environmental benefits in asphalt pavement construction.
- Evaluate the long-term durability of RAP: While the cost-benefit analysis indicates the potential advantages of using RAP, it is important to assess the long-term performance and durability of asphalt pavements incorporating recycled materials. Longitudinal studies and field trials can provide valuable insights into the structural integrity and maintenance requirements of RAP-based road surfaces.
- Assess the feasibility of RAP in different geographical regions: The study focused on Yalova, but it would be valuable to evaluate the applicability of RAP in other regions of Türkiye or even in different countries. Factors such as climate, traffic patterns, and aggregate availability can influence the performance and cost-effectiveness of RAP, making it essential to assess its viability in diverse contexts.

- Investigate alternative recycling methods and technologies: While the study focused on RAP usage, it would be worthwhile to explore other innovative recycling methods and technologies for asphalt pavements. Technologies such as warm mix asphalt and cold recycling techniques have shown promising results in terms of cost savings and environmental benefits. Assessing their suitability and potential implementation can broaden the range of sustainable options.
- Promote collaboration and knowledge-sharing among stakeholders: To accelerate the adoption of sustainable practices in road construction, fostering collaboration among government agencies, research institutions, industry stakeholders, and environmental organizations is crucial. Sharing best practices, lessons learned, and success stories can facilitate the widespread implementation of recycling methods and encourage the development of standardized guidelines and specifications.

These suggestions aim to expand the scope of future research and provide a broader perspective on utilizing recycled materials in asphalt pavement construction beyond the findings and limitations mentioned in the article.

ACKNOWLEDGEMENTS

There are no conflicts of interest among the authors or any institutions, organizations, or individuals related to this study. The authors would like to express their gratitude to Yalova Municipality and Yalova Special Provincial Administration for sharing data related to financial and construction activities.

REFERENCES

[1] Kaza S, Yao L, Bhada-Tata P, Van Woerden F (2018) What a Waste 2.0: A Global Snapshot of Solid Waste Management to 2050 Urban Development Series Washington, DC: World Bank. http://dx.doi.org/10.1596/978-1-4648 -1329-0
[2] The World Bank (2022) Trends in Solid Waste Management. https://datatopics.worldbank.org/what-a-waste/trends_in_solid_waste_management.html#:~:text=The world generates 2.01 billion,from 0.11 to 4.54 kilograms. Accessed 10 November 2022
[3] Heneash U (2013) Effect of the repeated recycling on hot mix asphalt properties. Ph.D. Thesis, University of Nottingham.
[4] Chesner WH, Collins RJ, MacKay MH, Emery J (2002) User Guidelines for Waste and Byproduct Materials in Pavement Construction https://www.fhwa.dot.gov/publications/research/infrastructure/structures/97148/rap132.cfm. Accessed 13 January 2023
[5] Pereira P, Picado-Santos L (2006) Technical-Economical Evaluation of Pavement Recycling Alternatives Third Gulf Conf. Roads, 1,8.
[6] Milad A, Taib AM, Ahmeda AGF, Solla M, Yusoff NIM (2020) A review of the use of reclaimed asphalt pavement for road paving applications Jurnal Teknologi 82,3:35–45. http://dx.doi.org/10.11113/jt.v82.14320.
[7] Tarsi G, Tataranni P, Sangiorgi C (2020) The challenges of using reclaimed asphalt pavement for new asphalt mixtures: A review. Materials (Basel) 13,18. http://dx.doi.org/10.3390/ma13184052.
[8] Jahangiri B, Majidifard H, Meister J, Buttlar WG (2019) Performance Evaluation of Asphalt Mixtures with Reclaimed Asphalt Pavement and Recycled Asphalt Shingles in Missouri. *TRR* 2673,2:92–403. http://dx.doi.org/10.1177/0361198119825638.
[9] Donaghy S, (2014) Reuse, Recycle, Reclaim https://www.forconstructionpros.com/ home/article/12028936/ how-to-reuse-recycle-reclaim-asphalt Accessed 11 September 2022.
[10] European Asphalt Pavement Association (2009) Asphalt in Figures 2019, Annual Report.
[11] European Asphalt Pavement Association (2020) Asphalt in Figures 2020, Annual Report.
[12] Oruç Ş, Yilmaz B, Mazlum MS (2018) Geri Kazanılan Asfalt Kaplamaların Sıcak Asfalt Karışımlarda

Yeniden Kullanabilirliğinin Araştırılması Fırat Üniversitesi Müh. Bilim. Derg., 30,1:87–93.
[13] Simge Group (2022) Asphalt Recycling https://www.simgemat.com.tr/tr/CevreArge/AsfaltGeriKazanimi, Accessed 18 Jun 2022
[14] Aurangzeb Q, Al-Qadi IL (2014) Asphalt pavements with high reclaimed asphalt pavement content: Economic and environmental perspectives, *TRR*, 2456:161–169. http://dx.doi.org/10.3141/2456-16.
[15] Redling A (2019)RAP use in new asphalt pavement at all-time high, according to report," 2019. [Online]. Available: https://www.wastetodaymagazine.com/article/recycled-asphalt-pavement-napa-report/ Accessed Jun 18 2022
[16] European Asphalt Pavement Association (2018) Asphalt in Figures 2018, Annual Report.
[17] European Asphalt Pavement Association (2010) Asphalt in Figures 2010, Annual Report.
[18] European Asphalt Pavement Association (2011) Asphalt in Figures 2011, Annual Report.
[19] European Asphalt Pavement Association (2012) Asphalt in Figures 2012, Annual Report.
[20] European Asphalt Pavement Association (2013) Asphalt in Figures 2013, Annual Report.
[21] European Asphalt Pavement Association (2014) Asphalt in Figure 2014, Annual Report.
[22] European Asphalt Pavement Association (2015) Asphalt in figures 2015, Annual Report.
[23] European Asphalt Pavement Association (2016) Asphalt in Figures 2016, Annual Report.
[24] European Asphalt Pavement Association (2017) Asphalt in Figures 2017, Annual Report.
[25] Anonymous (2022) Asfalt Fiyat Listesi https://danisasfalt.com/fiyat-listesi/ Accessed 18 Jun 2022
[26] Butler C (2020) Asphalt Pavement = America's Most Recycled Material? https:// www. pavementsolutions. org/ asphalt-pavement-americas-most-recycled-material/ Accessed 01 Feb 2023.
[27] Bolden J, Abu-Lebdeh T, Fini E (2013) Utilization of recycled and waste materials in various construction applications American J of Env. Science, 9,1:14-24. http://dx.doi.org/10.3844/ajessp.2013.14.24.
[28] Rafiq W et al (2021) Life cycle cost analysis comparison of hot mix asphalt and reclaimed asphalt pavement: A case study Sustainability 13,8. http://dx.doi.org/10.3390/su13084411.
[29] Yao L, Leng Z, Lan J, Chen R, Jiang J (2022) Environmental and economic assessment of collective recycling waste plastic and reclaimed asphalt pavement into pavement construction: A case study in Hong Kong *J of Cleaner Production* 336,September 2021:130405. http://dx.doi.org/10.1016/j.jclepro.2022.130405.
[30] Sönmez İ (2012) İSFALT'ın Asfalt Karışımlarında Geri Dönüşüme Bakışı Asfaltta Geri Dönüşüm Teknikleri ve Uygulamaları Semineri
[31] Güngör AG (2012) Asfaltta Geri Dönüşüm Teknikleri ve Uygulamaları Semineri Seminer Notları :1–44
[32]ODD (2022) Avrupa Yeşil Anlaşması https://www.odd.org.tr/web_2837_1/entitialfocus.aspx?primary_id=2680&target=categorial1&type=31&detail=single Accessed 10 Jul 2022
[33] Ceylan H (2009) Asfalt Endüstrisi Çevre Kanunu İlişkisi Erciyes Üni Fen Bilim Enst Derg 25,1/2:71–98.
[34] KM, Terzi S, Akbulut H (2017) Asfalt Geri Dönüşümü Sürdürülebilirlik İlişkisi 7. Ulusal Asfalt Sempozyumu ve Sergisi
[35] Pouranian MR, Shishehbor M (2019) Sustainability assessment of green asphalt mixtures: A review Environments - MDPI 6,6:73. https://doi: 10.3390/environments6060073.
[36] Yalova Municipality (2022) Nüfus https://www.yalova.bel.tr/sayfa/nufus Accessed: 07 Aug 2022
[37] Yalova Municipality (2022) İklim ve Coğrafya https://www.yalova.bel.tr/sayfa/iklim-ve-cografya Accessed: 07 Aug 2022
[38] Gong H, Huang B, Shu X (2018) Field performance evaluation of asphalt mixtures containing high percentage of RAP using LTPP data Constr Build Mater 176:118–128. http://dx.doi.org/10.1016/j.conbuildmat.2018.05.007.
[39] Abdo AMA (2015) Utilizing Reclaimed Asphalt Pavement (RAP) Materials in New Pavements - A Review Int J Therm Environ Eng 12,1:10–16. http://dx.doi.org/10.5383/ijtee.12.01.008.

J. Innovative Eng. Nat. Sci., vol. 3, no. 2, pp. 219-227, 2023.
http://dx.doi.org/10.29228/JIENS.70527

Journal of Innovative Engineering
and Natural Science
(Yenilikçi Mühendislik ve Doğa Bilimleri Dergisi)
journal homepage: https://jiens.org

Original Paper

Characterization of heating elements of different dimensions used in resistance welding of thermoplastic matrix composite materials

Hakan Öztürkmen[a, b*], Yusuf Usta[b], Serkan Toros[c], Fahrettin Öztürk[a,d]

[a]*Mechanical Engineering, Gazi University, 06570 Ankara, Turkey,*
[b]*Turkish Aerospace Industries, Inc., 06980 Ankara, Turkey.*
[c]*Niğde Ömer Halisdemir University, 51240 Niğde, Turkey.*
[d]*Mechanical Engineering, Ankara Yıldırım Beyazıt University, 06010 Ankara, Turkey.*

ARTICLE INFO

Article history:
Received 7 June 2023
Received in revised form 19 July 2023
Accepted 21 July 2023

Available online

Keywords:
Composite
Thermoplastic
Resistance welding
Composite welding
Heating element

ABSTRACT

Resistance welding is one of the most useful methods for joining of thermoplastic composite materials. In this method, the joining process between two thermoplastic composite materials by passing a current through a stainless-steel heating element under pressure for a certain period. Within the scope of this study, meshes with a width of 12.7, 25.4, 38.1, 50.8, 63.5, 76.2 mm and a length of 160 mm were used to characterize the joule heating performance. These meshes have a mesh range of 33, 45, 61, 91, 109 and 154 microns. The temperature values on the heating elements were observed with a thermal camera by giving different current values to the relevant elements. Results reveal that the 12.7 x 160 mm heating element with 33-micron mesh spacing reached 349 ℃ under 10 A current, and the temperature value increased with current. In addition, it was determined that the resistance values of the heating elements with different widths were determined by the relevant system and the resistance properties changed non-linearly with the width.

I. INTRODUCTION

A composite material is one that is created by mixing two or more components having dissimilar physical and chemical qualities to create a new material with enhanced properties over the components used alone. Utilizing their strengths, these elements, also referred to as the matrix and reinforcing elements, are joined to create a new material. While the reinforcing material contributes the required mechanical qualities, such as strength and stiffness, the matrix material surrounds the reinforcement material and gives it flexibility. Aerospace, construction, recreational goods, and healthcare devices are just a few of the industries that employ composite materials. High strength-to-weight ratio, longevity, resistance to corrosion, and wear resistance are only a few of their advantages. Metal matrix composites, polymer matrix composites, and ceramic matrix composites are typical forms of composite materials.

Polymer materials are classified based on their qualities, chemical structures, and production techniques. Polymers are categorized into natural and synthetic polymers, and they are further classified into thermoset, thermoplastic, and elastomers based on their heating behavior. Thermoplastic materials are polymers that can be melted and reformed repeatedly without enduring any chemical changes as a result of heat. Simultaneously, due to its simplicity of use in industrial studies as well as being an easily formed, light, durable, and cost-effective material,

*Corresponding author. Tel.: +95459685799; e-mail: hakan.ozturkmen@tai.com.tr

nowadays, its usage has grown popular, both in academic studies and in manufacturing operations, compared to other polymers.

Polyethylene (PE), polycarbonate (PC), polypropylene (PP), and polyamide (nylon, PA) are some of the most prevalent thermoplastics used today. In addition to these, the polyaryletherketone (PAEK) family and polyphenylene sulphide (PPS) are high-performance thermoplastic polymers. Injection molding, extrusion, and thermoforming are some of the processes used in order to treat thermoplastics. Composite material welding is used to combine two or more composite materials to build a bigger structure. It can be done in several ways, including adhesive bonding, fusion bonding, and mechanical bonding.

In addition to allowing complicated structures to be created in one piece depending on the manufacturing processes, composite materials necessitate joining procedures, which have drawbacks such as production mistakes, mold costs, and so on. However, thermoplastic matrix composites offer greater weldability than thermoset materials in polymer matrix composites due to their reversible features.

Assembling or joining thermoplastic composite structures is becoming more important to replace metallic or thermoset matrix composite materials in the aerospace, automotive, and marine industries to improve static and fatigue loads [1–2]. Many connecting procedures for unreinforced and reinforced thermoplastic polymers have been developed [3]. However, each approach has a narrow range of uses. Traditional connecting methods for thermoplastic composites are laborious and expensive. Boeing Corporation's Defense and Space Group conducted a cost comparison study and indicated that fusion bonding (welding) a composite wing structure vs. a bolted structure might result in labor savings more than 61% [4]. Thermoplastic adhesive bonding is challenging due to the difficulties of adhering adhesive compounds to thermoplastic polymers. Mechanical bonding methods have issues due to stress concentrations, galvanic corrosion, mismatch of the thermal expansion coefficient, and drilling damage to the reinforcing fibers. These issues can be greatly reduced using thermoplastic composite welding or fusion bonding [5].

Heat is generated by the contact resistance of the materials when a current is applied to the system in resistance welding. The heat generated is used to connect the materials. Thermoplastic composite materials have insulating qualities, and currents are supplied to the system via heating components. The heat required for bonding is provided by electrically resistive heating sources placed between material surfaces in this approach. There is no requirement for complex geometry molding for resistance welding [1-6]. When a current move through a heating element, heat is produced according to the Joule's Law. As shown below, the energy (*E*) emitted by the resistor is proportional to its resistance (*R*), current (*I*), and elapsed time (*t*).

$$E = I^2Rt \tag{1}$$

After the temperature losses on the materials are overcome, it increases towards the adhesion surfaces and after a while, it rises above the melting temperature of the thermoplastic materials and melts the material. The molten materials held under pressure adhere by pressure. After the materials adhere, the current flow is stopped, and it is expected to cool under pressure. After the materials have cooled, the pressure is released, and the thermoplastic composites are joined by the resistance welding [7].

Ageorges et al. [8] presented a comprehensive experimental investigation of resistance welding of carbon and glass fiber reinforced polyetherimide (PEI) sheets. Thermoplastic samples designed according to lap shear and double cantilever beam tests were resisted by using fabric and one-way heating elements. They characterized the statistical distribution of the resistance of the heating elements and evaluated the effects of temperature on the heating element resistance

Dube et al. [9] used carbon fiber reinforced polyetherketone ketone (CF/PEKK), carbon fiber reinforced polyetherimide (CF/PEI), and glass fiber reinforced PEI (GF/PEI) composite materials in their study to determine the effects of metal mesh heating element size on the resistance welding of thermoplastic composites. As heating elements, four different metal mesh sizes with mesh spacing of 0.152, 0.104, 0.089, and 0.043 mm were used. They discovered that the wire diameter and gap width had a significant impact on weld quality and performance.

Colak et al. [10] performed resistance welding process modelling for thermoplastic composites in their study. By developing heat transfer, degradation kinetics and consolidation models, they created the process window, which is defined as the applicable ranges of controllable process parameters. An optimization method called as Nelder-Mead was used to determine the process parameters. Thus, they have ensured that the welded joint results in the desired quality and with minimum processing time. They found the optimum process parameters and welding times corresponding to the process parameters for different thicknesses of APC-2 PEEK thermoplastic composites. It was determined that as the thickness of the APC-2 plates increased, the power requirement decreased, and the welding time shortened. They found that the thickness of the insulation material affects the welding time

Wei et al. [11] conducted an experimental study on resistance welding using three types of stainless steel (SS) mesh with different dimensions and electrical resistances as heating elements for welding carbon fiber reinforced polyetheretherketone (PEEK) composite composites. They conducted a study to determine the effect of metal mesh on welding process and performance at different power densities ranging from 29 to 82 kW/m^2. According to the given power densities, they observed the temperature value of the heating elements in which time.

Within the scope of this study, a series of experimental studies were carried out to determine the maximum temperature values that meshes with different properties can reach with the applied current, and to determine with which currents the operation temperature levels of thermoplastic materials to be used in joining processes can be reached.

II. EXPERIMENTAL METHOD / TEORETICAL METHOD

In this study, a resistance welding mechanism was designed as shown in Figure 1 in order to conduct experimental work. In the designed resistance welding mechanism, there is a plate that holds the copper plates and is controlled by pneumatic pistons for vertical movement. An insulating material, specifically Teflon, is placed between the plate and the copper plates. The power supplied by the power supply unit is delivered to the heating elements through the copper plates. There are pneumatic pistons that enable the movement of C10100 nickel-based copper alloys plates, which has electrical resistivity value 10 μΩ/cm, in the system. The meshes placed between the copper plates are then compressed and current is applied. In order for the system to work safely, necessary insulations are provided between the copper plates and the support parts. The temperatures generated by the current supply were measured by scanning the surface of the entire mesh with a Nikon thermal camera, and the maximum temperature data were determined separately for all type meshes with the relevant system.

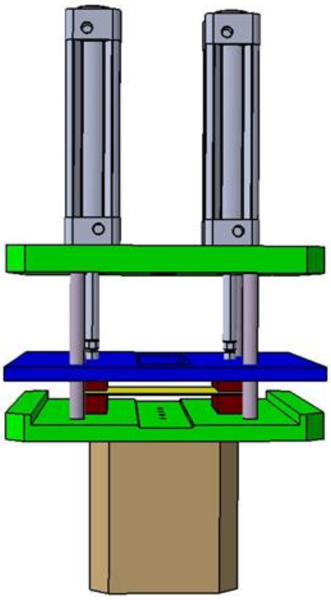

Figure 1. The designed resistance welding setup

The mesh spacing, mesh number, wire diameter, and opening area of the heating elements made of 316L stainless-steel material, which has electrical resistivity value 74 μΩ/cm, used in the study are shown in Table 1 and their 3D model images are shown in Figure 2. As known, 316L stainless steel material provides advantages in operation due to its austenitic characteristic.

In the study, the heating elements of different sizes in Table 1 were cut as 12.7 x 160 mm, 25.4 x 160 mm, 38.1 x 160 mm, 50.8 x 160 mm, 63.5 x 160 mm, 76.2 x 160 mm. The cut samples were powered by a DC programmable SORENSEN SGX50X200D-1DSAR model power supply. The temperatures formed on the heating elements were measured with the FLIR T530 thermal camera.

Table 1. Dimensions of heating elements

Mesh Spacing *(μ)*	**Mesh Number**	**Wire Diameter** *(mm)*	**Opening Area**
33	500	0.03	27%
45	300	0.04	28%
61	250	0.04	36%
91	180	0.05	42%
109	150	0.06	42%
154	100	0.1	37%

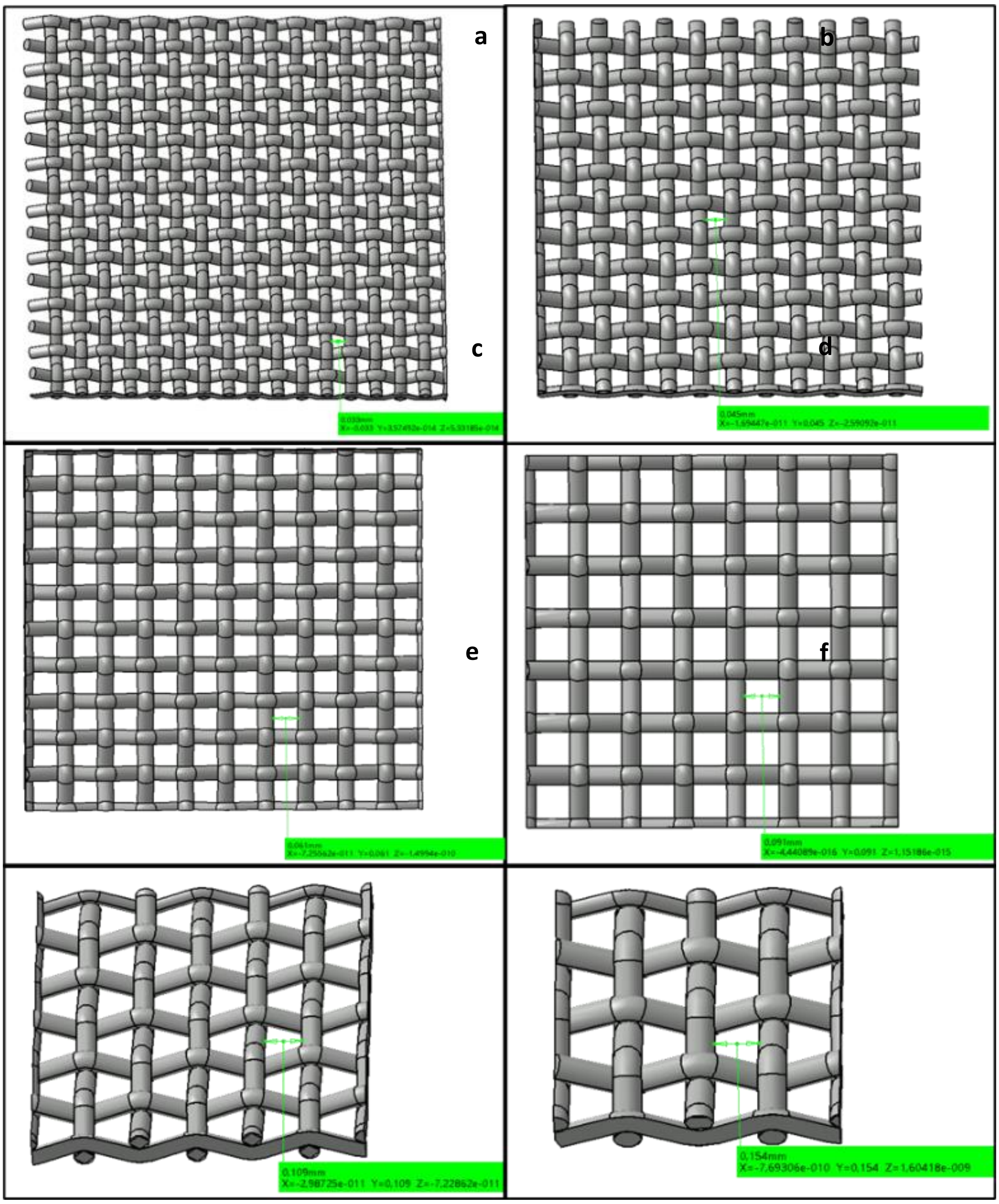

Figure 2. 3D model of heating elements with a length of 1x1 mm2 of heating elements with different mesh spacing a) 33 µm b) 45 µm c) 61 µm d) 91 µm e) 109 µm f) 154 µm

III. RESULTS AND DISCUSSIONS

The measured temperatures from 6 different heating elements according to different widths and different current values are shown in Figure 3. It was observed that more current is needed to reach high temperatures as the mesh gap increases. Considering the behavior of the heating element with 61-micron mesh spacing seen in Figure 3c, it is seen that the required current value to reach the desired temperature value is less than the heating element with 45-micron mesh spacing. The reason for this, was determined that the heating element with 61-micron mesh spacing and the heating element with 45-micron mesh spacing have the same thickness of wire diameter.

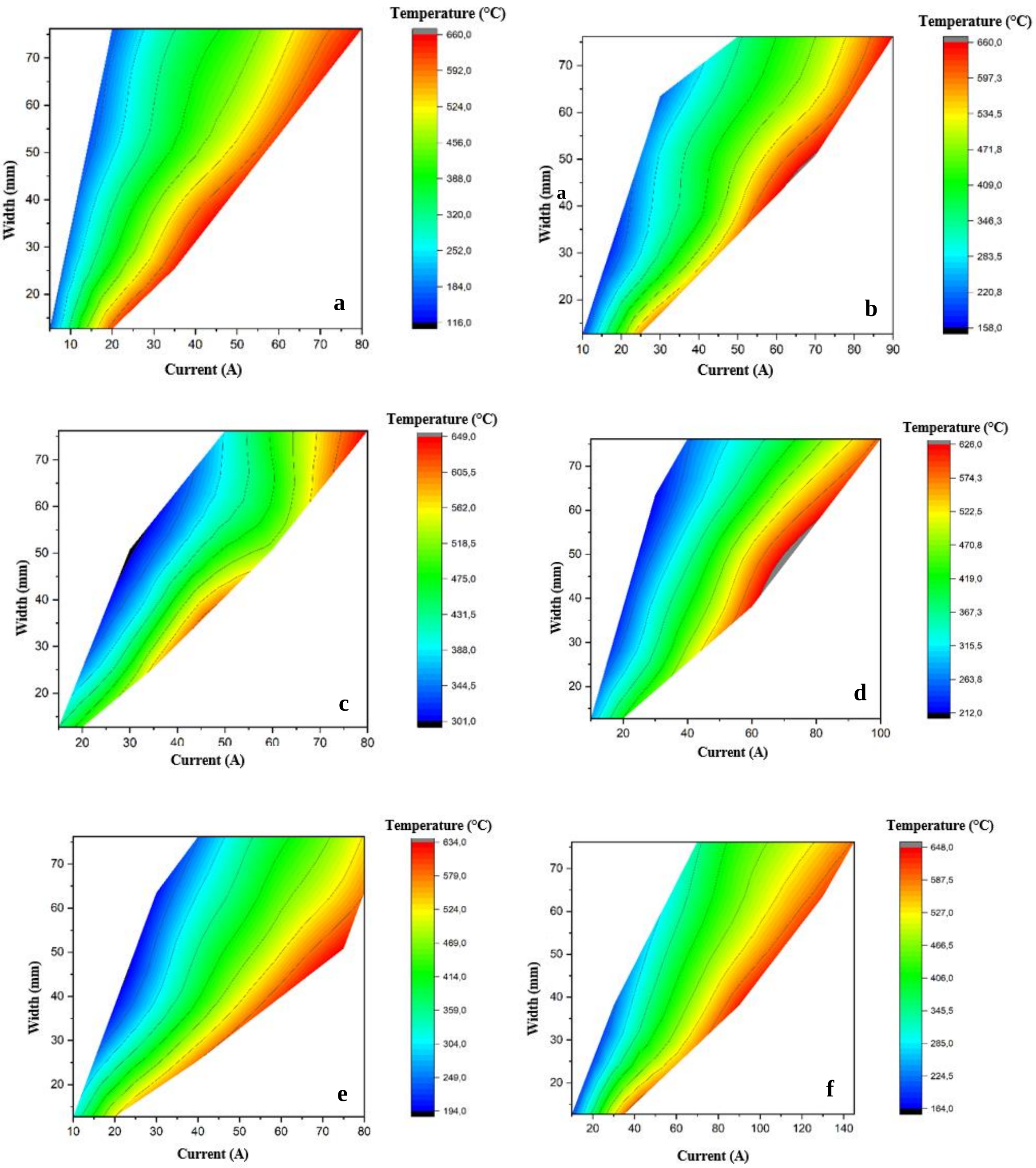

Figure 3. Current-width-temperature graph of the heating element with mesh spacing a) 33 µ, b) 45 µ c) 61 µ, d) 91 µ, e) 109 µ, f) 154 µ

In addition, it has been determined that as the width of the heating elements increases, the number of wires increases and the current per wire will decrease, and more temperature can be obtained by giving more current to the heating element. It has been observed that the current values given according to the width dimension do not increase linearly in order to reach the desired temperature value to be obtained from the heating elements.

The mathematical formulation for obtaining temperature values for each heating element was derived through regression analysis in the conducted study. The formulation, presented in Table 2, includes statistical metrics such as R-squared (R^2) and adjusted R-squared (R^2 adj) values.

Figure 4 shows the resistance values of the heating elements at different temperatures and currents. By reading the output voltage values of the heating elements, which are energized by the power source used, the resistance of the heating elements according to the varying temperatures and different widths, together with the given current values, was calculated from the connection between the current and voltage.

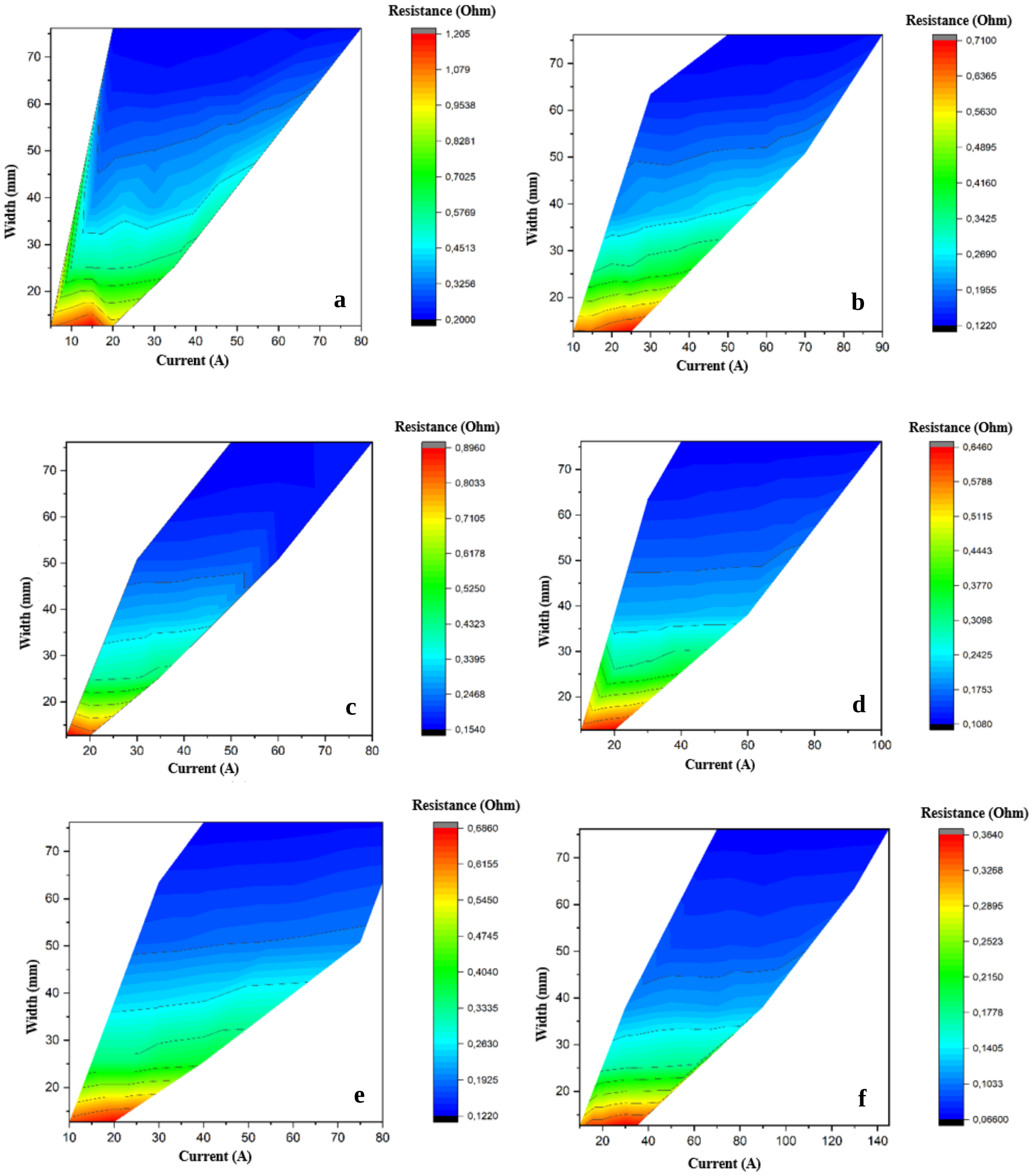

Figure 4. Current-width-resistance graph of the heating element with mesh spacing a) 33 µ, b) 45 µ c) 61 µ, d) 91 µ, e) 109 µ, f) 154 µ

The reason why the resistance value of the heating element with 61-micron mesh gap is higher than the heating element with 45-micron can be shown as the same wire diameter. It can be seen that this has a great effect since the resistance of the material depends on the cross-section area. In addition, since the heating elements produce energy according to the Joule law, the resistance values greatly affect the heating of the said elements.

Table 2. The formulas for temperature values of the heating elements based on current and width

Mesh Spacing *(μ)*	**Formulation**	**R^2**	**R^2 adj**
33	Temperature (°C) = 387,7 + 9,290 Current (A) - 5,849 Width (mm)	91.28 %	88.28 %
5	Temperature (°C) = 252,9 + 8,971 Current (A) - 5,047 Width (mm)	92.92 %	92.36 %
61	Temperature (°C) = 356,2 + 9,042 Current (A) - 6,113 Width (mm)	82.31 %	80.54 %
91	Temperature (°C) = 322,6 + 6,806 Current (A) - 5,013 Width (mm)	91.16 %	90.51 %
109	Temperature (°C) = 314,1 + 8,074 Current (A) - 5,553 Width (mm)	93.28 %	92.67 %
154	Temperature (°C) = 342,1 + 4,214 Current (A) - 4,259 Width (mm)	91.70 %	91.04 %

When we look at the study of Wei et al., [11], it was seen that the resistance value of the heating elements decreased as the mesh spacing of the these elements increased. In addition, it has been determined that the amount of current required to reach the desired temperature value increases with the increase in the width and thickness of the heating elements.

IV. CONCLUSIONS

In this study, a resistance welding unit was designed to weld thermoplastic matrix composite materials. By means of the designed resistance welding device, the temperature ranges that the heating elements made of stainless-steel material, which serves as an implant in the welding of composite materials, can be reached by cutting in 6 different sizes, the line length to which the current is supplied and in different widths, were measured. The measurement results show the minimum temperatures to be given to the composite material according to the melting and operating temperature of the thermoplastic composite materials to be welded. Due to the heat loss that may occur when composite materials are added on the materials, it has been determined that welding can be performed by taking 10% more of the current value in the current-width-temperature graph of the heating element desired to weld, in order to reach the operating temperature required for the welding of thermoplastic composite materials.

ACKNOWLEDGEMENT

The authors would like to thank to Turkish Aerospace Industries, Inc. for its all type of supports.

REFERENCES

[1] Benatar A, & Gutowski TG (1986) Method for fusion bonding thermoplastic composites. SAMPE Q.;(United States), 18(1).
[2] Stokes VK (1989) Joining methods for plastics and plastic composites: an overview. Polymer Engineering and Science, *29*(19), 1310-1324.
[3] Rudolf R, Mitschang P, Neitzel M, and Rueckert C (1999) Welding of high-performance thermoplastic composites. Polymers and polymer composites 7(5), 309-315.
[4] Wedgewood AR, Hardy PE (1996) Induction welding of thermoset composite adherends using thermoplastic interlayers and susceptors. Technology Transfer in a Global Community, 850-861.
[5] Maguire DM (1989) Joining thermoplastic composites. *SAMPE J.*, 25(1), 11-14.
[6] Xiao X, Hoa SV, Street KN (1994) Repair of thermoplastic resin composites bt fusion bonding. Compos Bond 1227, 30.
[7] Panneerselvam K, Aravindan S, Haq AN (2012) Study on resistance welding of glass fiber reinforced thermoplastic composites. Materials and Design 41, 453-459.

[8] Ageorges C, Ye L, Hou M (2000) Experimental investigation of the resistance welding for thermoplastic-matrix composites. Part I: heating element and heat transfer. Composites Science and Technology 60(7), 1027-1039.
[9] Dubé M, Hubert P, Gallet JN, Stavrov D, Bersee HE, Yousefpour A (2012) Metal mesh heating element size effect in resistance welding of thermoplastic composites. Journal of Composite Materials 46(8), 911-919.
[10] Colak ZS, Sonmez FO, Kalenderoglu V (2002) Process modeling and optimization of resistance welding for thermoplastic composites. Journal of Composite Materials 36(6), 721-744.
[11] Wei D. Gu Y, Zhu H, Li M, Wang S (2022) Influence of electrical heating metal mesh and power density on resistance welding of carbon fiber/PEEK composite. Polymers 14(13), 2563.